MECHANIKA

z. 80

SPIS TREŚCI

Yuliyan ANGELOV

University of Rousse, Bulgaria

MULTICRITERIA OPTIMIZATION OF METAL CUTTING MACHINE'S MAIN DRIVE

A parametric optimization problem is formulated for the metal cutting machine main drive as a multicriteria nonlinear optimization problem of robust dynamical system. A mathematical model determining amplitude-frequency characteristics of tortional forced-vibrations of the main drive is developed. An assessment system of the vibrational stability is presented. A procedure determining the unique Pareto optimal solution by means of direct approach and a compromising scheme based on the concept of the "utopical" point in the criteria space and procedure for a "μ-selection" are utilized for approximatelly solving the formulated problem. An example which considers the parametric optimization for the main drive of CNC machine CE063 is included.

INTRODUCTION

A variety of methods are employed for designing the main drives (MD) of metal cutting machines (MCM) and they all aim at construction optimization in a specific sense. Quality criteria are determined by different requirements - geometrical, kinematical, strength and deformation, dynamical, technological, economic, etc. Generally speaking, the selected criteria are conflicting, which leads to the necessity for formulating and solving a multicriteria design problem.

Quite often, despite the found optimal solution, the real construction of the designed object functions in an environment of various indeterminacies which can destabilize its performance and worsen the quality of technological processes. At the project development stage such indeterminacies are the unpredictable variations of some components of the unmanageable parameter vector. They are caused by different intervals of recommended coefficient values which give account for the elastic-dissipative characteristics according to the association conditions of the constructive components. This effect is intensified by unwanted stationary or non-stationary disturbances of the model parameters by external actions. Therefore, the solutions which are to be worked out in the process of synthesizing the object, have to show quality characteristics that are very little susceptible to parameter disturbances.

In general, the problems of robust dynamic systems synthesis are formulated as problems of robust dynamic model, robust phase coordinates, robust quality criterion, selection of optimal nominal of the unmanageable parameters, etc. [8].

Conditions for structure robustness are included in the optimization problem in different ways, because of the ambiguous interpretation and assessment of the property of robustness. In [7] robustness is achieved by varying the unmanageable vector components in a planned experiment, and the condition for robustness of the dynamic system is set as a limit in the optimization problem structure. Thus, parameter robustness is a priori present in the optimal solution which is found. The paper presents and solves the

multicriteria parameter optimization problem for the main drive of a metal cutting machine as a robust dynamic system synthesis in a given frequency domain.

OPTIMIZATION MODEL

Mathematical model

The examined object is a split MD with aggregate structure which includes a DC motor, a two-stage gearbox and a spindle unit connected with belt drives [1].

For steady-state operating modes with the assumptions for a discrete mechanical system with linear characteristics of the elastic-dissipative ties [4], MD is presented by an adapted dynamic model (DM) (Fig. 1) for each kinematic chain l with parameters – the adapted values of: mass moments of inertia J_j of concentrated masses, elasticity coefficient k_i, damping coefficient h_i and external influence moments M_j, where $j \in \mathbf{J} := [1:n]$, $i \in \mathbf{I} := [1:(n-1)]$, $l \in \mathbf{L} := [1:2]$.
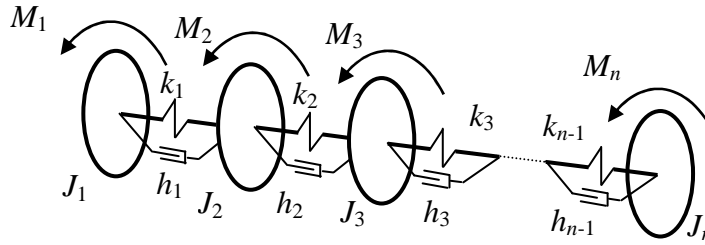
Fig. 1. Adapted model of a metal cutting machine main drive (MD)

For the case of a dissipative mechanical system with harmonic disturbances and generalized coordinates, the rotation angles of the concentrated masses, the differential equations of motion are worked out by Lagrange equations of the second kind. The mathematical model for determining the amplitude-frequency characteristics (AFC) of the adapted DM is found from their solution for the induced vibrations whose amplitudes D_l in a complex form are expressed by the equations

$$D_l = [(C_l - f^2 A_l) + i\, f\, B_l\,] \setminus Q_l, \quad l \in L. \tag{1}$$

Here A_l, B_l and C_l are square matrices which contain the respective generalized adapted inertia, resistance and elastic coefficients, Q_l is a vector whose elements are the generalized amplitudes of the external influence, and $\mathbf{f}$ is the vector of harmonic disturbance frequencies.

Parameters of the mathematical model

The elements of the matrices $\mathbf{A}_l$, $\mathbf{B}_l$ and $\mathbf{C}_l$ are expressed by the characteristics J_j, k_i and h_i of the adapted DM (fig. 1), which are determined unambiguously through the functional dependencies

$$J_j = J_j\,(\mathbf{r}, \boldsymbol{\rho}),\ k_i = k_i\,(\mathbf{r}, \boldsymbol{\rho}),\ h_i = h_i\,(\mathbf{r}, \boldsymbol{\rho}, \boldsymbol{\psi}). \tag{2}$$

Here r is the vector whose elements are the geometrical parameters of the structural elements of the main drive, worked out through the kinematic and strength - deformation dimensioning, ρ – the vector with elements that give account for the

8

physical-mechanical properties of the materials used, and ψ – is the vector with elements that gives account for the dissipation of mechanical energy, depending on the structural elements association conditions.

From the condition for keeping the prototype structure, the calculation diameters $u := \{u_\lambda \in r\}$, $\lambda \in [1:4]$ of the belt drives, are assumed as variable parameters. The parameters J_j, k_i and h_i of the adapted DM are explicit functions of u_λ and are presented by familiar theoretical and empirical dependencies [4].

In specialized literature, the elements of vectors ρ and ψ are usually presented within definite intervals with recommendations for a respective choice. Most often these are different coefficients which define the k_i and h_i characteristics. This results in certain indeterminacies in the found AFC and the respective quality assessment. In the optimization problem these values form the unmanageable parameter vector with limited interval disturbances $\alpha := \{\rho, \psi\} \in A$, where A is a given bounded set.

The vector of invariable parameters $p \subset r$, which determine unambiguously AFC of MD form the set of specified parameters $p \in P$.

The generalized load Q_l is assumed of a harmonic kind, and is applied on the concentrated mass. Its amplitude is defined by the tangent component of the cutting force for a frequently used technological operation – turning of workpieces with 5% variation of the feed rate per revolution with 4 mm cutting depth and filing 0,25 mm/rev. In the problem solved here, the tangent component is assumed to be the one respective to the spinning frequency of the spindle unit for the calculation chain. The adapted induced effects at such technological load are with frequency $f^E = 22,5$ Hz.

Constraints

The kinematic condition for preservation of the spindle spinning frequency is a functional constraint of an equality type $H(u) = 0$.

The strength and deformation conditions for the constructional elements and their joints are domain constraints, and are generalized as $G(u) \leq 0$.

The requirement for preservation of the main structural elements of the drive, causes interval constraints $u^- \leq u \leq u^+$ to the variation of controlling parameters.

With the set constraints, the optimization model can be generalized as follows

$$\Psi(D_l(f), u, \alpha, p) = 0, \quad l \in L,$$

$$u \in U := \{u \in E^3 : H(u) = 0, G(u) \leq 0, u^- \leq u \leq u^+ \}, \qquad (3)$$

$$\alpha := \{\rho, \psi\} \in A, \quad p \in P, \quad f \in [0, f_m] \in F,$$

where f_m is a point from the frequency range.

QUALITY CRITERIA

General assessment of the MD vibration resistance is given by the relative differences between the MD's proper vibrations f_l and the external disturbances vibrations f^E [1].

$$\phi_{1,2} = \left| 1 - f^E / f_l \right|, \quad l \in \mathbf{L}, \qquad (4)$$
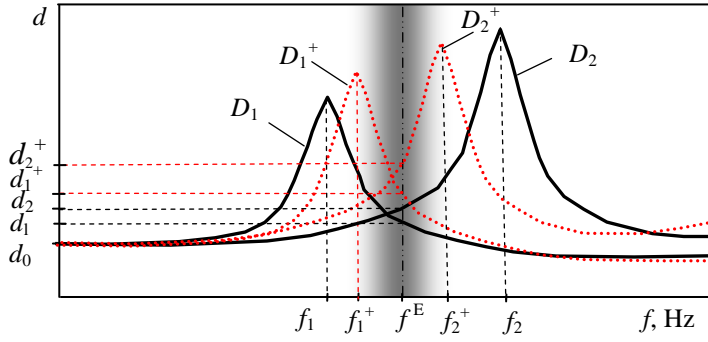
Fig. 2. Amplitude-frequency characteristics

Quantity assessment of the dynamic influence of disturbance forces on the mechanical system at a specific frequency f^E is given by the dynamism coefficients

$$\phi_{3,4} = d_l / d_{l,0}, \quad l \in \mathbf{L},$$

where d_l is the amplitude of induced vibrations at frequency f^E, and $d_{l,0}$ – its static deviation (Fig. 2).

The sensitivity of the designed structure at parameter disturbances [α…α..] of the α-vector elements is assessed through the relations of quantity variations forming the characteristics (4) and (5).

$$\phi_{5,6} = | d_l^+ - d_l | / | f_l^+ - f_l |, \quad l \in \mathbf{L}. \tag{6}$$

The quantity of the used material is of economic importance and is assessed through the relation of the designed object's mass m and the prototype's mass m_p

$$\phi_7 = m / m_p. \tag{7}$$

The adapted mass inertia moment is an indicator of a dynamic property in transient processes. In this problem it is assessed for a kinematic chain, which provides the wide spinning frequency sub-ranges, through its relative value to that of the prototype

$$\phi_8 = J / J_p. \tag{8}$$

The set criteria (4)-(8) form a vector criterion

$$\phi\,(u) \in \Phi = :\{\,\phi_v\}, \quad v{:=}[1{:}8], \tag{9}$$

subject to minimizing.

OPTIMIZATION PROBLEM

For the mathematical model (2) the optimization problem is formulated

$$\mathrm{P}min_{\,u \in \Delta}\,\Phi, \quad \Delta = :\{\,\Psi(D(f),\,u,\,\alpha,\,p) = 0,$$

10

$$u \in U, \ \alpha \in A, \ p \in P, \ f \in F\}, \ \phi(u) \in \Phi, \qquad (10)$$

where 'P*min*' is a Pareto-minimizing operator [6] of all components of vector $\phi(u)$.

The solution of problem (10) are two sub-sets: $\Delta^* \subset \Delta$ of effective points $u^* \in \Delta^* \equiv \{u^*: u^* = \text{arg Pmin}_{u \in \Delta} \Phi\}$; $\Pi^* \subset \Pi$ - from the corresponding to Δ^* Pareto-optimal points $\phi^* \in \Pi^* \equiv \{\phi^*: \phi^* = \phi(u^*)\}$. The choice of one compromising solution can be significantly facilitated through a well-grounded decrease of the sub-sets of Δ^* and Π^*.

CALCULATION PROCEDURE

A two-stage procedure is used to solve problem (10) [2]. At the first stage the sub-sets Δ^* and Π^* are builtemploying the PSI (Parameter Space Investigation) – method [6].

At the second stage, with the help of the so called "procedure for μ-selection" [2], the sub-sets $M_R \subset \Pi^*$ are defined and arranged according to their order of efficiency $R \in \{6, 5, \ldots, 1\}$. The sub-set of the highest order $M_{R=6}$ usually contains only one point, which is Salukvadze-optimal solution (u^S, f^S) [5]. It opens the possibility for a steady approach of the partitive criteria to their uncompromising optimal values (the utopian point u°).

The final compromising solution ($u^\#, f^\#$) can be chosen by means of a sequential analysis of the selected Pareto-optimal sub-sets M_R in a descending order.

NUMERICAL EXPERIMENT RESULTS

An iterative variation scheme in the domain U is used for the calculation process [6]. It is a sounding according to the PSI-method with 20741 Sobolev test points. 4096 of them form a legitimate sub-set $\Delta \subset U$. A set Π^*, of 2496 Pareto-optimal solutions, is selected in the reachable domain Π; these solutions are presented by the symbol "•" in fig.4.The corresponding points of the legitimate sub-set $\Delta^* \subset \Delta$ are presented in Fig. 3 by the same symbol.
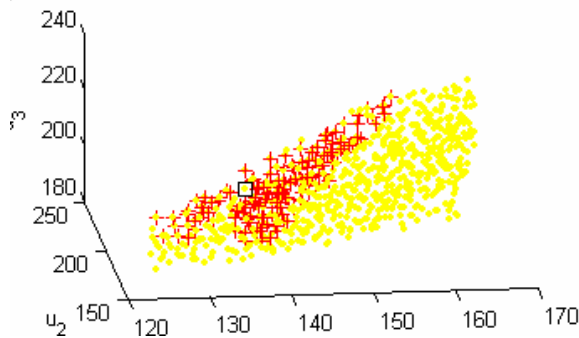
Fig. 3. A set of effective points $\mathbf{\Delta^*}$
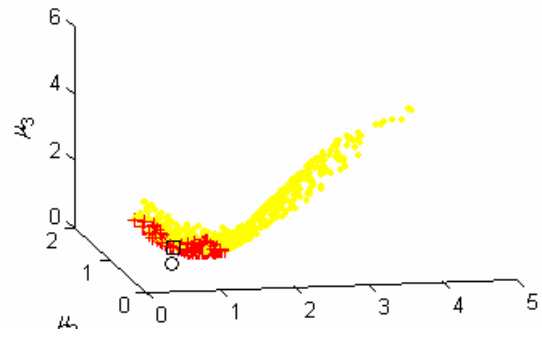
Fig. 4. A set of Pareto-optimal points $\mathbf{\Pi^*}$

Part of the results of the μ-selection ($\mu \equiv [\mu_j]$, $j = 1, 2, 3$) carried out, are presented in Fig. 4 and in Table 1. The utopic point u° in the μ-space is presented by

the symbol " ∘ ", and the Salukvadze-optimal solution (the test point from row $R = 6$ in Table 1) – by "□".

The $M_{R = 5}$ sub-set of the Pareto-optimal solutions from the next most efficient row, as well as the effective points which correspond to them are presented in fig.4 and fig.3 by the symbol "+". The analysis of their solutions makes it possible seven more compromising versions to be outlined. Two of them are shown in Table 1.

Table 1. Selected Pareto-optimal solutions

Row	Point №: u_1, u_2, u_3, u_4	f_1	f_2	f_3	f_4	f_5	f_6	f_7	f_8
–	u°	0.0486	0.0295	3.670	1.545	0.0115	0.0031	0.767	0.940
$R = 6$	95: 134,182,203,207	0.0588	0.0363	4.314	1.949	0.0255	0.0043	0.965	1.018
$R = 5$	292: 137,184,207,210	0.0588	0.0361	4.311	1.942	0.0251	0.0041	0.995	1.029
$R = 5$	1727: 144,182,209,225	0.0589	0.0379	4.396	2.049	0.0223	0.0040	1.057	1.086
$R = 2$	1640: 141,193,180,180	0.0602	0.0485	4.468	2.712	0.0303	0.0034	0.767	0.961

The number 292 point has minimal values according to the criteria ϕ_ν, $\nu:=[1:6]$, which means that the designed object will have better dynamic characteristics compared to the found Salukvadze-optimal solution, but with higher compromise levels according to the criteria ϕ_7 and ϕ_8.

The number 1727 point ensures the lowest sensitivity to AFC of DM for the two kinematic chains with parameter disturbances – the ϕ_5 and ϕ_6 criteria.

The minimal mass is given by the parameters of point 1640. It belongs to the $M_{R = 2}$ set and the minimal values according to criterion ϕ_7 are achieved at the expense of higher compromise levels according to the other criteria.

REFERENCES

1. Angelov Y.A.: *Parametrical research of the vibrational stability of the metal cutting machine's main drive*. Machines, Technologies, Materials, vol. 3/118, Sofia, 2010, (in Bulgarian)

2. Ivanov I.V., Vitliemov V.G., Koev P.A.: *Procedure for the selection of a reduced set of Pareto-optimal solutions*. Mechanics of machines, issue 55, (in Bulgarian).

3. Miettinen K.M.: *Nonlinear multiobjective optimization*. Kluver Academic, Boston, 1999.

4. Reshetov D.N., (edit.).: *Components and mechanisms of metal cutting machines*. Issue 2, Mashino-stroenie, Moscow, 1972, (in Russian).

5. Salukvadze M.E.: *Vector-valued optimization problems in optimal control theory*. Academic Press, New York, 1979.

6. Statnikov R.B., Matusov J.B.: *Multicriteria analysis in engineering*. Kluwer, Dordrecht, 2002.

7. Stoyanov S.G.: *Robust multicriteria optimisation of mechanical systems*. Mechanics of machines, issue 35, 2001, (in Bulgarian).

8. Tsonev, S.V., Vitliemov V.G, Koev P.: *Optimisation methods*. Ruse, 2004, (in Bulgarian).

Zuzana BAKSIOVA

Technical University of Košice, Slovakia

PRINCIPAL STRAIN SEPARATION ON COATED SPECIMEN

This paper deals with principal strain separation with strain gages. A normal-incidence photoelastic measurement on the PhotoStress coating provides the difference in principal strains at the test point. If the sum of the principal strains can be measured at the same point, then the separate principal strains are obtainable by simply adding and subtracting the two measurements. The measurement is performed on coated specimen.

1. GENERAL INFORMATION OF THE PHOTOSTRESS METHOD

PhotoStress is a widely used full-field technique for accurately measuring surface strains to determine the stresses in a part or structure during static or dynamic testing. With the PhotoStress method, a special strain-sensitive plastic coating is first bonded to the test part. Then, as test or service loads are applied to the part, the coating is illuminated by polarized light from a reflection polariscope. When viewed through the polariscope, the coating displays the strains in a colorful, informative pattern which immediately reveals the overall strain distribution and pinpoints highly strain areas (Figure1). With an optical transducer (compensator) attached to the polariscope, quantitative stress analysis can be quickly and easily performed. Permanent records of the overall strain distribution can be made by photography or by video recording [3].

Figure 1. Full-field interpretation of strain/stress distribution

PhotoStress testing provides an accurate and economical means for stress analysis of any part or structure, regardless of the part's complexity or material composition. With PhotoStress you can:

- Instantly identify critical areas, highlighting overstressed and understressed regions.
- Measure principal stress directions and principal stress magnitudes.
- Accurately measure peak stresses and determine stress concentrations around holes, notches, and other potential failure sites.
- Optimize the stress distribution for minimum weight and maximum reliability.
- Test repeatedly under varying load conditions, without recoating the part.
- Make stress measurements in the laboratory or in the field — unaffected by humidity or time.
- Detect yielding, and measure assembly and residual stresses [7].

2. RELATIONSHIPS BETWEEN FRINGE ORDERS AND MAGNITUDES OF STRAIN AND STRESS

The fringe orders observed in PhotoStress coatings are proportional to the difference between the principal strains in the coating (and in the surface of the test part). This simple linear relationship is expressed as follows:

$$\varepsilon_1 - \varepsilon_2 = N \frac{\lambda}{2\,tK} = N\,f\;. \qquad (1)$$

where: $\varepsilon_1, \varepsilon_2$ = principal strains in coating, N = normal-incidence fringe order, λ = wavelength of yellow light (575 nm), t = thickness of PhotoStress coating, K = strain-optic coefficient of coating, $f = \lambda/2tK$ = fringe value of coating.

Assuming the strains in the coating precisely replicate those in the test-part surface, and assuming the part is stressed below its proportional limit, Hooke's law can be applied as follows to determine the difference of principal stresses:

$$\sigma_1 - \sigma_2 = \frac{E}{1+\mu}(\varepsilon_1 - \varepsilon_2)\;. \qquad (2)$$

where: σ_1, σ_2 = principal stresses in test part, E = elastic modulus of test material, μ = Poisson's ratio of test material.

Equations (1) and (2), which are the primary relationships used in photoelastic coating stress analysis, give only the difference in principal strains and stresses, not the individual quantities. To determine the individual magnitudes and signs of either the principal strains or stresses generally requires, for biaxial stress states, a second measurement, such as the sum of the principal strains [5].

3. PRINCIPAL STRESS SEPARATION WITH STRAIN GAGES

In addition to its unique capability as a full-field technique for visualizing stress distribution, the PhotoStress method provides quantitative stress measurement at any selected point or points on the coated surface of the test object. At interior locations, removed from a free edge, the stress state is commonly biaxial; and it is sometimes necessary to determine the separate principal stresses, as well as their difference. This paper describes a method of making the required additional measurement for determining the separate principal stresses from the photoelastically derived stress difference. The procedure uses a specially designed strain gage (stress-separator gage) which is applied to the coating surface after the normal-incidence reading has been made.

The PhotoStress Separator Gage embodies a number of special features designed for ease of use and optimum performance in PhotoStress applications. First in importance, of course, is that the gage does not require any particular angular orientation. It is simply bonded at the point where separation measurements are desired. Separator Gauges must be used with a specially designed interface module in conjunction with the Measurements Group P-3500 Strain Indicator. The Model 330 Interface Module is a four-channel switch-and-balance unit with precision resistive circuits for reducing gauge excitation voltage to minimize self-heating effects, supplying bridge-completion for the 200-Ohm Separator Gauge and attenuating the gauge output so that the P-3500 Strain indicator reads out in units of 10 microstrain.

As noted earlier, a normal-incidence photoelastic measurement on the PhotoStress coating provides the difference in principal strains at the test point. If the sum of the principal strains can be measured at the same point, then the separate principal strains are obtainable by simply adding and subtracting the two measurements [4].

Representing the gage output signal by the symbol S_G, for convenience in algebraic manipulation:

$$S_G = \frac{\varepsilon_1 + \varepsilon_2}{2},$$ (3)

and

$$\varepsilon_1 + \varepsilon_2 = 2\,S_G.$$ (4)

Adding and subtracting with Equation (1),

$$\varepsilon_1 = S_G + \frac{N\,f}{2},$$ (5)

$$\varepsilon_2 = S_G - \frac{N\,f}{2}.$$ (6)

4. EXAMPLE OF SEPARATION ON COATED SPECIMEN

The following example is provided to illustrate the calculating the separate principal stresses from the combined photoelastic and separator strain gage measurements.

Specimen of steel ($E = 2,1 \cdot 10^5\,MPa$, $\mu = 0,3$) has been coated with Type PS-1 photoelastic sheet, 3,1 mm thick. For plane surfaces, premanufactured flat sheets are cut to size and bonded directly to the test part. The fringe value f for the coating is $605\,\mu\varepsilon/\text{fringe}$. Using the Model 040 reflection polariscope, the normal-incidence measurement at a point of interest on the coating yields a reading of $0,26\,\text{fringes}$ (N).

The load is then removed from the specimen, and a PhotoStress Separator Gage is installed on the coating at the same point. Gage orientation is arbitrary, since the sum of any two perpendicular strains is equal to the sum of the principal strains. The strain gage is connected to a portable strain indicator through the Model 330 Interface Module and the instrument is balanced to zero indication for the no-load condition (Fig. 2).
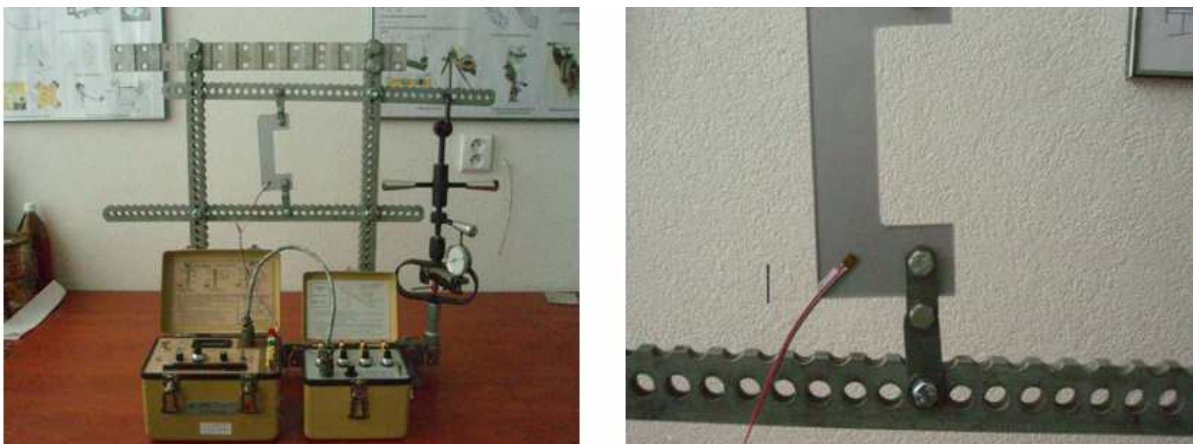
Fig. 2. The model 330 interface module in conjunction with the P-3500 strain indicator and PhotoStress separator gage

For example, with the multiplier switch of a P-3500 set to X1, the same load is reapplied to the specimen, after which the indicated strain ($\sum \varepsilon = 10$ times the display reading) is $\varepsilon_1 + \varepsilon_3 = 10\,\mu\varepsilon$. In this case, it is not corrected either N or $\sum \varepsilon$ for reinforcement or strain-extrapolation errors. Substituting N, f and $\sum \varepsilon = 2S_G$ into Equations (7) and (8):

$$\varepsilon_1 = \frac{\sum \varepsilon + Nf}{2} = \frac{10 + 0,26 . 605}{2} = 84\,\mu\varepsilon \text{ ,(7)}$$

$$\varepsilon_3 = \frac{\sum \varepsilon - Nf}{2} = \frac{10 - 0,26 . 605}{2} = -74\,\mu\varepsilon . \tag{8}$$

These principal strains are then substituted into the biaxial Hooke's law to determine the principal stresses:

$$\sigma_1 = \frac{E}{1-\mu^2}\left(\varepsilon_1 + \mu\varepsilon_3\right) = \frac{2,1.10^5}{1-0,3^2}\left(84.10^{-6} + 0,3.\left(-74.10^{-6}\right)\right) = 14,262\ MPa \tag{9}$$

$$\sigma_3 = \frac{E}{1-\mu^2}\left(\varepsilon_3 + \mu\varepsilon_1\right) = \frac{2,1.10^5}{1-0,3^2}\left(-74.10^{-6} + 0,3.84.10^{-6}\right) = -11,262\ MPa \tag{10}$$

Conclusions

This paper describes a unique method of making the required additional measurement for determining the separate principal stresses from the photoelastically derived stress difference. The procedure uses a specially designed strain gage (stress-separator gage) which is applied to the coating surface after the normal-incidence reading has been made. Practical experience with the method demonstrates that it offers several advantages over oblique-incidence measurements. It is quick, easy to use, and it completely eliminates the need for highly developed photoelastic skills. In most cases, it is also more accurate than oblique-incidence determinations.

Bibliography

1. Instruction Bulletin S-116-H: *Photoelastic Materials*. Raleigh: Measurements Group, 1996.
2. Instruction Bulletin S-127-F: *PhotoStress Separator Gage*. Raleigh: Measurements Group, 1996.
3. Tech Note TN-702-2: *Introduction to Stress Analysis by the PhotoStress Method*. Raleigh: Measurements Group, 1996.
4. Tech Note TN-708-2: *Principal Stress Separation in PhotoStress Measurements*. Raleigh: Measurements Group, 1996.
5. Trebuňa, F.: *Princípy, postupy, prístroje v metóde PhotoStress*: Košice: Typopress, 2006. 360 s. ISBN 80-8073-670-7
6. *Strain Measurment with the 040-Serie Reflection Polariscope*: Raleigh: Measurements Group, 1996.
7. www.vishay.com

Elena BEZVESILNAJA
Yuryj PODCHASHINSKY*

National Technical University of Ukraine "KPI", Kiev; *Zhitomir State Technological University

INCREASE OF ACCURACY OF LINEAR ACCELEROMETERS USING OF ARTIFICIAL NEURAL NETWORK

In the article the algorithmic method of increase of accuracy of linear accelerometers is considered. In the gyroscopic accelerometer the angle of deviation of a sensing element consists of a constant and variable making. The constant making is proportional to acceleration, which is considered constant on an interval of one measurement. Variable making is determined by precessions of a sensing element. In conditions of presence of correlated distortion of determined and random character it is necessary with high accuracy to define values of a constant making. This problem is solved in the article because of method of a maximum probability. The realization of algorithm of identifycation of an angular rule of a sensing element because of artificial neural network application is offered. This network contains a delay line and three adaptive linear neurons. The procedures of training and adaptation of a network provide additional error reduction in non-stationary and unfavorable conditions. The obtained outcomes can be used for a construction of high-precision navigational and gravimetric systems.

INTRODUCTION

For perfecting high-precision gravimetric and navigational systems the broad application of algorithmic methods of processing of measuring signals is necessary. Let's consider algorithmic methods of identification of a condition of a gyroscopic sensing element in linear accelerometers. By an outcome of an evaluation the condition is identification of an angular position and parameters of an attitude of a sensing element $\alpha(t) = \alpha_{\ddot{I}} + \alpha_{\c{C}\grave{I}}(t)$. Thus amplitude useful making $\alpha_{\ddot{I}}$ Is considered by a constant on an interval of observation. This amplitude is proportional to linear acceleration, which is measured. The parameters variable making $\alpha_{\c{C}\grave{I}}(t)$ Motion of a sensing element are necessary in further procedures of algorithmic processing for compensation of errors of an evaluation of a condition and increase accuracy of linear accelerometers.

Variable making $\alpha_{\c{C}\grave{I}}(t)$ is determined by the solution of a non-linear differential equation [1]

$$\ddot{\alpha}_{\c{C}\grave{I}} + 2\xi_{\c{C}\grave{I}}\,\dot{\alpha}_{\c{C}\grave{I}} + \omega_0^2 \sin\alpha_{\c{C}\grave{I}} = 0, \tag{1}$$

where $\omega_0, \xi_{\text{Çì}}$ – circular frequency and decay coefficient of precessions of a sensing element.

In case of small oscillations $\sin(\alpha_{\text{Çì}}) \approx \alpha_{\text{Çì}}$, and the solution of an equation (1) has a kind [1]: $\alpha_{\text{Çì}}(t) = A_{\text{Çì}} \, e^{-\xi_{\text{Çì}} t} \sin(\omega_{\text{Çì}} \, t + \varphi_{\text{Çì}})$, where $\omega_{\text{Çì}} = \sqrt{\omega_0^2 - \xi_{\text{Çì}}^2}$, $A_{\text{Çì}}, \varphi_{\text{Çì}}$ – amplitude and initial phase of precessions of a sensing element. If $\xi_{\text{Çì}} \to 0$, mathematical model of ideal trajectory of motion of a sensing element

$$\alpha(t) = \alpha_{\ddot{I}} + \alpha_{\text{Çì}}(t), \quad \alpha_{\ddot{I}} = const, \quad \alpha_{\text{Çì}}(t) = \alpha_C \sin \omega_{\text{Çì}} \, t + \alpha_S \cos \omega_{\text{Çì}} \, t, \qquad (2)$$

where $\alpha_C = A_{\text{Çì}} \cos \varphi_{\text{Çì}}$, $\alpha_S = A_{\text{Çì}} \sin \varphi_{\text{Çì}}$. In this case state vector of a sensing element, which is necessary for identifying, is equaled: $Z_\alpha = (\alpha_{\ddot{I}}, \alpha_C, \alpha_S)^T$.

The evaluation is executed because of data processing α_i^* from the sensor of an angular position of a sensing element. Thus

$$\alpha_i^* = \alpha(t_i) + \delta_\alpha(t_i), \quad i = \overline{1, K}, \quad t_i = i \cdot \delta_{\ddot{a}}, \quad T_c = K \cdot \delta_{\ddot{a}},$$

where $\alpha(t_i)$ – value, which correspond of ideal trajectory of motion of a sensing element, $\delta_\alpha(t_i)$ – errors of the measured trajectory of motion in view of handicaps which are operational on a sensing element, and errors of the sensor of a angle, K – quantity of references, which goes from the sensor of an angle and are used for an evaluation of a condition, T_c – time of observation behind a sensing element, $\delta_{\ddot{a}}$ – the interval of time between references.

Generally errors $\delta_\alpha(t_i)$ measured trajectory of motion can be correlated. It is stipulated by presence of handicaps of determined character and kinematics nonlinearities of a sensing element. For example, the operation of a harmonic handicap is stipulated by a non-stationary thermal mode of a sensing element and influence of periodic motions on frequency of oscillations of this element [2]. It is possible to consider distribution of amplitude of an error normal, proceeding from presence of a set of the factors calling these errors. Therefore it is necessary to apply a method of a maximum probability to an evaluation of a condition of a sensing element.

IDENTIFICATION OF AN ANGULAR POSITION OF A SENSING ELEMENT

For an evaluation of a condition of a sensing element we shall make a functional because of of method of a maximum probability [3]:

$$J(Z_\alpha) = \frac{1}{(2\pi)^{K/2}(\det(R_\alpha))^{1/2}} \cdot \exp\left(-\frac{1}{2}\Delta_\alpha^T \cdot R_\alpha^{-1} \cdot \Delta_\alpha\right), \qquad (3)$$

where

$$R_\alpha = \sigma_{\ddot{A}\hat{E}}^2 \cdot I_K + R_{\times\ddot{A}} \qquad (4)$$

18

– correlation matrix of errors of the measured trajectory of motion of a sensing element, $\sigma^2_{\ddot{A}\hat{E}}$ – dispersion of an error of the sensor of a angle, I_K – unit matrix by the size $K \times K$, $R_{\times\dot{A}}$ – correlation matrix of errors stipulated by an operation of correlated handicaps on a sensing element, $\Delta_\alpha = (\delta_\alpha(t_1), ..., \delta_\alpha(t_K))^T$ – vector of errors of the measured trajectory of motion of a sensing element.

For simplification of further evaluations we shall pass to a log of a functional (3):

$$\ln J(Z_\alpha) = \ln\left(\frac{1}{(2\pi)^{K/2}(\det(R_\alpha))^{1/2}}\right) - \frac{1}{2}\Delta_\alpha^T \cdot R_\alpha^{-1} \cdot \Delta_\alpha. \tag{5}$$

The evaluation of a maximum probability $\hat{Z}_\alpha$ for state vector Z_α because of (5) is determined from an equation [3]

$$\frac{d(\ln J(\hat{Z}_\alpha))}{d\hat{Z}_\alpha} = A^T \cdot R_\alpha^{-1}\left(\alpha^* - \alpha(\hat{Z}_\alpha, T)\right) = 0, \tag{6}$$

where

$$A^T = \begin{bmatrix} \dfrac{\partial\alpha(\hat{Z}_\alpha, t_1)}{\partial\hat{\alpha}_\ddot{I}} & \dfrac{\partial\alpha(\hat{Z}_\alpha, t_2)}{\partial\hat{\alpha}_\ddot{I}} & \cdots & \dfrac{\partial\alpha(\hat{Z}_\alpha, t_K)}{\partial\hat{\alpha}_\ddot{I}} \\[3mm] \dfrac{\partial\alpha(\hat{Z}_\alpha, t_1)}{\partial\hat{\alpha}_C} & \dfrac{\partial\alpha(\hat{Z}_\alpha, t_2)}{\partial\hat{\alpha}_C} & \cdots & \dfrac{\partial\alpha(\hat{Z}_\alpha, t_K)}{\partial\hat{\alpha}_C} \\[3mm] \dfrac{\partial\alpha(\hat{Z}_\alpha, t_1)}{\partial\hat{\alpha}_S} & \dfrac{\partial\alpha(\hat{Z}_\alpha, t_2)}{\partial\hat{\alpha}_S} & \cdots & \dfrac{\partial\alpha(\hat{Z}_\alpha, t_K)}{\partial\hat{\alpha}_S} \end{bmatrix},$$

$\alpha^* = (\alpha_1^*, ..., \alpha_K^*)^T$ – vector of outcomes of measurement of trajectory of motion of a sensing element, $\alpha(\hat{Z}_\alpha, T) = (\alpha(\hat{Z}_\alpha, t_1), ..., \alpha(\hat{Z}_\alpha, t_K))^T$ – vector of values of a angle of deviation of a sensing element calculated for mathematical model (2) because of ideal trajectory of motion in view of an evaluation $\hat{Z}_\alpha$ state vector, $T = (t_1, ..., t_K)^T$ – vector of instants, for which the references of the measured trajectory of motion are obtained.

In this case

$$\alpha(\hat{Z}_\alpha, t_i) = \hat{\alpha}_\ddot{I} + \hat{\alpha}_C \sin(\omega_{\c{C}\grave{I}} t_i) + \hat{\alpha}_S \cos(\omega_{\c{C}\grave{I}} t_i), \tag{7}$$

$$A^T = \begin{bmatrix} 1 & 1 & ... & 1 \\ \sin(\omega_{\c{C}\grave{I}} \delta_\ddot{a}) & \sin(2\omega_{\c{C}\grave{I}} \delta_\ddot{a}) & ... & \sin(K\omega_{\c{C}\grave{I}} \delta_\ddot{a}) \\ \cos(\omega_{\c{C}\grave{I}} \delta_\ddot{a}) & \cos(2\omega_{\c{C}\grave{I}} \delta_\ddot{a}) & ... & \cos(K\omega_{\c{C}\grave{I}} \delta_\ddot{a}) \end{bmatrix}. \tag{8}$$

In an equation (6) return correlation matrixes of errors of the measured trajectory of motion are calculated according to (4) and numerically is equaled

$$R_\alpha^{-1} = [w_{ji}], \; i, j = \overline{1, K}.$$ (9)

Let's calculate an evaluation of a maximum probability for state vector of a sensing element because of (6) with the registration (7), (8) and (9):

$$\begin{bmatrix} 1 & 1 & ... & 1 \\ \sin(\omega_{\text{ÇÌ}} \delta_{\ddot{a}}) & \sin(2\omega_{\text{ÇÌ}} \delta_{\ddot{a}}) & ... & \sin(K\omega_{\text{ÇÌ}} \delta_{\ddot{a}}) \\ \cos(\omega_{\text{ÇÌ}} \delta_{\ddot{a}}) & \cos(2\omega_{\text{ÇÌ}} \delta_{\ddot{a}}) & ... & \cos(K\omega_{\text{ÇÌ}} \delta_{\ddot{a}}) \end{bmatrix} \times \begin{bmatrix} w_{11} & w_{12} & ... & w_{1K} \\ w_{21} & w_{22} & ... & w_{2K} \\ ... & ... & ... & ... \\ w_{K1} & w_{K2} & ... & w_{KK} \end{bmatrix} \times$$

$$\times \begin{bmatrix} \alpha_1^* - \hat{\alpha}_{\ddot{I}} - \hat{\alpha}_C \sin(\omega_{\text{ÇÌ}} \delta_{\ddot{a}}) - \hat{\alpha}_S \cos(\omega_{\text{ÇÌ}} \delta_{\ddot{a}}) \\ \alpha_1^* - \hat{\alpha}_{\ddot{I}} - \hat{\alpha}_C \sin(2\omega_{\text{ÇÌ}} \delta_{\ddot{a}}) - \hat{\alpha}_S \cos(2\omega_{\text{ÇÌ}} \delta_{\ddot{a}}) \\ ... \\ \alpha_1^* - \hat{\alpha}_{\ddot{I}} - \hat{\alpha}_C \sin(K\omega_{\text{ÇÌ}} \delta_{\ddot{a}}) - \hat{\alpha}_S \cos(K\omega_{\text{ÇÌ}} \delta_{\ddot{a}}) \end{bmatrix} = 0.$$

From here

$$\begin{cases} \hat{\alpha}_{\ddot{I}} \sum_{i=1}^{K} \sum_{j=1}^{K} w_{ji} + \hat{\alpha}_C \sum_{i=1}^{K} \left(\sin(i\omega_{\text{ÇÌ}} \delta_{\ddot{a}}) \sum_{j=1}^{K} w_{ji} \right) + \\ + \hat{\alpha}_S \sum_{i=1}^{K} \left(\cos(i\omega_{\text{ÇÌ}} \delta_{\ddot{a}}) \sum_{j=1}^{K} w_{ji} \right) = \sum_{i=1}^{K} \left(\alpha_i^* \sum_{j=1}^{K} w_{ji} \right), \\ \hat{\alpha}_{\ddot{I}} \sum_{i=1}^{K} \left(\sin(i\omega_{\text{ÇÌ}} \delta_{\ddot{a}}) \sum_{j=1}^{K} w_{ji} \right) + \hat{\alpha}_C \sum_{i=1}^{K} \left(\sin^2(i\omega_{\text{ÇÌ}} \delta_{\ddot{a}}) \sum_{j=1}^{K} w_{ji} \right) + \\ + \hat{\alpha}_S \sum_{i=1}^{K} \left(\sin(i\omega_{\text{ÇÌ}} \delta_{\ddot{a}}) \cos(i\omega_{\text{ÇÌ}} \delta_{\ddot{a}}) \sum_{j=1}^{K} w_{ji} \right) = \sum_{i=1}^{K} \left(\alpha_i^* \sin(i\omega_{\text{ÇÌ}} \delta_{\ddot{a}}) \sum_{j=1}^{K} w_{ji} \right), \\ \hat{\alpha}_{\ddot{I}} \sum_{i=1}^{K} \left(\cos(i\omega_{\text{ÇÌ}} \delta_{\ddot{a}}) \sum_{j=1}^{K} w_{ji} \right) + \hat{\alpha}_C \sum_{i=1}^{K} \left(\sin(i\omega_{\text{ÇÌ}} \delta_{\ddot{a}}) \cos(i\omega_{\text{ÇÌ}} \delta_{\ddot{a}}) \sum_{j=1}^{K} w_{ji} \right) + \\ + \hat{\alpha}_S \sum_{i=1}^{K} \left(\cos^2(i\omega_{\text{ÇÌ}} \delta_{\ddot{a}}) \sum_{j=1}^{K} w_{ji} \right) = \sum_{i=1}^{K} \left(\alpha_i^* \cos(i\omega_{\text{ÇÌ}} \delta_{\ddot{a}}) \sum_{j=1}^{K} w_{ji} \right), \end{cases}$$

or in the matrix form

$$B_\alpha \cdot \hat{Z}_\alpha = C_\alpha,$$ (10)

where

$$B_\alpha = \begin{bmatrix} \sum\limits_{i=1}^{K} w_i & \sum\limits_{i=1}^{K} w_i \sin(i\omega_{\zeta i}\,\delta_{\ddot{a}}) & \sum\limits_{i=1}^{K} w_i \cos(i\omega_{\zeta i}\,\delta_{\ddot{a}}) \\ \sum\limits_{i=1}^{K} w_i \sin(i\omega_{\zeta i}\,\delta_{\ddot{a}}) & \sum\limits_{i=1}^{K} w_i \sin^2(i\omega_{\zeta i}\,\delta_{\ddot{a}}) & \sum\limits_{i=1}^{K} w_i \sin(i\omega_{\zeta i}\,\delta_{\ddot{a}})\cos(i\omega_{\zeta i}\,\delta_{\ddot{a}}) \\ \sum\limits_{i=1}^{K} w_i \cos(i\omega_{\zeta i}\,\delta_{\ddot{a}}) & \sum\limits_{i=1}^{K} w_i \sin(i\omega_{\zeta i}\,\delta_{\ddot{a}})\cos(i\omega_{\zeta i}\,\delta_{\ddot{a}}) & \sum\limits_{i=1}^{K} w_i \cos^2(i\omega_{\zeta i}\,\delta_{\ddot{a}}) \end{bmatrix},$$

$$C_\alpha = \left[\sum\limits_{i=1}^{K} w_i\alpha_i^* \quad \sum\limits_{i=1}^{K} w_i\alpha_i^* \sin(i\omega_{\zeta i}\,\delta_{\ddot{a}}) \quad \sum\limits_{i=1}^{K} w_i\alpha_i^* \cos(i\omega_{\zeta i}\,\delta_{\ddot{a}}) \right]^T, \quad w_i = \sum\limits_{j=1}^{K} w_{ji}.$$

The solution of a system (10) concerning an evaluation of state vector $\hat{Z}_\alpha$ also is by an outcome of identification of parameters of motion of a sensing element in the linear accelerometers. This solution can be obtained because of known rules of the solution of systems of linear algebraic equations and is by a linear function of the rather measured values of references α_i^*:

$$\hat{\alpha}_{\ddot{I}} = \frac{B_{11}c_1 + B_{21}c_2 + B_{31}c_3}{\det(B_\alpha)}, \quad \hat{\alpha}_C = \frac{B_{12}c_1 + B_{22}c_2 + B_{32}c_3}{\det(B_\alpha)}, \quad \hat{\alpha}_S = \frac{B_{13}c_1 + B_{23}c_2 + B_{33}c_3}{\det(B_\alpha)},$$

where B_{ji} – cofactors of elements b_{ji} matrix B_α, c_j – elements of vector C_α.

Thus, the solution of a problem of identification because of method of a maximum probability has a kind:

$$\hat{\alpha}_{\ddot{I}} = \sum\limits_{i=1}^{K} \alpha_i^* \cdot l_{\alpha\ddot{I},i}, \quad \hat{\alpha}_C = \sum\limits_{i=1}^{K} \alpha_i^* \cdot l_{\alpha C,i}, \quad \hat{\alpha}_S = \sum\limits_{i=1}^{K} \alpha_i^* \cdot l_{\alpha S,i}.$$

In this case for definition of state vector of a sensing element the constants factors $l_{\alpha\ddot{I},j}$, $l_{\alpha C,j}$, $l_{\alpha S,j}$, $j = \overline{(n-k+1), n}$ are used. These factors depend on frequency of oscillations of a sensing element ω_0, decay coefficient ξ_1, frequency $\omega = \sqrt{\omega_0^2 - \xi_1^2}$, which is used in algorithm of identification, slice of time $\delta_{\ddot{a}}$ between references acting from the sensor of a angle.

REALIZATION OF ALGORITHM OF IDENTIFICATION AFTER OF ARTIFICIAL NEURAL NETWORK APPLICATION

All listed values can be certain with some error and the means of measurements can vary on some interests under an operation of the various destabilizing factors while in service. All this requires adaptation and optimum set-up of parameters in algorithms of an evaluation. In an outcome the additional error of linear

accelerometers, stipulated by unfavorable and non-stationary conditions of measurements decreases.

The adaptation and optimum set-up of parameters of algorithm of an evaluation can be executed during adaptation and training artificial neural network. Such network is offered to realize algorithms of an evaluation of a condition of the linear accelerometers. The built-in algorithms and methods of set-up of weight factors are essential advantage artificial neural network on a comparison with usual means of processing of the measuring information [4].

For an evaluation of state vector of a sensing element we shall use artificial neural network, which consists of delay lines and three adaptive linear neurons (Fig. 1). Training of such network and set-up it of weight factors we shall execute because of modifications of a method of least squares [4].
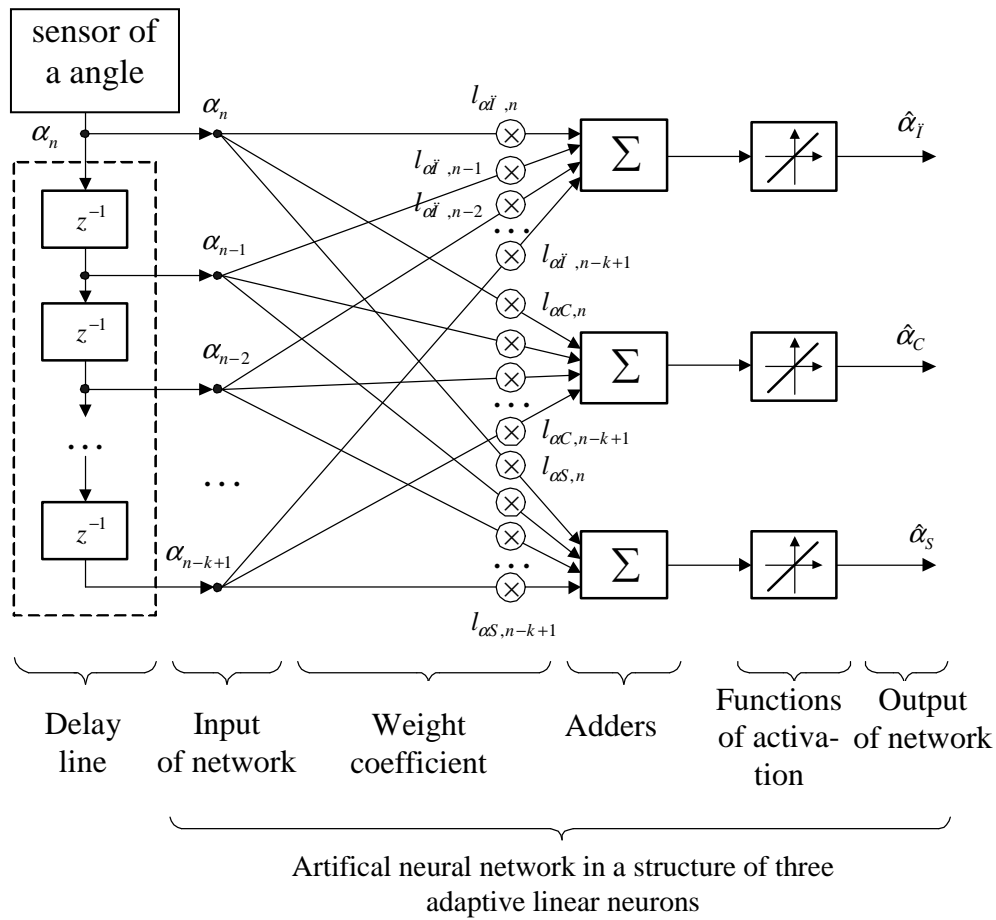
Fig. 1. Block of diagram of an evaluation of state vector of linear accelerometer because of artificial neural network

The degree of approximation of an output signal of a network $\hat{Z}_N = \left(\hat{\alpha}_{\ddot{I}}, \hat{\alpha}_C, \hat{\alpha}_S\right)^T$ to precisiouly value $Z_N = \left(\alpha_{\ddot{I}}, \alpha_C, \alpha_S\right)^T$ can be appreciated by a functional of quality of activity of a network. For example, for the first output of a network this functional $J_{\alpha\ddot{I}} = E\left[F\left(\Delta_{\alpha\ddot{I}}\left(\alpha_{\ddot{I}}, \hat{\alpha}_{\ddot{I}}, \tilde{c}\right)\right)\right] \rightarrow \min$, where $E[.]$ – expectation of a loss function $F(\Delta_{\alpha\ddot{I}}) = \left(\Delta_{\alpha\ddot{I}}\right)^2$ from an error $\Delta_{\alpha\ddot{I}} = \hat{\alpha}_{\ddot{I}} - \alpha_{\ddot{I}}$ network. The outcome of training is

optimum vector of weight factors $c^* = \left(l^*_{\alpha \ddot{\imath},n}, l^*_{\alpha \ddot{\imath},n-1},...,l^*_{\alpha \ddot{\imath},n-k+1}\right)^T$, which minimizes a functional $J_{\alpha \ddot{\imath}}$. This vector takes into account influence of the destabilizing factors and non-stationary conditions of measurements. The value $\tilde{c} = c^*$ can be obtained from an equation

$$\nabla J_{\alpha \ddot{\imath}}(\tilde{c}) = E\left[\nabla F\left(\Delta_{\alpha \ddot{\imath}}(\tilde{c})\right)\right] = 0.$$

Recurrent algorithm of training artificial neural network:

$$\tilde{c}(q) = \tilde{c}(q-1) - \Gamma(q) \cdot \nabla F\left(\Delta_{\alpha \ddot{\imath}}\left(\alpha_{\ddot{\imath}\ddot{\imath}}, \hat{\alpha}_{\ddot{\imath}}, \tilde{c}(q-1)\right), \tilde{c}(q-1)\right), \tag{11}$$

where $q = \overline{1, N_{\hat{\imath}\hat{a}\hat{a}\div}}$ – number of a step of recurrent algorithm of training because of signal $\alpha_{\ddot{\imath}\ddot{\imath}}$, $N_{\hat{\imath}\hat{a}\hat{a}\div}$ – duration of a procedure of training (total of steps), $\Gamma(q)$ – matrix of amplification, which determines speed of a procedure of training,

$$\frac{\partial F}{\partial l_{\alpha \ddot{\imath},n}} = \frac{\partial(\Delta^2_{\alpha \ddot{\imath}})}{\partial l_{\alpha \ddot{\imath},n}} = -2\alpha_{\ddot{\imath},r}\left(\alpha_{\ddot{\imath}\ddot{\imath}} - \sum_{j=n-k+1}^{n}\alpha_{\ddot{\imath},j}l_{\alpha \ddot{\imath},j}\right) = -2\alpha_{\ddot{\imath},r}\left(\alpha_{\ddot{\imath}\ddot{\imath}} - \hat{\alpha}_{\ddot{\imath}}\right). \tag{12}$$

Because of (12) and (11) is obtained:

$$\tilde{c}(q) = \tilde{c}(q-1) + \Gamma(q) \cdot 2\alpha_{\ddot{\imath},r} \cdot \left(\alpha_{\ddot{\imath}\ddot{\imath}} - \hat{\alpha}_{\ddot{\imath}}\right), \tag{13}$$

Because of (13) is obtained a resultant expression for an evaluation of weight factors of neurons in learning process:

$$\tilde{l}_{\alpha \ddot{\imath},j}(q) = \tilde{l}_{\alpha \ddot{\imath},j}(q-1) + 2\alpha_{\ddot{\imath},r} \cdot \left(\alpha_{\ddot{\imath}\ddot{\imath}} - \hat{\alpha}_{\ddot{\imath}}\right) \cdot \gamma_{\ddot{\imath}} / \|\alpha_{\ddot{\imath}}\|,$$

$$\tilde{l}_{\alpha C,j}(q) = \tilde{l}_{\alpha C,j}(q-1) + 2\alpha_{\ddot{\imath},r} \cdot \left(\alpha_{\ddot{\imath}C} - \hat{\alpha}_{C}\right) \cdot \gamma_{\ddot{\imath}} / \|\alpha_{\ddot{\imath}}\|,$$

$$\tilde{l}_{\alpha S,j}(q) = \tilde{l}_{\alpha S,j}(q-1) + 2\alpha_{\ddot{\imath},r} \cdot \left(\alpha_{\ddot{\imath}S} - \hat{\alpha}_{S}\right) \cdot \gamma_{\ddot{\imath}} / \|\alpha_{\ddot{\imath}}\|,$$

where $\|\alpha_{\ddot{\imath}}\| = \alpha_{\ddot{\imath}}^{\grave{O}} \cdot \alpha_{\ddot{\imath}}$ – Euclidean norm of vector of references of a test signal on an input of a network.

Indication of the ending of a procedure of training is the fulfillment of conditions

$$\alpha_{\ddot{\imath}\ddot{\imath}} - \hat{\alpha}_{\ddot{\imath}\ddot{\imath}}(q) \le \varepsilon_{\alpha \ddot{\imath}}, \ \alpha_{\ddot{\imath}C} - \hat{\alpha}_{\ddot{\imath}C}(q) \le \varepsilon_{\alpha C}, \ \alpha_{\ddot{\imath}S} - \hat{\alpha}_{\ddot{\imath}S}(q) \le \varepsilon_{\alpha S}, \tag{14}$$

where $\varepsilon_{\alpha \ddot{\imath}}, \varepsilon_{\alpha C}, \varepsilon_{\alpha S}$ – allowed values of an error of an evaluation of state vector for the linear accelerometer (error of an output artificial neural network). Let's consider that $\varepsilon_{\alpha \ddot{\imath}} = \varepsilon_{\alpha C} = \varepsilon_{\alpha S}$. Then for mathematical model (2) the root-mean-square value of an

error of a signal $\alpha(t)$, stipulated by errors (14), is equaled $\sigma_\alpha = \varepsilon_{\alpha\ddot{i}} / \sqrt{3} \leq \sigma_{\ddot{A}\hat{E}} / 3$, where $\sigma_{\ddot{A}\hat{E}}$ – root-mean-square value of an error of the sensor of a angle. From here

$$\alpha_{i\ddot{i}} - \hat{\alpha}_{i\ddot{i}}(q) \leq \sigma_{\ddot{A}\hat{E}} / \sqrt{3}, \ \alpha_{iC} - \hat{\alpha}_{iC}(q) \leq \sigma_{\ddot{A}\hat{E}} / \sqrt{3}, \ \alpha_{iS} - \hat{\alpha}_{iS}(q) \leq \sigma_{\ddot{A}\hat{E}} / \sqrt{3}.$$

These ratios determine the ending of a procedure of training artificial neural network. These ratios are also guaranteeing theoretically calculated accuracy of assessments of state vector for the linear accelerometer in unfavorable and non-stationary conditions of measurements.

CONCLUSIONS

The algorithmic method of increase of accuracy of linear accelerometers is considered. In conditions of presence of correlated distortion of determined and random character it is necessary with high accuracy to define values of a constant making. This problem is solved in the article because of method of a maximum probability.

The realization of algorithm of identification of an angular rule of a sensing element with artificial neural network application is offered. This network contains a delay line and three adaptive linear neurons. The procedures of training and adaptation of a network provide additional error reduction in non-stationary and unfavorable conditions.

The obtained outcomes can be used for a construction of high-precision navigational and gravimetric systems.

REFERENCES

1. Безвесільна О. М.: *Авіаційні гравіметричні системи та гравіметри: підручник*. Житомир, ЖДТУ, 2007.

2. Синицын И. Н.*: Фильтры Калмана и Пугачева: учебное пособие*. М. : Университетская книга; Логос, 2006.

3. Кузьмин С. З.: *Основы теории цифровой обработки радиолокационной информации*. Советское радио, 1974.

4. Руденко О. Г.: *Штучні нейронні мережі: навчальний посібник*. Харків: ТОВ "Компанія СМІТ", 2006.

Velina BOZDOUGANOVA
Marko TODOROV

University of Rousse, Bulgaria

COMPUTATION OF PLANE STRUCTURES EIGENFREQUENCIES BY HYBRID FINITE ELEMENT METHOD USING TREFFTZ FUNCTIONS

A hybrid stress method for eigenfrequencies analysis is developed using a plane rectangular hybrid element. Complex Trefftz functions which are solutions of elastostatic problem are used. By the complementary energy variational equation a relationship between the stress parameters and the nodal displacements is obtained. The Lagrange's variational equation for the dynamic case gives an expression for computation of eigenfrequencies.

INTRODUCTION

It is known that in the free vibration finite element analysis both shape functions and element matrices depend on frequencies [5, 8]. That is why so-called dynamic finite elements are created [4, 2, 10]. Their element stiffness and mass matrices are presented in ascending powers of the natural frequency. In this case the computation of associated matrices is complicated and eigenvalues equation becomes nonlinear one.

In the conventional displacement finite element free vibration analysis the dynamic correction terms are not taken into account in computation of element mass and stiffness matrices (static element matrices are included instead). Necessary accuracy is achieved either by mesh refinement or by increasing the power of the approximating polynomials.

A hybrid stress method for eigenvalue analysis is described in [1], where the element internal displacements are obtained by least squares method.

In this study free vibrations of plane stress or plane strain structures are investigated by an approach, which does not take into account dynamic terms, but instead of standard polynomials Trefftz functions are used and hybrid stress model is chosen [9]. As in every hybrid variant of the finite element method [9, 3, 6] independently two fields are approximated – one of them in the interior of the element and the other – on the element boundary. Equilibrated stresses in the interior, expressed in stress parameters are introduced and, independently – displacements on the boundary, represented in their nodal values. The stress parameters could be substituted by nodal displacements on the element level. This is reached by complementary energy functional and associated variational Castigliano's equation. Taking into account the dependence between stress parameters and nodal

displacements in Lagrange's variational equation for dynamic case eigenvalue problem is obtained.

PROBLEM FORMULATION

Variational equation of eigenvalue problem

Displacements of a structure in free vibrations vary according to

$$w = u\,(x, y, z)\,\sin\omega t, \tag{1}$$

where $u\,(x, y, z)$ are their amplitude values. To investigate the free vibrations Lagrange's variational equation for dynamic problems is used in the form [12]:

$$\int_V \delta\varepsilon^T \sigma\, dV + \int_V \delta w^T \rho \ddot{w}\; dV = 0. \tag{2}$$

The strains $\varepsilon = Dw$ and stresses $\sigma = E\varepsilon = EDw$ (D is the differential operator matrix, E – the elasticity matrix and ρ – the volume density) are substituted in the above equation. Taking into account that $\ddot{w} = -\omega^2 u \sin\omega t$ it is obtained

$$\int_V (D\delta u)^T E\,(Du)dV - \omega^2 \int_V \delta u^T u \rho\, dV = 0. \tag{3}$$

Stiffness and mass matrices of hybrid Trefftz element

The eigenvalue problem for membrane (plane stress or plane strain state) is solved. Rectangular hybrid finite elements of volume V are used for discretization.

According to hybrid procedure stresses in the interior of the element V and independently – displacements on the boundary S are approximated. The stresses inside the element are not expressed in their nodal values, but in stress parameters β

$$\sigma = A\,\beta \text{ in } V. \tag{4}$$

Trefftz functions, which satisfy homogeneous equilibrium and compatibility conditions, are used as shape functions in the matrix A. In the plane case these conditions are, respectively

$$D^T\sigma = 0 \text{ in } V, \tag{5}$$

$$\Delta(\sigma_x + \sigma_y) = 0 \text{ in } V, \tag{6}$$

where

$$\Delta \equiv \partial^2/\partial x^2 + \partial^2/\partial y^2.$$

By integration of the stress shape functions it is possible to obtain displacement shape functions, which are needed for the element matrices. So the internal displacements could be expressed in stress parameters β, i. e.

$$\boldsymbol{u} = \boldsymbol{W}\boldsymbol{\beta}\ \text{in}\ V. \tag{7}$$

Element boundary displacements can be approximated, using their nodal values $\boldsymbol{v}$

$$\boldsymbol{u}_S = \boldsymbol{G}\boldsymbol{v}\ \text{on}\ S, \tag{8}$$

where $\boldsymbol{G}$ is the shape functions matrix. If an element boundary sector coincides with a portion of external boundary S_u of the region, on which the displacements $\overline{\boldsymbol{u}}$ are given, kinematical boundary conditions must be satisfied

$$\boldsymbol{u}_S = \overline{\boldsymbol{u}}\ \text{on}\ S_u. \tag{9}$$

In order to obtain equations for determining the eigenvalues the stress parameters must be expressed in the nodal displacements $\boldsymbol{v}$. For this purpose Castigliano's variational equation can be used

$$\int_V \boldsymbol{\varepsilon}^{\mathrm{T}} \delta\boldsymbol{\sigma}\,\mathrm{d}V - \int_S \boldsymbol{u}_S{}^{\mathrm{T}} \boldsymbol{n}^{\mathrm{T}} \delta\boldsymbol{\sigma}\,\mathrm{d}S = 0, \tag{10}$$

deduced from the complementary energy functional

$$\Pi_{\mathrm{C}}(\boldsymbol{\sigma}) = 1/2 \int_V \boldsymbol{\varepsilon}^{\mathrm{T}} \boldsymbol{\sigma}\mathrm{d}V - \int_S \boldsymbol{u}_S{}^{\mathrm{T}} \boldsymbol{n}^{\mathrm{T}} \boldsymbol{\sigma}\,\mathrm{d}S = 0, \tag{11}$$

where $\boldsymbol{n}$ is the matrix of direction cosines of the boundary normal. Since the shape functions are Trefftz ones the volume integral can be reduced to surface integral by Gauss-Ostrogradskiy's formula [11], i.e. the first integral in (10) is written down as follows

$$\int_V \boldsymbol{\varepsilon}^{\mathrm{T}} \delta\boldsymbol{\sigma}\,\mathrm{d}V = \int_V (\mathbf{D}\boldsymbol{u})^{\mathrm{T}} \delta\boldsymbol{\sigma}\,\mathrm{d}V = \int_S \boldsymbol{u}^{\mathrm{T}} \boldsymbol{n}^{\mathrm{T}} \delta\boldsymbol{\sigma}\,\mathrm{d}S - \int_V \boldsymbol{u}^{\mathrm{T}} \mathbf{D}^{\mathrm{T}} \delta\boldsymbol{\sigma}\,\mathrm{d}V. \tag{12}$$

The last integral equals zero and the variational equation (10) becomes

$$\int_S \boldsymbol{u}^{\mathrm{T}} \boldsymbol{n}^{\mathrm{T}} \delta\boldsymbol{\sigma}\,\mathrm{d}S - \int_S \boldsymbol{u}_S{}^{\mathrm{T}} \boldsymbol{n}^{\mathrm{T}} \delta\boldsymbol{\sigma}\,\mathrm{d}S = 0. \tag{13}$$

It contains boundary integrals only. Putting in the expressions of $\boldsymbol{\sigma}$, $\boldsymbol{u}$ and $\boldsymbol{u}_S$, determined by (4), (7) and (8) into (13) it is obtained

$$\boldsymbol{\beta}^{\mathrm{T}} \int_S \boldsymbol{W}^{\mathrm{T}} \boldsymbol{n}^{\mathrm{T}} \boldsymbol{A}\ \mathrm{d}S\ \delta\boldsymbol{\beta} - \boldsymbol{v}^{\mathrm{T}} \int_S \boldsymbol{G}^{\mathrm{T}} \boldsymbol{n}^{\mathrm{T}} \boldsymbol{A}\ \mathrm{d}S\ \delta\boldsymbol{\beta} = 0. \tag{14}$$

Introducing the compliance and leverage matrices, respectively

$$\boldsymbol{C} = \int_S (\boldsymbol{n}^{\mathrm{T}} \boldsymbol{A})^{\mathrm{T}} \boldsymbol{W}\mathrm{d}S, \boldsymbol{H} = \int_S (\boldsymbol{n}^{\mathrm{T}} \boldsymbol{A})^{\mathrm{T}} \boldsymbol{G}\mathrm{d}S, \tag{15}$$

it is found

$$\boldsymbol{\beta} = \boldsymbol{C}^{-1} \boldsymbol{H}\boldsymbol{v}. \tag{16}$$

In the equation (7) element rigid body displacements are not taken into account. The static analysis does not require them since they do not provoke appearance of strains and stresses. In dynamics the rigid body displacements influence the inertia and it is necessary to introduce them writing down (7) in the form

$$\boldsymbol{u} = \boldsymbol{W}\boldsymbol{\beta} + \boldsymbol{W_r}\,\boldsymbol{\beta_r} \text{ in } V. \tag{17}$$

Using the relationship (16) the stress parameters $\boldsymbol{\beta}$ are excluded from (17) and it is obtained

$$\boldsymbol{u} = \boldsymbol{W}\,\boldsymbol{C}^{-1}\boldsymbol{H}\boldsymbol{v} + \boldsymbol{W_r}\boldsymbol{\beta_r} \text{ in } V. \tag{18}$$

Since the parameters $\boldsymbol{\beta_r}$ must be expressed in the nodal displacements $\boldsymbol{v}$ too, the collocation method is used. The internal displacements must coincide with the displacements in two nodes and thus it is obtained

$$\boldsymbol{\beta_r} = \boldsymbol{L}\boldsymbol{v}. \tag{19}$$

Therefore (18) becomes

$$\boldsymbol{u} = \boldsymbol{W}\,\boldsymbol{C}^{-1}\boldsymbol{H}\boldsymbol{v} + \boldsymbol{W_r}\,\boldsymbol{L}\boldsymbol{v} \text{ in } V. \tag{20}$$

If for the sake of convenience, it is introduced the matrix

$$\boldsymbol{B} = \boldsymbol{W}\,\boldsymbol{C}^{-1}\boldsymbol{H} + \boldsymbol{W_r}\,\boldsymbol{L}, \tag{21}$$

the expression (20) can be written down so

$$\boldsymbol{u} = \boldsymbol{B}\boldsymbol{v} \text{ in } V. \tag{22}$$

Now it is possible to derive the element stiffness and mass matrices, substituting the displacements from (22) into the variational equation (3), applied to the individual finite element. That equation becomes

$$\delta\boldsymbol{v}^{\mathrm{T}}\int_V (\mathbf{D}\boldsymbol{B})^{\mathrm{T}}\boldsymbol{E}\,(\mathbf{D}\boldsymbol{B})\mathrm{d}V\,\boldsymbol{v} - \omega^2 \delta\boldsymbol{v}^{\mathrm{T}}\int_V \boldsymbol{B}^{\mathrm{T}}\boldsymbol{B}\rho\,\mathrm{d}V\,\boldsymbol{v} = 0. \tag{23}$$

The first integral is reduced to surface one, applying (12) and realizing that Trefftz approximation functions are used and the rigid body displacement terms vanish. Thus from the above equation the well-known form of eigenfrequencies problem is obtained

$$\boldsymbol{K}\boldsymbol{v} - \omega^2\boldsymbol{M}\boldsymbol{v} = 0, \tag{24}$$

where $\boldsymbol{K}$ and $\boldsymbol{M}$ are the element stiffness and mass matrices, respectively

$$\boldsymbol{K} = \boldsymbol{H}^{\mathrm{T}}\boldsymbol{C}^{-1}\boldsymbol{H}, \tag{25}$$

$$M = \int_V \boldsymbol{B}^\mathrm{T}\boldsymbol{B}\rho \, \mathrm{d}V . \tag{26}$$

Shape functions

In order to obtain the necessary element Trefftz approximation functions it is possible to use the complex solutions of the plane elasticity problem [7]

$$2\mu \, (u + \mathrm{i}v) = \chi\varphi\,(z) - z\,\overline{\varphi'(z)} - \overline{\psi(z)} , \tag{27}$$

$$\sigma_x + \mathrm{i}\,\tau_{xy} = \varphi'(z) + \overline{\varphi'(z)} - \overline{z\varphi''(z)} - \overline{\psi'(z)} , \tag{28}$$

$$\sigma_y - \mathrm{i}\,\tau_{xy} = \varphi'(z) + \overline{\varphi'(z)} + \overline{z\varphi''(z)} + \overline{\psi'(z)} , \tag{29}$$

where $\varphi\,(z)$ and $\psi\,(z)$ are analytic complex functions. Lame's constants μ and χ can be written in the form: $2\mu = e\,/\,(1+\theta)$, $\chi = (3 - \theta)\,/\,(1 + \theta)$ and $\chi = (3 - 4\theta)$ for plane stress and plane strain state, respectively; e is the Young's modulus and θ – the Poisson's ratio.

Since the finite element is simple connected domain, the two complex functions $\varphi\,(z)$ and $\psi\,(z)$ can be represented by power series, i.e.

$$\varphi(z) = \sum_{k=1}^{n} a_k z^k , \;\; \psi(z) = \sum_{k=1}^{n} b_k z^k . \tag{30}$$

Using the complex coefficients in the form $a_k = \beta_{k,1} + \mathrm{i}\beta_{k,2}$ and $b_k = \beta_{k,3} + \mathrm{i}\beta_{k,4}$, substituting them into (27) – (29) and regrouping it is obtained the following representation of the displacements $\boldsymbol{u}^\mathrm{T} = [u \; v]$ and of the stresses $\boldsymbol{\sigma}^\mathrm{T} = [\sigma_x \; \sigma_y \; \tau_{xy}]$:

$$\begin{array}{l} 2\mu u = \mathrm{Re} \\ 2\mu v = \mathrm{Im} \end{array} \left\{ \sum_{k=1}^{n} \begin{bmatrix} \beta_{k,1} & \beta_{k,2} & \beta_{k,3} & \beta_{k,4} \end{bmatrix} \begin{bmatrix} z(\chi z^{k-1} - k\overline{z}^{k-1}) \\ \mathrm{i}z(\chi z^{k-1} + k\overline{z}^{k-1}) \\ -\overline{z}^k \\ \mathrm{i}\overline{z}^k \end{bmatrix} \right\}, \tag{31}$$

$$\begin{array}{l} \sigma_x = \mathrm{Re} \\ \tau_{xy} = \mathrm{Im} \end{array} \left\{ \sum_{k=1}^{n} \begin{bmatrix} \beta_{k,1} & \beta_{k,2} & \beta_{k,3} & \beta_{k,4} \end{bmatrix} \begin{bmatrix} k[z^{k-1} + \overline{z}^{k-1} - (k-1)z\overline{z}^{k-2}] \\ \mathrm{i}k[z^{k-1} - \overline{z}^{k-1} + (k-1)z\overline{z}^{k-2}] \\ -k\overline{z}^{k-1} \\ \mathrm{i}k\overline{z}^{k-1} \end{bmatrix} \right\}, \tag{32}$$

$$\sigma_y = \text{Re}\left\{\sum_{k=1}^{n}\left[\beta_{k,1} \quad \beta_{k,2} \quad \beta_{k,3} \quad \beta_{k,4}\right]\begin{bmatrix} k[z^{k-1} + \overline{z^{k-1}} + (k-1)z\overline{z^{k-2}}] \\ ik[z^{k-1} - \overline{z^{k-1}} - (k-1)z\overline{z^{k-2}}] \\ k\overline{z^{k-1}} \\ -ik\overline{z^{k-1}} \end{bmatrix}\right\}. \tag{33}$$

The elements of the matrices (31) – (33) represent Trefftz approximation functions, which are used in computing the element stiffness and mass matrices.

NUMERICAL RESULTS AND CONCLUSIONS

The membrane from the example in [4] is used to compare eigenfrequensies, obtained in this study (HTM), in [4] (DEM), in [1] (HM) and by conventional displacement-based finite element method (FEM). It is a square cantilever membrane 10x10x1, vibrating in its own plane, with material constants $e = 2.1 \bullet 10^{11}$ Pa, $\theta = 0.3$, $\rho = 7850$ kg/m^3.

Table 1. Eigenfrequencies percentage error

Mesh	Model	ω_1	ω_2	ω_3	ω_4	ω_5	ω_6
4x4	FEM	3.14	1.10	5.71	8.31	9.35	6.97
	HM [1]	2.70	0.73	4.26	5.43	7.81	2.80
	HTM	2.64	0.695	3.48	4.63	6.84	1.71
	DEM [4]	-2.83	0.50	-3.56	-3.39	-3.34	-0.82
5x5	FEM	2.16	0.747	3.88	5.85	6.29	4.51
	HM [1]	1.86	0.497	2.95	3.74	5.13	1.88
	HTM	1.79	0.479	2.40	3.19	5.00	0.59
	DEM [4]	-1.97	0.28	-2.51	-2.61	-2.38	-0.41
10x10	FEM	0.64	0.23	1.19	2.08	1.80	1.32
	HM [1]	0.56	0.16	0.99	1.47	1.45	0.72
	HTM	0.52	0.15	0.79	1.32	1.36	0.35
	DEM [4]	-0.60	-0.64	-4.09	-1.25	0.81	-0.24

The numerical results for hybrid Trefftz, hybrid from [1] and displacement-based methods are obtained by the computer system VIMKE for finite element method application. The four-node rectangular finite elements are used. Table 1 presents percentage error in the first six eigenfrequencies. The results, obtained for 20x20 mesh size in [4], are used as reference values.

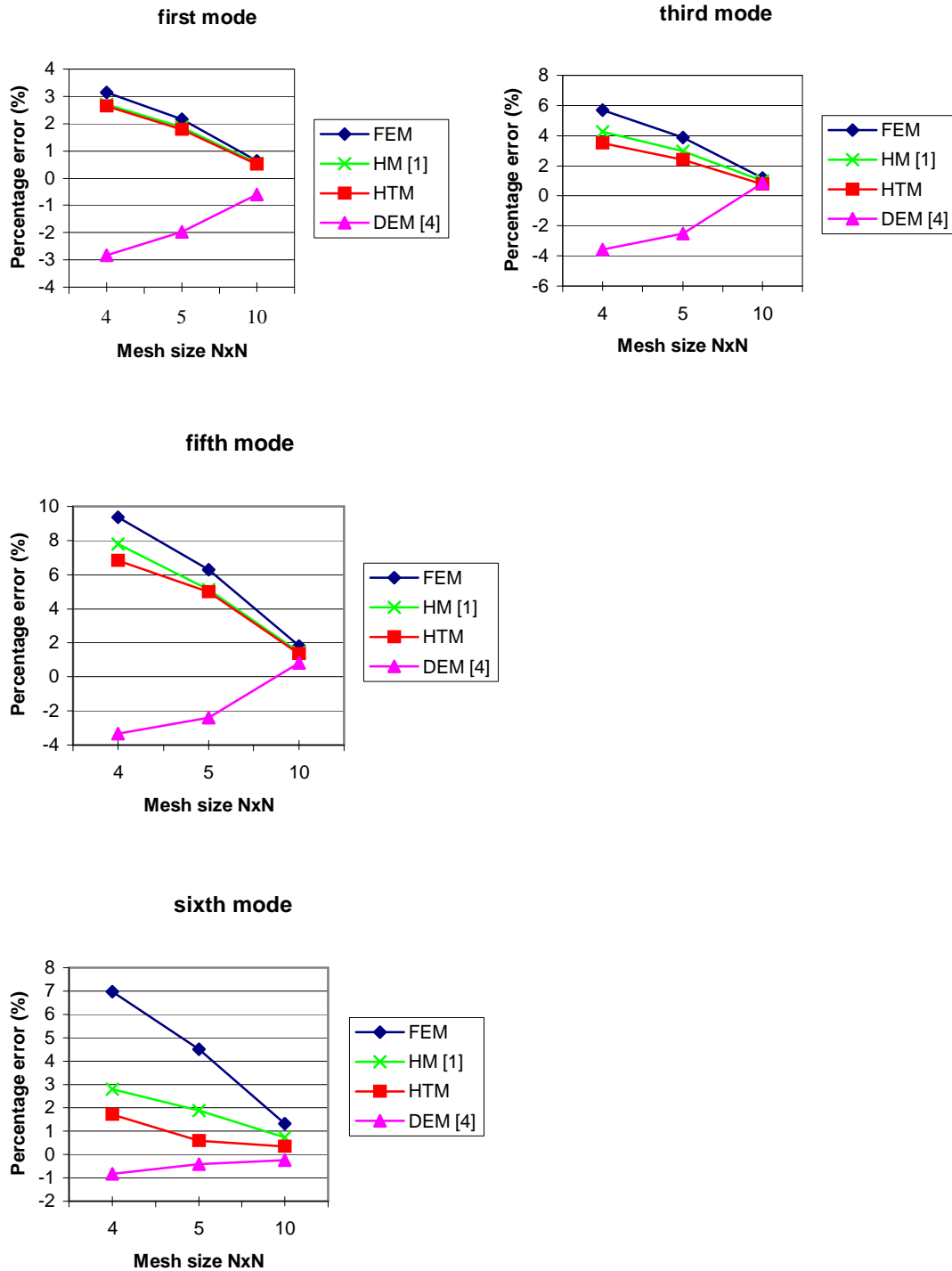Figure 1 shows the convergence characteristics of the four methods.

Figure 1. Convergence characteristics of eigenfrequency solutions

It is seen that the hybrid Trefftz element gives more accurate values than those of displacement-based and hybrid element [1]. The present element is better than the dynamic element [4] for the first and third eigenfrequencies. For the higher eigenfrequencies the dynamic element [4] is more accurate. This is explicable because it takes into account the dependence of element matrices from eigenfrequencies and leads to a more complicate nonlinear eigenvalue problem.

REFERENCES

1. Bozdouganova V. Todorov M.: *Eigenfrequencies determination by hybrid stress finite element method* (in print).

2. Freitas J., Teixeira A.: *Hybrid finite element formulations for elastodynamic analysis in the frequency domain*. IJSS, 36, 1883-1923, 1999.

3. Gallagher R. H.: *Finite element analysis. Fundamentals*. Prentice-hall, Inc., New Jersey, 1975.

4. Gupta, K.K.: *Development of a finite dynamic element for free vibration analysis of 2-D structures*. IJNME, 12, 1311-1327, 1978.

5. Dumont N.A., De Oliveira R.: *From frequency-dependent mass and stiffness matrices to the dynamic response of elastic systems*. IJSS, 38, 1813-30, 2001.

6. Jirousek J., Zieliński A.P.: *Survey of Trefftz–type element formulations*. Comp.&Str., 63, No 2, 225-242, 1997.

7. Muskhelishvili N.I.: *Some basic problems of the mathematical theory of elasticity*. Noordhool, Groningen, 1953.

8. Przemieniecki J. S.: *Theory of matrix structural analysis*. McGraw-Hill, New York, 1968.

9. Pian T.H.H.: *Derivation of element stiffness matrices by assumed stress distributions*. AIAA J., 2, 1333-36, 1964.

10. Pilkey W.D., Fergusson N.J.: *Some charachteristics of frequency-dependent structural matrices*. Comp.&Str., 35, No 4, 413-416, 1990.

11. Rozin L.A.: *Variational formulations of elastic structure problems*. Leningrad, 1978 (in Russian).

12. Washizu K.: *Variational methods in elasticity and plasticity*. Pergamon Press, 1982.

Velina BOZDOUGANOVA
Marko TODOROV

University of Rousse, Bulgaria

EIGENFREQUENCIES DETERMINATION
BY HYBRID STRESS FINITE ELEMENT METHOD

An application of hybrid stress method in studying the free vibrations of two-dimensional continuum in plane stress or plane strain problems by finite elements is investigated. The basis of the method is the assumed parametric stress field giving equilibrium of the internal forces inside the element area. The displacements on the element boundary are independent of the stress field and fully determined by the nodal displacements. The displacement field inside the element is independent of the assumed stress field and it is determined by parameters different than the assumed stress field parameters. Differentiating the assumed displacement field, a new stress field is obtained, which parameters are set to approach the assumed stress field by the least squares method.

INTRODUCTION

In hybrid finite element method, applied for solid mechanics problems, element characteristics are presented by several fields [1, 2, 3]. It can be assumed displacement or stress field in the element interior. Independently it is assumed another form of these fields on the element boundary. Only one of the assumed fields is expressed by the physical degrees of freedom (nodal displacements or nodal forces) and all others – by generalized parameters.

In the hybrid stress formulation of a dynamic problem, in contrast with the static case, not only the element boundary displacements are needed, but these ones in its interior, as the inertia forces depend from them. In the displacement-based finite element method the displacements *u* are the basic unknown quantities, from which the strains and the stresses can be obtained readily by a differentiation. In the hybrid stress method basic unknowns in the interior of the finite element are the stresses. Therefore the displacements *u* can be either introduced in appropriate manner or can be obtained from the selected stresses by integration.

When a variational formulation of the problem is used, the functional is initially written in all introduced parameters and then it is required stationary conditions to be fulfilled. As a result a system of equations is obtained, in which general parameters and physical degrees of freedom are contained. This system is used for elimination of the generalized parameters.

In this contribution it is discussed an application of hybrid stress finite element method in studying the free vibrations without a resistance of plane stress or plane strain continuum. The basis of the method is the assumed parametric stress field giving equilibrium of the internal forces inside the element area. The boundary forces correspond to this field. The displacements on the element boundary are independent of the stress field and fully determined by the nodal displacements.

PROBLEM FORMULATION

Free vibrations of 2-D structure are investigated. It is accepted [6] that the structure is free on the surface (the portion of the whole boundary, where traction is prescribed) and is fixed on the surface S_u (the portion of the boundary with prescribed displacements). Small displacements are considered, so all equations are linear and the displacements, the strains and the stresses are harmonic with a circular frequency ω. Further the amplitude values of stresses, strains and displacements are used, denoted by σ, ε and u, respectively. The structure is discretized with two kinds of finite elements. These one, which are on the structure boundary with prescribed traction, further are noted as external finite elements, and the other – as internal. The external finite elements (Fig. 1a) have a side, which is a part of the boundary S_σ. The internal finite elements (Fig. 1b) have no side with prescribed traction.
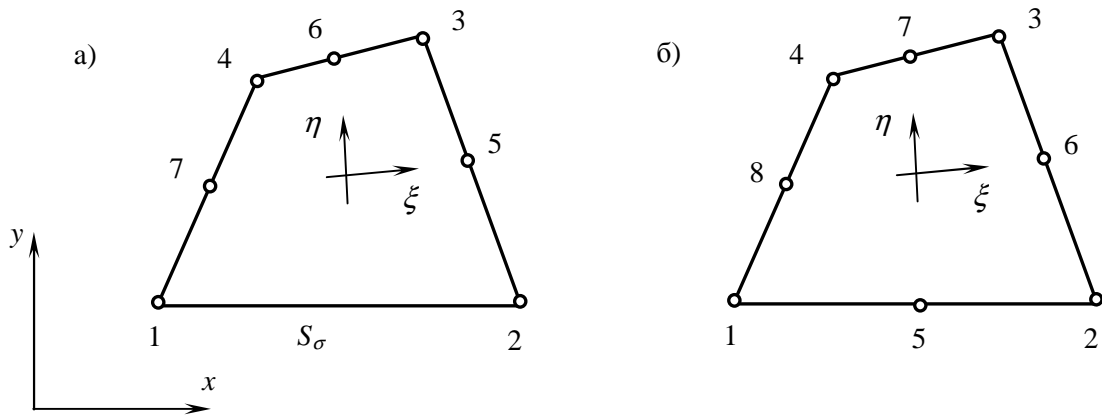

Fig. 1. External (a) and internal (b) finite elements

It is known [6], that the eigenvalue problem of a mechanical system with finite degrees of freedom has a form

$$Kv = \lambda M v, \tag{1}$$

where K and M are the stiffness and the mass matrices of the system, respectively, v is the nodal displacement vector, and λ is an eigenvalue of the system. By the finite element method the structure is reduced to a system with finite degrees of freedom and the matrices K and M are obtained.

ELEMENT MATRICES

In accordance with hybrid stress method [4] in the volume of the individual element V the stresses are expressed in terms of stress parameters vector β

$$\sigma = A\beta, \tag{2}$$

where A is a matrix, whose elements are functions of coordinates.

On the boundary of the element S displacements are expressed in terms of nodal displacements v by compatible interpolation functions.

$$u_S = Gv. \tag{3}$$

The assumed stresses are required to satisfy the homogeneous equations of equilibrium in V

$$D^T \sigma = 0, \tag{4}$$

For internal finite element the condition (4) has to be fulfilled but for external finite element – condition (4) and on the portion S_σ the condition

$$n^T \sigma = T, \tag{5}$$

where D is a matrix-differential operator, T – the boundary traction vector, n – the matrix of directional cosines of the boundary normal.

In order to obtain the finite element stiffness matrix the complementary energy functional is used in the form [6]

$$\Pi_C = 1/2 \int_V \sigma^T E^{-1} \sigma \, dV - \int_{Su+S} T^T u_S \, dS, \tag{6}$$

where E^{-1} is the elastic compliance matrix.

After a substitution of (2) and (3) in (6) the functional is transformed to

$$\Pi_C = 1/2 \, \beta^T \int_V A^T E^{-1} A \, dV \, \beta - \beta^T \int_{Su+S} A^T n^T G \, dS v. \tag{7}$$

From the extremum condition $\delta \Pi_C(\beta) = 0$, i.e. the first variation of (7) with respect to stress parameters β equals zero it follows

$$\beta = C^{-1} Hv, \tag{8}$$

where

$$C = \int_V A^T E^{-1} A \, dV \tag{9}$$

is the compliance matrix (positive definite, if all functions in A are linear independent),

$$H = \int_{Su+S} (n^T A)^T G \, dS = \int_{Su+S} A^T n G \, dS \tag{10}$$

is the leverage matrix.

If equation (8) is substituted in the deformation energy expression it is obtained

$$U = 1/2 \int_V \sigma^T E^{-1} \sigma \, dV = 1/2 \, \beta^T C \beta = 1/2 \, v^T H^T C^{-1} Hv = 1/2 \, v^T K \, v, \tag{11}$$

where

$$K = H^T C^{-1} H \tag{12}$$

is the hybrid stress finite element stiffness matrix.

The element mass matrix can be obtained by the kinetic energy expression in the form [6]

$$E_k = 1/2 \, \lambda \int_V u^T \rho \, u \, \mathrm{d}V . \tag{13}$$

The displacements u inside the element can be selected in a different manner. In the suggested hybrid method the stresses σ are assumed. The obtaining of displacements u from σ is connected with fulfilment of Beltrami-Michell conditions, which complicates the procedure, because of that it is suggested another way. The displacements inside the element are independent of the assumed stresses and they are determined by parameters different than the assumed stress parameters. In general case [5]

$$u = L_1 a_f + L_2 a_s, \tag{14}$$

where a_s are the parameters, associated with rigid body displacements, and a_f – the parameters, associated with displacements causing deformations.

Differentiating the assumed displacements (14), new stresses are obtained

$$\tilde{\boldsymbol{\sigma}} = EDL_1 a_f, \tag{15}$$

To approach these stresses to stresses (2) it is used the functional of the least squares

$$\Phi = \int_V (\tilde{\boldsymbol{\sigma}} - \sigma)^2 \, \mathrm{d}V . \tag{16}$$

The extremum condition $\delta\Phi\,(a_f) = 0$, i.e. the first variation of (16) with respect to a_f equals zero, yields

$$a_f = R^{-1} N \beta. \tag{17}$$

By substitution of (8) in (17) it is obtained

$$a_f = R^{-1} N C^{-1} H v. \tag{18}$$

It is necessary to express the parameters a_s in (14) by the nodal displacements v. For that purpose the collocation method is used, supposing that displacement function in the interior of the finite element, considered as a rigid body, has values in the nodes 1 and 2, coinciding with their displacements, i.e.

$$a_s = \hat{\boldsymbol{L}}_2 \, v. \tag{19}$$

The resulting displacements then become

$$u = Qv, \tag{20}$$

where

$$Q = R^{-1}NC^{-1}H + \hat{\boldsymbol{L}}_2. \tag{21}$$

The dependence (20) is substituted in (13) and the expression for kinetic energy takes the form

$$E_k = 1/2 \, \lambda v^{\mathrm{T}} \int_{Su} Q^{\mathrm{T}} \rho \, Q \, \mathrm{d}V v = 1/2 \, \lambda v^{\mathrm{T}} M v, \tag{22}$$

where

$$M = \int_V Q^{\mathrm{T}} \rho \, Q \, \mathrm{d}V \tag{23}$$

is the mass matrix of the hybrid stress method.

Computer programs are created for calculation of described element matrices. The stress functions in the matrix A fulfill conditions (4) and (5) for external and condition (4) for internal finite element. In this matrix polynomials of third power for internal and of fourth power for external finite element are used. The functions contain a sufficient number of unknown parameters β according to the condition $m \geq n - p$, where m is the number of the stress parameters β, n – the number of finite element degrees of freedom, p – the number of degrees of freedom of the element as a rigid body.

To compute the matrices a transformation of Cartesian coordinates in normal natural ones is done. For computation of integrals Gauss quadrature formulae are used. The displacement approximation inside the elements is with polynomials of fourth power.

NUMERICAL RESULTS AND CONCLUSION

In order to estimate the possibilities of the suggested hybrid stress method it is investigated the problem of eigenfrequency determination of homogeneous membrane 10x10x1m, fixed on the two opposite sides (Fig. 2). The described before external and internal elements are used.

The discretization variants with 25, 64 and 100 quadratic finite elements are investigated. It is used the computer system VIMKE for finite element method application to obtain the first

Fig 2. Homogeneous membrane

three eigenfrequencies of the membrane (Table 1) by the hybrid and displacement methods (denoted with HM and DM, respectively).

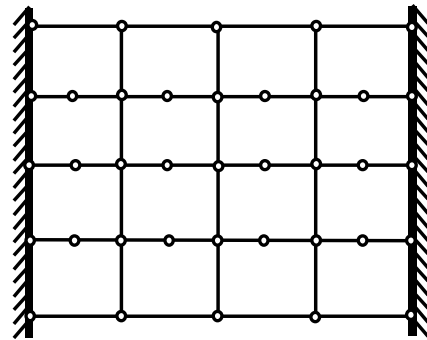In the graphics from Fig. 3 the changes of eigenfrequencies are shown when the mesh is refined.

Table 1. Eigenfrequencies of the membrane

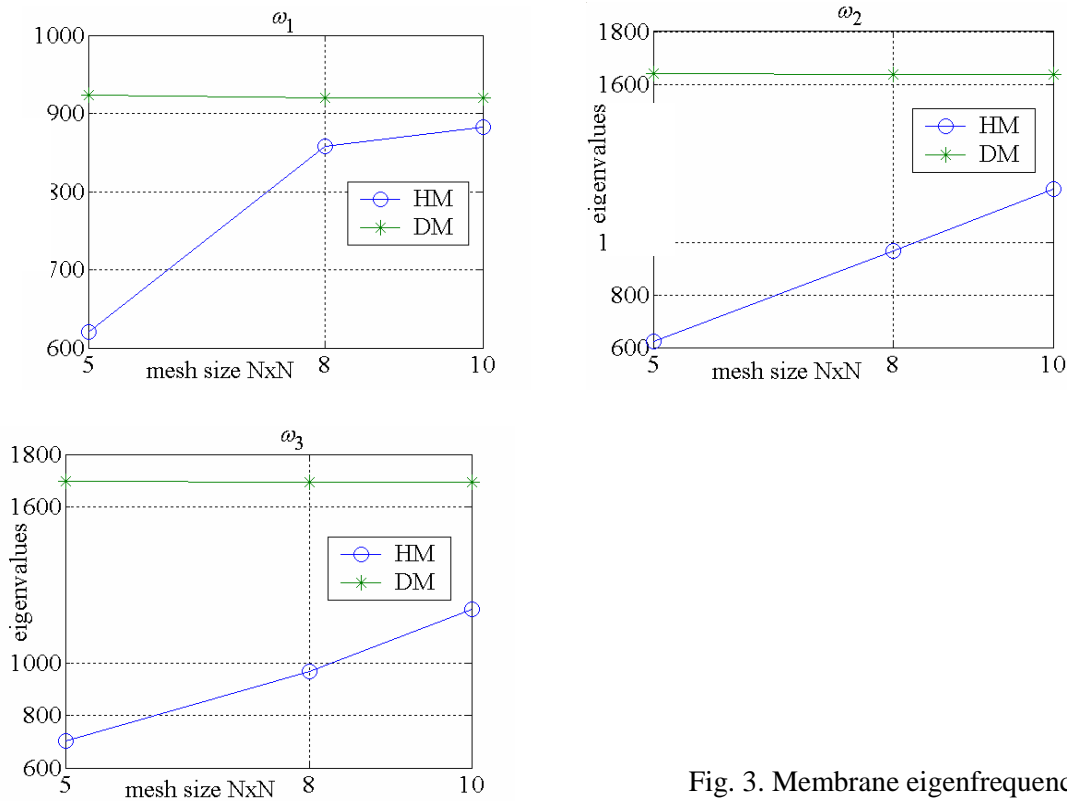| Mesh	Method	ω_1	ω_2	ω_3
5x5	HM	621.02	623.36	703.52
	DM	923.59	1641.22	1698.41
8x8	HM	858.28	965.89	969.21
	DM	920.09	1638.41	1693.26
10x10	HM	882.30	1203.13	1207.65
	DM	919.35	1637.73	1692.54

Fig. 3. Membrane eigenfrequencies

It is followed from the results that with increasing of the finite elements number the values of eigenfrequencies, obtained by hybrid stress method grow, remaining smaller than ones, obtained by the displacement-based method, which have a decreasing tendency. This confirms the known fact [6] that the displacement method gives the upper bound for the eigenfrequencies.

REFERENCES

1. Altenbach J., Todorov M.: *Generalized variational principles and hybrid finite elements in elasticity*. Dynamics and strength of machines, 32, Harkov, 1980 (in Russian).

2. Gallagher R. H.: *Finite element analysis*. Fundamentals. Prentice-hall, Inc., New Jersey, 1975.

3. Pian T. H.: *Some notes on the early history of hybrid stress finite element method*. IJNME, 47, 419-425, 2000.

4. Todorov M.: *Anwendung finiter hybrider Spannungselemente in der Elastostatik*. Dissertation. TH Magdeburg, 1978 (in German).

5. Todorov M., Savova A.: *Hybrid finite elements with stress functions, satisfying Beltrami-Michell differential equations*. University of Russe, vol. 28, 11, 1986 (in Bulgarian).

6. Washizu K.: *Variational methods in elasticity and plasticity*. Pergamon Press, 1982.

Janette BREZINOVÁ
Anna GUZANOVÁ
Milan GUZAN
Jozef MALEJČÍK

Technical University of Košice, Slovakia

THE ELECTROCHEMICAL CHARACTERISTICS OF SURFACE PRE-TREATED BY ABRASIVE BLASTING

The paper presents results of research aimed on evaluation of electrochemical characteristics of metal surfaces after mechanical pretreatment by blasting. Corrosion resistance was evaluated by materials identification at fixed time intervals after their exposure in an electrolyte. Electrochemical characteristics of the blasted surfaces were evaluated in 0.1 mol NaCl solution by electrochemical impedance spectroscopy (EIS). There was used monodispersive blasting media based on different materials in conditions of pneumatic blasting. The results of EIS measurements were a Nyquist diagrams from which there was determined the polarization resistance values Rp on the basis of their circular regression.

INTRODUCTION

One of the most important part of the technology of machine production are the processes of changes in the surface, so-called finalization technologies that improve the quality and the condition of the surface. To the finalization technologies, we can include some of the processes of material joining and coating technology. Each of these technologies includes specifications that determine the resultant nature of the products.

From the whole range of ways of the surface pretreatment before following application of functional as well as protective coatings the abrasive blasting technology comes to the fore. It can be used to prepare the surface of required quality to ensure good adhesion of applied coatings to the substrate. Blasted surface has a very high surface activity. In real conditions, its activity rapidly decreases by the chemical adsorption of gases from the atmosphere and oxidation. The consequence is a reduction of the electrode potential of the metal [1- 3].

In the industrial sphere, there are several standardized tests for the rapid estimation of the corrosion properties such as cyclic wetting and drying tests, tests in salt spray or resistance to ultraviolet radiation. However, the corrosion research is determined for continuous development due to the upcoming challenges in this field of science such

as increasing diversification of products - the diversity of sortiment, using of new types of materials and the application of high-tech technologies.

To determine the corrosion resistance of metals in conductive environments electrochemical methods based on the electrochemical theory of corrosion are used. Continuously increasing demands on the life of corrosion protection of the materials lead to the development of new electrochemical methods, which can be used to determine protection effectiveness of the coatings, respectively other surface treatments in a relatively short time. The modern methods of corrosion monitoring include "Scanning Kelvin Probe" techniques (WCL), electrochemical impedance spectroscopy (EIS) and electrochemical noise method (ENM) [4-7].

The contribution presents the use of EIS in the evaluation of the electrochemical characteristics of the blasted surfaces on the different material basis in the corrosive environment.

MATERIAL AND METHODS

For the experimental work the following materials were used:

a) structural steel S235JRG2 (EN 10025A1)

b) stainless steel X8CrNiTi18-10 (EN10095)

c) aluminium AW-1080A (EN 573-3)

Chemical and mechanical properties of particular investigated materials are shown in Table 1 and 2.

Table 1 Chemical composition of used materials

Material / Element [max %]	C	N	P	S	Cr	Mn	Ni	Si	Ti	Cu	Zn	Fe	Al
S235JRG2	0.17	0.007	0.045	0.045									
X8CrNiTi18-10	0.12		0.045	0.03	20	2	11	1	0.05				
AW-1080A								0.15	0.03	0.02	0.05	0.15	bal.

Table 2 Mechanical properties of used materials

	Rm [MPa]	Re [MPa]
S235JRG2	373-980	195-637
X8CrNiTi18-10	480-2240	170-1000
AW-1080A	40-60	85

The test samples were turned into cylindrical shape Ø11.3 x 20 mm and then the front areas were adjusted by common metallographic procedures. The front areas of all samples were blasted by following blasting media with grain size $d_z = 0.4$ mm:

    a)   Brown Corundum (Al_2O_3),

    b)   Glass beads.

Pretreatment of the surface was carried out by the air blasting on laboratory device TVJP - 320 at pressure of 0.4 MPa using a necessary amount of the blasting medium, so that the surface was completely covered with impacts of blasting media grains.

After the blasting the surface roughness was evaluated using the roughness tester Surftest SJ - 301, Mitutoyo, according to EN ISO 4287. Surfaces of the blasted samples were studied on a light microscope Olympus BXM. Electrochemical characteristics of the surfaces were evaluated using electrochemi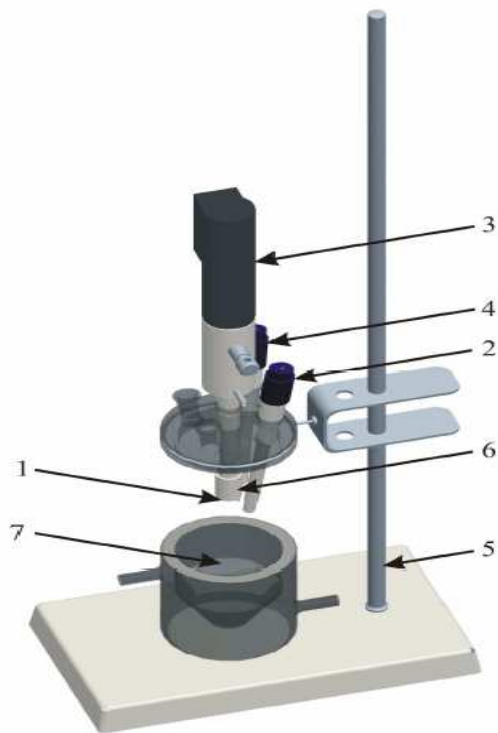cal impedance spectroscopy (EIS) on the laboratory device VoltaLab 10. The measurements were carried out using the measuring unit PGZ 100 and the control unit CTV 101. Corrosive environment consisted of 0.1 M NaCl solution. Time of the sample´s free potential stabilization was 5 min. and 1, 4 and 8 hours. The frequency changes ranged from 100 kHz to 10 MHz with the change in frequency 20 times per decade. AC voltage amplitude was 20 mV. The temperature during measurement was 22°C ± 1°C. The sample during the measurement was rotating on the rotary electrode at the speed of 70 min^{-1}. Circuit diagram and measurement principle is shown in Fig. 1. Determination and calculation of the polarization resistance Rp was carried out from the measured courses of the EIS by circular regression from Nyquist diagrams, which are provided for the illustration for the material S235JRG1 in Figs. 2 and 3.

Fig. 1. Experimental device for potentiodynamic and galvanostatic tests: 1 - sample, 2 - calomel reference electrode, 3 - rotating electrode, 4 -platinum auxiliary electrode, 5 - stand, 6 - sample holder, 7 - corrosion bank
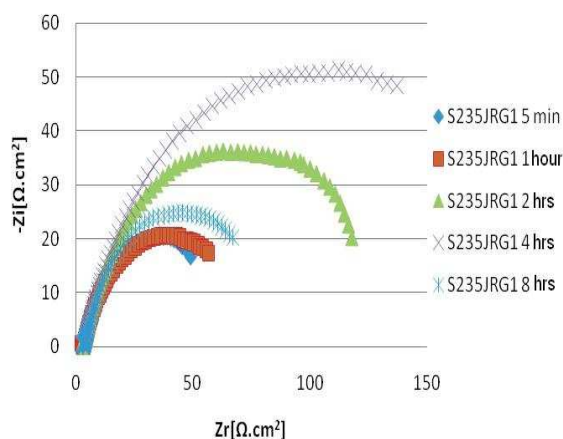

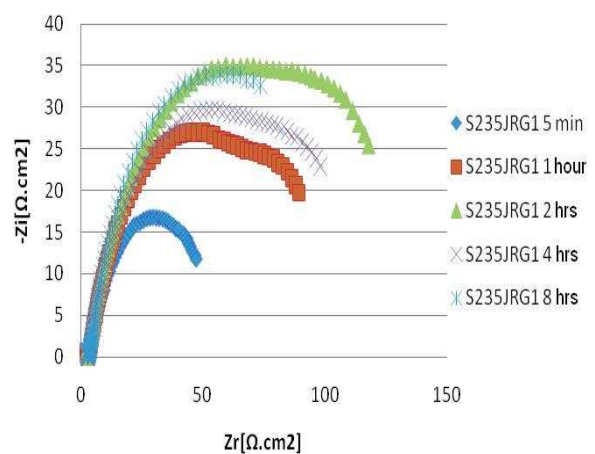Fig. 2. EIS curves of steel S235JRG1 in 1 M NaCl solution after blasting by corundum

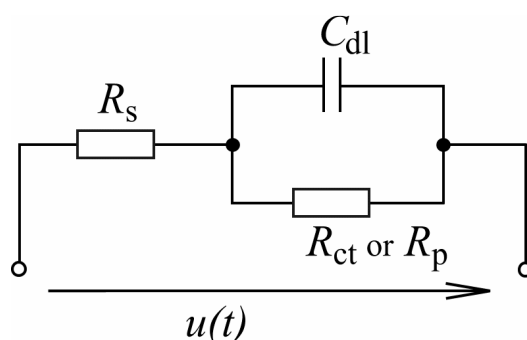Fig. 3. EIS steel curves S235JRG1 in 1 M NaCl solution after blasting by glass beads

Fig. 4. Equivalent circuit of the porous corrosion system with inductive part [4]

For the analysis of the measured curves, based on their shape, the equivalent circuit shown on figure 2 was used. It is one of the most common cell models, when $u(t)$ represents AC voltage, R_s presents resistance of 0.1 M NaCl solution, C_{dl} corresponds to double layer capacitance which exists on the interface between an electrode and its surrounding electrolyte and R_{ct} or R_p is charge transfer resistance or polarization resistance. For more information on the elements listed in the equivalent circuit can be found in [4]. The values of the parameters that characterize the particular components in the equivalent circuit were determined by software analysis using the program VoltaMaster 4.

DISCUSSION

Based on this methodology microgeometry of the blasted surfaces was evaluated. In Fig. 5 we can see two profilographs of the material surface S235JRG2 after blasting with corundum (a) and glass beads (b). After blasting with corundum we obtained very rough surface consisting of sharp notches, depending on the shape of the used blasting media, Fig. 6a. Blasted surface using glass beads consisted of spherical indents according to the shape of blasting media (Fig. 6b) and the values of the roughness after blasting with glass beads were lower for all evaluated materials, see Table 3. The values of the arithmetical mean deviation of the profile Ra and maximum height of profile Rz depend on the relation of the blasting medium and blasted substrate hardness, as well as on the technological parameters of the blasting process.

For individual types of the materials, the shape of Nyquist diagrams changed, Figs. 3 and 4. Polarization resistance for this shape of the curves equals to the semicircle diameter in the Nyquist diagram, therefore only the presence of insulating-layer was recorded.

With increasing of the exposure time of samples in electrolyte, the value of polarization resistance Rp increased, Fig. 7. In all blasted materials the higher values of Rp were measured using brown corundum, which may be related to the size of the real surface area after blasting as well as the kinetic energy of incident grains of blasting medium. The maximum value of Rp for S235JRG2 steel was found in exposure time 4 hrs. For the other two materials (stainless steel X8CrNiTi18-10, aluminium AW-1080), the maximum Rp moves according to the increasing time of the exposure of samples. With the increasing Rp value corrosion rate decreases.
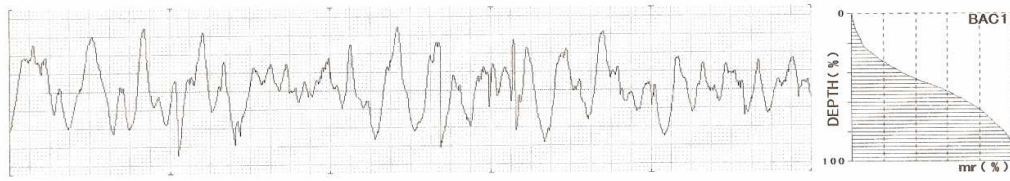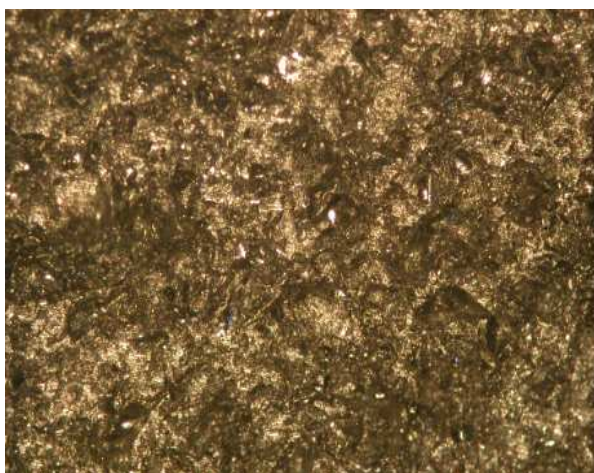
a)

b)

Fig. 5. Profilographs of the surfaces of S235JRG2 steel after blasting by: a) brown corundum, b) glass beads

Table 3 Roughness values for individual materials

substrate	Ra [µm]		Rz [µm]	
	corundum	glass beads	corundum	glass beads
S235JRG2	1.44	1.04	15.64	5.85
X8CrNiTi18-10	2.31	0.61	17.42	4.44
AW-1080A	7.12	2.81	39.28	15.32

a)

b)

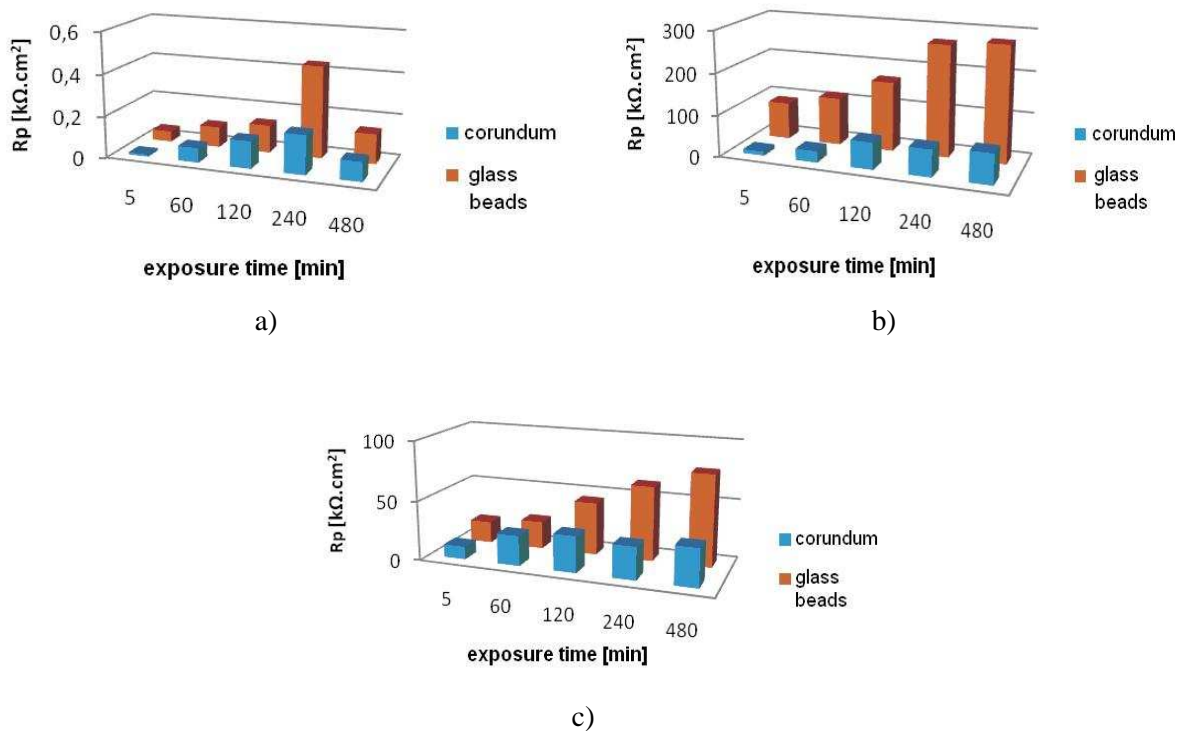Fig. 6. Appearance of the blasted surface using a) corundum, b) glass beads

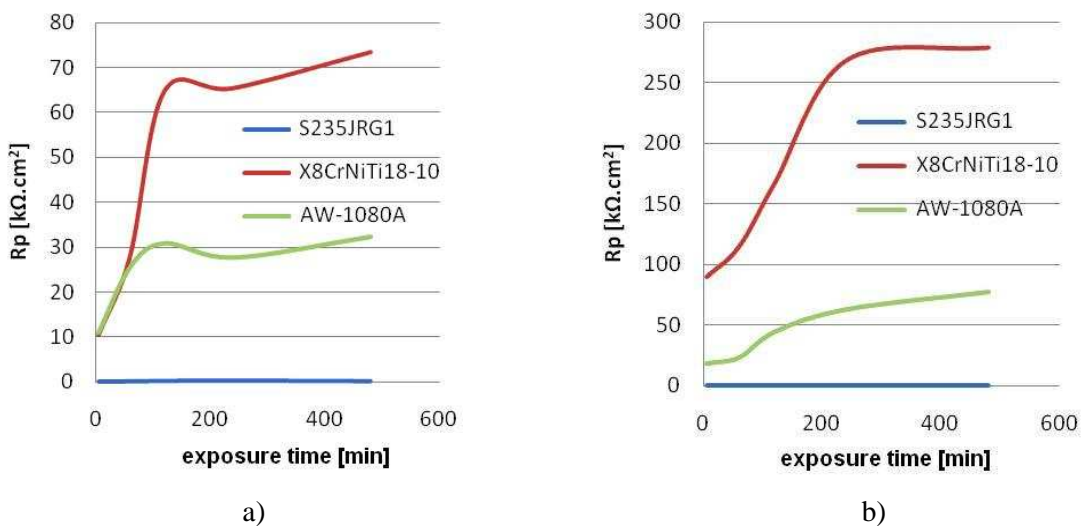Fig. 7. Time dependence of the polarization resistance Rp for the material a) S235JRG2, b) X8CrNiTi18-10, c) AW-1080A

Fig. 8. Time dependence of Rp for materials blasted using: a) corundum, b) glass beads

The decrease in the polarization resistance Rp is caused by the diffusion of the corrosive products into the electrolyte, which were partially protective in nature, resulting in the creation of new surfaces and the further active development of the corrosion process. Corrosive products are better able to adhere to the blasted surface, and if their breaks occur, it leads to faster corrosion process. The increase in the total resistance at the interface material - electrolyte is caused by the increase in resistance of the porous layer. At the same time we can observe the increase in resistance, which

may be caused by the activation of more corrosive microcells near the surface during the corrosion process. Corrosion microcells may occur between the particular microstructural compounds with the different nobility or between the microstructure and more noble corrosion products.

CONCLUSIONS

The experiments were carried out to establish the influence of blasting the surface by various blasting media on corrosion resistance of materials with different properties – structural steel S235JRG1, stainless steel X8CrNiTi18-10 and aluminium AW-1080A using EIS method – electrochemical impedance spectroscopy. Mentioned materials were exposed in the corrosion environment - 1 M NaCl solution. Parameter which characterizes the properties of the material in these tests is the polarization resistance Rp.

Evaluation of surface microgeometry showed that blasting by brown corundum created very rough surface formed by sharp notch, depending on the shape of the blasting media. The surface blasted by glass beads consists of spherical impacts and values of roughness after blasting by glass beads for all evaluated materials were lower.

From the analysis of Nyquist diagrams and from the measured polarization resistances it can be concluded that the highest value of Rp was found for stainless steel X8CrNiTi18-10, the lower value for aluminium AW-1080 and the lowest value were measured for structural steel S235JRG1. There was also noted shape change of Nyquist diagrams, what suggests a change in the nature of the corrosion products layer and a decrease in the total Rp. The decrease of Rp is due to detachment of corrosion products that are of protective character. With increasing the exposure time of samples in the electrolyte the potential value increases, which corresponds to the reduction of surface activity. A larger decrease was noticed in materials blasted by brown corundum.

Experimental works have shown that the use of electrochemical impedance spectroscopy (EIS) as a modern non-destructive method is the possibility of new rapid method of quantitative description of the local corrosion process, progress of corrosion processes and their management. It represents the future in corrosive industrial monitoring because it allows obtaining information about the corrosion relatively quickly, or continuously. Quick response to the intensification of corrosion is needed for an operational action to either adjust the conditions of its own technology and corrosion protection so in order to reduce corrosion to acceptable levels or to avoid serious damage of the premises and accidents.

REFERENCES

1. Winstone R., Herbert H.U.: *Corrosion and corrosion control, At Introduction to Corrosion Science and Engineering.* Copyright 2008 by John Wiley & Sons, Inc.
2. Hadzima B., Suchý P., Škorík V.: *The dependence of electrochemical characteristics on heat treatment of AZ80 Mg alloy.* In: DAS 2006 (23rd Danubia-Adria, Symposium on Experimental Methods in Solid Mechanics), s. 185.
3. Nauer G.E.: *Modern electrochemical surface treatments for automotive applications.* Kplus ECHEM, University of Viena, 2008.

4. http://www.gamry.com/App_Notes/EIS_Primer/EIS_Primer.htm#Model2

5. Raja V.S. et al: *Electrochemical impedance behavior of graphite-dispersed electrically conducting acrylic coating on AZ31 magnesium alloy in 3.5 wt.% NaCl solution*. Progress in Organic Coatings, Vol. 67, 1, January 2010, pp. 12-19.

6. Mansfeld F.: *Electrochemical impedance spectroscopy (EIS) as a new tool for investigating methods of corrosion protection*. Electrochimica Acta, Vol. 35, 10, October 1990, pp. 1533-1544.

7. Dornbusch M.: *The use of modern electrochemical methods in the development of corrosion protective coatings*. Progress in Organic Coatings, Vol. 61, 2-4, February 2008, pp. 240-244.

Janette BREZINOVÁ
Maroš HALAMA
Ľuboš KAŠČÁK
Ján VIŇÁŠ

Technical University of Košice, Slovakia

ANALYSIS OF SPOT WELDS QUALITY OF ZINC-COATED SHEETS AND THEIR CORROSIVE PROPERTIES

The contribution presents results of research aimed on evaluation of spot welds quality formed by resistance spot welding at zinc-coated sheets joiing processes. There were determined electrochemical properties of materials with help of linear voltammetry. Change of spot weld strength was evaluated before and after their exposure in selected corrosive media.

INTRODUCTION

One of the most dynamically developing industries today is the automobile industry. Significant contribution to its rapid development is provided by continuous improvement of quality and performance parameters of produced vehicles. One of the important requirements for materials used for vehicle construction is their corrosion resistance, which, when provided, leads to the increasing share of the automobile parts with protective, especially zinc coatings. Galvanized sheet produced by zinc electro-lyzing or dipping shows very good resistance to atmospheric corrosion and is therefore suitable for outdoor using. Surface treatment by galvanizing ensures good corrosion resistance of metal chassis and allows producers to offer more than 10 year life guarantee of the chassis. However, this type of surface treatment causes considerable problems in the methods of joining metal chassis, when using conventional methods (MIG welding, resistance spot welding), but also unconventional methods (laser welding) leads to evaporation of protective layers of weld due to the heat and thus to decrease of the corrosion resistance of the assembly parts [1, 2, 4, 10].

The contribution presents results of the research aimed at analysis of the quality of joints on galvanized sheets and their corrosive properties. Protective efficiency of zinc coatings for automobile sheets was evaluated, based on the determination of their electrochemical characteristics in passivated and non-passivated state, as well as their corrosion resistance in simulated corrosion environments.

MATERIALS AND METHODS

For experimental work following materials were used:
a) ZINKOHAL 220 sample A – chemical and mechanical properties in Table 1 and 2,
- sheet thickness 0.70 mm; zinc coated 140 $g.m^{-2}$
- surface treatment: non-passivated
- use: for exterior body panels for cars – DACIA LOGAN – the roof

Table 1. Chemical composition of the Zinkohal 220 steel [%] according to EN 10327/04

C	Mn	Si	P	S	V	B	Mo	Sn	Sb	N	Cu	Ti	Al	Te	Ni	Cr	As
0.002	0.141	0.008	0.007	0.005	0.003	0.0002	0.002	0.002	0.002	0.004	0.015	0.052	0.042	0.001	0.005	0.013	0.001

Table 2. Mechanical properties of the Zinkohal 220 steel [%] according to EN 10327/04

Tensile strength R_m [MPa]	Yield strength $Rp_{0.2}$ [MPa]	Ultimate elongation A_{80} [%]	Normal anisotropy coeficient r [-]	Strain hardenig exponent n [-]
max. 288	155	43	2	0.24

b) ZINKOHAL 220 sample B - chemical and mechanical properties in Table 3 and 4,
- sheet thickness: 0.70 mm; zinc coated 140 g.m^{-2}
- use: for exterior body panels for cars – DACIA LOGAN – doors
- surface treatment: passivated Cr3+

Table 3 Chemical composition of the Zinkohal 220 steel [%] according to EN 10327/04

C	Mn	Si	P	S	V	B	Mo	Sn	Sb	Ni	Cr	Ti	Zr	Al	N	Cu	Te
0.002	0.153	0.008	0.005	0.004	0.001	0.0002	0.002	0.003	0.002	0.007	0.011	0.052	0.001	0.001	0.005	0.013	0.001

Table 4 Mechanical properties of the Zinkohal 220 steel [%] according to EN 10327/04

Tensile strength R_m [MPa]	Yield strength $Rp_{0.2}$ [MPa]	Ultimate elongation A_{80} [%]	Normal anisotropy coeficient r	Strain hardenig exponent n
max. 282	162	47	2.5	0.22

Test samples of stated materials were cut according to the norm STN EN 051 122 to size 90 x 40 mm, length of lapping was 30 mm. Spot welding was carried out on pneumatic spot-welder BPK 20 with welding electrodes CuCr with diameter ø5 mm. Selection of the welding parameters were based on the recommendations of British Standard (BS 1140) for spot welding of coated sheets, while the correction of the parameters was necessary, given the options of specific spot-welders. Welding parameters: contact force Fz = 2.6 kN, welding time t = 14 periods, welding current 85 kA. [3, 5] For the evaluation of mechanical properties of spot welds before and after the exposure to the corrosive environments tensile test according to STN 05 1122 was realised. The tensile test of spots and full penetration welded joints were carried out on a test machine TIRA-test 2300, VEB TIW Rauenstein [6]. Created joints were exposed to an environment of 5% NaCl solution and organic solution Solmag. The above environments simulated influence of the spreadings in vehicle operation conditions. [8, 9] For the evaluation of the corrosion processes gravimetric method was used. For determination of the electrochemical characteristics of these materials potentio-dynamic polarization curves for the assessment of Ek - corrosion potential by Tafel, Ik – corrosion current density and Rp - polarization resistance were measured. Electrochemical characteristics of the tested samples were evaluated before exposure to the corrosive environment and after 240, 480 and 720 hrs of exposure by Tafel and Stern method. For potentiodynamic measurement a computer-controlled potentio-

stat/galvanostat VOLTALAB 21 PGP201 (producer Radiometer Analytical, Denmark) with software VOLTAMASTER 4 was used; a schematic diagram of apparatus in three-electrode wiring is in Fig. 1. For the SEM analysis electron microscope JEOL JSM - 7000F was used.
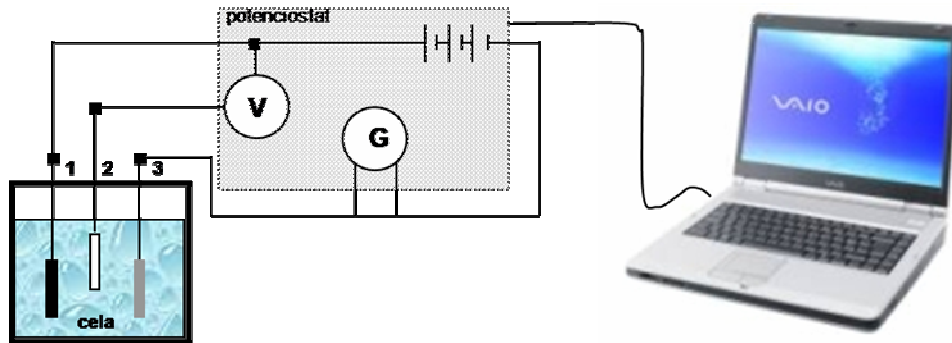

Fig. 1. Scheme of measurement of base corrosion characteristic with linear voltammetry method: V – voltmeter, G – ammeter, 1 – sample, 2 – SCE – saturated calomel electrode, 3 – Pt – auxiliary electrode

RESULTS

Maximum power for the destruction of spot joints before their exposure to the corrosive environments were 10.7% higher for samples B (passivated state) compared with samples A (nonpassivated state), Fig. 2. After the exposure the test samples in the corrosive environment of 5% NaCl solution, increased carrying capacity of joints was observed in samples B (passivated state). When comparing the values of Fmax before and after the exposure to the corrosive environment it was ascertained, that for both types of samples the spot-welds strength increased (for samples A by 0.45%, and samples B by 5.1%). After the exposure of the test samples to the corrosive environment made up of Solmag ecological solution, higher carrying capacity of the joints for samples B (passivated state) was found again.

Fig. 3 presents the macrostructure of the cross-section of the welded joint. We can observe good penetration with no signs of defects and nonpenetrations, heat affected areas and local flashing of the Zn layer in the contact place of welding electrodes. Fig. 4 presents the formation of the zinc corrosion products on the surface of the test samples after the corrosion tests in NaCl environments. It is possible to observe produced zinc hydroxide, called white corrosion, which was confirmed by EDX analysis as well. The main factor behind the formation of white corrosion on zinc layer is condensation of air moisture, respectively the impact of the electrolyte.

Due to the moisture galvanized sheet behaves like a galvanic cell, where zinc layer with a lower electric potential is the anode and steel represents the cathode. A very important factor in the atmospheric corrosion is oxygen, because the thin layers of moisture pose as minimal barriers for its diffusion into the condensed moisture [11]. Therefore, it is not necessary for the process of the electrochemical reaction to reach the dew point. Therefore, already at a lower humidity, which is usually referred to as the critical corrosion humidity (60%), a very thin layer of electrolyte solution (0.005 to 0.15 mm) is created on a metal surface. The cause is the surface roughness and the presence of settled solid particles.
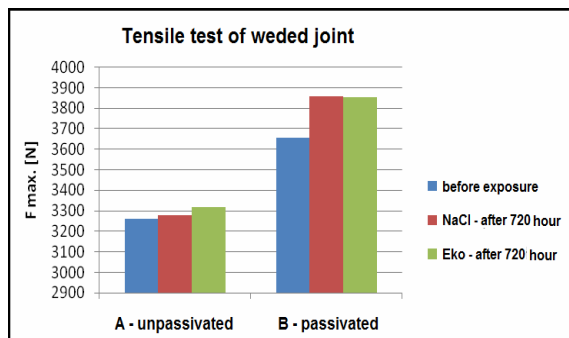
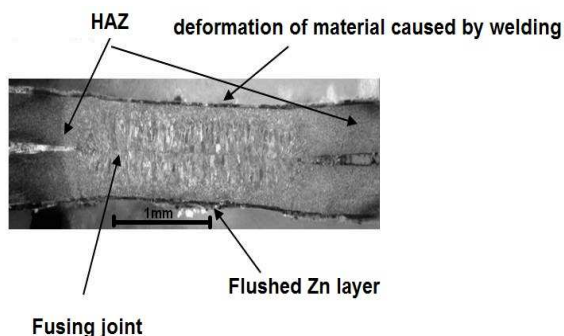Fig. 2. Average values of maximum strenght of A and B samples

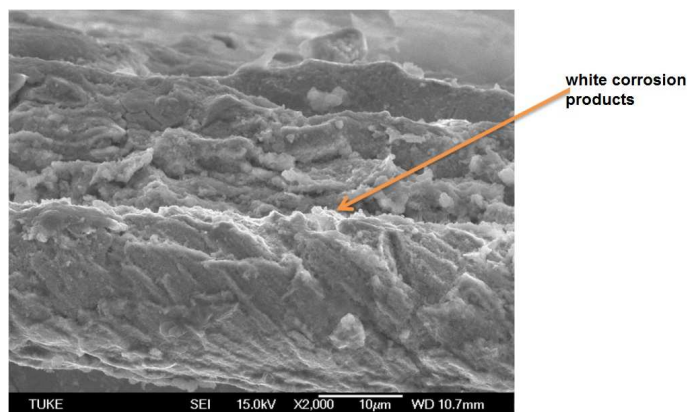Fig. 3. Macrostructure of the cross section of welded joint [7]

Fig. 4. SEM of Zn layer on sample surface after corrosion test

In the environment of 5% NaCl solution during the exposure time 240 hrs increasing of samples weight occurs, what is possible to attribute to corrosion products mainly of zinc formation. After crossing this threshold there is a significant weight loss of zinc coating in chloride environments, causing the release of corrosion products in the electrolyte. Since it is an aggressive environment, the protective efficiency of Zn signi-ficantly reduces destruction of the coating occurs. When comparing the weight losses of A and B samples in 5% NaCl solution, the difference is 53.66%, Fig. 5, 6.
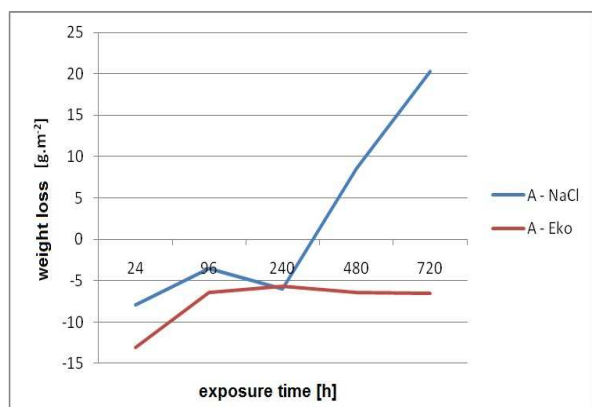

Fig. 5 Weight loss of A samples exposed in corrosion enviroments
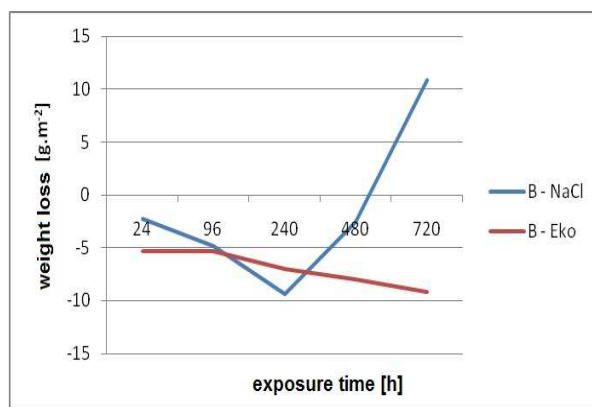

Fig. 6 Weight loss of B samples exposed in corrosion enviroments

It follows that the passivated samples are more resistant to mass loss than non-passivated in 5% NaCl solution. In environment of the ecologic solution weight losses with time of exposure didn't significantly change and the weight loss of samples du-ring the samples immersion didn't occur. Measured potentiodynamic polarization cur-ves of the samples in both states (non-passivated and passivated surface) evaluated by

Tafel method are shown in Fig. 7. From the results of the potentiodynamic measurements there were determined particular electrochemical characteristics of materials.

a)   b)
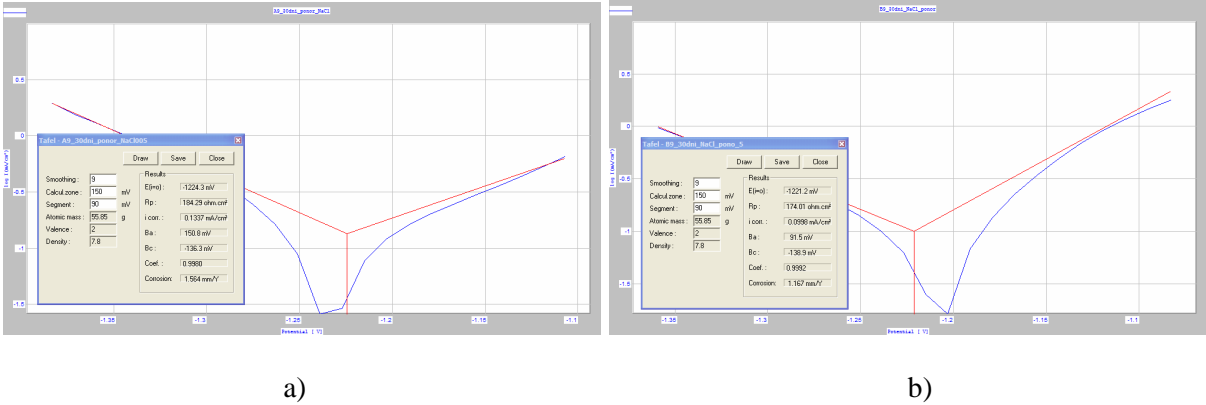
Fig. 7. Tafel evaluation of polarisation curves after 30-day exposition of samples in 5% solution of NaCl – immersion tests, a - samples A (nonpassivated surface), b – samples B (passivated surface)
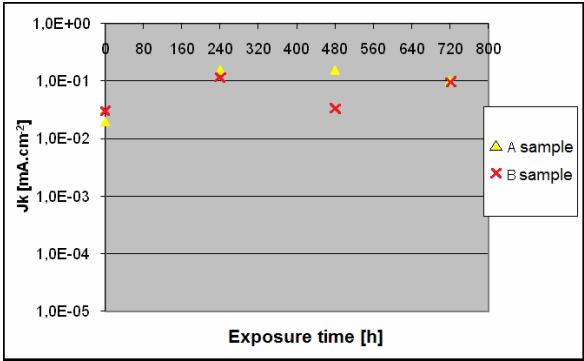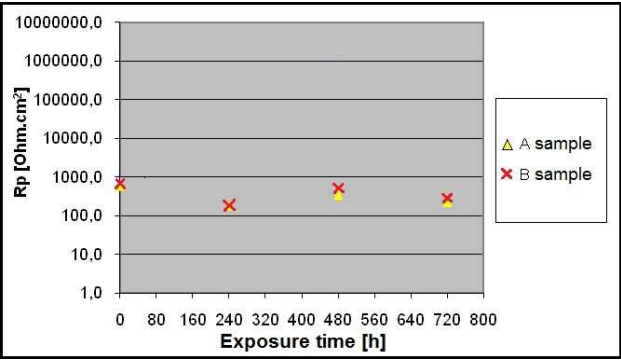

Fig. 8. Tafel method for determination of Jk

Fig. 9. Stern method for determination of Rp

Non-passivated zinc-coated sheet (A) and passivated zinc-coated sheet (B) in 5% NaCl solution after 720 hours exposure show the same corrosion current densities J_k, i.e. passivation makes sense only in the early phase of exposure, Fig. 8. Chloride corrosion environment operates on galvanized sheets so aggressive that after the first tens of hours of exposure is not significant difference between passivated and non-passivated surface in zinc-coated steel sheet. An interesting phenomenon occurs between 240 to 480 hours of exposure passivated zinc-coated steel in non-aggressive environment, when corrosion products show a high polarization resistance R_p to corrosion current flow (1.2 – 1.6 MΩ; see Fig. 9). But this passive layer is even in low aggressive environment after 720 hours of exposure violated and predominates "run-off" effect of Zn into the environment.

CONCLUSIONS

Welded joints made from passivated sheets showed higher carrying capacity in initial state. After exposure of samples in both corrosive environments there was found higher carrying capacity of joints in the passivated samples. This increase is possible to refer to accrued zinc corrosion products, which, despite their low adhesion to the substrate caused an increase in the strength of joints.

Microscopic analysis confirmed the formation of high-quality welds, which confirmed the correctness of the technological parameters of welding. It has been observed locally flashing of Zn layer in contact of welding electrodes and after exposure of samples in corrosive environments formation of zinc corrosive products, so called „white corrosion" occurs in consequence of condensation of air moisture or action of the electrolyte.

Samples immersed in ecologic solution SOLMAG reached during corrosion tests increasing of weight in consequence of accrued zinc corrosive products, corrosion process was running slower than in immersion in NaCl solution. In this relatively aggressive corrosive environment weight loss occured. Based on potentiodynamic electrochemical measurements both types of sheets showed after 720 hours of exposure the same corrosion current densities, i.e. passivation makes sense only in the early phase of exposure of samples in corrosive environments. On surface of passivated samples were created corrosion products with a high polarization resistance Rp, which hold their favorable properties up to approximately 500 hours of exposure [12].

REFERENCES

1. Lipa M.: *Odporové zváranie*. 1. vyd.. Bratislava: Weldtech, 1995. 265 s.

2. Zhang H., Senkara J.: *Resistance Welding: Fundamentals and Applications*. Taylor&Francis Group, New York. 2006, 420 s.

3. Tumuluru D. M.: *The Effect of Coatings on the Resistance Spot Welding Behavior of 780 MPa Dual-Phase Steel*. In.: Welding Journal vol. 86. 2007. p. 161 – 169.

4. Viňáš J., Kaščák Ľ.: *Hodnotenie kvality zvarových spojov karosárskych plechov*. In: Transfer inovácií : Špecializovaná publikácia / vedecko-technické výstupy grantových úloh. Košice : TU-SjF, 2005. č. 8 (2005), s. 112-115.

5. *Matta M., Gatial M., Tumuluru D.M., Kaščák Ľ., Viňáš J.:* Optimalizácia parametrov odporového bodového zvárania žiarovo zinkovanej ocele DP600. *In: Moderné konštrukčné materiály a technológie ich spájania. Stará Lesná, Slovensko. Bratislava 1 elektronický optický disk (CD-ROM) : Výskumný ústav zváračský, 2009. s. 1-14.*

6. Kaščák Ľ. Viňáš J.: *Možnosti bodového zvárania kombinácie vysokopevných a hlbokoťažných plechov*. In: Súčasný stav odporového zvárania : Zborník prednášok z konferencie : 18. februára 2009, Bratislava. Bratislava : Slovenská zváračská spoločnosť, 2009. s. 12-16.

7. Kaščák Ľ., Viňáš J.: *Metalografická analýza bodových zvarov karosárskych plechov*. In: Přínos metalografie pro řešení výrobních problémů : 11. česko-slovenská konference: Lázně Libverda, 17. - 19. červen 2008. Praha : ČVUT, 2008. p. 220-223. ISBN 978-80-01-04039-3.

8. Nauer G.E.: *Modern electrochemical surface treatments for automotive applications*. Kplus ECHEM, University of Vienna, 2008

9. Mabbutt S. et al.: *Developments of the electrochemical noise method (ENM) for more practical assessment of anti-corrosion coatings*. Progres in Organic Coatings 59 (2007), pp.192-196,

10. Chang B.H., Shi Y.W., Dong, J.: *A study on the Role of Adhesives in Weld-Bonded Joints*. In.: Welding Research Supplement, 1999. p. 275 - 279.

11. Yeung, K.S., Thornton H.: *Transient Thermal Analysis of Spot Welding Electrodes*. In.: Welding Research Supplement, 1999. p. 1 – 6.

12. Šulek M.: *Analýza kvality bodových spojov pozinkovaných plechov a ich korózne vlastnosti*. Diplomová práca, 2010. 89 s.

Alexey DROBOTOV
Mark KRISTAL

Volgograd State Technical University, Russia

PROGRAM CONTROLLED AIR CUSHION ROTARY TABLE WITH PNEUMATIC STREAM DRIVE

Design of the rotary table which uses energy of compressed air to drive necessary movements is proposed in the article. This design increases reconfigurability, performance, and should facilitate to increase in durability due to absence of rigid kinematic connections and dry friction units. Turning angle and stop moment are determined by control program which algorithm is presented in the article. To maximize efficiency of the rotary table it was necessary to study laws of rise of the moving part of the table, its fixation and rotation. Some results of research on time of rise, fixation, rotation, and overall performance of the device are presented in the article.

Rotary Tables (RT) are used as transportation units of automatic devices. Because of lack of reconfigurability they rarely find applications in a small scale production. This is due to presence of kinematic couples in their design. It is advantageous to use energy of compressed air in the drive of these devices.

We proposed a new design of the RT [1] principle scheme of which is depicted in Fig. 1. This device performs a turning according to the angle given by the control program which reduces time of reconfiguration on a new working mode.

The RT consists of the frame *1*, the rotary unit *2*, which holds the faceplate from the top and the turbine *3* and the magnetic ring *5* of the contactless sensor of the turning angle *4* from the bottom. There are two contradirected nozzles 6_1 and 6_2 for forward and backward rotations in the frame *1* against turbine blades *3*. The RT works as follows. In the initial position the clearance between the rotary unit *2* and the frame *1* is connected to the vacuum source and compressed air flowing from the nozzle 6_1 acts on the blades of the turbine *3*. Compressed air is then fed to the clearance between the frame *1* and rotary unit *2* which leads to the rise of the latter on the air cushion. The stream of compressed air flowing from the nozzle 6_1 drives the moving part. The control system backtraces the position of the moving part with aid of the sensor *4* and determines the reverse moment. At the reverse moment the nozzle 6_1 is disconnected from the source of compressed air and oppositely located nozzle 6_2 is connected to the source in order to accomplish smooth braking of the moving part *2*. The reverse moment t_{rev} is calculated in such a way that the velocity of the moving part is close to zero by the moment when it reaches the desired position. By the time t_{fix} before stop of the moving part the clearance between the rotary unit *2* and the frame *1* is connected to the vacuum. The latter causes lowering and fixation of the rotary part in the current

position. Information on position of the moving part is constantly fed to the control system via the sensor *4*. The time of stop t_{op} is determined by the control system. The loop is then repeated. The order in which nozzles 6_1 and 6_2 are turned on determines direction of the rotation.
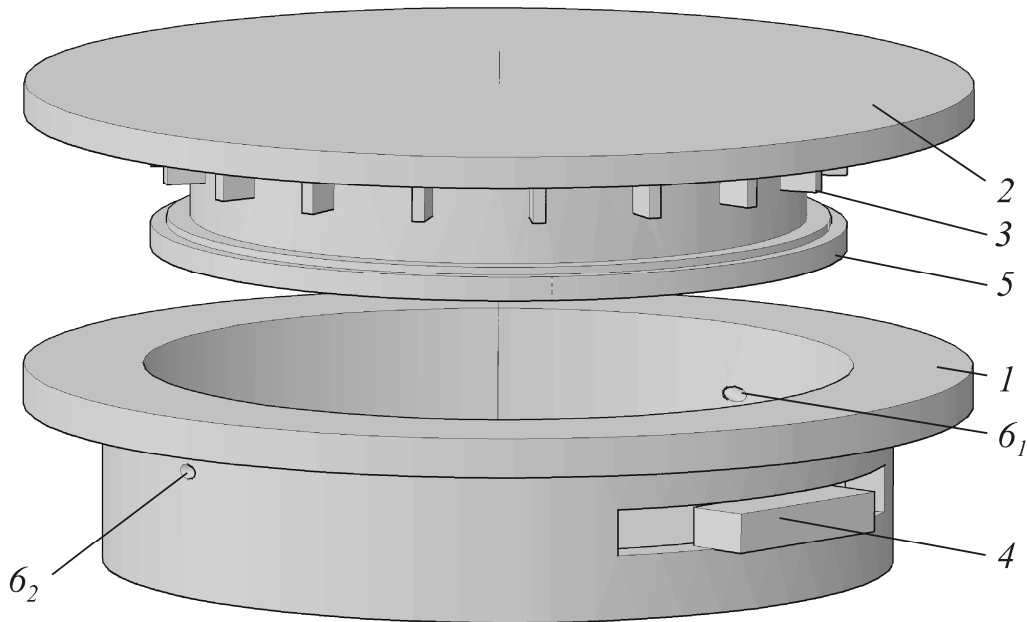

Fig. 1. Scheme of program controlled rotary table

Control of the RT is done according to the algorithm presented in Fig. 2. The program starts with input (block *1*) of the required turning angle (*NA*), the accuracy (*A*), the delay between experiments (*P*); the value for angle correction (*CA*) is set to zero, the variable *DoRotate*, which is responsible for repetition of experiments, is set to "*true*" (block *2*). Work of the RT is started in the block *3*. The function "*RotateAngle*" does turning by given angle (*NA+CA*) and returns deviation from the given angle. It is stored in the variable *CA*. Then, in the block *5*, the comparison of the obtained deviation (*CA*) with the acceptable deviation (*A*) is done. If obtained deviation (*CA*) is more than the acceptable deviation (*A*) the correction of the position of the moving part is performed (block *6*) according to the obtained deviation (*CA*). Return to the block *5* is then done until deviation of the turning angle is less than the acceptable deviation. The block *7* is used to set the delay time before experiment is repeated. The work is stopped when the variable *DoRotate* is set to "*false*".

The function "*RotateAngle*" receives the angle *NA* of the turning. The angle could be positive, for a rotation in one direction, or negative, for a rotation in another direction. In the block *1* the values of the variables, φ - the current angular position of the moving part and *PA* - the desired angular position, are set to zero. In the block *2* the command to rise the moving part is given and after the rise time t_{rise} the command to rotate is issued. While the current angle φ is less than 35% of the required angle (*NA*) (block *3*) the data on the velocity ω and the acceleration ε of the moving part are collected (block *4*). Afterwards, in addition to mentioned actions (block *6*), the desired

angular position (*PA*) at the stop moment is calculated (block *7*) according to the data on the position φ, the velocity ω, and the acceleration ε of the moving part. When the
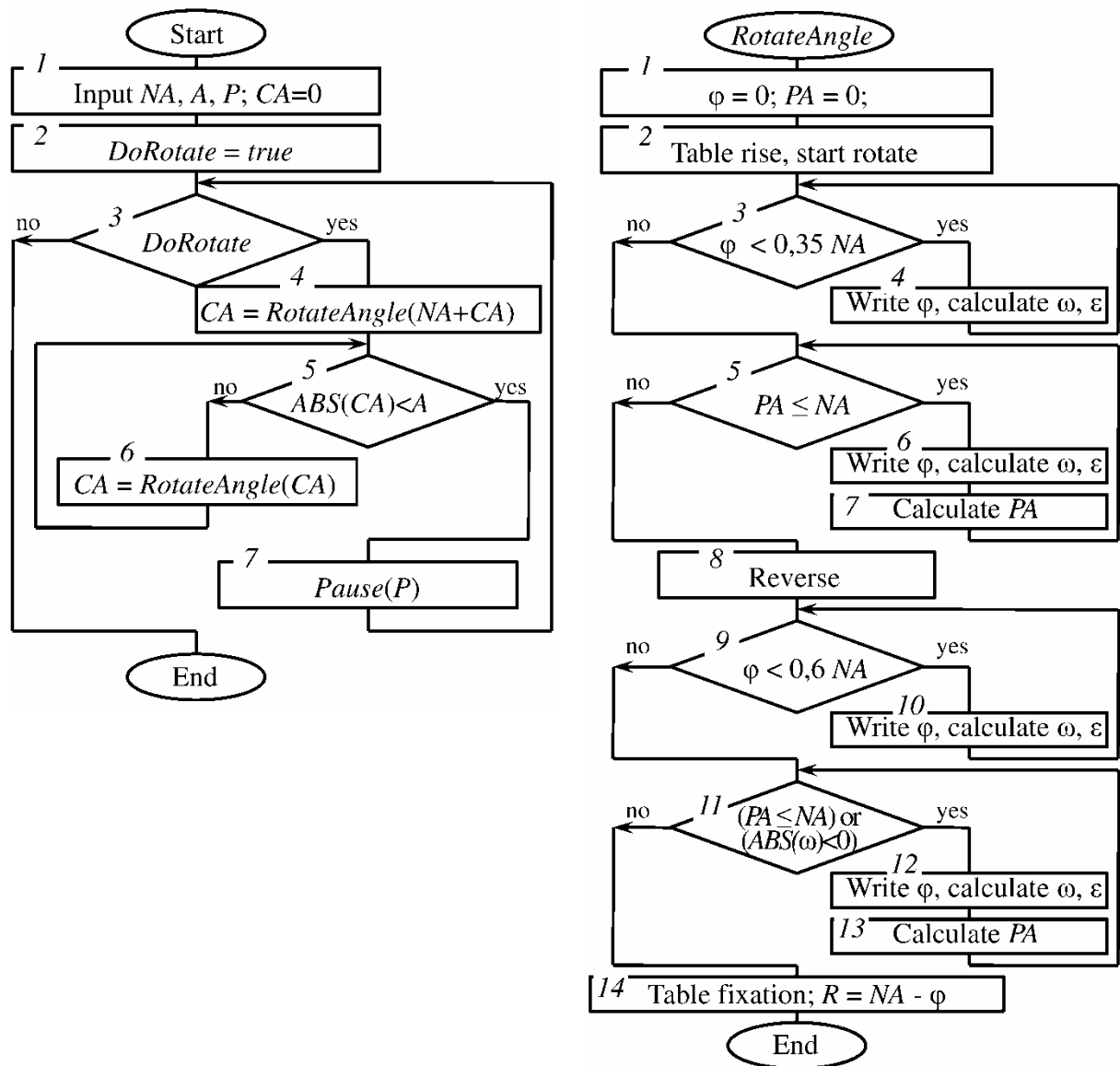

Fig. 2. Algorithm of control program of the rotary table

desired angle (*PA*) equals or more to the required angle (*NA*) (block *5*) braking of the moving part is turned on (block *8*). Then, in the blocks *9, 10*, collection of data on the velocity ω and the acceleration ε of the moving part is done until the current angle is less than 60% of the required angle *NA*. Afterwards, in addition to the same actions (block *12*), the desired angle of the stop moment (*PA*) is calculated according to the data on the position φ, the velocity ω, and the acceleration ε of the moving part. This is done (block *11*) until the desired angle (*PA*) is less than the required angle (*NA*) and the moving part revolves in needed direction. Then (block *14*), the command of fixation of the moving part is issued. When the moving part is finally stationary the deviation (*R*) from the given position is calculated. The flow then goes to the main algorithm.
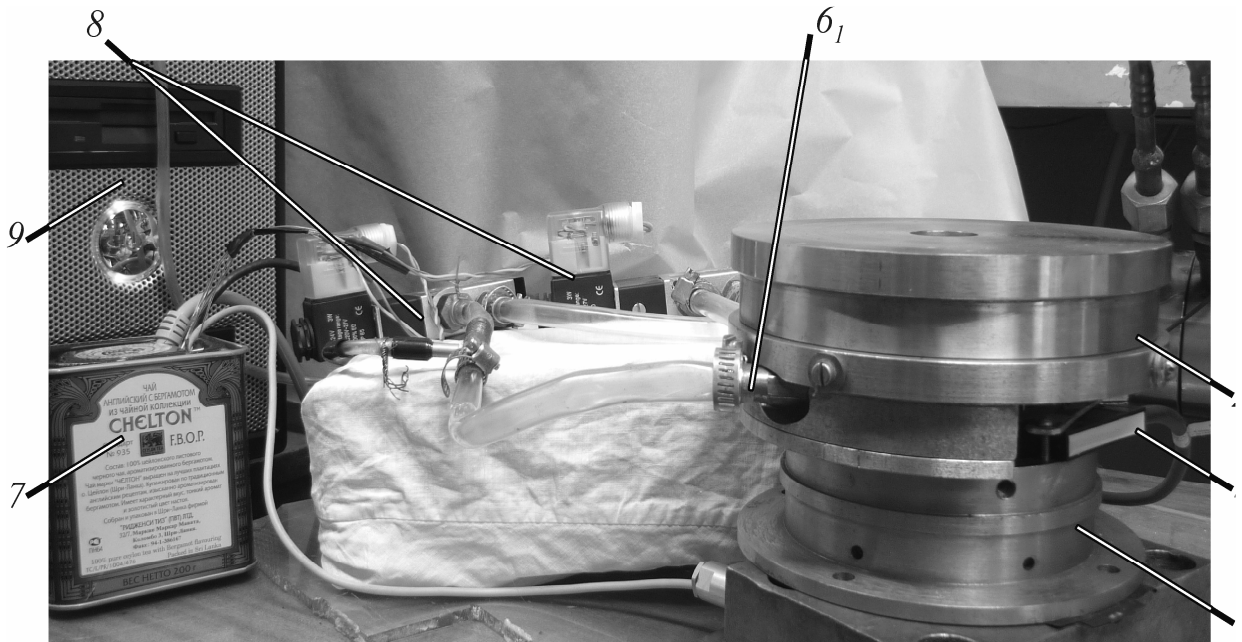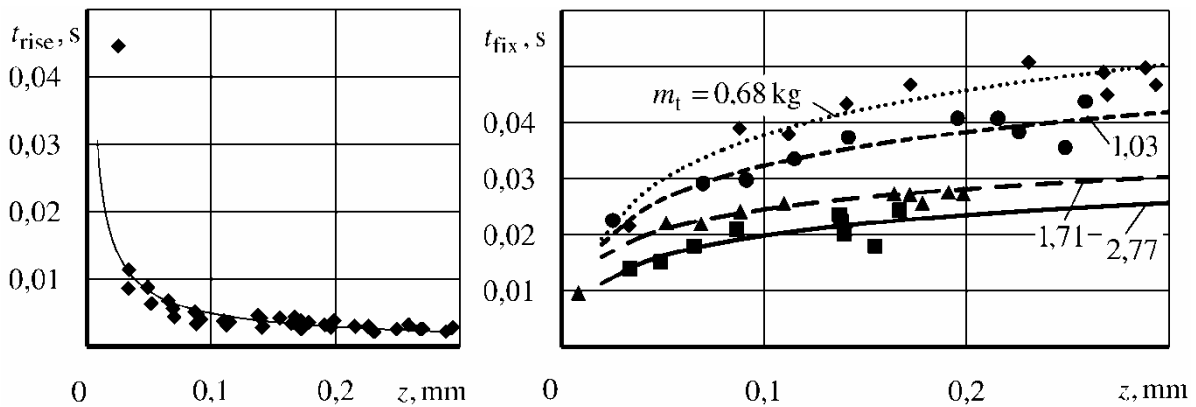
Fig. 3. Experimental setup of program controlled RT

Fig. 4. Dependence of the rise time t_{rize} (a) and the fixation time t_{fix} (b) on the height of rise z

As it was shown above in order for the RT to work properly it is necessary to determine t_{rise}, t_{fix} and t_{rev}. To calculate these parameters mathematical models have been developed and published in [2].

Study of rise, fixation and rotation mechanisms of the moving part of the RT has been done using an experimental setup of the RT (Fig. 3). Apart from described above elements the setup contains air distributors 8 (Freeway 4V210-08), computer connection device 7, control computer 9 (based on 2GHz AMD Sempron 3600+ CPU). As the contactless sensor of the turning angle 4 the sensor GCI0K.0411200 with the magnetic ring 5 - Z161.M06 is used.

Our study has found that the most pronounced effect on the rise time t_{rise} is due to the height of rise z, Fig. 4 a. The rise time t_{rise} is more than 0.01 s only when the height of rise z is less than 0.033 mm. Further reduction of the height z of rise significantly (8-fold by 0.07 s) increases the time t_{rise} of rise о 0.079 s at $z = 0.021$

mm). Increase of the height of rise z by more than 0.04 mm leads to insignificant (by 0.007 s) reduction of the time t_{rise} of rise to 0.0022 s at the height of rise $z = 0.287$ mm.

Dependence of the fixation time t_{fix} on the height of rise z and the mass m_t of the faceplate is shown in Fig. 4 b. The results are approximated by the equation:

$$t_{fix}(z, m_t) = (0.0021 \cdot m_t^2 - 0.01172 \cdot m_t + 0.02172) \cdot \ln(z) +$$

$$+ 0.00907 \cdot m_t^2 - 0.04978 \cdot m_t + 0.10142$$

where z is the height of rise in mm. Deviation between the experimental and calculated data is within 14% with average deviation of 4%.

Experimental study of the law of rotation of the moving part has demonstrated adequacy of the proposed mathematical models. As an example, disagreement of the experimental and theoretical data for the time of turn of the moving part by 50 degrees is no more than 5% and is always within the confidence interval.

It is thus reasonable to conclude that proposed mathematical models of rise and rotation laws of the faceplate on the air cushion of the reconfigurable rotary table with stream drive are adequate and could be used to justify design and working parameters of these devices.

Usage of calculated values for the time of rotation, rise, and fixation in the control program allowed achieving good performance of the device. In most cases the positioning of the moving part of the device includes 2-3 iterations with step-by-step approach to the given angle of turn. The average time of turn t_{rot} according to 150 experiments is presented in Fig. 5 *Mid*. The parameter is about two times larger than the minimal time (the time of getting given angle by first effort), Fig. 5 *Min*.
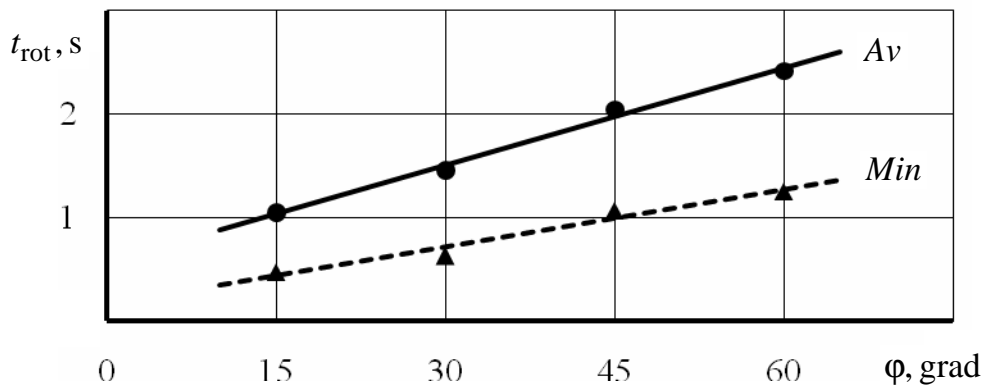

Fig. 5. Dependence of the time t_{rot} of turn on the turning angle φ (Min - minimal, Av - average)

It was experimentally found that the minimal turning angle of the setup is 40'. The precision of the fixation is thus ±20'. The parameter is mostly limited by the time of response of the air distributors, by the time of rise t_{rise} and fixation t_{fix} of the moving part.

Proposed RT is therefore characterized by high performance which is comparable with performance of other high speed models of RT. The additional advantage of a stream drive, small acceleration and high velocity which is unaccessible for other discrete turning devices, is of particular importance when turning angles are large.

REFERENCES

1. Kristal M.G., Drobotov A.V., Stegachev E.V., Astapenko A.A., Chuvilin I.A.: Russian Federation Patent № 2 376 123, МПК B23Q 16/10. Rotary table. B.I. 2009, №35.

2. Drobotov A.V, Kristal M.G.: *Control features of working process of rotary stream devices.* Assembling in mechanical engineering, instrument making. (In Russian). Assembling in mechanical engineering, instrument making. - 2010. – 3, p. 13-16.

Ľudmila DULEBOVÁ
František GREŠKOVIČ

Technical Univerzity in Košice, Košice, Slovakia

THE INFLUENCE OF AMOUNT OF FILLER ON MECHANICAL PROPERTIES FOR ELECTRO PRODUCTS

In order to favorably influence some product manufacture qualities of plastics (an increase of mechanical properties, chemical resistance, etc.), or by reason of reduction in price of finished plastic product, the fillers are added to plastic materials. The contribution deals with the change of mechanical properties of selected types of plastics with different % of glass filler. The mechanical properties were measured by tensile test and Charpy impact test in a standard ambient and after degradation of materials by UV radiance. The fracture areas of studied materials were observed on scanning microscope.

INTRODUCTION

The main cause of high interest in using plastics is a good understanding of their properties. Plastics are materials with good properties for universal use and are especially affordable. Despite of advantages, plastics are changing with time, maturing, getting older as well as living organisms. These changes are often referred to as aging, degradation, damage or failure.

The aging of plastics can be defined as a file of chemical and physical processes. We know the natural aging and comparable alternative to natural aging is the aging artificial. Artificial aging is the aging of plastics in artificial conditions, in our case, as we examine specific types of plastics used in electrotechnical industry - it is exposure to UV radiation in the chamber. In order to favourably influence some properties of plastics (an increase of mechanical properties, chemical resistance, etc.) there are added in fillers into the plastics.

The meaning of filling is in order to modify of product properties as required under the terms of their adjustment applications and products. This led to the development of new polymer filled materials with fillers. The dosage of filler must be followed precisely because with increasing amount of plastic filler, the plastic properties can be increased, decreased or passed through a maximum. It is very important to select the appropriate amount of filler in order to avoid undesirable properties [1, 2].

In fact, there is no filler, which would be completely inert, because the properties of filled material are change and depend on considered in terms. The improving of plastic properties is accompanied by deterioration in other properties. Differences between the effects of fillers are not be chemical composition of filler and the size of particles, shapes and surface activity [3].

The experiment was to test the influence of UV radiation on the change of selected the mechanical properties of plastics. From the spectrum of mechanical properties of plastics there was chosen these mechanical tests – tensile test, Charpy Impact test in standard ambient and after UV exposure chamber.

MATERIAL AND TREATMENT

Three types of materials were used for the experiments with different percentages of filler - glass fibres. The selection of materials was made in view of their extended use in the manufacture of plastics products for the electrical industry.

The material used in the experiments:
• Slovamid 6 GF 30, in the experiments marked A,
• Slovamid 6 GF 25 FRA, in the experiments marked B,
• Makrolon 9415 / Z, in the experiments marked C.

Material Slovamid 6 GF 30 - is chemically reinforced plastic with 30% glass fibres. It is used for plastic products with high strength and toughness. Material is used in automotive, electronics, engineering and consumer industries. The material can be in natural form and in various colours. The manufacturer of the material is company Plastcom.

Material Slovamid 6 GF 25 FRA - is chemically reinforced plastic with 25% glass fibres, retarded with halogen flame retardants. It is mainly used in the electronics industry for circuit breakers, body coils and phase segregated terminal box. The manufacturer of the material is firm company Plastcom.

Material Makrolon 9415/Z - is a polycarbonate moulding and extrusion type. It is chemically reinforced with 10% glass fibres and flame retardants retarded. The manufacturer of the material is company Bayer Material Science.

The selected mechanical properties of tested materials are listed in Table 1.

Table 1. Mechanical properties of tested materials [4]

Material for experiments		A	B	C
Mechanical properties	Unit	The Value		
Tensile strength	MPa	170	135	45
Modulus of elasticity	MPa	8 600	10 000	3 800
Relative elongation	%	3	2	10
Charpy impact test (23˚C)	kJ/m^2	12	2	10

The test samples were produced on the injection moulding machine (ARBURG ALLROUNDER 320C). It was used injection mould with replaceable mould boards. Processing conditions during the injection moulding were according to the recommendation of the producers. The evaluation of tensile properties of plastics was made according to EN ISO 527-1, 2 and was used sample type 1A for testing. The test samples were controlled scilicet after injection moulding and after the conditioning time. Tensile test was carried out on tensile machine TIRA- test 2300. It was tested in 5 samples of each type of materials. The establishment of Charpy Impact test was performed according to EN ISO 179-1. The test was carried out by Charpy hammer - type PS V500. It was tested in 10 samples of each type of materials. Artificial   aging

test by fluorescent UV lamps were made in the UV chamber according to EN ISO 4892-3, exposure time 28 days at 12 hour cycles for all test materials. The test samples after removal of UV chambers were conditioned according to ISO 291:2008. Subsequently, tensile test was performed and Charpy Impact test to detect changes in the properties of the materials after artificial aging by UV fluorescent lamps in accordance with the above methodology.

EXPERIMENTAL RESULTS

The graphic dependence of the measured average values of tensile strength of test samples in a standard ambient and degradation in UV chamber is shown in Figure 1.

☐ Standard ambient ◼ Degradation of material after UV radiance
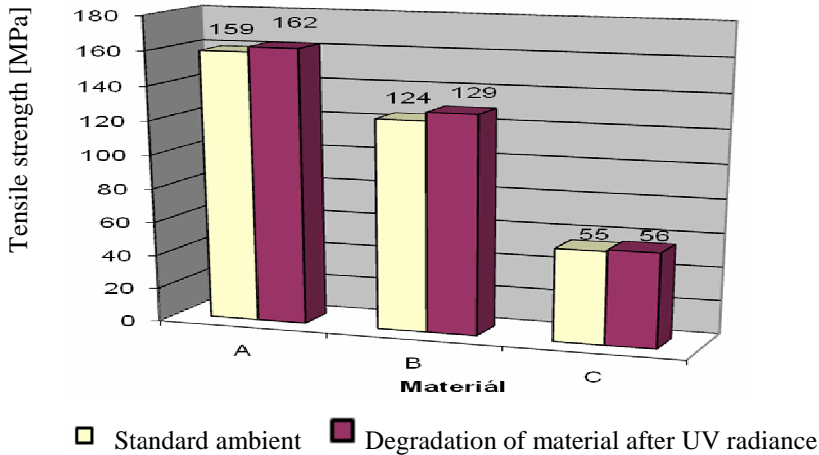
Fig. 1. Comparisons of tensile strength of tested materials

The graphic dependence of the measured average values of relative elongation of test samples in a standard ambient and degradation in UV chamber in Fig. 2.

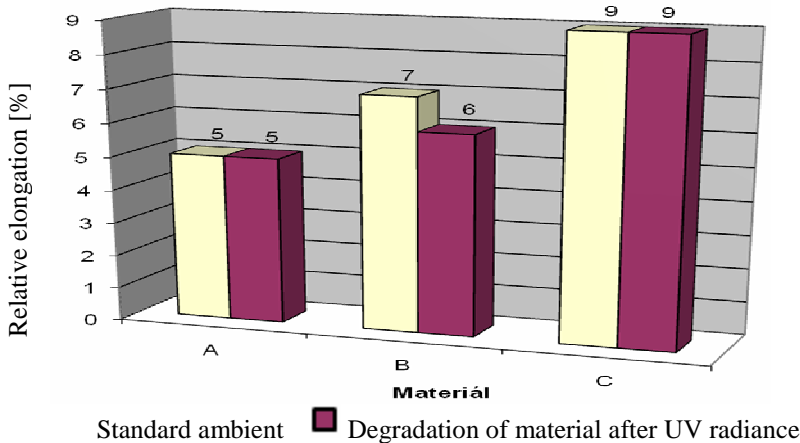☐ Standard ambient ◼ Degradation of material after UV radiance

Fig. 2. Comparisons of relative elongation of tested materials

The fracture areas of test samples after tensile test were observed on scanning electron microscope JEOL JSM - 7000F, Japan - Fig. 3 to Fig. 6.
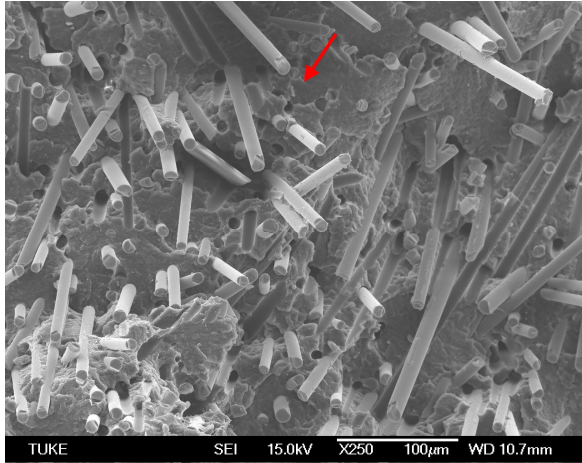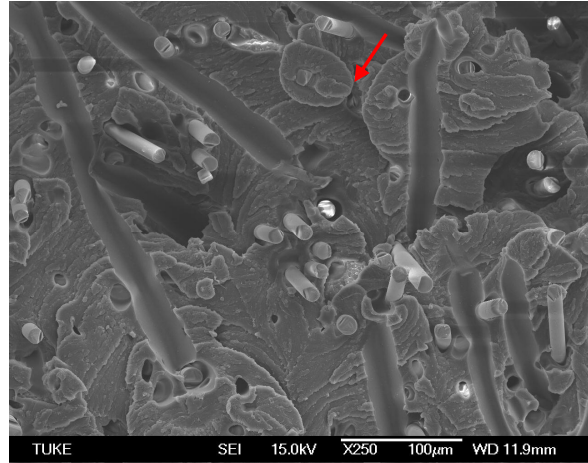
Fig. 3. The fracture area- material A

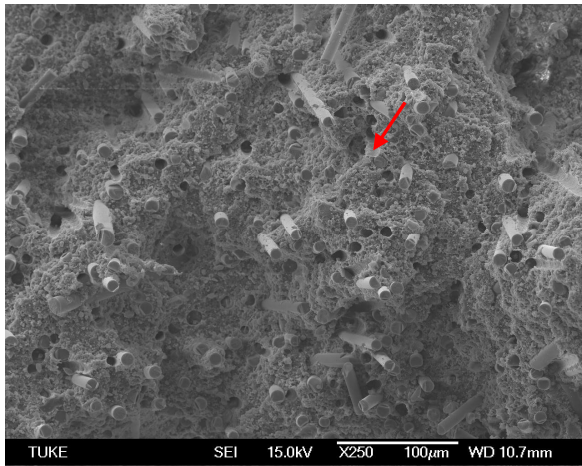Fig. 4 The fracture area - material C

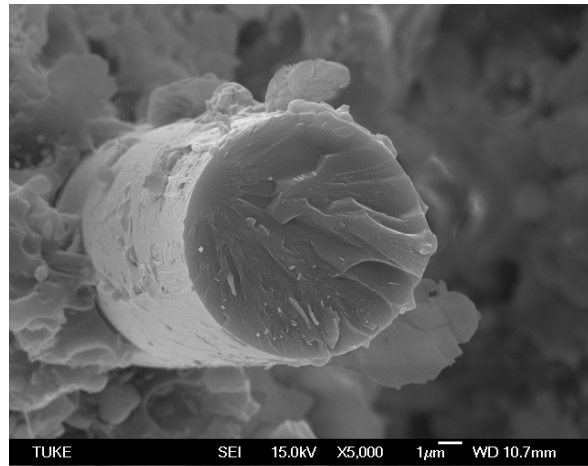Fig. 5. The fracture area material B

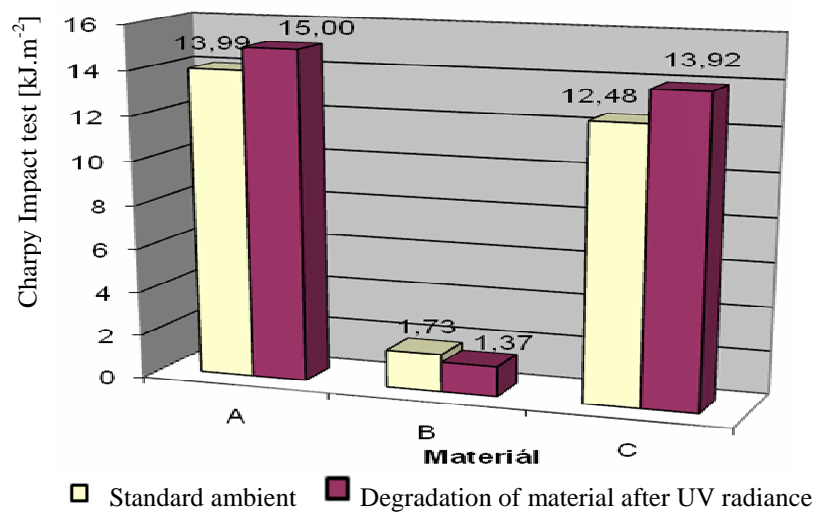Fig. 6. The fracture glass filler - material B

Fig. 7. Comparisons of Charpy Impact test of tested materials

In Fig. 3 to Fig. 5 are presented fracture surfaces of tested materials. It can be seen that there is also a breaking of glass fibres.

Fig. 6 shows fracture in the glass fibres of material B. In addition to structure of fibres, peeling of another layers can be used. These fibres are covered with layers for better wettability.

Graphic dependence of the average measured values from Charpy Impact test of test samples in the standard ambient but also after the degradation in the UV exposure chamber shown in Fig. 7. The all of test samples were complete broken. In Fig. 8 to Fig. 10 is the fracture surface of tested materials and in Fig. 11 is detail fracture of glass fibres- material B.
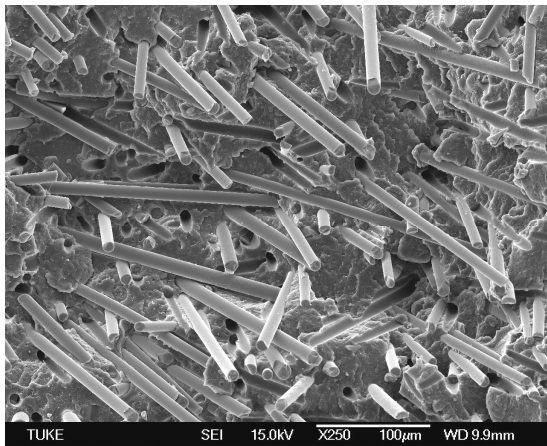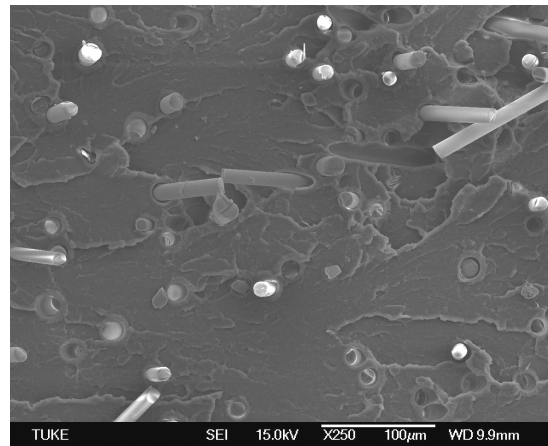

Fig. 8. The fracture area- material A

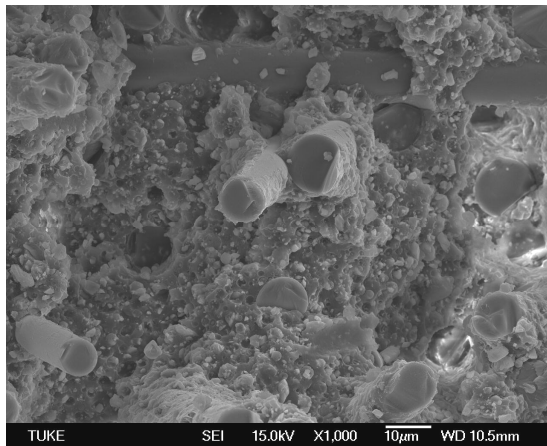Fig. 9. The fracture area- material C

Fig. 10. The fracture area- material B

Fig. 11. The fracture glass filler - material B
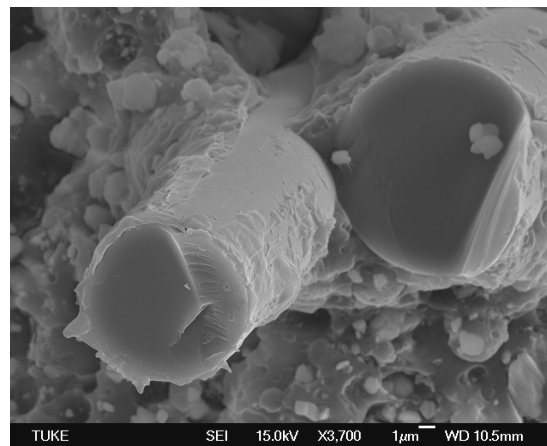
DISCUSSION

On the basis of the experimental results of mechanical tests the following conclusions could be formulated:

- The highest value of tensile strength (162 MPa) was measured for the material Slovamid 6 GF 30 after UV exposure chamber. We can state that artificial aging in the UV chamber had not influence on the value σ_M of tested materials – Fig. 1.

- The highest value of relative elongation was measured for material Makrolon scilicet 37% in the standard ambient, and 34% after degradation in the UV exposure chamber. The measured values correspond to those given in the material sheets of tested materials. We can state that artificial aging in the UV chamber had not influence on the value ε_M of tested materials – Fig. 2.
- The values of Charpy impact test of the aging of the UV chamber for each test materials increased by only small amount (1-2 $kJ.mol^{-2}$). In material Slovamid 6 GF 25 was obtained the value Charpy impact test $a_{CN} = 2$ $kJ.mol^{-2}$, which is consistent with the letter of materials. This value is results from Fig. 10 of the scanning microscope, the structure of the material (especially matrix) is different from the others tested materials. The measured values correspond to those given in the material sheets of tested materials and artificial aging in the UV chamber had not influence on the value a_{CN} of tested materials.

Mechanical properties of composites depend on many parameters, from which most important properties are the matrix and reinforcement, the type or length of filler reinforcement, the volume fraction and arrangement of reinforcement and consistency of the surface of the matrix. Filler composites always show a preferential orientation. The holder of the strength of the reinforcing filler, which is anchored in the matrix only the force of friction.

CONCLUSION

Obtained knowledge in this paper are only parts of the general problem of testing the technical plastics. Selected made tests desire for deeper investigation of the issue of changing the structure of plastic material and supplement other tests in technological applications plastic parts of the investigated materials in practice for electrotechnical industry.

REFERENCES

1. Hrivňák I.: *Fraktografia*. STU MTF v Trnave. Bratislava 2009

2. Greškovič F., Dulebová Ľ., Varga J.: *Technológie spracovania plastov*. Vstrekovanie. TU v Košiciach, Strojnícka fakulta. 200 s. ISBN 978-80-553-0369-7

3. Förtsch W., Franz H.E., Friedrich K.: *Microfractographic Aspects of Interfaces in Creep under Fatigue Loading*. Proc.28th Risø International Symposium on MaterialsScience: Interface Design of Polymer Matrix Composites – Mechanics, Chemistry,Modelling and Manufacturing, Risø National Laboratory, Roskilde, Denmark,2005.

4. *Materiálové listy materiálov:* Slovamid 6 GF 30, Slovamid 6 GF 25 FRA, Makrolon 9415 / Z,

Emil EVIN
Jaromír AUDY*

Technical University Košice, Slovakia; *Edith Cowan University, Australia 6230

EVALUATION OF COEFFICIENT OF FRICTION OF UNCOATED AND TIN COATED TOOLS IN DEEP DRAWING

The present investigation was set up to examine both predicted and experimental values of forces, power and friction in drawing cups from low carbon steel blanks using the same die set but in different uncoated and TiN coated conditions. The results showed a good agreement between predicted and experimental values. In addition, the findings demonstrated that the TiN coated tools reduced the friction at a tool – blank – die – interface (by about 5%), which in turn reduced the forces (by about 7%) and improved the final product quality, when compared to the performance of uncoated tools.

INTRODUCTION

Drawing is a metal forming operation successful in production of cylindrical hollow cups from blanks. It involves a circular blank that is formed, simultaneously, over a punch and a die profile radius by stretching and drawing [1]. A stress ring is used to apply some pressure to the blank in order to prevent it from wrinkling and buckling. This requires an extra attention to detail. It is because if the pressure is too high the reductions in blank thickness are excessive and the material may tear. When insufficient pressure is applied, the material enters the die cavity too fast. It is not stretched enough and when it reaches the die cavity there is not enough clearance between the punch and the die. Because of this, the thickness of material is reduced by ironing when dragging it against the side of the die as component travels in the direction of the punch. As a result the drawing forces increase, the component quality is poor, and the die life is reduced due to scratching, micro-welding and localised heating effects at the die cavity – work piece material – and punch interfaces. In seeking improved deep drawing performance, researchers and manufacturers have made significant advances through the modification of die-punch geometry and advanced coatings. The selection of compromise geometrical features for die-sets and punches has resulted in setting up the limits to the radii of punch corners, radii of die entries, depth of draw and reductions in blank diameters achievable, if tearing of the material is to be avoided [2, 3]. With respect to coatings previous empirical studies on metal drawing [1] and metal forming [4] have shown that TiN coated forming tools were more efficient than uncoated tools [1] and hard chrome plated tools [4]. Audy [5] studied the influence of hard coatings on the performance of industrial tools employed in practical machining and forming operations. His work suggested that the

hardness and chemical stability of coatings have been identified among the most desirable properties, since this would lead to reduced tool wear and increased tool life. With respect to metal forming operations, the TiN coated tools were reported [4] to provide about 70% tool life increase for about 14% cost increase compared to uncoated tools. Most recently market offers a large variety of single and multi-layer surface coatings, each claiming to significantly improve the technological performance measures such as increased tool-life, and reduced forces and power. Much of the reported information appears to be descriptive and qualitative, leaving the many 'hard decisions' to the users and customers. Further research aimed at providing reliable quantitative evidence of improvements in forming performance for each and every coating available in the market is clearly required [6].

Consequently, this study involved investigations of efficiency of TiN coated tools in deep drawing cylindrical cups from steel blanks. It looked at predicted and experimentally measured technological performance measures such as forces, power and press work. Uncoated die-set and punch were also included in the study for comparison.

EXPERIMENTAL DETAILS

A type Ruwolt - 50 tonnes – hydraulic press was employed to carry out the experimental investigations. It was equipped with a die-tool set specially designed for deep drawing operations. Relevant drawing tooling set up showing the position of tools and work piece blank materials including photographs of the actual stress ring and the die are shown in Figure 1.
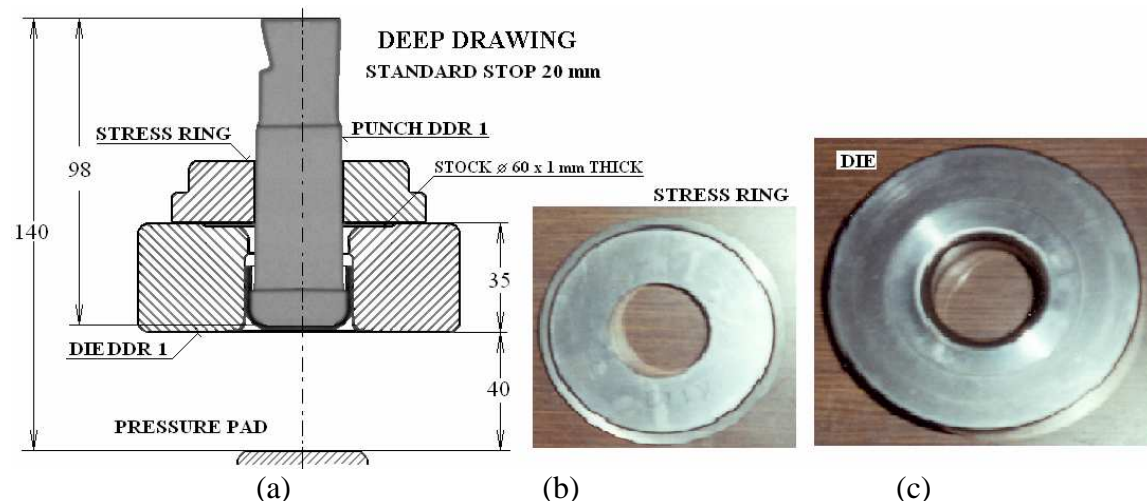

Figure 1. The experimental cup forming set-up showing (a) the actual position of drawing tools and blank material, (b) the stress ring – blank holder, and (c) the die

The deep drawing experimental set up (i.e. the actual experimental arrangement) for the force, power and work tests is shown in Figure 2. The press was equipped with a load cell for force measurements and a linear voltage displacement transducer (LVDT) for stroke measurements. A computer was used to record and plot the out put data. The intended blank diameter, D, and the thickness, t, values were 60 mm and 1 mm, respectively. The actual value of the blank diameter was 59.99±0.005 mm. The

relevant values of actual experimental die set / tool geometrical features are shown in Table 1.
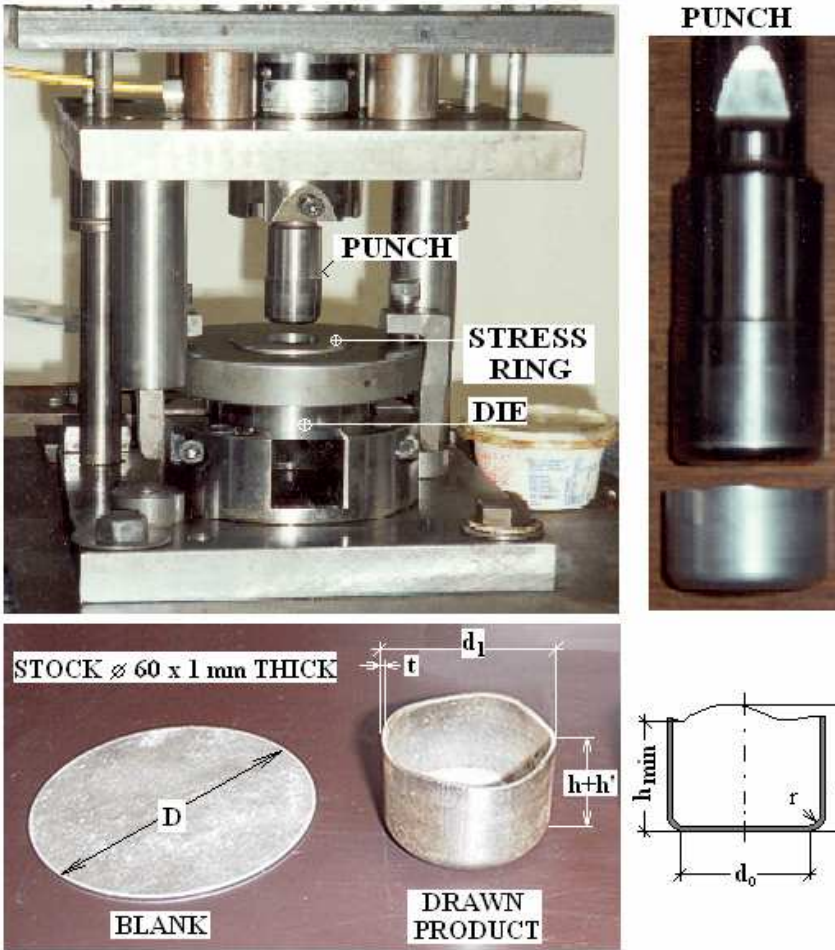

Figure 2. General experimental arrangements for cup forming tests showing the die-set with tools; drawing punch and drawn product; including both the blank and the drawn product with their key dimensional features

Table 1 Geometrical data of tools employed in the deep drawing experiments

Punch diameter [mm]	Punch corner radius [mm]	Mid-corner radius [mm]	Die entry radius [mm]	Angle of radial stress at die entry, α, [°]
32.88	5	5.5	3	90

The tools were tested firstly in uncoated conditions and then in TiN coated conditions. The coating was deposited by a physical vapour cathodic arc system. With reference to source [1] the base pressure in the coating chamber was 5×10^{-3} Pa; the tool substrate material was argon ion etched at a pressure of 5Pa and a bias voltage of -1kV; the metal ion etching was conducted at a bias voltage of -800V; the actual TiN was deposited as a single layer (up to a thickness of ~1μm) using a substrate bias voltage of -100 V and a chamber pressure of 5×10^{-1} Pa.

EXPERIMENTAL RESULTS

Prior conducting the actual experimental test it was decided to calculate (predict) the height of the cup, and drawing forces, the friction coefficient and degree of performance.

Estimated applied force [7, 9, 10]:

$$F_{t\,max} = (F_{i\,max} + T_1 + T_2 + F_O).\exp(\alpha.f/2) = (F_{i\,max} + 2.f.F_N + F_O).\exp(\pi.f/2)$$

where F_{imax} represents a component of the drawing force required for deforming the blank i.e. the deformation resistance of the blank material. The symbols T_1 and T_2 represent friction forces between the blank, the blank holder and the die. The T_3 is the friction force at the die radius, while F_o - the bending force, α - the angle (for radial stress) at the die entry, $\alpha = 90°$, F_N - blank holder force, f – coefficient of friction.

Degree of performance - η_c:

To evaluate the influence of the change in the uncoated and coated tools properties of the die contact surfaces on technological characteristics of deep drawing process it is essential to determine the degree of performance [2]:

$$\eta_c = \frac{F_{tc}}{F_{tunc}} \tag{2}$$

where: η_c is performance of coated tool, F_{tc} – drawing force of coated tool, F_{iunc} – drawing force uncoated tool.

Coefficient friction:

Consequently, the maximum drawing force can be calculated using (1) for uncoated tool [7, 9, 10]:

$$F_{tun} = (F_{id\,max} + 2.f_{unc}.F_N + F_o).(1 + 1.16 f_{unc}) \tag{3}$$

and for coated tool

$$F_{tc} = (F_{id\,max} + 2.f_c.F_N + F_o).(1 + 1.16 f_c) \tag{4}$$

The friction coefficients of the actual friction forces T_1 and T_2 are responsible for about 10% of the total drawing force (we assumed, that $2.f_c.F_N \cong 2.f_{unc}.F_N$. After the substition and adjustment of formula (2) we will have:

$$\eta_c = \frac{F_{tc}}{F_{tunc}} = \frac{Exp(\pi.f_c/2)}{Exp(\pi.f_{unc}/2)} \tag{5}$$

and

$$f_{unc}.\ln(\eta_c) = f_c \tag{6}$$

The values of friction coefficients $f_{unc} = 0.095$ for uncoated tool for materials DC 04 [11].

The experimental outputs recorded the press stroke and force for each produced cup, see an example shown in Figure 5.
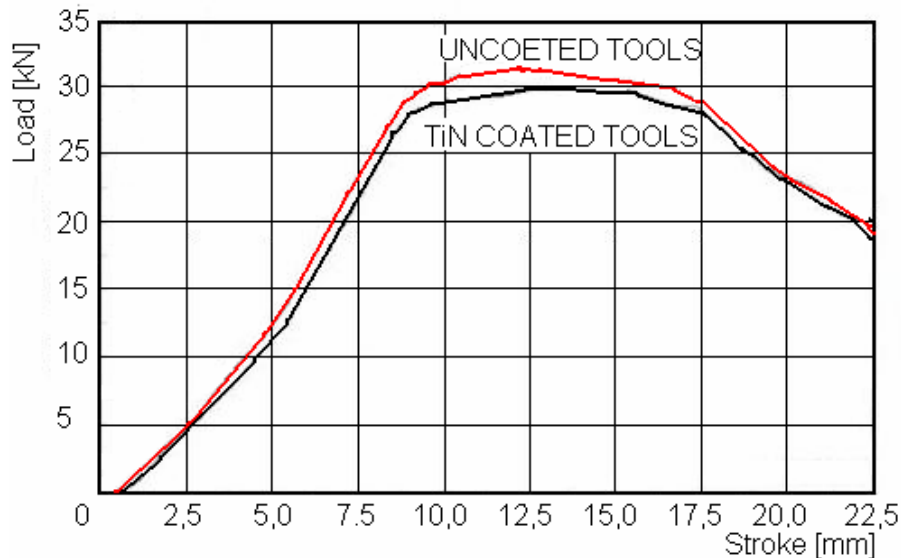

Figure. 5 An example of experimental load/stroke out puts showing 'qualitative' comparison for forces and work generated by the same tool set employed, in both uncoated and TiN coated conditions

The press work was calculated as the area under the force-stroke curve. In addition, the as produced cups were measured in order to quantify the changes in the work material thickness and the cup height, and their surfaces were visually inspected for scratches and defects. These experiments were conducted by Audy at Melbourne University.

From Figure 5 it is evident that the die set and tools employed in these deep drawing tests produced qualitatively similar pattern in both uncoated and coated conditions. However, from the quantitative point of view, the uncoated tools produced greater forces, and hence greater press work than the coated tools. The mean values of forces and press work for 15 measurements were statistically different at 95% and higher confidence level (C.L.) for both the uncoated and coated tools. The same was found for the variances – they were different at 95% C.L and greater for the uncoated tools. This allowed to use the grand mean values for quantifying the overall benefit of coated tools against uncoated tools.

The following experiments were conducted independently by Evin at Technical University in Kosice city in Slovakia [8]. Figure 6 shows the outputs from extensive computer simulations for uncoated and coated tools employed in drawing a Type 1010 (DC1) steel blanks.

Comparison of computer assisted predictions in Figure 6 with experimental trends in Figure 5 showed strong similarities in pattern/trends, and a reasonable good agreement from qualitative and quantitative point of view. This agreement was for force-stroke displacement at different stroke lengths ranging from 0 mm to 12 mm. At strokes greater that 12 mm the differences between experimental trends and simulations became more distinctive. It is because in the experimental tests the drawing

clearance was similar to the blank thickness. This caused increasing of the cup thickness at the top of the product, and reducing its wall thickness during deep drawing. Consequently, the range / duration of maximum drawing force (of ~30 kN 'on average'), see Figure 5, was quite long i.e. at the stroke lengths ranging from ~10 mm to ~17 mm. In contrast, when looking at Figure 6 (simulations) this range/duration of maximum drawing force was much shorter i.e. occurring at strokes ranging from ~10 mm to ~12 mm. This happened because in simulations the drawing clearance was 1.2 times greater than the blank thickness. Because of this no wall thickness reduction was involved and the values of forces, friction and power were slightly lower than those obtained from experiments on drawing caps by wall reduction.

Table 2. Comparison of experimental data for uncoated and coated tools, predicted values, and differences between measures produced by the coated and uncoated tools. After Audy et al [1]

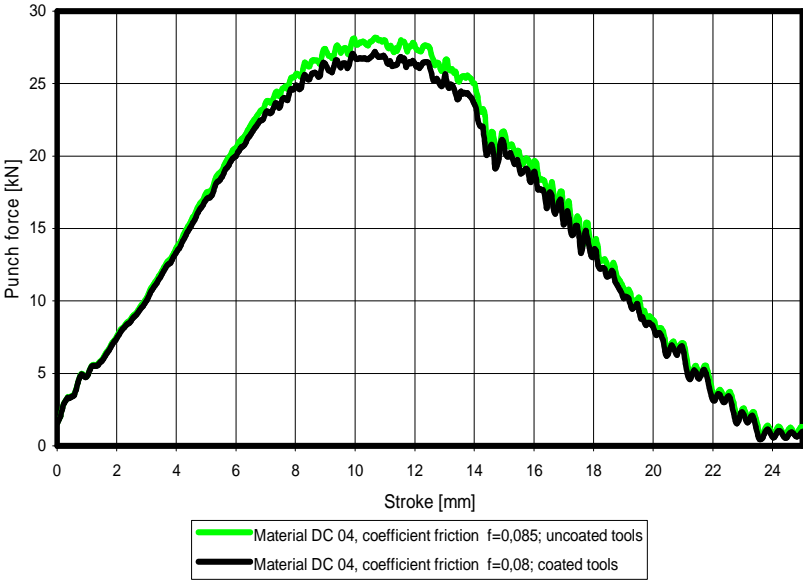| Feature	Uncoated tools (UT)	Coated Tools (CT)	CT versus UT Difference [%]
Cup Height [mm]	20.1	19.8	-1.5
Force [kN]	32.18±0.94	30.2±0.65	-6.2
Performance	1	0.941	–
Coefficient friction	0.095	0.894	–

Figure 6. Predicted load/stroke outputs for uncoated and TiN coated tools employed in drawing a Type 1010 steel blank

Referring to data in Table 2 it is evident that the coated tools reduced the press force and press work by about 6.2 and 7.4 percent, respectively. Comparison of predicted data with experimental data indicated a reasonable good comparison for forces and cup height. Empirical rules for predicting press work provided only rough

70

approximation. Visual observations of cup surfaces indicated more scratches and surface defects hence occurrence of some ironing in drawing with uncoated tools.

It needs to be noted that the drawing force has to be lower than the maximum force (or ultimate tensile strength) of blank material. The use of TiN coated tools was found to reduce the friction coefficient by about 4% which improved material flow and reduced drawing work, forces and power needed in drawing cups from a Type DC 04 steel material. Similar improvements are expected in drawing products from eg CrNi – austenitic steel used in automotive industry.

CONCLUSIONS

The experimental deep drawing tests conducted in the present study have shown that that the pattern of forces versus stroke produced by the uncoated and the coated tools showed qualitative agreement and quantitative differences at 95% and higher confidence level. The coated tools reduced the force by 6.2%, work by 7.4%, and improved the friction coefficient by ~5%. The cup height values were very similar i.e. 20.1 for the uncoated tools and 19.8 for the coated tools with main differences in earring (wavy pattern around the top of the cup) and scratches due to ironing close to the earring which were greater for tool sets in uncoated conditions than in coated conditions. Predictions were reasonable good for forces and cup height values, not so good for work values. In addition it appears that there is a need to establish more reliable predictive equations for coated tools.

REFERENCES

1. Audy J., Doyle D., Audy K.: *A study of effects of physical vapour deposition coated tools on the forces in deep drawing cylindrical cups from ferrous and non-ferrous materials*. In "Asia Pacific Forum on Precision Surface Finishing and Deburing Technology", Swinburne University of Technology, Melbourne, March 2003, pp. 325 to 335.

2. Maj M., Maj S.: *Metal and ceramic forming process*. Department of Mechanical and Manufacturing Engineering, University of Melbourne, Australia, 1997.

3. Maj S., Maj M., Dunstall S.: *Metal Forming Processes*. Lectures 436-363, Department of Mechanical and Manufacturing Engineering, University of Melbourne, Australia, 2000.

4. Lemon K.S., Doyle E.D.: *Performance of PVD coatings in cold forging*. Tooling 99, Conference proceedings, Melbourne, Australia, March 1999, pp. 71 to 76.

5. Audy J.: *The Influence of Hard Coatings on the Performance of Twist Drills*. Thesis for Master of Engineering Science in Research, The University of Melbourne, Australia, June 2002, p. 93.

6. Streefland G.J., Melsen J., Hoffman J., Benmalek M.: *Hot Melt Tempory Dry Coat for Aluminium Protection and Lubrication*. In.: IDDRG Working Group 2 Materials, Ann Arbor Michigen, 2000.

7. Hrivňák A., Evin E.: Predikcia lisovateľnosti oceľových plechov s vyššími pevnostnými vlastnosťami. ALFA, Košice, 2000.

8. Evin, E., Hrivňák, A., Tkáčová, J.: *Simulation of Friction Ratios at Deep-Drawing Process*. In.: International Conference on Industrial Tools 2003, Cejle, TECOS Slovenian Tool and Die Development Centre, 2003, p.57.

9. Lange, K.: *Umformtechnik – Blechbearbeitung*. Springer/Verlag, Berlin, 1990.

10. Čada R.: *Tvářitelnost ocelových plechu*. REPRONIS, Ostrava 2001

11. Evin, E., Piňko P., Kmec J.: *Štúdium trecích pomerov na kontaktných plochách lisovacích nástrojov*. Acta Mechanica Slovaca. 2007, vol. 4C, s. 54-59. ISSN 1335-2393.

72

Michal FABIAN
Emil SPIŠÁK
Jaroslav ŠEMINSKÝ
Ján SLOTA

Technical University of Košice, Slovakia

THE LATEST ACTUAL TRENDS IN PROCESS OF DESIGN AND PRODUCTION IN AUTOMOTIVE INDUSTRY

Time of innovation cycle in automotive industry is being reduced thanks to increasing market competition. It is possible to follow this trend first of all by means of CA-applications in the design and production phase of product life cycle. Regarding to systematic shortening of design process and manufacturing, the main accent is put on application of CAD/CAM technologies for serial production of shaped-complicated parts. The aim of this paper is to show some aspects of actual trends in process of design and production in automotive industry.

CURRENT REQUIREMENTS FOR DESIGN AND PRODUCTION OF SHAPES

Intensive improvement of the consumer and automotive industry puts more and more demands on technologies of plastic material processing and forming.

Design, analysis and production of parts and components is in these industry branches inconceivable without using CA technologies and CA approaches connected with them for design and production.

Current requirements on design and production of shapes in the automotive and consumer industry result from the way of shape design and its next production. An automobile is composed of many components: supporting skeleton consists of shape profiled sheets. External shapes are from sheets or plastic materials (Fig. 1). Interior is mainly from plastic materials or textile fabrics by using which hard foams are covered with. Every part has its own tool by using which is produced. Tools production for serial production of shape parts is related with the fact.

Fig. 1. Plastic and metallic external components of car body, plastic mouldings of interior

Final shape production in technologies of injection moulding and sheet-metal pressing is made by using a tool that is called a form. Form active parts contain information of product shape that is produced with their help [1].

DESIGN AND PRODUCTION: IN THE PAST AND TODAY

Comparison of shape solution for front-end car section

Shape design for mentioned car part was quite restricted by possibility of production of individual components not long ago. Headlights were mainly with circular diameter 160 or 130 mm. Škoda 105/120 had the same headlights as e.g. Lada 1200/1500. Similarly it was also in the West of our continent. Alfa Romeo, VW, Fiat, Ford and Simca had also circular headlights. Bumpers were mostly chromium-plated molded panels. One of components the most different among various automobile marks was shape of direction indicators that were the molded plastic parts [2].

Fig. 2. Comparison for shapes of car bodies [2]

Designers at past times were able to model other various shapes for bumpers, headlights or direction indicators but technologies of the past times did not allow their mass production.

In the past

Complicated shapes were produced on the basis of the manually produced models from wood or modelling material. Off-print of the model again into the modelling material the model negative was created. According to it was created by using profiler the form cavity.

Model shape acquirement – a clay model

Shape designers in the automotive industry materialized their primary ideas by using paper and a pencil into the sketch which represented individual views on shape of designed car body. Materialization of the idea into the 3D model was made by modelling clay according to the sketches. There were created the shape designs and models in scaling factor 1:10 in initial phase and after shape adjustment in scaling factor 1:5 or 1:1 [5] (Fig. 3). In the end the accurate model from clay and laminates was produced in its real size, so called „master model", which served as the unique car body reference (Fig. 3).
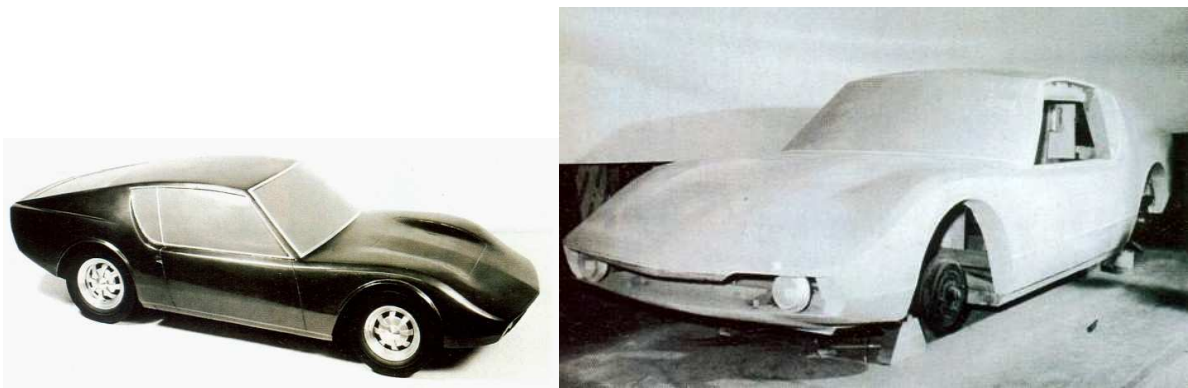
Fig. 3. Model 1:5 and „Master model" intended for shape scan for tools production [5]

The approach for shape design was described by very simplified scheme. In fact many activities were several times repeated [6].

Copying – by profiler

Demonstration of copying of shape for part of dies by using a laminate model is shown in Fig. 4.
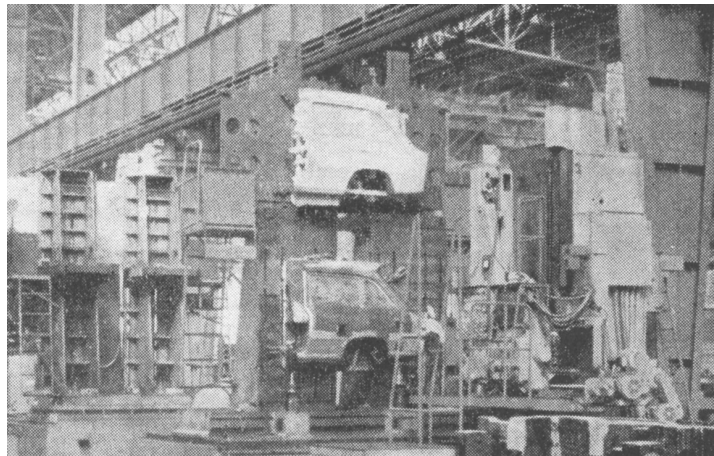

Fig. 4. Copying of shape by profiler for dies by using a laminate model [6]
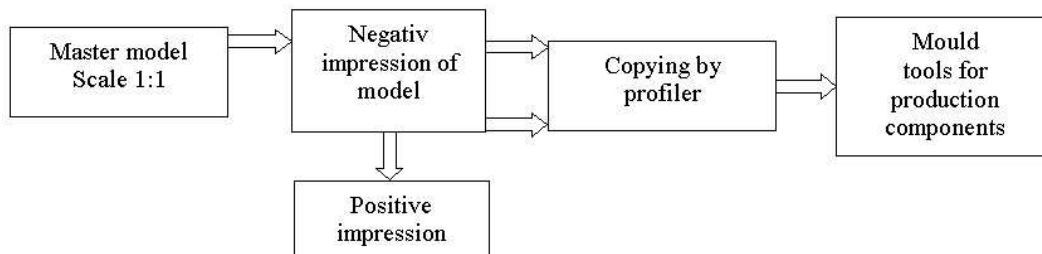

Fig. 5. Classical design process based on clay model

The whole process (Fig. 5) could be shortly described as follow: Model shape was created by using modelling approaches on clay or laminates basis. There were scanned shapes from completed model in scaling factor 1:1.The shapes served for negative

shape production by using profiler or the clay model was laminated or moulded into the cavity off-print. The model was then used for production of the form insertion by profiler. By the classical approach a profiler was used as a tool for shape transformation from laminate model as a pattern into the active tool part – the form produced from tool steel. Profilers were used for the purpose.

Today

By using CA approaches for design and production the boom was made in design of mentioned car parts. (Fig. 2). CA technologies lining as well as progressive technologies for material processing connected with them allow to mass production of shapes that have not been able to snag nor produce by classical manner.

The clay model production for negative shape acquisition losses its meaning at present. The model negative is obtained directly in CAD system by using simply Boolean operation of subtraction. If the problem is snagging of cavity shape but it is possible to snag the positive shape then the approach for model production is as "electrode". Shape cavity of the form is then reached by electro erosion machining.

Simply said from shapes designed in CAD system with support of NC modules CAM system data for NC machines can be generated. The machines are able according the data to produce desired shape of parts into tools for their production (tools for sheet-metal pressing, forms for plastic materials injection moulding, and so on).

Also thanks to this fact progress in car shape image for various automobile marks was reached. Headlights and direction indicators are today contour and create one complete whole in connection with splash-board and bumper [2].

Shape acquisition for virtual model and copying CAD/CAM-CNC

Product shape can be obtained by:

Creation of computer virtual model (Fig. 6) in graphical environment of CAD system by using approaches of surface or volume modelling. A model is created either directly by CA skilled designer or by CAD expert (a modeller) on the ground of sketches and idea designs of a designer. A model is created in an environment of surface modeller from basic elements in 2D. On ground the elements are then created 3D shape surfaces. The result is the surface model of the shape.
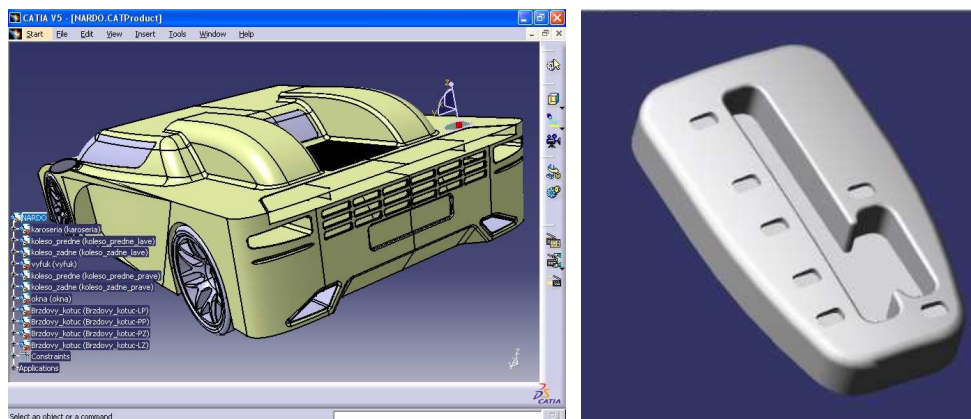

Fig. 6. Virtual automobile model and sceneries of gear control created in SW CATIA [9]

On the ground of virtual (CAD) model there are generated CNC data by using system CAM modules (Fig. 7). The data are description of model surface position data on which a tool has to go through for snagging desired shape. It is not a case of mechanical, electro mechanical or hydraulic systems of profilers which transfer shape from template into the form shape. There are the modern CNC milling centres which on the ground of digital data created on CAD model basis with support of CAM module will snag desired shape. The template or pattern is mentioned CAD model on which „surface" the tool of CNC machine is led.

Demonstration of snagging on the ground of virtual model is shown in Fig. 8 and 9.
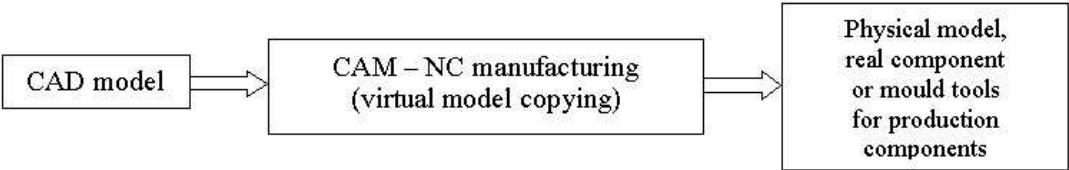
Fig. 7. Scheme of manufacturing process based on CAD/CAM
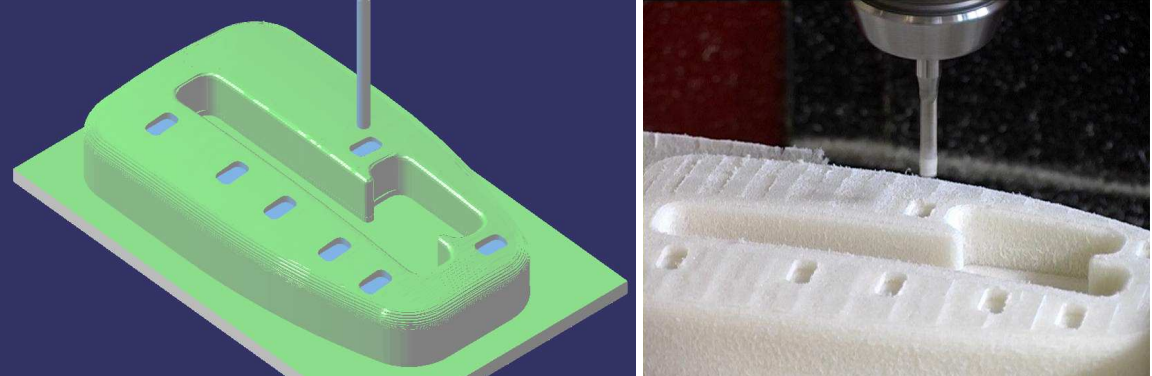
Fig. 8. Simulation of tool path and a model production [3]

Fig. 9. A maquette production 1:1 on CNC machine in development centre PSA [8]

Reverse Engineering

By scanning of points position data for the clay model (Fig. 8) are obtained by using three-dimensional digitizing machine - scanner. The first step in model transfer from real into the digital environment is its detail measure. For needs of „reverse

engineering" (Fig. 12) it is used at present the principle of contact-less scanning by optical or laser 3D scanners. The result of measurement is high number of points with X, Y, Z measures – it means „a cloud of points" (Fig. 11) usually exported with triangular net in data format STL for the next processing. The measured STL model is in the follow phase transformed into the CAD surface data. The digital model is always a compromise among surface smoothness, deviation from measured data and speed of their creating [4].

Fig. 10. Making a clay model [10]

Fig. 11. „Cloud of points" with s triangular net and smoothed surface model in ICEM Surf [7]
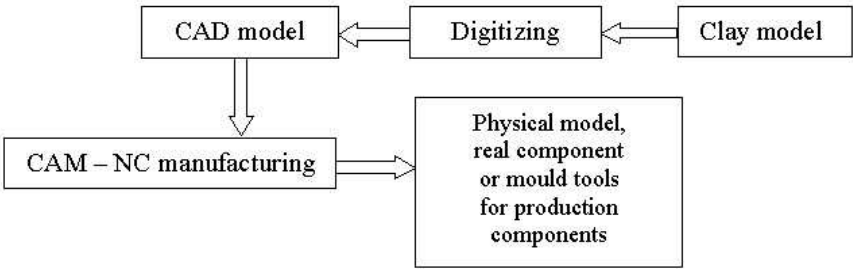

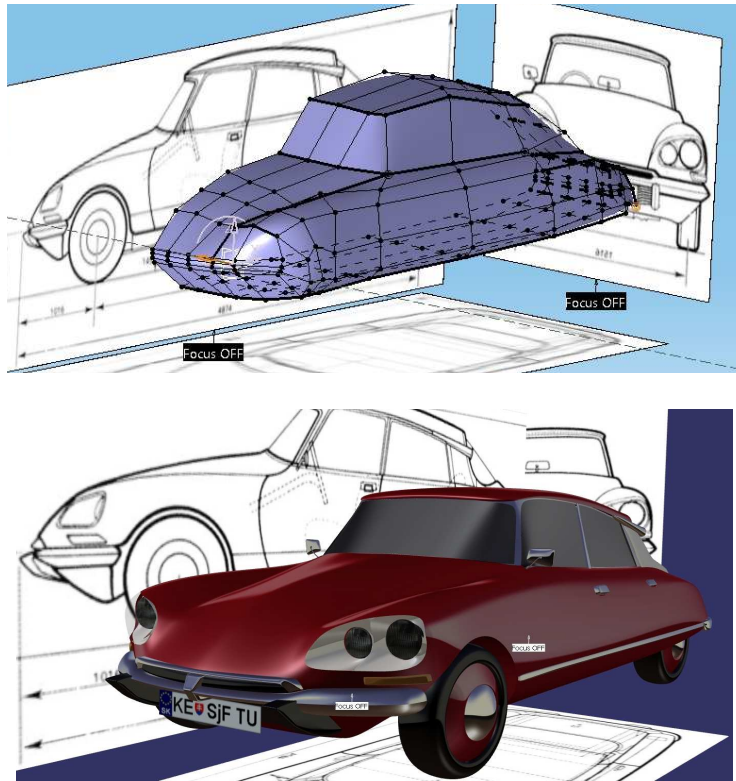Fig. 12. Scheme of reverse engineering process

Fig. 13. Digitized of automobile shape in Image&Shape CATIA V5 (R. BOSLAI – student of 3rd year)

Fig. 14. Virtual tuning in Image&Shape CATIA V5 (Robert BOSLAI – student of 3rd year)

An example of the software Image&Shape CATIA V5 using for digitizing of shapes is shown in Fig. 13. Fig. 14 shows possibilities of Image&Shape module of CATIA V5 software in the area of virtual tunning.

CONCLUSION

In connection with start in business of concerns like Volkswagen, PSA and KIA in Slovakia requests for competent technical staff experienced with CA.. technologies will always increase. Our university has the tradition in teaching the systems on basis of software CATIA and Pro/ENGINEER. Many of our graduates were successfully practiced in the automotive industry in Czech Republic and Germany thanks to CA.. approaches handling of design and production.

REFERENCES

1. Fabian M.: *Analýza vplyvu výrobných činiteľov na kvalitu povrchu a tvaru činných častí lisovacích nástrojov*. Písomná práca k dizertačnej skúške, Košice 2004

2. Fabian M.: *Znalosť CAM-nutnosť? Nie. Nevyhnutnosť!*. In: itCAD 6/2003, Brno 2003, s. 40-42, ISSN 0862-996X

3. Fabian M.: *CAD/CAM v procese prípravy odborníkov pre automobilový priemysel*. In: itCAD 4/2005, Brno 2005, s. 32,34, ISSN 0862-996X

4. Hendrych T.: *Reverse engineering v automobilovom priemysle*. In: itCAD 6/2004, Brno 2004, p. 28, ISSN 0862-996X

5. Tuček J.: *Kupé ÚVMV 1100GT – Elegán z Vysočan*. In: automobil revue 8/2000 Unipress Praha, s. 39. ISSN 1211-9555

6. Líkař O., Sedlák I.: *Výroba automobilů a technický pokrok*. In: automobil 5/1977 SNTL Praha, p. 23.

7. Waterman P.: *3D Data at Work , Desktop Engineering*. August 2004, [cited 09.11.2005], accesible on WWW <http://www.deskeng.com/Articles/Feature/3D-Data-at-Work-004081728.html>

8. Hyan T.: *Továrna na nápady*. Zdroj: automobil revue 12/2004, [cited 09.11.2005], accesible on WWW <http://www.dopravnimedia.cz/default.aspx?section = 1&server = 1&article = 1067 >

9. Centrum informatiky SjF TU v Košiciach, CAD/CAM – modelovanie, NC obrábanie, [cited 2.1.2007], accesible on WWW < http://www.sjf.tuke.sk/ci/catia/index.htm >

10. Car Design online, Clay Modelling, <http://www.cardesignonline.com/design/modelling/ clay-modelling.php>

11. Fedorko G. Molnár V.: *Catia základy projektovania*. 1. vyd. Košice : ES/AMS, TU, 2006. 105 s. ISBN 80-8073-648-0

12. Fabianová J. Greškovič F.: *Vplyv technologických parametrov na výsledné mechanické vlastnosti plastových výliskov*. In: Plasty a kaučuk. vol. 46, no. 7-8 (2009), p. 196-198. ISSN 0322-7340

13. Fabianová J. Greškovič F.: *Využitie CA technológií v procese návrhu a výroby plastových výliskov*. In: Acta Mechanica Slovaca. roč. 10, č. 2b (2006), s. 493-498. ISSN 1335-2393

14. Spišák E.: *Matematické modelovanie a simulácia technologických procesov – ťahanie*. TYPO Press, Košice,2000

15. Stachowicz F., Spišák E.: *Sposoby oceny zdolności blach cienkich do ksztaltowania plastycznego na zimno*. Rzeszów 1998, s.121, ISBN 83-7199-078-2.

Ivan GAJDOŠ
Peter KAŤUCH

Technical University of Košice, Slovakia

COMPLEX APPROACH
TO THE REVERSE ENGINEERING TECHNIQUES

This paper describes possibilities of integration newest technologies in reverse engineering process. The integration of computer tomography and FDM rapid prototyping technology allows to reproduce plastic parts without any documentation (blueprints, CAD model...) in very short cycles lasting few hours. Even complex shaped parts, with difficult geometry become no problem for combination of these two technologies, where the conventional approach in reverse engineering would last weeks if ever possible. On experimental part with complex geometry was presented modern complex approach in reverse engineering including measuring and digitalizing of part, data preparation for printing, printing and finishing of new part. Computer tomography was also used to compare shape and dimensions of original and reproduced part.

INTRODUCTION

Reverse engineering could be defined as the process of discovering the technological principles of a device, object or system through analysis of its structure, function and operation. In the area of mechanical engineering especially production technologies, reverse engineering serves for reproducing of parts. Following are reasons for reverse engineering a part or product:

1. The original manufacturer of a product no longer produces a product
2. There is inadequate documentation of the original design
3. The original manufacturer no longer exists, but a customer needs the product
4. The original design documentation has been lost or never existed
5. Some bad features of a product need to be designed out. For example, excessive wear might indicate where a product should be improved
6. To strengthen the good features of a product based on long-term usage of the product
7. To analyze the good and bad features of competitors' product
8. To explore new avenues to improve product performance and features
9. To gain competitive benchmarking methods to understand competitor's products and develop better products
10. The original CAD model is not sufficient to support modifications or current manufacturing methods
11. The original supplier is unable or unwilling to provide additional parts
12. The original equipment manufacturers are either unwilling or unable to supply replacement parts, or demand inflated costs for sole-source parts

13. To update obsolete materials or antiquated manufacturing processes with more current, less-expensive technologies

Reverse engineering enables the duplication of an existing part by capturing the component's physical dimensions, features, and material properties. Before attempting reverse engineering, a well-planned life-cycle analysis and cost/benefit analysis should be conducted to justify the reverse engineering projects. Reverse engineering is typically cost effective only if the items to be reverse engineered reflect a high investment or will be reproduced in large quantities. Reverse engineering of a part may be attempted even if it is not cost effective, if the part is absolutely required and is mission-critical to a system.

Conventional process of reproducing parts via reverse engineering includes a dimensional analysis. The detail dimensional analysis should be conducted using at minimal calipers, however a more complete analysis my facilitated using a Coordinate-measuring machines (CMM), which can be used to digitize the entire part and the information can be utilized in computer-aided modeling [1]. More sophisticated methods in reverse engineering include laser scanning which, as the name implies, uses laser beams to scan across the surface of components of any shape and display the results in real time. Representing geometry of the part in terms of surface points is the first step in creating parametric surface patches. A good polymesh is created from the point cloud using reverse engineering software. The cleaned-up polymesh, NURBS (Non-uniform rational B-spline) curves, or NURBS surfaces are exported to CAD packages for further refinement, analysis, and generation of cutter tool paths for CAM. Finally, the CAM produces the physical part.

It can be said that reverse engineering begins with the product and works through the design process in the opposite direction to arrive at a product definition statement (PDS). In doing so, it uncovers as much information as possible about the design ideas that were used to produce a particular product.

MODEL DIGITALIZATION VIA COMPUTED TOMOGRAPHY

Reverse engineering of mechanical parts involves acquiring three-dimensional position data in the point cloud using laser scanners or computed tomography (CT). Modern measuring technique utilizing computer tomography allows to obtain digital model independent on complexity of measured part geometry , which were impossible to measure by non-destructive approach by conventional measuring technique. For our research, part as shown in Fig. 1 made from ABS polymer was used. The goal was to join advantages of computer tomography and FDM technology, to produce part reproduction in shortest possible time. This part is conventionally produced by combination of injection molding technology and welding and its complex shape is suitable to present application and synergy effect of computer tomography and FDM technology.

This part was measured with help of industry tomograph Metrotom 1500^{TM} (Fig. 2). The part is placed into measuring chamber of 1500^{TM}, between source of X-ray and detector. The part rotate 360° around vertical axis, to obtain a set of 2D pictures (typically 700 – 1000).
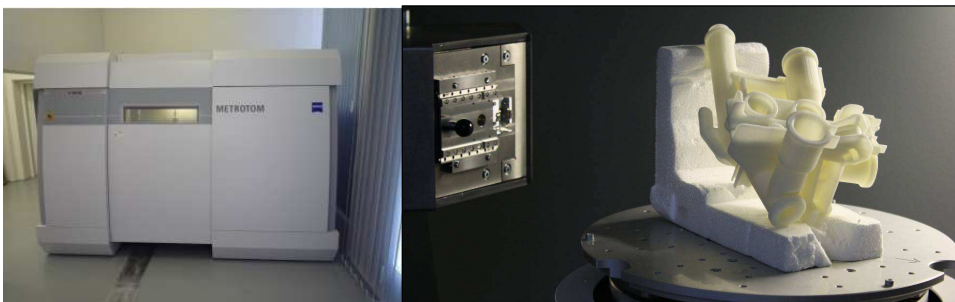
Fig. 1. Selected part (fitting) used for experiment

Fig. 2. Metrotom 1500^{TM} computer tomography measuring device (left), and its measuring chamber (right)

From these pictures with help of computing techniques is generated an 3D model of measured object, known as cloud of points (Fig. 3). This format is not suitable for use as base in any CAD modeling software, or as information for direct 3D printing [2]. To be able to print reproduced part with FDM printer, obtained data (cloud of points) were processed with software VG StudioMax. VG StudioMAX converts cloud of points to suitable format for any rapid prototyping technology STL (Fig. 3). Whole process from part measuring to finished STL file of measured part takes about 2-3 hours.
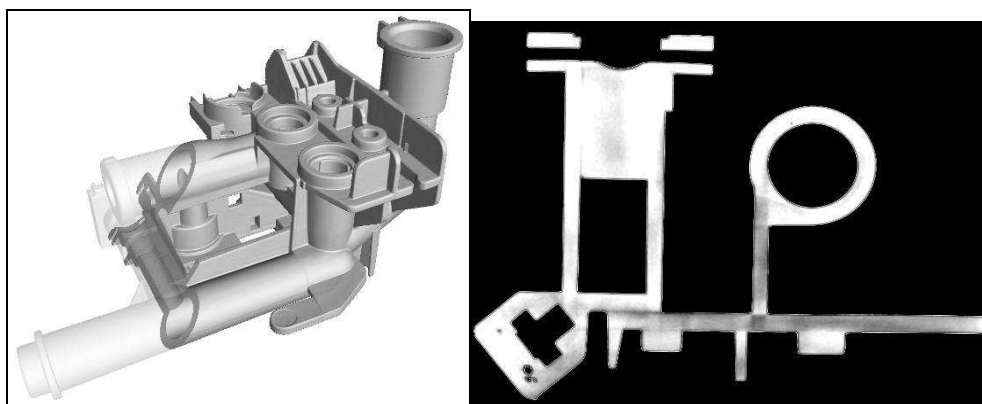

Fig. 3. Cloud of point representing measured part (left) and single view in interior of part (right)

PRODUCING OF PART

Obtained STL file, is imported into CATALYST 4.3, software that could be compared with CAM software used in machining processes. This software also prepares and compute toolpaths for modeling material and support material. These toolpaths are then send into the FDM 3D printer. Used FDM technology with SST modification (Soluble support) is ideal for such types of complex shaped parts, because of easy removal of support in water solution even in hided corners etc. If another rapid prototyping technology would be used, removal of support inside of this part would significantly more problematic. In CATALYST 4.3 proper orientation in building chamber of printer was selected, and toolpaths were generated (Fig. 4.).
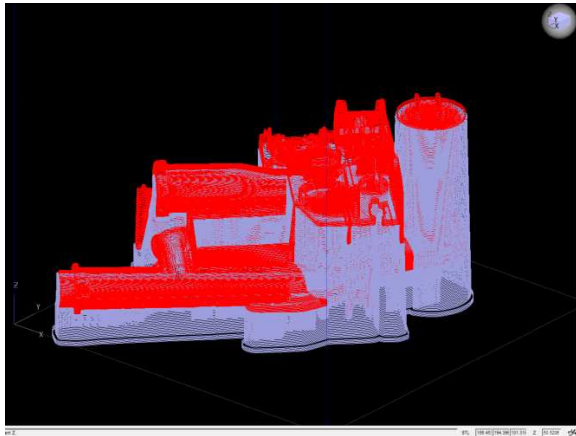
Fig. 4. Data representing scanned part suitable for printing, with toolpaths for modeling material (red) and toolpaths for support material (gray)

Prepared toolpath file in CMB format was sent to Dimension SST 768 printer (Fig. 5) with ABS material used as modeling material and printed in 22 hours. To speed up the process, from printed part were mechanically removed all support structures that were reachable. Remaining support structures were solved in water solution in cleaning station (Fig. 5). After 15 hours all the support material was removed and part was ready to use.

Fig. 5. Dimension SST768 printer (left) and cleaning station (right)

RESULTS

Whole reverse engineering process of selected part was finished in about 40 hours. Printed part was visually compared with original as displayed in Fig. 6.

Fig. 6. Visual comparison of original and printed part

Printed part was also measured in Metrotom 1500^{TM}. Measured data from original part were compared as shown in Fig. 7.

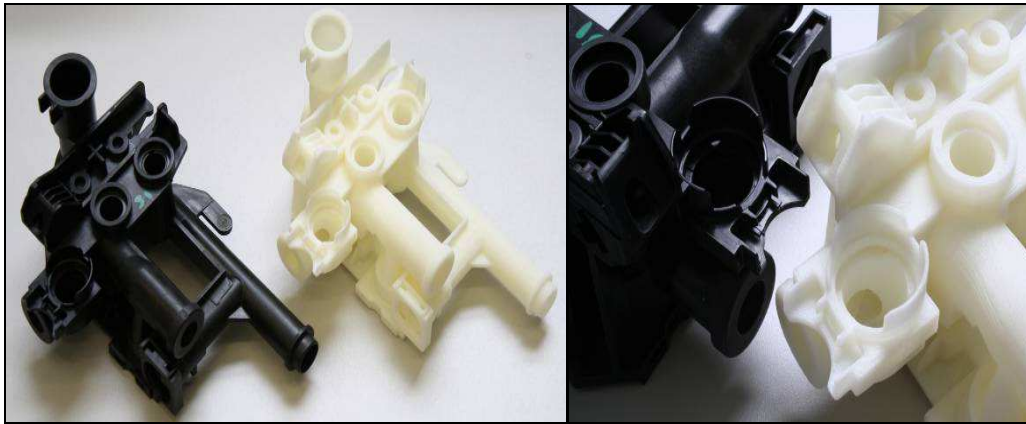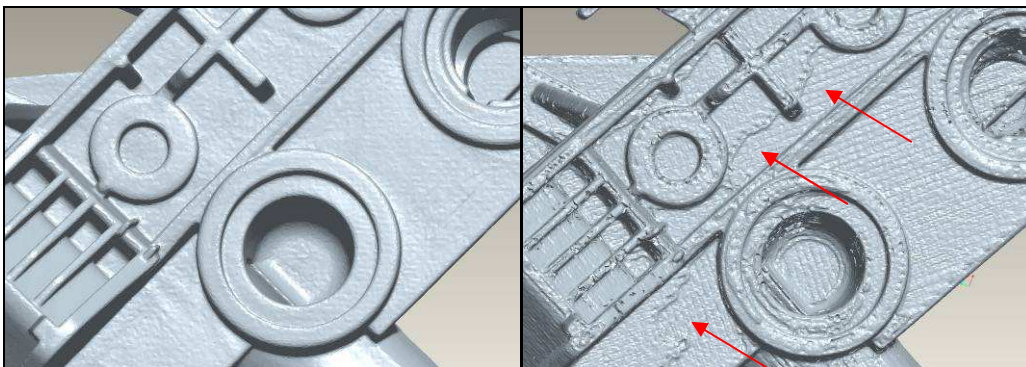Fig. 7. Measuring results form Metrotom 1500^{TM}: left – original part, right –printed part. Red arrows points to area with staircase effect

From Fig. 7 obvious limitations of FDM technology are visible, especially the staircase effect resulting from nature of all additive technologies and strongly dependent on building layer thickness. Staircase effect could be also eliminated with proper orientation of model during generating toolpaths [3], to do this is necessary an STL file generated from original CAD file. STL file generated from cloud of points measured in Metrotom does not contain any planar surfaces (as in CAD file or on original part), and the surface of generated STL file looks like blasted.

To check if this combination of technologies is not only fast, but also suitable for reverse engineering , was selected the aspect of dimensional, and shape accuracy. In the Fig. 8 displacements between original and printed part are displayed. From Fig. 8 is obvious that printed part has high dimensional accuracy and the shape displacement is maximally 0.2 mm.

Fig. 8. Comparison of shape displacement between original part an printed part

DISCUSSION AND CONCLUSION

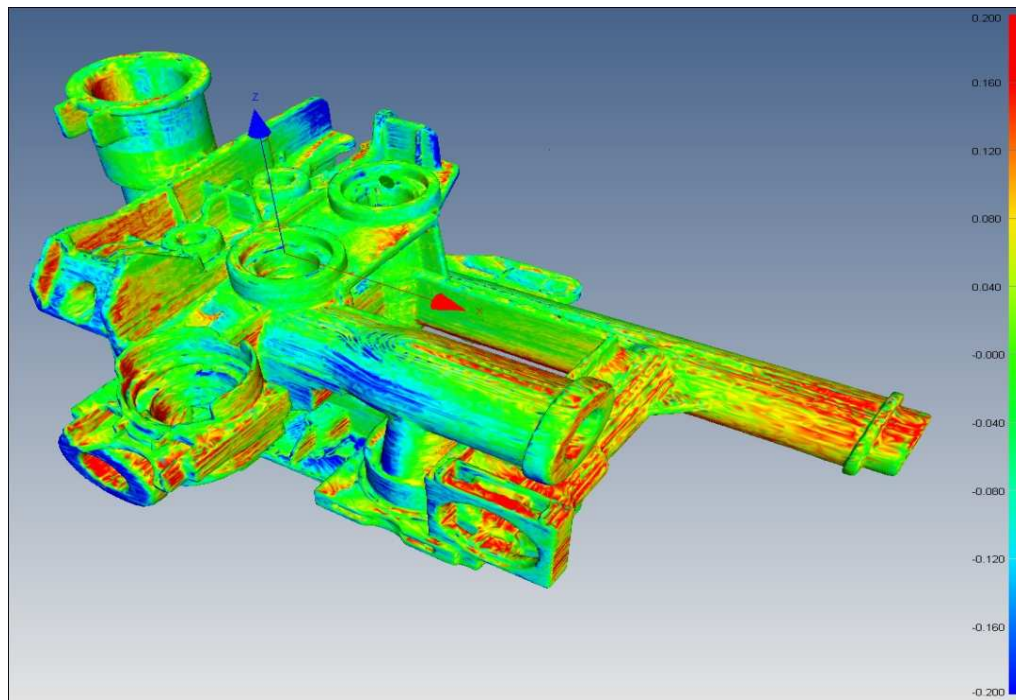Presented paper describes application and integration of modern technologies in process of reverse engineering. Selected part (fitting) was ready to use in less than 48 hours, this time would be unable to reach using common techniques of measuring and manufacturing. Copied part shows excellent dimensional accuracy, however there is lot of possibilities to further development. There is a need to generate more accurate STL file after measuring. For better quality of printed parts there is possibility to use nanofillers to fill out empty space inside of FDM prototype structure. Also it is possible to use surface finishing techniques (blasting, painting) to improve visual quality of produced parts.

REFERENCES

1. Janecki D., Stępień K., Adamczak S.*: Calculation of reference surface parameters for elements whose generatrix is a fragment of a circle*. XIX IMEKO World Congress, Fundamental and Applied Metrology, September 6 – 11, 2009, Lisbon, Portugal.

2. Kaťuch P., Živčák J., Dovica M., Kováč J., Kelemenová T.: *Počítačová tomografie pro přesné měření, defektoskopii i reverzní inženýrství*, ItCad 6/2009.

3. Gajdoš, I., Slota, J., Spišák, E.: *Visualisation of FDM prototypes*. Proceedings of ICAT 2008: 2nd International Conference on Additive Technologies: DAAAM Specialized Conference, Ptuj, Slovenia.

Ivan GAJDOŠ
Ján SLOTA

Technical University of Košice, Slovakia

IMPROVING SURFACE FINISH QUALITY OF FDM PROTOTYPES

Rapid prototyping technologies decrease production time and costs in engineering industry but also in other industries. One of most widely used technology FDM suffers under low surface finish quality. This paper is aimed on research of surface finishing technologies applicable to improve the quality of FDM prototypes surface finish. Pre-treated samples were blasted with sodium bicarbonate and glass beads. The values of R_a and R_z were measured on the samples and compared the impact of selected blasting medium and blasting conditions on surface finish quality of FDM prototypes.

INTRODUCTION

Because of increasing complexity of products, rapid prototyping (RP) technologies are gaining important place in product development process, and industrial demand is driving manufacturers to improve the specifications of RP machines. These technologies are widespread used for RP, rapid tooling (RT) or rapid manufacturing (RM) has lead to research effort to improve their characteristics.

One of the most commonly used technologies is fused deposition modeling (FDM). Advantages of this technology are: wide variety of materials available, quick material change, low maintenance costs, quick production of thin parts, a tolerance equal to -+0.1 mm overall, no need for supervision, no toxic materials, very compact size, low temperature operation. The main disadvantages are surface quality, the need of support structures, axial weakness perpendicularly, a larger area of slices requires longer building times, and temperature fluctuations during production could lead to delamination, and high surface roughness.

In practical application, poor surface finish affects the function of RP parts, depending on the geometry of the enclosing surface, the building strategy, layer thickness and orientation of the part; this drawback may outweigh the advantages of RP parts.

Decreasing of layer thickness leads to the better surface finish of produced prototypes in RP machines, but this issue is also affected by the angle between the vertical axis and surface tangents (staircase effect). Moreover, since the solid model is approximated by series of triangles (STL format), this results in a chordal approximation error that will also negatively affect the surface smoothness. As regards FDM, the road width, air gap between roads and model temperature will also have an impact on the surface roughness. As a consequence, customers often demand hand finishing for even the most basic levels of part quality, with the result that the geometrical features of the prototypes are strongly dependent on the operator's skill.

In literature a wide variety of approaches has addressed the problem of analyzing [1, 2] and improving surface roughness of rapid prototyped parts. This category can be divided into four categories: (1) optimal build direction, (2) slicing strategy (3) fabrication parameters optimization, (4) post-treatment. Optimal build direction and slicing strategy address the reduction of roughness due to the staircase effect. Fabrication parameter optimization and post-treatment are more general approaches that can also be applied to surfaces not affected by the staircase effect, such as horizontal surfaces. Advantage of post-treatment approaches is also that they are independent on used FDM machine and can be used also in combination with existing FDM printers.

POST-TREATMENT OF FDM PROTOTYPES

Blasting belongs to the often used post-treatment technologies, applicable also for prototypes made by FDM technology. In the experiment were used two types of blasting agents sodium bicarbonate and glass beads.

Samples as displayed in figure 1, were prepared in Dimension SST 768 FDM 3D printer from ABS polymer with two types of layer thickness standard (0,254 mm) and draw (0,33 mm). The height of the samples was different in both thickness variations. Samples thickness was set to obtain desired filament orientation as presented in figure 1 and the sample has to consist of minimum four layers.
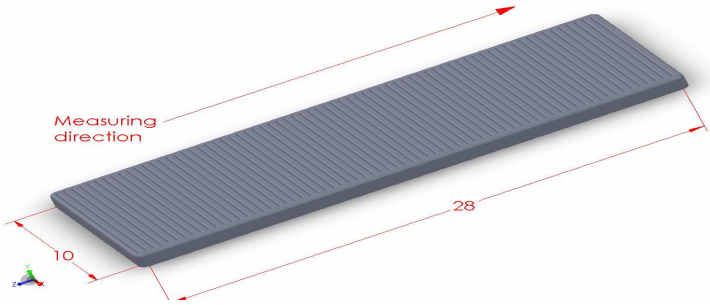
Fig. 1. Sample dimension and measuring direction

As displayed in figure 1 , the orientation of the samples were set according to demands on measuring length (12,5 mm + inlet and outlet probe path) and filament orientation (motion of measuring probe perpendicular to the filament orientation). Printed samples were left on modeling base to ensure uniformly conditions when blasting samples as shown in figure 2.
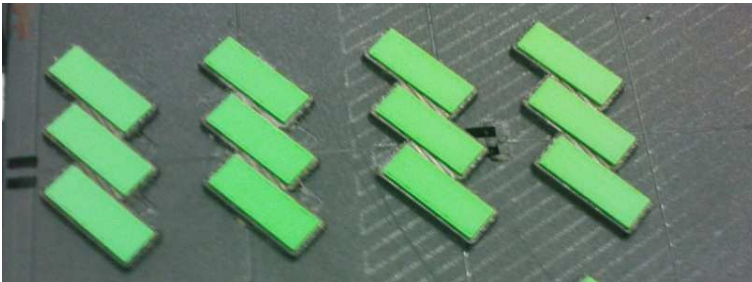

Fig. 2. Printed samples on modelling base

On printed samples surface quality determined by roughness test and values R_a and R_z [3] was measured. Measuring of R_a and R_z was carried out on printed samples before blasting and after blasting with help of Elcometer 7060/4 SURFTEST SJ-301 roughness tester.

As mentioned earlier blasting was performed with two types of blasting media: sodium-bicarbonate and glass beads, with air blasting device at the pressure 5000 kPa and blasting angle 70 degrees. Sodium-bicarbonate is already used solution, commercially available as finishing station for FDM prototypes. The samples were exposed to 12, 24 resp. 36 crossings of blasting beam with sodium bicarbonate. Form the nature of the glass beads (higher hardness), is the abrading effect stronger. That is why for blasting with glass beads were selected 4 and 8 crossings with blasting beam.

RESULTS AND DISSCUSION

Data obtained from surface tester were separated in two groups according to layer thickness. In the figure 3 are presented R_a and R_z data for samples with layer thickness 0,254 mm.
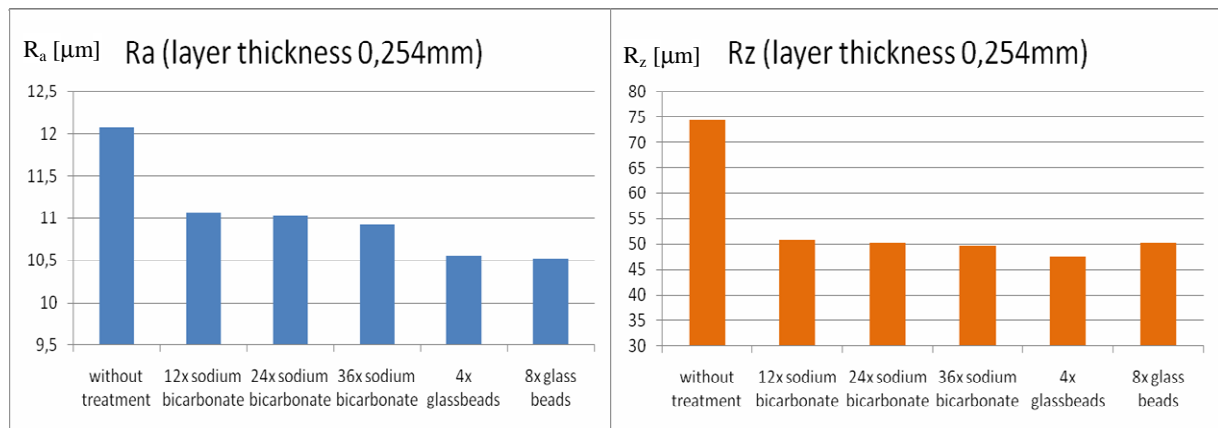
Fig. 3. Data values R_a and R_z [µm] for specimens made with layer thickness 0,254 mm

Data presented in figure 3 confirm justness of using blasting process as surface finishing process for FDM prototypes. Sodium-bicarbonate as blasting agent decrease the value of R_a in 9% after 12 blasting beam crossings. Increasing the number of crossings leads to slower decreasing of R_a to the value 10% lower than R_a value of specimen without treatment. Glass beads as more intensive blasting agent, decrease R_a value in about 13%, and no big difference was observed between 4 and 8 blasting beam crossings. On the other side intensive blasting leads to increasing of R_z value. Nevertheless both blasting agents decrease the value of R_z between 32% and 36%, compared to the samples without treatment.

In the figure 4 results for samples built with 0,33 mm layer thickness are presented. These results corresponds, to observed result from specimens with 0,254 mm layer thickness. The value of R_a and R_z from 0,33 mm sample without treatment is almost two times higher than values from 0,254 mm samples.
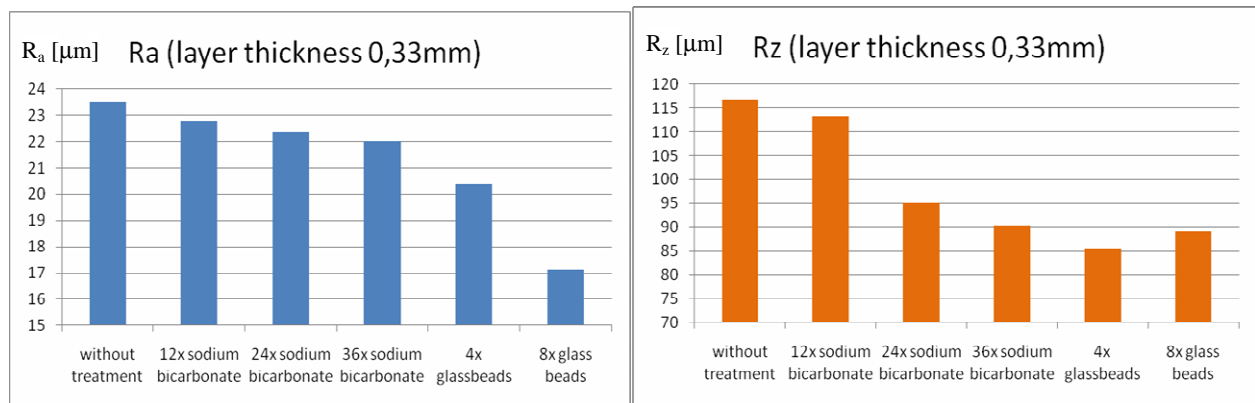
Fig. 4. Data values R_a and R_z [μm] for specimens made with layer thickness 0,33 mm

CONCLUSION

Blasting as finishing surface technology for treatment of prototypes made by FDM technology has notable potential in this area. Some commercial solutions based on using sodium-bicarbonate as blasting agent are already available, but as it is obvious from results, the glass beads are also applicable blasting agent with better results than sodium-bicarbonate. Further test of surface structure and blasting conditions are necessary to gather complex information about this process and processing conditions to improve surface quality of FDM prototypes.

REFERENCES

1. Ippolito R., Iuliano L., Gatto A.: *Benchmarking of Rapid Prototyping Techniques in Terms of Dimensional Accuracy and Surface Finish*. Annals of the CIRP 44(1):157–160, 1995.

2. Armillotta A.: *Assessment of Surface Quality on Textured FDM Prototypes*. Rapid Prototyping Journal 12(1):35–41., 2006.

3. Janecki D., Stępień K., Adamczak S.: *Calculation of reference surface parameters for elements whose generatrix is a fragment of a circle*. XIX IMEKO World Congress, Fundamental and Applied Metrology, September 6 – 11, 2009, Lizbona, Portugalia.

František GREŠKOVIČ
Ľudmila DULEBOVÁ
Ján VARGA

Technical University in Košice, Slovakia

THE NEW TRENDS IN DESIGN MOULDS FOR PLASTIC

The paper presents new trends and new materials used in the design of moulds for plastics processing. Application of CAD / CAM / CAE systems reduces the time of the design of forming tool. Tool materials produced by new technologies are compared with standard materials. Wear of tool materials were examined for plastics injection molding. Simulation of technology of plastic injection molding process was examined as a tool to improve the quality of plastic parts.

INTRODUCTION

The range of products for the automotive and electrotechnical industry consists mainly of the formed metal and plastic products. Their production is secured by shaping tools, moulds and by fixtures. For high production of these components is necessary in a short time to design and produce precious metal forming tools. Delivery companies are trying to reduction of time of advance workings, which allows a flexible response to the manufacturer for changing market requirements [1].

We have a tradition in Slovakia in the design of forming tools and then its production. Engineers of forming tools must get under control with more areas and to monitor the development of new tool materials and unconventional technologies. They must still be competitive and in the market. The use of new technologies such as Rapid Prototyping and Reverse Engineering succeed is already a matter of course. The latest manufacturing technology, CAD, CAM and CAE systems require qualified personnel.

For a number of CAx systems in the design and manufacture of these tools are mainly use:

- *CAD (Computer Aided Design),*
- *CAM (Computer Aided Manufacturing) ,*
- *CAD/CAM (Computer Aided Design / Computer Aided Manufacturing,*
- *CAE (Computer Aided Engineering)* [2].

Fig. 1 shows examples of parts used in design of forming tools. Besides CAD and CAM systems wide application in the design of forming tools has CAE system.
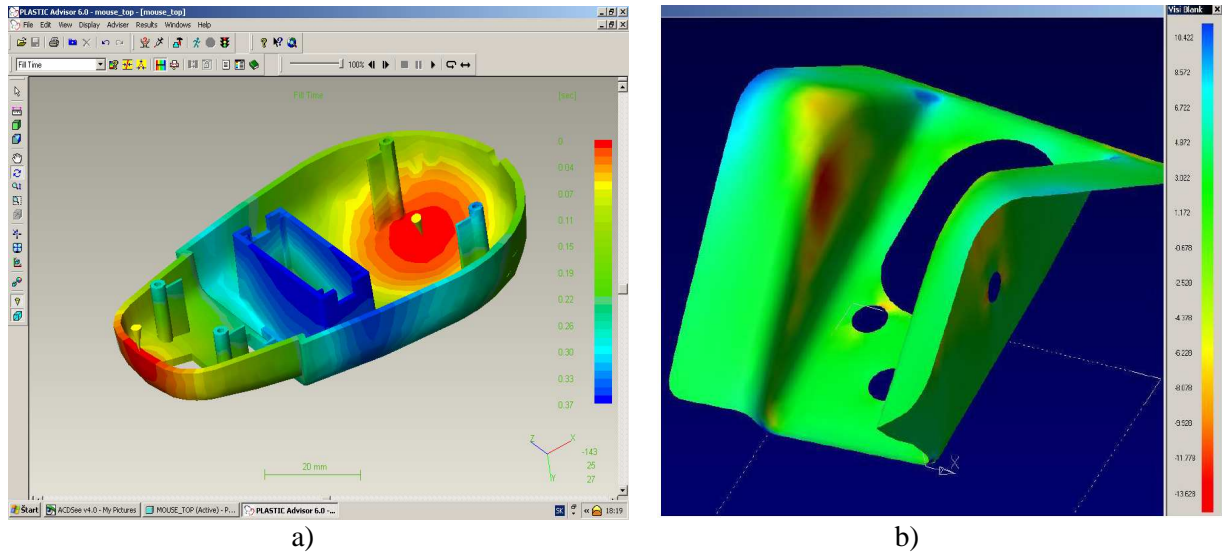
Fig. 1. Examples of parts used in design of forming tools [3]: a) model of plastic product in CAE system, b) model of sheet part in CAE system

TOOL MATERIALS USED TO PRODUCE OF MOULDS

The economy of production of components by forming tools depends on the cost of production tool i.e. injection mould, die, shear tool or other tool. In most cases, is required in mass production high lifetime of forming tools. The lifetime of forming tool is subject to particularly good choice of materials and chemical-heat treatment (sometimes with surface finishing). Lifetime of forming tool affects its constructive design, dimensioning, maintenance and storage. Nowadays are used for production injection moulds non-ferrous materials. Alloys of copper and aluminium have good heat conductivity (fourteen until fifteen higher than the steel used for the manufacture of injection moulds). The advantages of copper alloys are also a low friction coefficient, which is particularly useful for moving parts of moulds and tools [4, 5].

ADHESIVE WEAR OF TOOL MATERIALS

By solution to the Grant Project VEGA 1/4166/07 - Research and development of prototype moulds for moulding of small parts, experiments were made for the purpose of properties used of tool materials for various polymeric materials and composites. It was followed weight decrease of tool material used in application of plastic friction couples plastic – tool material [6] were analysed. The friction coefficients with lubrication and without it. Experiments were used in different temperature regimes (room temperature and increased temperature). The friction coefficient diagram for each friction pairs after 1800 seconds of friction is shown in Fig. 2. The comparison of friction coefficients found that the lowest value measured friction coefficient was reached in friction pair with material X37CrMoV5-1 and scilicet in contact by both polymer materials.
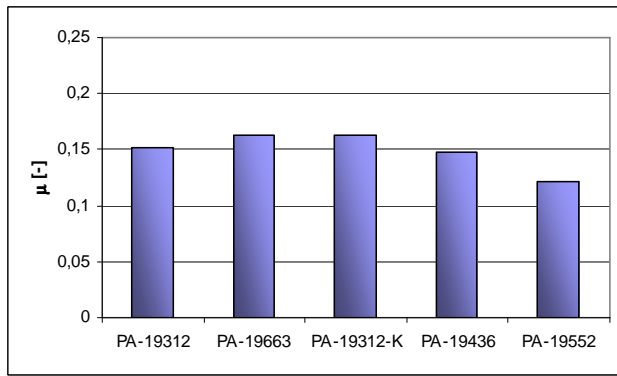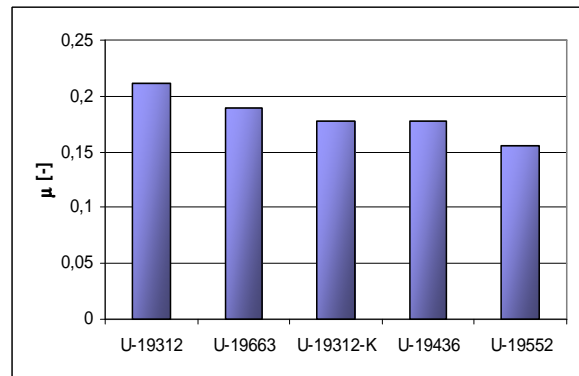
a)   b)

Fig. 2. The values of friction coefficient of tested materials in combination with plastic material:
a) material PA, b) material Ultradur B430 G4

Weight decrease of tool steels after 1800 seconds of wear displays Fig. 3. Based on the experimental results obtained in the simulation of wear of steel materials in combination with PA 6 one can see that the highest wear resistance after 1800seconds contact with those materials showed a steel 90MnV8 despite the lowest of alloying elements content. That fact can be justified by influence of ferrite - pearlite material structure. For wear mechanism size of weighting is the main factor. In these conditions could be affected by alloying elements in other materials for their resistance to wear.

By evaluation of wear of selected materials in friction pair of semi-crystalline polymer materials filled by glass fibres has been the largest material reduction X210Cr12. Course wear shows that hardness material reduction is not always ultimate factor in choosing the appropriate type of material injection moulds. Main role has wear mechanism of each material in relation to their structural construction. Best resistance against a given wear showed samples of material made to 720 Böhler and X37CrMoV5 -1. Fig. 3 shows weight decrease of tested materials in combination with different materials.
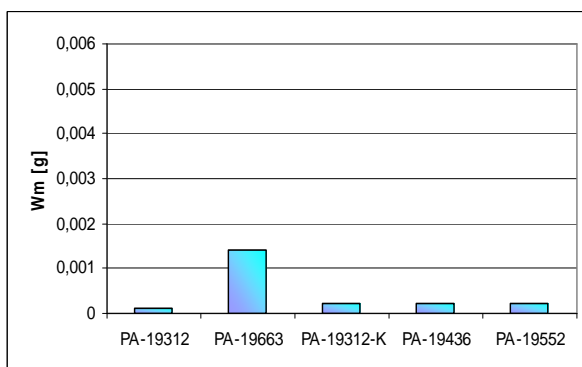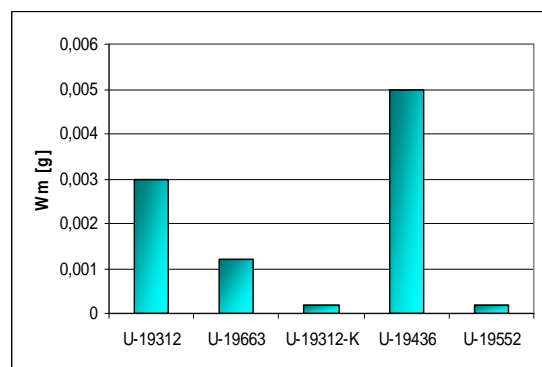
a)   b)

Fig. 3. Weight decrease of tested materials in combination with different materials: a) material PA, b) material Ultradur B430 G4

Another important factor affecting the size of the wear of tested materials is evaluated macro undulation and micro undulation of contact surfaces of the pair given

by production genesis. At the frictional contact of materials is elastic deformation and subsequently plastic deformation by top undulations of functional surfaces. During plastic deformation the surface layers of the area touch was be broken. At the same time there is a transfer of particulate material, to the contact surface in dependence on the material characteristics of contact pairs. The dependences of friction time on coefficient of friction of tested materials are presented in Fig. 4. and weight decrease of alloys at the same time are shown in Fig. 5.

Alumec 89   Moldmax HH
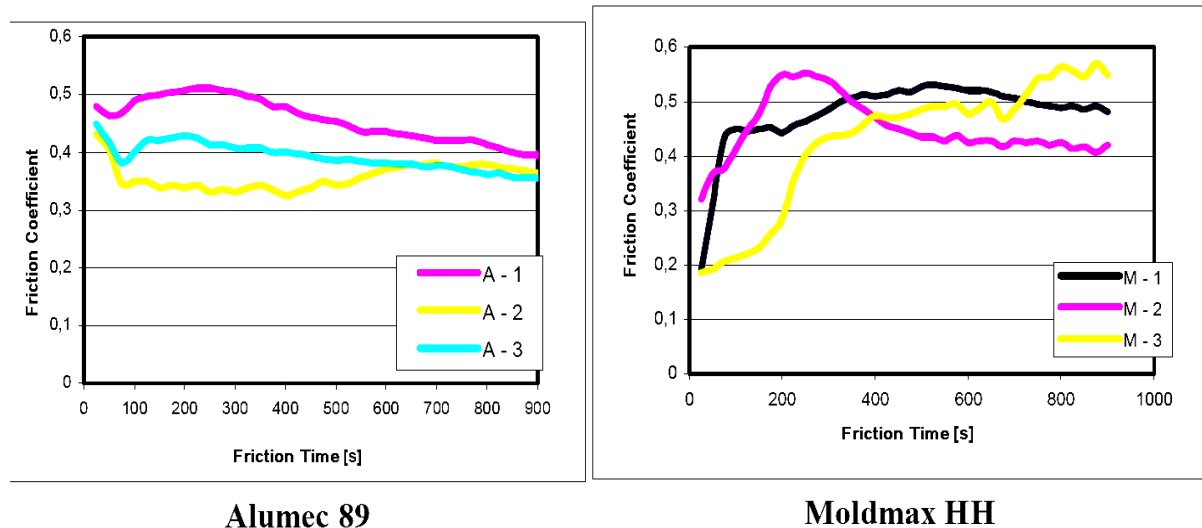
Fig. 4. The courses of the coefficient of friction alloys depending on the time - materials Alumec 89, Moldmax HH 89

Alumec 89   Moldmax HH
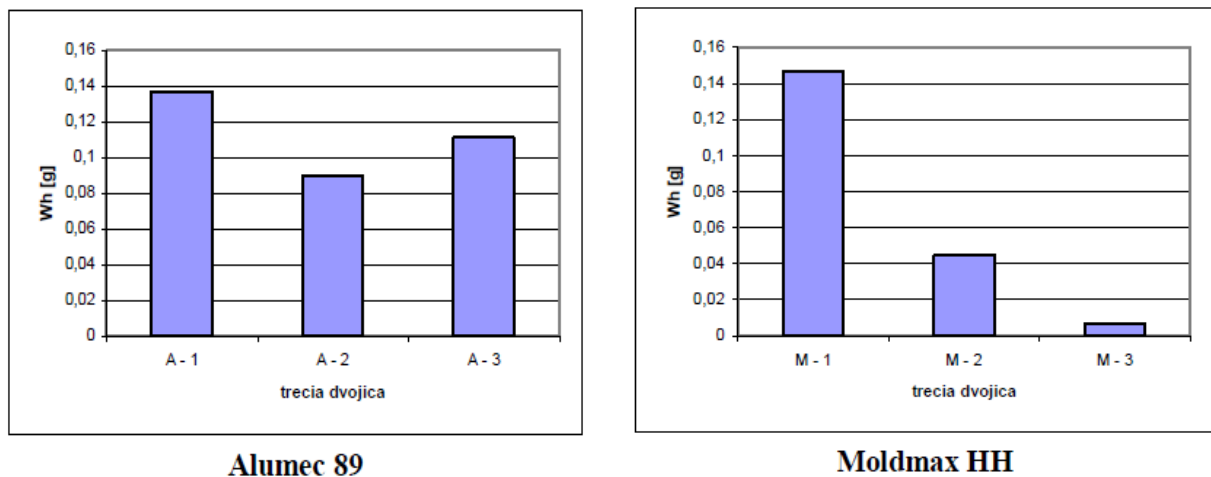
Fig. 5. Weight decrease of alloys at the same time – materials Alumec 89, Moldmax HH

The main role in this case has the interaction of various phases and adhesion to the matrix interface - glass fibres. On the basis of calculating time of injection moulding, the number of plastics products and wear tolerance of moulds can be obtained to help in specified the concrete form of life.

SIMULATION MODULES FOR PROPOSAL OF MOULDS

By design of forming tools is necessary with regard to decide about gate location system for plastic product, or by the choice of suitable material components or designing dimensions of exposed parts to predict the result. For this activity used different modules for analysis and simulation of strains, or for filling in the form of cavities. It is required 3D model parts examined and defined technological conditions, whether strain or pressing process. Verification of the strain - tension analysis, location of critical areas, second finish and control verify of the result of changes. Fig. 6 shows simulation results of the technological process of injection moulding plastic product.
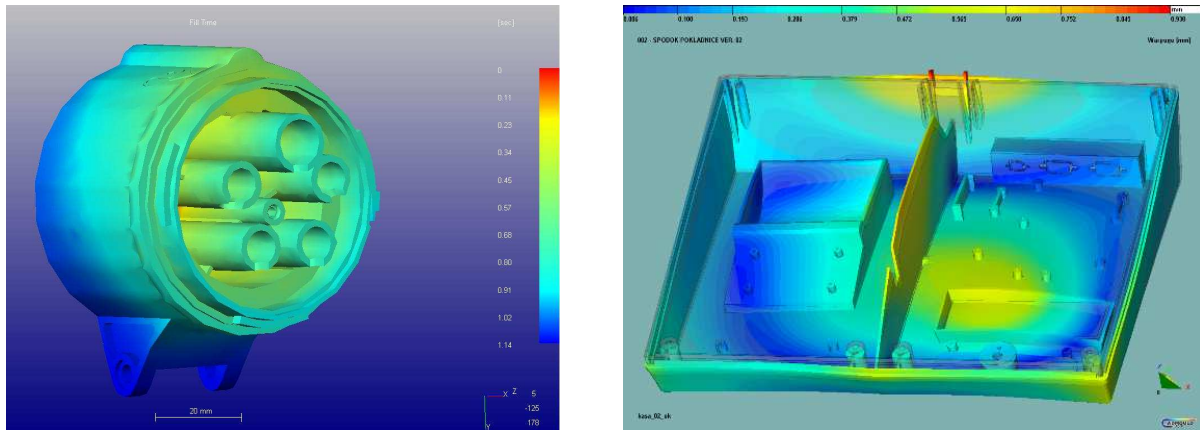
Fig. 6. Simulation results of the technological process of injection moulding plastic product

The introducing of computers into the drawing office and the use CAD systems with buildings in the design of forming tools has resulted in [7]:

- higher productivity of designers,
- rationalization of the draft design documentation,
- standardization of design documentation,
- reduction of time needed for draft design documentation,
- reduction the setup time of production,
- possibility of integration with other application programs and systems,
- greater flexibility changes of produced range - CAD parameterization and associativity of CAD design
- substantially reduce of development cycle (design, product, project),
- greater opportunity to design optimization,
- improve of work quality.

## THE INFLUENCE OF PRODUCTION FACTORS ON FINAL PROPERTIES OF PLASTIC PRODUCTS

The main objective was to experimentally verify and describe the influence of changes in selected technological parameters to change the properties of plastic mouldings products for various polymer materials. Materials were selected to use in the automotive industry. The second aim was to verify the impact of the quantity of granulate into the basic material on properties of plastic products. The amount to be

added granulate was from 0% to 100% of regranulate. Experiments are beneficial by reason of economic aspects of reuse granulate in companies that use plastic materials for production of plastic parts.

CONCLUSIONS

Problems of design tools for shaping metal forming and plastics came to the surface right nowadays. This is connected with start of the automobile and the development of electrical industry. The area of metal forming and design tools had a long tradition in Slovakia. We can say that the production of forged pieces and sheet metal parts forming is in a high technical level. However, plastics processing sector in Slovakia has been relatively neglected and this is proved in the arrival of car. The capture of new trends in plastics processing and forming tools for the design industry's needs to build laboratories and offices for training education professionals, but also for support research in the following areas:

- technology applications of reverse engineering and rapid prototyping,
- applications of polymeric materials with modified properties (composites, nano – composites),
- application of non-traditional processing methods of polymers,
- the introduction of recycling technologies and systems,
- reduction of cost of the manufacturing process based on the automation of production and logistics systems.

REFERENCES

1. Pötsch G., Michaeli W.: *Injection molding: An introduction*. 2nd ed. München (Germany): Hanser Publishers, 2008. ISBN 978-1-56990-419-0.
2. Beaumont J.P., Nagel R., Sherman R.: *Successful injection molding*. Hanser publisher, Mníchov, 2002. ISBN 3-446-19433-9.
3. Greškovič F. a kol.: *Technológie spracovania plastov*. Vstrekovanie plastov, SjF TU v Košiciach, 2009, 200 s., ISBN 978-80-553-0369-7.
4. Greškovič F. a kol.: *Nástroje na spracovanie plastov*. Vstrekovacie formy. SjF TU v Košiciach 2009, 225 s., ISBN978-80-553-0369-7.
5. Greškovič F., Mihok J., Stachowicz F.: *The Investigation of Tool Life in Blanking of Elektric Motor Laminations*. In. MECHANCS 2002, Scientific buletin of Rzeszow Univerzity of Technology No.193, Mechanics 58, Rzeszow júl 2002, str.81-84. ISSN 0209-2689
6. Greškovič F., Guzanová A., Brezinová J.: *Opotrebenie funkčných častí foriem pri vstrekovaní kompozitov na báze plastomérov*. In: Acta Mechanica Slovaca. roč. 12, č. 3-a pro-tech-ma (2008), s. 145-150. ISSN 1335-2393.
7. Greškovič F., Dulebová Ľ., Varga J.: *The applications of tool steels for different technologies of plastics processing*. In: Materials Engineering. roč. 14, č. 2 (2007), s. 77-80. ISSN 1335-0803.

Natalia GRIGORIEVA

Lutsk National State Technical University, Ukraine

DESIGNING OF TECHNOLOGICAL ASSEMBLY MODULES

The features of construction a modular assembly technology, shaping of modules, designing assembly of technological processes are described. The optimizations approaches for reach of practical construction of modules are shown on a criterion of an amount executed assembly movements.

INTRODUCTION

On designing of modular assembly technology have an influence: special and own structure of modular technology, technological possibilities of assembly equipments, degree of concentration technology, levels of automation and adaptability to manufacture of a construction object of assembly and other [1]. The process of designing such technology can be represented as selection of a subset of assembly movements from sets of modular technology, possibilities of the robot and requests of assembly. For reaching an object in view it will be possible to use operations of intersection of these sets circumscribed by the equations which are subject to optimization on selected criterions.

As that known [2] modular assembly technologies are represented by some set of the interconnected technological assembly modules enveloping main varieties of assembly works. Each module is good spent and optimized technological unit of repeated use, which the constructional module answers, on which modular technology is executed. Assembly module is understood as the completed population of main and auxiliary assembly movements (operations) executed in a demanded sequence in one working zone, in which the necessary gang of assembly tools and adaptations, i.e. technological tooling for a modification of the form and properties is indicated the object of assembly. Such assembly module is depending on a degree of concentration of technology, is for assembly of some number of assembly junctions. For reach of such approach the technological modular designing can be shown to an automatic selection necessary, docked among them, modules executed in a system of automatic design of technological processes. The assembly modules should be docked as to other modules of a technological line-up of assembly process, and modules of the equipment, tooling and management. Therefore generalized parameter joint of modules should include not only technological, also constructional and operational parameters of technologies.

The features of designing environments of modules on a comparison with simple assembly are, that for want of it is necessary to such development to take into account

technological possibilities of used robots, i.e. menu of assembly and auxiliary movements, other degree of concentration of operations, levels of automation of process and adaptability to manufacture of a construction of a collected item. It is necessary to take into account also constructional and organizational features robot's of assembly. A main evaluation of efficiency modular environments of technology in the issue is the maintenance of high productivity and flexibility for reach such restrictions as an accuracy, reliability and technological production cost.

STATEMENT OF CONTENTS

For reach of development such technology basis, on which the designing is executed are the features of designing of automated assembly technology with program control. On these basis the designing robot's of technological and constructional modules of the assembly component an essence of modular assembly technology is executed. Such develop are well known [3] generally which brief essence consists in the following. For a realization local (route of assembly) and global (maintenance of parameters of quality for want of issue of items) purposes the techniques of ascending and descending designing are used. The ascending designing has an empirical character and uses the approach to solution of problem, unequivocal engineering solution without a comparison of possible versions absence of an economic optimality of a solution. The descending designing is based towards methods of the theory of production management and mathematical programming. It is characterized by orientation to parameters of productivity and cost, comparison of variants and maintenance of profitability of an optimum solution. Main principles of designing robots of assembly processes are: the overlapping of high efficiency and universality; the hierarchy; the primary program resetting-up; the maintenance of the greatest object closure.

It is supposed that before designing robots of assembly technology the objects of assembly are selected correctly which, in general should meet the requirements which were program of assembly, i.e. technological possibilities of the used equipment, tooling and program control. It in main restriction on a mass of collected units, their overall dimensions, number of component details (no more than 20-30 pieces), absence of flexible details or made from soft materials, significance of some parameters of quality (exactitude, productivity, cost price), character of assembly movements.

As milestones of development robot's of technological assembly process it is possible to consider: a selection of assembly units, their grouping, classification of surfaces and conjugations, analysis of adaptability to manufacture of a construction of units, unification of constructional elements, analysis and development of specifications, technological analysis of a construction, choice of methods of assembly of conjugations, maintenance of a required the exactitude, development of a route of assembly process for the dimensional analysis, development of technological operations, actigrams of assembly and control programs for robots, feasibility report.

For want of development of technology robots of assembly the highest degree of concentration of operations is used, for which maintenance the necessary grabs, technological equipment and execution time are selected. For reach of number of items should be minimum. However upper bound of a degree of concentration of operations is the parameters of reliability and cost of the assembly robot with technological tooling [4]. Further such elements of assembly operation as submission of details, their

automatic orientation, interface, fixing, monitoring and pick up of the assembled unit in details are considered. For this purpose the necessary standard and original systems are selected. For reach that even at these stages the further improvement of a construction of collected details both units on adaptability to manufacture and correcting of groups of objects, collected on robots is conducted. As most effective are consider varied program resetting-up assembly systems of a modular construction. Final stage is the feasibility report of the designed assembly technology will be evaluation of competitiveness.

To indications of competitiveness of assembly processes can be referred: high technical characteristics and parameters of quality of assembly and low production costs. For reach of such evaluation we can use a method of a ratio of parameters of process to base variant or to conduct an evaluation on an integrated rate of competitiveness [5]. In most cases is inherent in the first method some indeterminacy. The integrated parameter of a technological level settles up as $A_T = \sum_1^n a_i f_i$, where a_i - weight factor i parameter have been assigned to the expert; n - number of such parameters; f_i - parametrical index. Such parameter on economic parameters is similarly determined A_E. Then the integrated rate of competitiveness assembly robots of process is determined from expression

$$A_\phi = A_T \Big/ A_E = \sum_1^n a_i f_i \Big/ \sum_1^n a_i^* f_i^* . \qquad (1)$$

For reach of $A_\phi > 1$ the assembly process exceeds analog on competitiveness and on the contrary. For reach of negative outcomes the assembly process is subject redesigning.

SHAPING OF ASSEMBLY MODULES

It is possible to approach construction such modules as were specified point of view from the point of view of maximum use of technological possibilities of assembly robots, i.e. assembly movements executed by them. In a general view such robot can be p of coordinate systems (Fig. 1) each of which can be executed till three linear and attitudes. The total is noted of executed movements by a rectangular matrix

$$D = \begin{vmatrix} x_1 & y_1 & z_1 & \alpha_{x1} & \beta_{y1} & \xi_{z1} \\ x_2 & y_2 & z_2 & \alpha_{x2} & \beta_{y2} & \xi_{z2} \\ . & . & . & . & . & . \\ x_p & y_p & z_p & \alpha_{xp} & \beta_{yp} & \zeta_{zp} \end{vmatrix}, \qquad (2)$$

there x_i , y_i , z_i – linear transitions of elements of the robot concerning coordinate; $\alpha_{xi}, \beta_{yi}, \xi_{zi}$ - that, angular; p – number of coordinate systems of the robot. Actually of such movements in robots the small amount is executed, so for shown in Fig. 1 of the robot the matrix of executed movements has a simple kind

$$D_R = \begin{vmatrix} & & & \xi_{zo} \\ & & & \xi_{z1} \\ & z_2 & & \\ & z_3 & \beta_{y3} & \xi_{z3} \\ y_6 & & & \end{vmatrix}. \qquad (3)$$

As the assembly movements are executed motor-operated hand of the robot it is better to emanate from a transformation matrix i^{-n} of a link circumscribing it a position in an initial frame of the robot

$$S = \begin{vmatrix} (BC)_x & B_x & C_x & P_x \\ (BC)_y & B_y & C_y & P_y \\ (BC)_z & B_z & C_z & P_z \\ 0 & 0 & 0 & 1 \end{vmatrix}, \qquad (4)$$

in which second column B describes a vector of orientation, C – vector of the approach and P – vector position of a point P_i motor-operated hand.

Thus in one coordinate system of the assembly robot the various movements can be executed which set can be expressed by a ratio of association
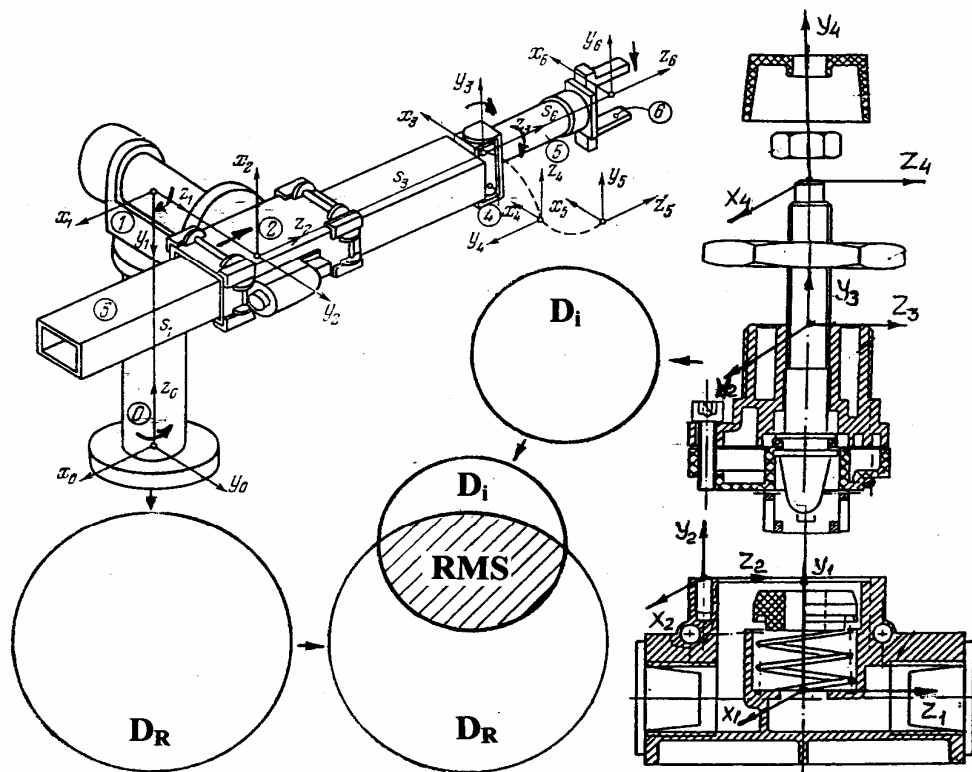

Fig. 1. Shaping of a set assembly movements of the robot and assembly unit.

$$d_1 = x_1 \bigcup y_1 \bigcup z_1 \bigcup \alpha_x \bigcup \beta_y \bigcup \xi_z \bigcup l \bigcup \vartheta = \bigcup_1^a d_i, \qquad (5)$$

there l, ϑ - additional special transitions and rotations for example vibrating, discontinuous, trajectory auto search etc., indicated for a completeness of a spanning; a – their amount. Then it is possible to present the previous formulas (2, 3) as

$$D_R = d_1 \bigcup d_2 \bigcup ..... \bigcup d_p = \bigcup_1^p d_i, \qquad (6)$$

i.e. each robot can be described as a system, in which there is a possibility to execute the certain linear, angular and special movements. Selection will require if some group of movements for example for analysis it also rather simply to execute in an outcome of additional operations above appropriate sets. The image of some set can be obtained with the help of circles of the *Euler* [2] (Fig. 1).

The similar approach is applied and for reach of analysis of assembly movements of object robot's of assembly, i.e. assembly unit, that is a basis for correct installation of group of collected units on the robot and selected for this purpose. In general view the typical representative group of units also can have p^* coordinate systems (fig.1), in each of which is necessary to execute a number of linear, angular and special movements, that can be noted by similar matrices (2, 3, 4) and equations (5, 6). Finally, the necessary assembly movements for a unit are noted as

$$D_j = d_1^* \bigcup d_2^* \bigcup .... \bigcup d_p^* = \bigcup_1^{p^*} d_j, \qquad (7)$$

Graphical it is represented by the circles of the *Euler.*

Thus, technological robot's the module of assembly process is represented as intersection of final sets of the robot and assembly unit

$$RMS = D_i \bigcap D_j = (d_{p1} \bigcup d_{p2} \bigcup ..... \bigcup d_{pk}) = \bigcup_1^k d_i, \qquad (8)$$

there d_{pi} – *a*ssembly movements, which can be executed by the robot and are necessary for assembly of a unit. The executed assembly movement robot's by the module answer the shaded area of intersection of the considered sets. Technological robot's the module with the indicated assembly movements also will have maximum concentration of such movements may be will be optimum on a criterion, for example, cost costs.

The approaches to solution and this problem can be the further analysis of the indicated equations of sets. There are starting up some robots with the executed assembly movements (Fig. 2) which together with technological equipment are characterized by the various costs. On the other hand, there is also number of collected units requiring for assembly those or other assembly movements.

As it is visible from a Fig. 2, the areas of intersection of the indicated sets can be rather various. The broad possibilities are opened for search of optimum solutions on various criterions. So view from the point of view of deriving the greatest area of intersection for example for unit K_1, the robot R_1 is most approaching for fulfillment robot's of assembly. If cost of the robot R_2 will be smaller, it can be selected for a realization of assembly process, but for reach of structure robot's of the module will be already other. To improve the position it will be possible

Fig. 2. The product of sets assembly movements of various robots and assembly units

expense of correcting group of units for assembly, modification of the typical representative of group etc. For this purpose the composition of objects, putting in the correspondence to pair of objects of operands (robot and assembly unit) third object - composition, i.e. robots the module of assembly can be used
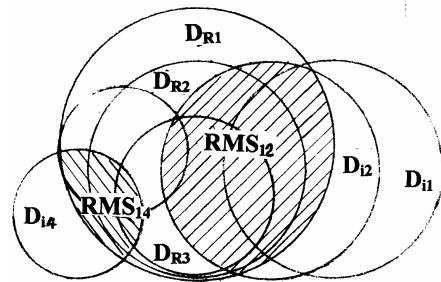
$$D_i \perp D_j = RM S, \qquad (9)$$

There are corresponds matrix and columns of grouped and it allows rather simply to reconsider more number of objects of assembly units using known rules of the sum and product, formula of inclusion and elimination, recurrent ratio and generating function that especially it is important for a simple visual solution of this practical problem: shaping robot's of the assembly module.

SUMMARY

Technological assembly robot's modules representing a basis of modular technologies on assembly robots can be rather simply at the first stage generated on a criterion of a maximum of assembly movements. For this purpose the sets of possible assembly movements on the robot and necessary - for the typical representative of group collected units are composed with use of the theory sets. The intersection of these sets also determines a structure robot's of the module. For reach that the broad practical possibilities for the reasonable selection of group collected units and choice of the assembly robot most answering definite conditions are opened.

REFERENCES

1. Bozhidarnik V., Grigorjeva N., Shabaykovitch V.: *Automatic assemblage of article*. Lutsk, „Nadstir'ya", 2005. - 386 s. (in Ukrainian).

2. *Book of reference on industrial robotics: 2 books*. Translation from engl. Sh. Shofa. - M.: Mashinostroenie, 1990.-480+480 s. (in Russian).

3. *Machine building*. Book of reference. Technology of assembling at machine building. T III-5. Editor J.N. Solomencev. - M.: Mashinostroenie, 2001.-640 s. (in Russian).

4. Grigorjewa N.: *Scientific-technological foundations of elastic automatic -modular of article*. Lutsk, „Nadstir'ya", 2008. - 520 s. (in Ukrainian).

5. Kofman A.: *Introduction on applied combinatorial analysis*. Moscow: Nauka, 1975. 386 s. (in Russian).

Mikuláš HAJDUK
Matej ČIRIP
Marek SUKOP

Technical University in Košice, Slovakia

PLANNING AND CALCULATION OF TRAJECTORY OF HUMANOID ROBOT MOTION

This paper describes the basic principles of kinematic structure design for biped walking robots and also provides a description of planning the movement trajectory for a particular construction of two-legged walking robot. The aim of this work is the creation and description of the principle of mathematical model of biped robot's movement and its correct mathematical interpretation for other using in electronics.

1. INTRODUCTION

In recent years the designers have began to focus mainly on the walking systems in design of the service robots. Major advantages of such systems lay in the fact that they are not limited by the height of the wheel diameters while overcoming the obstacles and they possess improved terrain adaptability for the highly demanding conditions. Versatility and terrain adaptability is limited up to certain level due to the complexity of the walking principle and the control of robot movement alone. The paper deals with a concrete solution to the issue of principle and a mathematical model for calculating the movements of the proposed two-legged walking robot.

2. KINEMATIC AND CONSTRUCTION DESIGN OF LEGS OF ROBOT MC - 01

When designing the kinematic structure of legs for bipedal walking robot constructed according to human as model, it is necessary to take into the account the fact up to which level we wish to imitate the human walk and to simplify accordingly the actual kinematics of the biological model [1].

We reduced the proposed kinematical structure of the model of lower extremities of robot shown in Fig. 1a into the mechanism with 12 degrees of freedom of movement.

The hip joint possesses 3˚ of movement freedom in all planes of robot body with the axis of rotation intersecting in one common point. This joint operates as the ball hip (spherical) joint. Knee joint is realised with 1˚ of movement freedom. The ankle

joint has got 2° of movement freedom and may rotate with the foot so in sagital as frontal plane of the system, while axis of rotation intersect in common point.

Letters **Ji** (Joint) designate the individual joints in the kinematic structure, where:

       J1, J3, J5 form the spherical hip joint of the right leg

       J2, J4, J6 form the spherical hip joint of the left leg

       J7 is the knee joint of the right leg

       J8 is the knee joint of the left leg

       J9, J11 form two-axis joint of the ankle of the right leg

       J10, J12 form two-axis joint of the ankle of the left leg

a)   b)
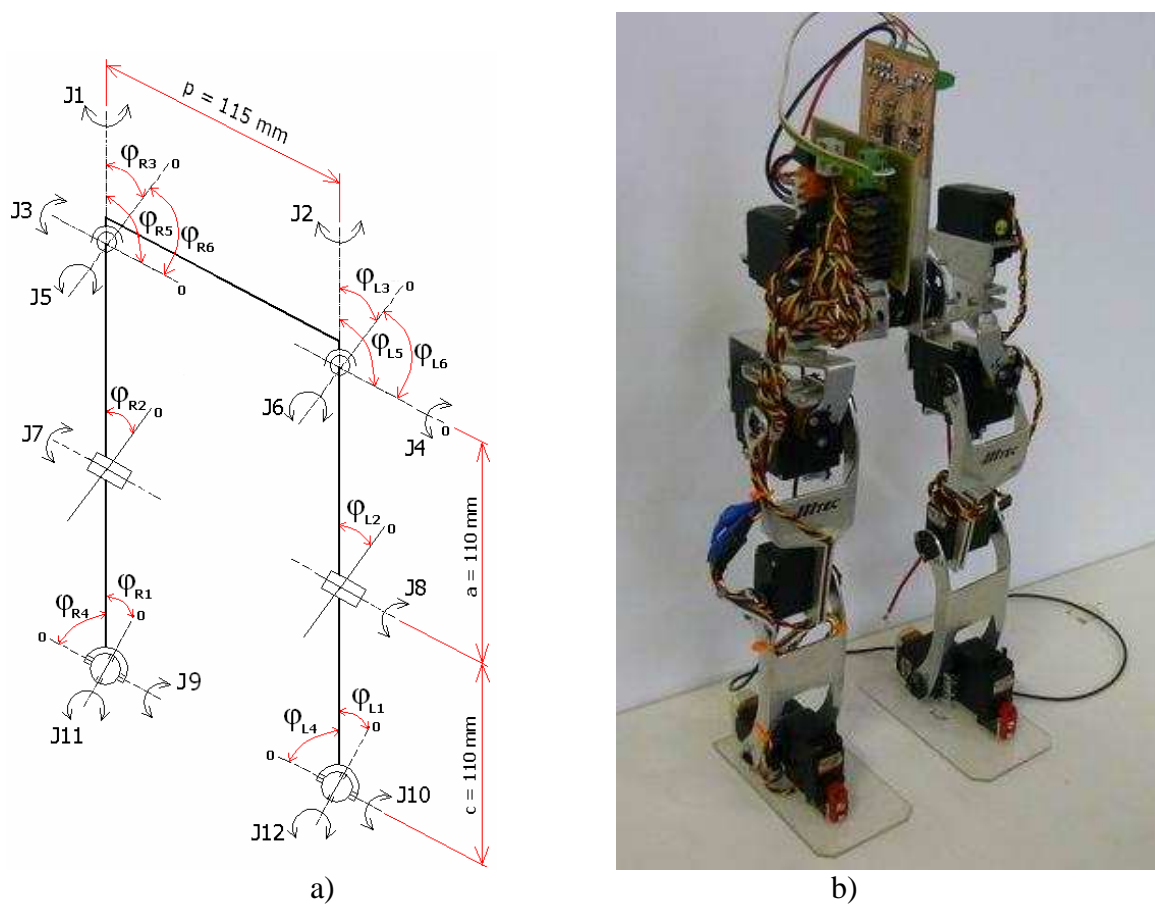
Fig. 1.: a) Kinematics of robot legs, dimensions b) functional model of the robot leg

    The proposed kinematical system is connected in the point of the hipbone by the flexible rubber elements, see Fig. 1b. These will partially absorb the inertial energy of the moving mass between robot legs and attenuate the unwanted oscillation transferred from one leg to other during the transferring phases of legs. This attenuating element is made of four rubber rotating bodies, which are pressed among five duraluminium plates. System of the flexible clutch of hip joints permits small attenuating movements only and changes the distance and mutual position of the right and left hip joint negligibly only.

Functional model of the lower extremities of two-leg walking robot is given in Fig. 1b. It was constructed at the Department of Manufacturing Technology and Robotics TU in Košice [3]. Functional robot is furnished with controlling and powering electronics to control the movement of twelve servo-motors.

3. PLANNING OF TRAJECTORY ON ROBOT MOVEMENT

The structure of walk of two-leg walking robot depends up to high degree on the complexity of applied kinematic chain of the given mechanism, i.e. mainly on the number of the degrees of freedom of robot movement.

Walking of biped humanoid robot consists of number sub-movements. If we want to direct the whole movement of robot so as to maintain stability in walking properly we need to know to plan each movement trajectory and also to correctly interpret mathematically for control purposes. In this paper it is shown a description of the partial movement of two-legged walking robot. Specifically in Fig. 2 shows the movement of carrying the robot center of gravity for over the left foot.
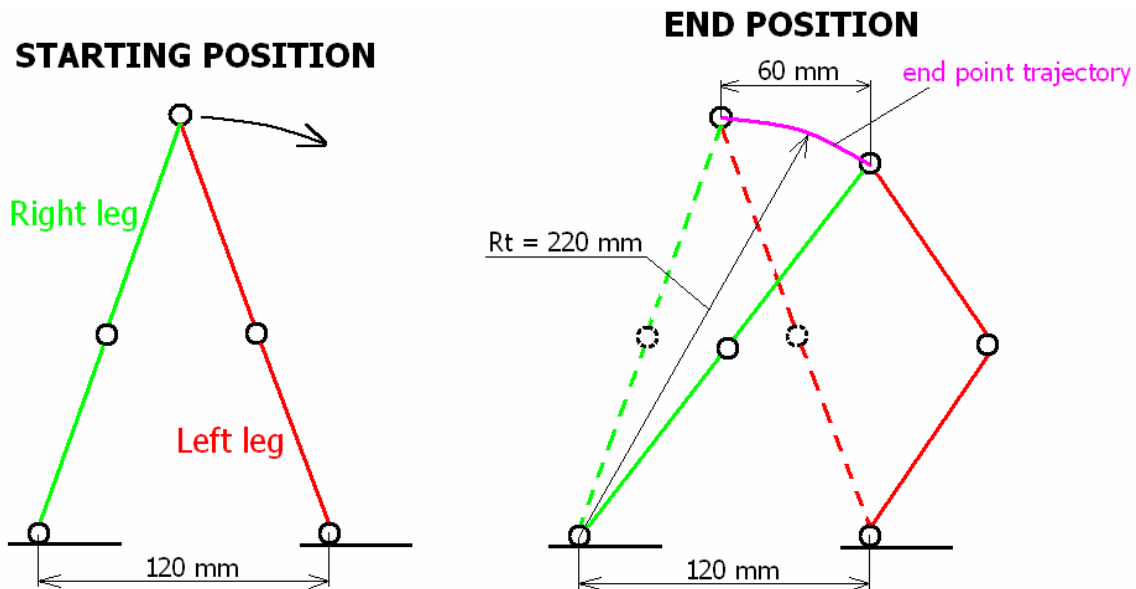
Fig. 2. Description of the planned trajectory of the robot movement

The movement of the robot outlined in Fig. 2 is made by joint in the sagittal plane of robot body. This is the reverse position of both hip joints of the foot supporting surface of the left leg in the vertical sight of sagittal plane. At this movement is changing its rotation five joints, namely **J3, J9, J4, J8**, and **J10** described in Fig. 1 and also the belonging angles φi are change their size.

4. MATHEMATICAL CALCULATION OF THE ROBOT´S LEG MOVEMENT TRAJECTORY

To calculate the individual robot movements within the space applied have been the calculations using the vector method of the inversion kinematics. Known are the parameters of the end element trajectories of the kinematic chain and applying the

goniometrical functions and cosine theorem calculated can be the angular displacement φ_i of the individual robot joints. Application of the vector method calculation of the angular co-ordinates significantly simplified the overall calculations of the robot movements and the drives control as well [2].

The length of the thighbone is a = 110 mm, length of calf bone is c = 110 mm and distance of the hip joint is p = 115 mm. The designation of the calculation angles needed for the drives movement and basic dimensions of the kinematic structure are given in Fig. 1a.

Calculation sample of trajectory movement using vector method is shown at hips movement in a circle with a diameter of Rt = 220 mm, which we described in Fig. 2. The hip joints are moving in a circle with a radius fall in Rt see Fig. 3, left leg bends in a knee and right leg at the knee remains stretched. Control variables for the total calculation of joint steering angle φi is the length of p = (0-60) mm crossed by hip joints in the axis x.
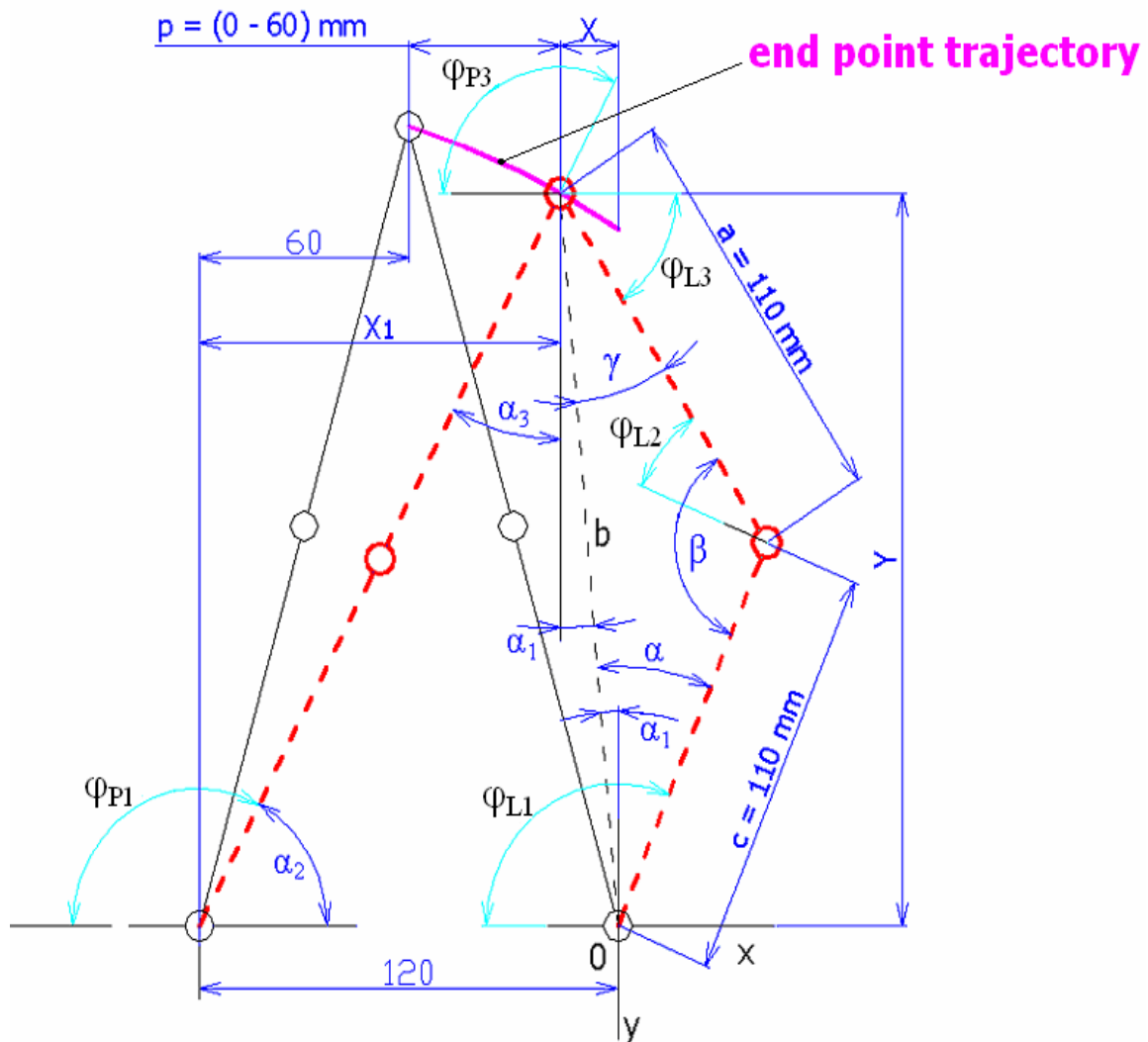

Fig. 3. Graphic representation of the joint on selected movement trajectory

Based on Fig. 3 for the co-ordinates of the ankle joint position hold equations

106

$$X_1 = 60 + p \; ; \qquad X = 60 - p \; ; \qquad Y = \sqrt{(a+c)^2 - X_1^{\,2}} \tag{3.1}$$

For the created triangle with sides X, Y, b according to Fig. 3 holds equation

$$b = \sqrt{Y^2 + X^2} \tag{3.2}$$

For the triangle with the sides a, c, b holds according to Fig. 3 cosine theorem and following out relations for the individual angles α, β, γ

$$\alpha = \arccos\left(\frac{b^2 + c^2 - a^2}{2 * b * c}\right) \quad \beta = \arccos\left(\frac{a^2 + c^2 - b^2}{2 * a * c}\right) \quad \chi = \arccos\left(\frac{a^2 + b^2 - c^2}{2 * a * b}\right) \tag{3.3}$$

For the auxiliary angles α_1, α_2, α_3 hold:

$$\alpha_1 = \arccos\frac{Y}{b} \; ; \qquad \alpha_2 = \arccos\frac{X_1}{a+c} \; ; \qquad \alpha_3 = \arccos\frac{Y}{a+c} \tag{3.4}$$

For the angles of the drives rotation of right leg according to Fig. 1 and Fig. 3 hold equation

$$P_1 = 180 - \alpha_2 \; ; \qquad P_3 = 90 + \alpha_3 \tag{3.5}$$

For the angles of the drives rotation of left leg according to Fig. 1 and Fig. 3 hold equation

$$\varphi_{L1} = 90 + \alpha - \alpha_1 \; ; \qquad \varphi_{L2} = \beta - 90 \; ; \qquad \varphi_{L3} = 90 - \chi - \alpha_1 \tag{3.6}$$

Main objective of the calculations is to determine the angles of the individual joints rotation designated in Fig. 1 and Fig. 3 as φ_i. Relations for the individual angles calculations are based on the positioning of the local co-ordinate systems in Fig. 1. The size and alternation of angles depend on the selected trajectory, along which the individual parts of robot move. These generalised angles are following their value calculation directly implemented into the controlling electronics of robot, which rotates the individual drives into the correct positions accordingly.

5. CONCLUSION

The aim of this contribution was a description of the locomotor system proposal to the biological basis of human beings. We are the problems the application of different movements on a kinematic structure presenting with 12 degrees of freedom of movement, which are designed to optimize the movements of the robot walking. After the planned path of movement that we want the robot to achieve the necessary mathematical describing those movements. The mathematical description is important

for the further use of these data on steering angles to achieve the best possible management of the overall movement of the walking robot.

REFERENCES

1. Živčák J. et al.: *Základy bioniky a biomechaniky*. Grafotlač Prešov, 2004.

2. Smrček, J., Kárnik, L.: *Robotika. Servisné roboty. Navrhovanie, konštrukcia, riešenie*. Edícia vedeckej a odbornej literatúry SjF TU v Košiciach. Vydavateľstvo Vaško Prešov. Košice 2008.

3. Hajduk M., Sukop M., Vagaš M., Čirip M.*: Humanoid robot for robosoccer*. Acta Mechanica Slovaca. - ISSN 1335-2393. - Roč. 13, č. 2-A, 2009.

Andrey V. ILCHENKO
Elena V. ZABASHTA
Vladimir A. LOMAKIN

Zhitomir State Technological University, Ukraine

A FLYWHEEL OF VARIABLE MOMENT OF INERTIA

A new construction of a flywheel of variable moment of inertia of the internal combustion engine is offered.

INTRODUCTION

A flywheel is usually called a massive rotary disk, which is used as a kinetic energy accumulator. That's why they are widely used in cars, having irregular entering or usage of energy.

Descriptions of flywheels are known from medieval literature; the variety of a flywheel can be considered a well – known from ancient times pottery wheel.

With the beginning of industrial revolution flywheels were used in different mechanisms: stationary and movable.

ANALYSIS OF PUBLICATIONS

It is known that at car's operation regime some irregularity of its movement is observed [1]. These fluctuations and the reasons that cause them are determined as internal vibration activity of a car. To estimate velocity fluctuations at movement regime relative value, called a coefficient of average speed change [1] or a coefficient of non-uniformity of movement, is used δ [2, 3].

To reduce rotational irregularity a flywheel must be installed. The bigger the flywheel the less is the coefficient of non-uniformity of movement. But the application of such simple method leads to extra increase of flywheel mass, reduction of speed characteristics of an engine, impairment of its start conditions, etc.

STATEMENT OF RESEARCH TASK

The task of the given research is the development of a construction of the internal combustion engine flywheel which ensures a given fluctuation level of rotation frequency with regard for change of a moment of inertia of crank-connecting rod mechanism (CCRM).

A FLYWHEEL OF VARIABLE MOMENT OF INERTIA

Let's consider well-known constructions of flywheel of variable moment of inertia and their usage in internal combustion engines (ICE).

There is a flywheel of variable moment of inertia (VMI) [4] with a hollow chamber like a truncated cone, filled with magnetic working substance. A stationary magnet is attached on a lesser base of chamber cone. In time of rotation of the flywheel a working substance under the action of centrifugal forces which exceed magnetic forces, directs to the bigger chamber base, increasing moment of inertia of the device. So, construction ensures good conditions of internal combustion engine start, because in the time of rotation of a crankshaft by a starter, crankshaft's resistance to rotation is minimum.

If ICE is started, its rotational frequency increases quickly and a moment of inertia of a flywheel also increases. The short-coming of such construction is control of a flywheel of variable moment of inertia only by change of its rotation frequency, that reduces the opportunities of change of moment of inertia and limits the speed of its change, because it is impossible to regulate attractive force of a stationary magnet, and this attractive force considerably attenuates with the increase of a distance. High accuracy of a change of a moment of inertia is not also provided, because the moment of inertia control takes place only due to slowing-down or acceleration of the flywheel.

There is also a flywheel of variable moment of inertia [5] which has a hollow chamber like a system of uniaxial truncated cones. As in previous case, the chamber is filled with magnetic working substance. On the bases of the hollow chamber there are the first and the second electrical magnets of alternating current, which are controlled by electronic unit. There is a sensor of working substance position in the construction. The sensor provides the electronic unit with information about the current value of a moment of inertia of a flywheel. Such construction allows to change the moment of inertia not depending on rotation frequency of the engine shaft, but it can't ensure quick change of a moment of inertia of a flywheel.

Bulkiness of the construction at increase of the range of change of moment of inertia and impossibility of change of the moment of inertia during revolution limit the usage of such construction in the internal combustion engine. Original construction of a variable flywheel mechanism for internal combustion engine is offered in [6]. Moment of inertia depends on position of weights which are fastened on arms, rigidly attached to planetary gears. Planetary gears mesh with the sun gear, which is linked with the crankshaft of the internal combustion engine. Such construction allows at idle movement to increase to maximum a movement of inertia, and in this case the unevenness of rotation frequency considerably reduces, which is maximum at such régime. At increase of rotation frequency of the internal combustion engine weights move closer to rotational centre of the crankshaft, and a moment of inertia reduces. As weights can move very close to the rotational centre a flywheel moment of inertia strives to minimum value. This allows the internal combustion engine to accelerate quickly. At reduction of rotation frequency the process repeats in reverse order.

However, such constructions doesn't take account of necessity of change of a flywheel moment of inertia during revolution [7] and impedes the starting of the engine, because at low revolution frequency of the shaft by the starter a flywheel

moment of inertia is maximum. Inertia forces of resistance to shaft acceleration are increased.

A construction of the flywheel which corresponds to the demands of the internal combustion engine operation is offered by the authors. A variable flywheel mechanism contains a mechanism 20 of change of moment of inertia, switching clutch mechanism 40 and mechanism of periodic change of moment of inertia (Figure 1).
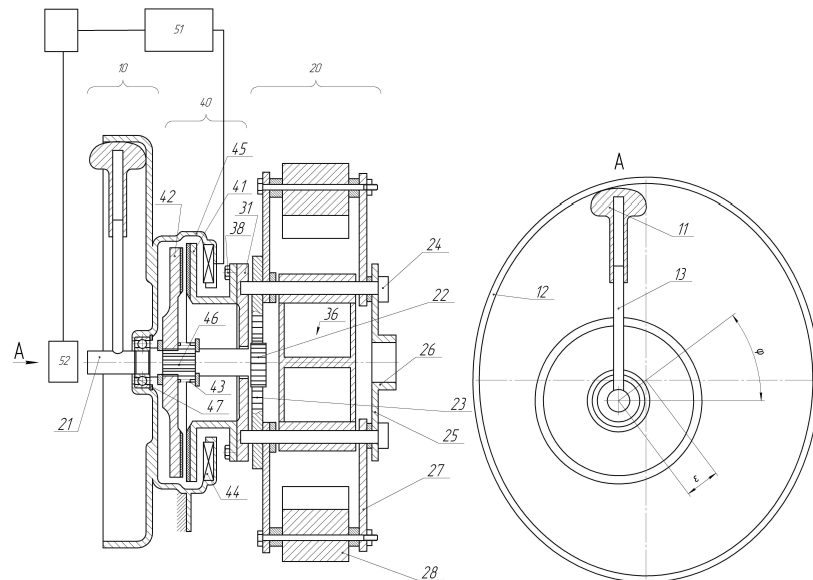

Fig. 1. General form of a flywheel of variable moment of inertia.

The variable flywheel mechanism 20 has a sun gear 22 connected to an output shaft 21 of an engine, one or two multiple planetary gears 23 that mesh with the sun gear 22, one or multiple carrier shafts 24 for rotatable supporting the planetary gears23. The variable flywheel mechanism also has one or multiple arms 27, which are swingably mounted on the carrier shafts 24, and which are swung by the planetary gears 23. There are one or multiple elements 36 in the construction. Their shape is like weights 28, which are placed near rotational centre of the output shaft of the internal combustion engine. Elements 36 include weights 28 which are mounted on arms 27 at a minimum moment of inertia of a flywheel. The switching clutch mechanism 40 is composed of a stationary clutch plate 41 fixed to the shaft and support plate 21 with bolts 38, a movable clutch plate 42 disposes to face the stationary clutch plate 41. The flywheel apparatus10 contains a stationary hollow chamber in the form of a straight cylinder, which has an ellipsis in its base. The ellipsis centre may not be on the rotational centre of the output shaft 21 of the internal combustion engine. In this case its position will be characterized by a value of eccentricity ε and angle φ.

In fixed hollow chamber 12 there are one or multiple links 13, which are connected with the output shaft 21 of the engine in perpendicular plane. On link 13 there is a bearing 11. The number of links is 13, their reciprocal arrangement, the weight of bearings 11, parameters of ellipsis, which is in the stationary chamber 12, the quantity of eccentricity ε and angle 4 are selected individually for reproduction of the given law of change of the moment of inertia. To reduce friction force the bearing 11 may contain pivotable bearings.

During engine 52 operation at idle stroke weights 22 are removed from rotational centre, switching clutch mechanism 40 is turned on, and so sun gear 22, planetary gears 23, arms 27 and weights 28 are blocked from displacements. In this case moment of inertia of a flywheel is maximum.

When the engine 52 is accelerating (slowing) the control device 51 switches off the current at electromagnet coil 44, switching clutch mechanism 40 is turned off and a sun gear 22 stars to revolve, revolving planetary gears 23. At acceleration (slowing) of the engine 52 the revolution frequency of planetary gears 23 that leads to approach (removal) of weights 22 to rotational centre of the output shaft 21 of the engine. At switching off of the engine 52 the control device 51 turns off the switching clutch mechanism 40.Owing to the revolution of a sun gear 22 and planetary gears 23 weights 28 through arms 27 displace to the nearest to the rotational centre position. Then a switching clutch mechanism 40 is switched on and only after that the engine 52 switched off. This provides minimum resistance of the flywheel at engine starting. At all operation regimes of the engine 52 at revolution of the output shaft 21 the link 13 with a bearing 11 also revolves. Owing to centrifugal forces the bearing 11 moves along link 13 till it starts touching the walls of a stationary cylinder 12. When the link 13 is revolving the bearing 11 is moving along it, constantly touching the surface of the stationary cylinder 12. A moment of inertia of the device changes during revolution at all operation regimes of the engine.

CONCLUSION

The construction of the flywheel of the internal combustion engine, which provides easy start, low level of fluctuation of revolution frequency, good parameters of acceleration capability in comparison with the existed constructions of the flywheels of variable moments of inertia, is offered.

REFERENCES

1. Тарабаріна В. Б.: *Курс лекцій з теорії механізмів і машин МГТУ*. [електронний ресурс]: – Режим доступу до матеріалів.: http://tmm-mk.bmstu.ru/lectures/ lect_8.htm – Назва з екрану.

2. Абрамчук Ф.І., Гутаревич Ю.Ф., Долганов К.Є., Тимченко І.І. – К.: Арістей.: *Автомобільні двигуни: Підручник*. 2007, 476.

3. Колчин А.И.: *Расчет автомобильных и тракторных двигателей*. М.: Высшая школа, 1980. 400 с.

4. Шустер Л.Ш., Волкова Л.А., Сафонов А.В.: *Маховик переменного момента инерции*. Патент РФ № 2147700, МПК F16F15/30. № 98113483/28; Заявл. 1998.07.14; Опубл. 2000.04.20, Бюл. № 25.

5. Богословский С.В., Павлов С.Н.: *Маховик переменного момента инерции*. Патент РФ № 2 265 761, МПК F16F15/31. № 2004113587/11; Заявл. 30.04.2004; Опубл. 10.12.2005, Бюл. № 34.

6. Kimura Y., Tsuboi T., Endoh T.: *Variable Flywheel Mechanism and Flywheel Apparatus*. Patent Application Publication United States US 2007/0179012 A1, МПК F16H57/08. № P2006-022445; Filed 31.01.2006, Publish 02.08.2007 Appl. № 11/699,368.

7. Ільченко А.В., Ломакін В.О.: *Моделювання роботи поршневого двигуна внутрішнього згоряння за нерівномірністю ходу*. Вісник Донецького інституту автомобільного транспорту. – 2009. №3. С.14-18. Бібліогр.: с. 3.

Daniel JANKURA

Technical University in Košice, Slovakia

RESEARCH OF THE STRUCTURE AND ADHESIVE PROPERTIES OF CERAMIC COATINGS

The paper presents the research results of adhesive properties of plasma sprayed ceramic coatings on Al_2O_3 and $ZrSiO_4$ base in tribological couples with 19 436 and 12 050 materials and polyamide. Ceramic layers are formed by three types of particles that differ, from each other in form and compactness. Non-compactness in the structure of the layer degrades its properties and it is possible to divide it into voids, pores, branched cracks and large particles. Among the investigated ceramic Al_2O_3 and $ZrSiO_4$ based coatings the Al_2O_3 coating showed the best properties under adhesive wear conditions; this material, mainly in combination with 19436 material, is suitable for friction nodes. The wear value is in accordance with the course of the friction coefficient of the investigated tribological couples. The wear value is connected with the surface hardness of materials in the friction couple. The ceramics-polyamide couple appears to be high-prospective, since it shows a low friction coefficient and minimum wear and seizure tendency.

INTRODUCTION

Specific physical and chemical properties of ceramic materials predetermine them for application under extreme loading conditions. Ceramic materials show, in comparison with classical engineering materials, better properties mainly under thermal loading conditions, as well as better corrosion resistance, wear resistance, etc. One of possible technical applications of ceramic materials is the formation of ceramic coatings on metal structural (engineering) parts. Plasma spraying of powder ceramic materials is the basic production technology of such layers. Considering the heat capacity and the temperature, plasma spraying is a very suitable technology [1, 2, 3].

The major advantages of the plasma spraying process, which enable its relatively universal utilization, include:

- A significantly wider range of sprayed materials (from high-melting metals, oxides, alloy combinations up to plastics),
- A negligible heat effect on the basic material (200°C), which guarantees the dimensional and structural stability of the substrate and makes it possible to use its diversity, i.e. metals, alloys, ceramics, concrete, wood, graphite, etc.,
- A possibility to form coatings at micron to millimetre thicknesses on small, as well as large areas,
- A high spraying output, especially when water-stabilized plasma units are used,
- Simple operation of plasma equipment [4].

For spraying powder materials and welding with powder filler materials, a wide range of various types of equipment is used all over the world. Plasma spraying equipment consists of a set of individual apparatuses and devices. A plasma torch is a powerful spraying unit. In dependence on the method of plasma formation in the torch, plasma torches can be divided into non-transferred arc torches, transferred-arc plasma torches and combined torches.

According to the sprayed material type, torches can be constructed for wire spraying or powder spraying. The advantage of wire spraying is a higher purity of wire and, as a result, a higher purity and quality of the sprayed layer. The advantages of powder spraying consist in a wider selection of powder, even among materials that cannot be produced in the form of wire, such as high-melting materials, oxides, carbides, etc.

According to the stabilization medium, there are water-stabilized and gas-stabilized plasma torches. In the gas-stabilized torches, the influence of parameters is much more complex. Besides the current, the voltage and the rate of the plasma jet, also the quantity of the fed plasma, focusing and protective gas, the shape and design of the orifice, the nozzles and the diameter of the tungsten electrode play an important role. By increasing the current, the plasma temperature and electric conductivity increase. Gases have a great influence on the thermal relations of plasma [5].

Basic experimental research of the water-stabilized arc was conducted at the beginning of 1960s. A commercially manufactured water-stabilized plasma torch consists of a specially shaped arc chamber, a rotary cooled anode and a consumable graphite cathode. A schematic picture of the arc chamber is shown in Fig. 1. The chamber is divided into several sections by the baffles with central holes. Water is injected tangentially into the sections where the vortex is created. The anode made of a copper disc with internal cooling is located outside the arc chamber. The anode disc rotates to reduce strong electrode erosion in the atmosphere containing oxygen.
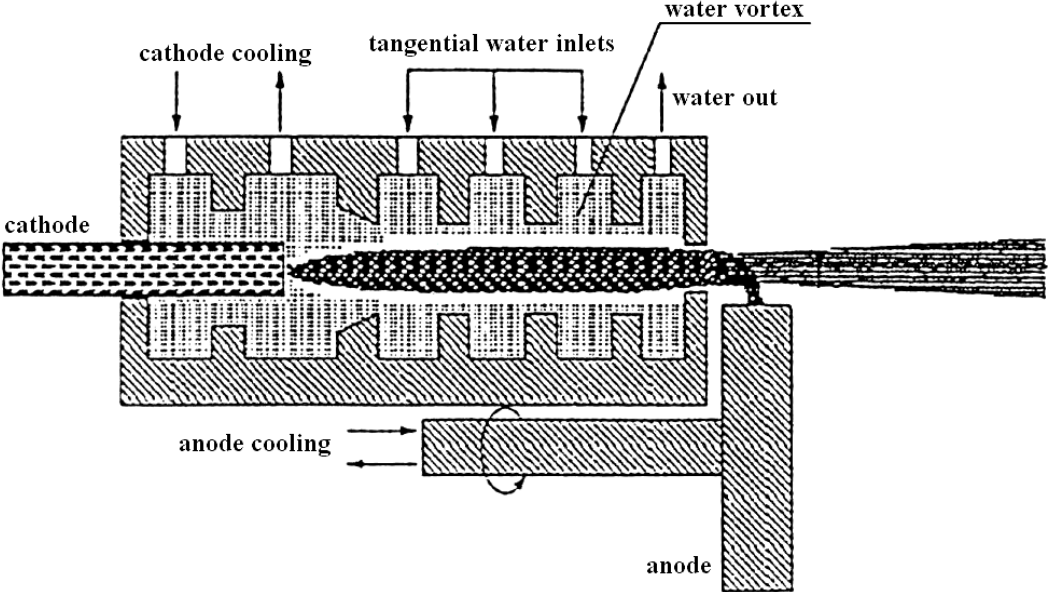

Fig. 1. Schematic picture of the arc chamber

Evaporation from the inner cylinder wall of water vortex surrounding the arc column is a principal mechanism that produces an arc plasma medium. The evaporation is induced by the absorption of a fraction of the total ohmic power of the arc. The ionized vapour inflows and its heating create an overpressure inside the arc chamber, which accelerates the plasma towards the exit orifice of the chamber. Thus, the arc properties are controlled by processes influencing the evaporation from the wall and by the radial transport of energy from the arch centre towards the walls (inner surface of the water vortex). The resulting properties of the generated plasma jet are strongly dependent on the used amount of arc current [6]. The plasma arc temperature achieves 25-30 000 K or more. The mechanism of formation and properties of hot sprayed coatings are also substantially influenced by technological parameters such as heat input, spraying distance, granularity of added material, etc.

The literature [7] presents the comparison of systems with water (LP) and gas (GP) stabilization of plasma.

GP: For high quality small area coatings using rather special and/or expensive spray materials;

LP: For large area coatings, production of free-standing shapes and for powder production (spheroidization).

The majority of applied ceramic based added materials consist of ceramic materials with a dominant portion of Al_2O_3, followed by the other oxides (Cr_2O_3, $ZrSiO_4$, ZrO_2, MgO, CaO, HfO_3, MoO_2), applied either in the pure condition or with various doping agents, and other chemical compounds (nitrides, borides, etc.) [8].

The paper presents the research results of adhesive properties of plasma sprayed ceramic coatings on Al_2O_3 and $ZrSiO_4$ base in tribological couples with 19 436 and 12 050 steels and polyamide.

TEST METHOD

Ceramic coatings were prepared using a plasma torch of the AC - 160 type with water stabilization of plasma and with the electric input of 160 kVA. Prior to spraying, the surface of samples was pre-treated by blasting with corundum grains with the grain size $d_{zk} = 0.9$ mm. The spraying distance was 350 mm. The thickness of sprayed coatings ranged from 180 to 220 μm.

For evaluation of the tribological properties of selected material couples, the surface roughness, the wear value, the seizure time and the friction coefficient were measured. The ceramic coating was applied to the face of samples with $\Phi = 20$ mm and the thickness of 12 mm, made of steel 11523. As counterparts, ring samples were used with the outside diameter $\Phi = 40$ mm, the inside diameter $\Phi = 40$ mm and the thickness of 10 mm, made of steel 12050, 19436 and polycrystalline thermoplastic polyamide PA6. Steel 12050 is structural carbon steel with 0.5% C and the hardness of 189 HV. Material 19436 is chromium tool steel – HV = 723, (Table 1).

Table 1. Used steels and their designation

STN Standard	DESIGNATION	EN STANDARD	DESIGNATION
STN 41 1523	11 523	EN 10025A1	S355J0
STN 41 2050	12 050	EN 10083-2	C45
STN 41 9436	19 436	-	X20Cr12

For spraying, ceramic Al_2O_3 and $ZrSiO_4$ powders were used. Al_2O_3 coatings show high hardness, low thermal conductivity, excellent heat resistance, corrosion resistance in molten materials and wear resistance at elevated temperatures. The mean powder particle size determined using screen analysis was $d_{z50} = 0.079$ mm. $ZrSiO_4$ coatings are corrosion resistant in molten metals, resistant against acid slag of non-ferrous metals, etc. The mean powder particle size was $d_{z50} = 0.029$ mm. After spraying, the samples were ground with diamond grinding wheels with various grain sizes. After grinding, multi-stage polishing with diamond pastes followed. The roughness of polished coatings was measured using Surftest SJ - 301– Tester [10, 11].

The determination of friction properties and wear was conducted using AMSLER tester. The coated sample and the counterpart (ring) are screwed on two parallel shafts. The ring rotates and is mechanically pressed onto the sample with a force that can be controlled in the range of 200-4000 N. The wear tests were conducted under dry friction conditions, with the pressing force of 250 N and the ring rotation speed of 200 rev.min.[-1] The friction coefficient was determined by calculation from the friction moment recorded by the apparatus. When measuring the wear value, the test was interrupted in regular intervals and the wear value was calculated based on the wear marks using mathematical formulas [12].

RESULTS AND THEIR DISCUSSION

The structure of the Al_2O_3 coating is shown in Fig. 2, 3. The surface of the coating is markedly heterogeneous and consists of individual disc-shaped splats. The particles (splats) are well-spread and form a smooth surface. Overheated melted particles form local lobes from which small oval or spherical particles were separated. On the surface of splats, various defects, such as voids and cracks, can be observed, which were formed due to dilatation stresses in the coatings during cooling. The $ZrSiO_4$ coating structure is similar to that of Al_2O_3 coatings, Fig. 4.

A real structure of ceramic coating is shown in Fig. 5. This is a typical structure of the sandwich type with a relatively small number of voids, pores and other structural defects.
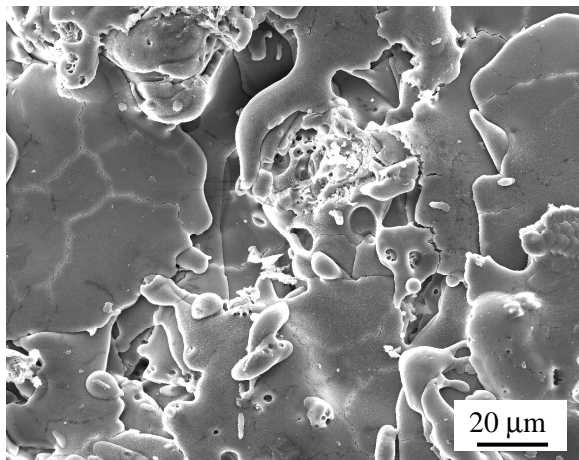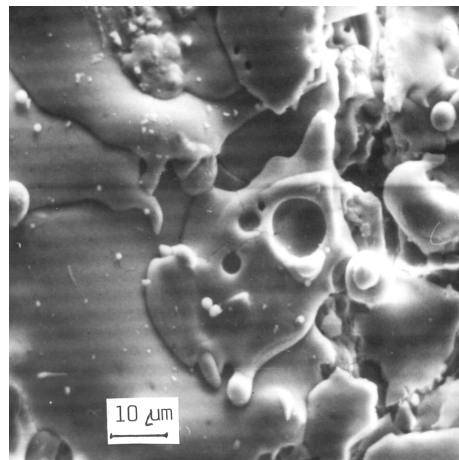

Fig. 2. Surface of the Al_2O_3 coating

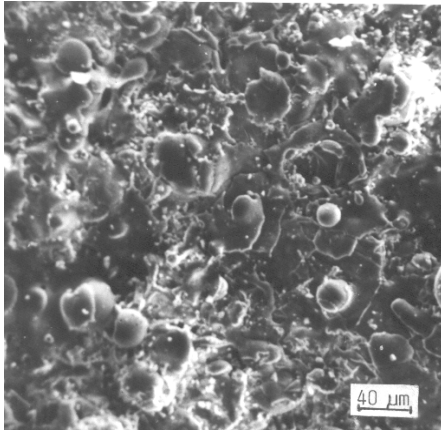Fig. 3. Surface of the Al_2O_3 coating
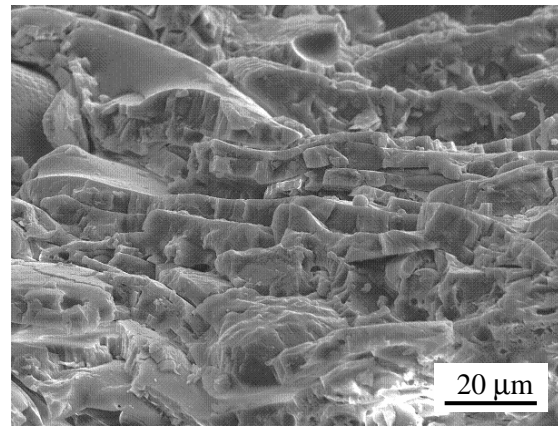
Fig. 4. Surface of the ZrSiO₄ coating

Fig. 5. Fracture surface of the ceramic coating Al_2O_3

Despite the fact that the added material is sufficiently plastic upon impact, structural defects may be found in coatings and these defects may be classified as follows:

- Discontinuities of the void type;
- Discontinuities of the pore type;
- Large ball particles, insufficiently melted;
- Cracked particles;
- Small ball particles on the coating surface.

A smoother surface was achieved for Al_2O_3 coating, which was also confirmed by the measured roughness values shown in Table 2.

Table 2. Roughness of coatings and its counterparts

Coating	R_a [μm]	R_m [μm]		Material	R_a [μm]	R_m [μm]
Al_2O_3	0.37-0.60	3.52-7.31		19436	0.45-0.60	2.10-2.90
$ZrSiO_4$	0.80-1.01	6.66-8.19		12050	0.43-0.65	3.70-5.95

The results of coating wear measuring are shown in Figs. 6 and 7. The wear of the $ZrSiO_4$-19436 couple shows higher values than that of the Al_2O_3-19436 couple. Fig. 8 shows the structure of the worn out $ZrSiO_4$ coating coupled with steel 19436. The surface is very articulated due to intensive fragmentation and taking-up of the grains from the coating. A slight grooving effect of these particles takes place, which results in the formation of a combined adhesive-abrasive type of wear, which increases the wear intensity.

In the ceramics-12050 steel couples, very intensive wear of coatings was recorded – down the basic material, which was higher than in the $ZrSiO_4$ coating. This increased intensity can be explained by a strong roughening of the relatively soft surface of 12050 steel (180 HV), the formation of micro-joints and the subsequent intensive taking-up of particles from the ceramic surface, despite checking the surface cleanness during the test. A grooving effect of these particles takes place, which leads to the formation of an adhesive-abrasive type of loading. The worn-out Al_2O_3 coating is shown in Fig. 9. The failure of coating takes place by fragmentation and taking-up of particles.
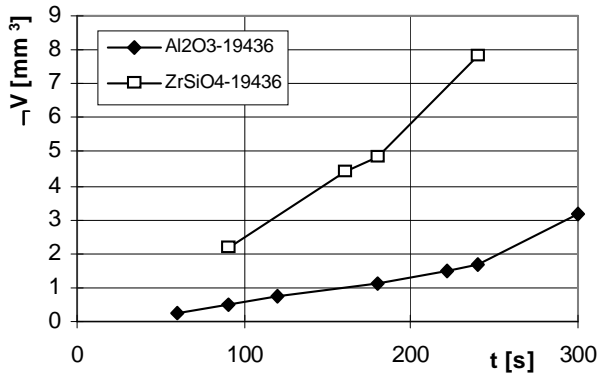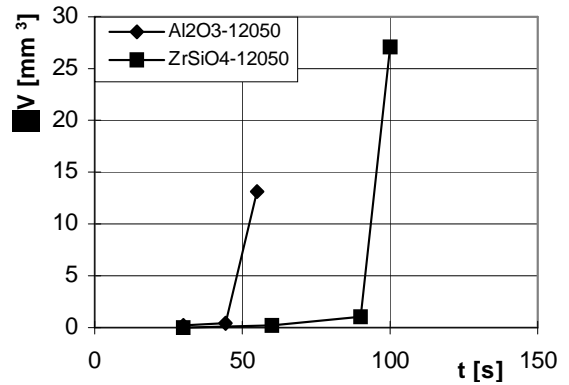
Fig. 6. Course of wear: ceramics-19436 steel

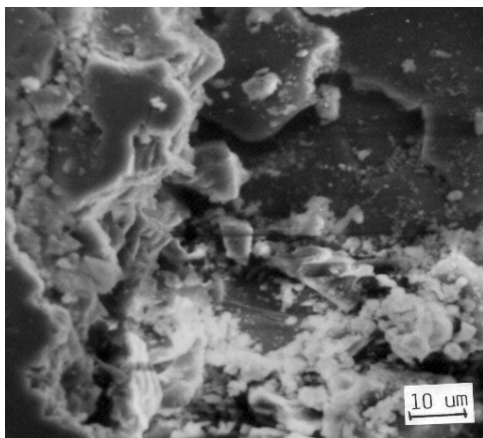Fig. 7. Course of wear: ceramics-12050 steel

Fig. 8. ZrSiO$_4$ coating detail after wear
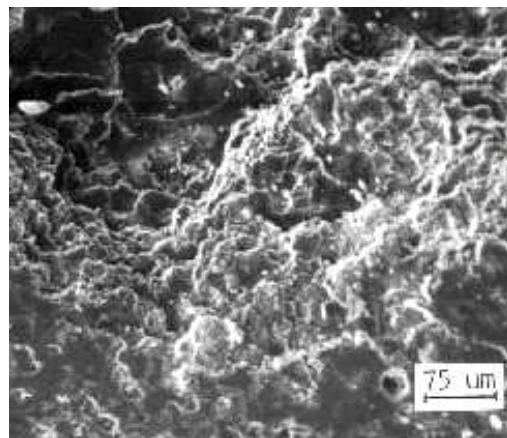
Fig. 9. Al$_2$O$_3$ coating after wear

The graphs of friction coefficient-time relationships for the tested tribological couples are shown in Figs. 10 and 11. They are characterized by various increments of the friction coefficient and various times to sample seizure (the last point in the graph). There is an evident difference between the ceramics-19436 steel friction couple and the ceramics-12050 steel friction couple. The different course of these curves for these friction couples corresponds to their wear value. This can be observed mainly in the ceramics-12050 couple, where a sudden increase of the friction coefficient within a short time interval takes place, which also resulted in increased wear intensity.

Fig. 10. Time response of friction coefficient

Fig. 1.1 Time response of friction coefficient

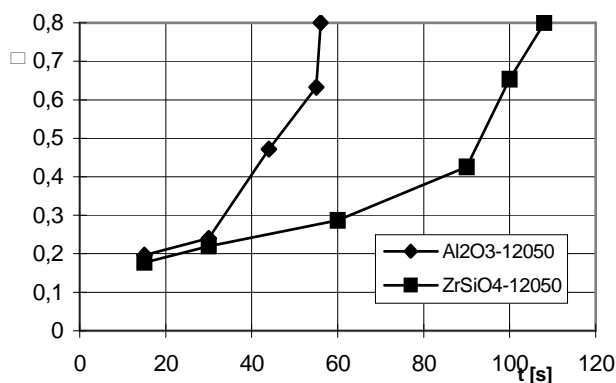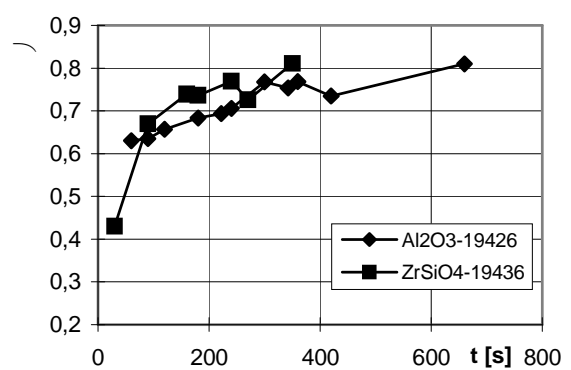In the tribological couple ceramics-polyamide, no marks of wear were observed even after 3 hours of machine running at the sample load of 800 N, therefore only the friction coefficient in dependence on load was determined for this couple. The results of these tests for the investigated tribological couples are shown in Figs. 12-14. The tests were conducted in the load range of 200-800 N. In the friction couples ceramics-12050 steel, the friction coefficients were only determined up to the load value of 400N. When the load was further increased, the samples seized within a few seconds and the record was confused due to great amplitude of the dynamometer. It results from the graphs that the best course of the friction coefficient was showed by the friction couple ceramics- polyamide, which had the longest and the smoothest running with a low increase of the friction coefficient. This couple shows a low bounding energy and high plasticity of polymer, which reduce the adhesive wear coefficient, prevent the development of plastic deformation and decrease the seizure tendency. The most adverse results were obtained for the ceramics-12050 steel couple.
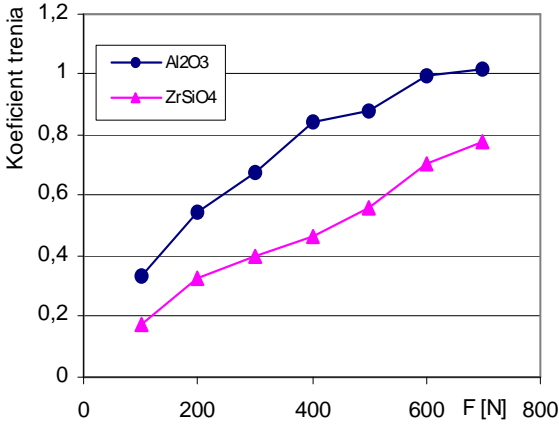
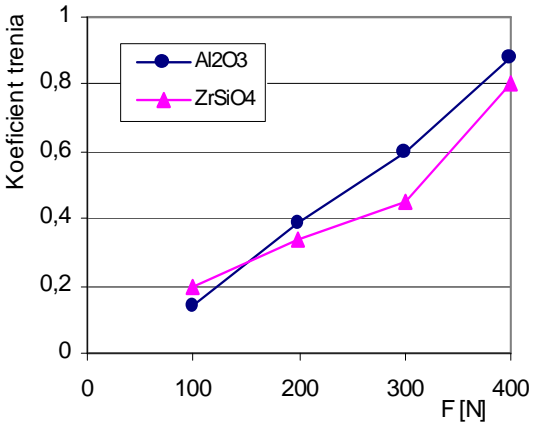Fig. 12. Course of friction coefficient depending on load of ceramics-19436 steel couple

Fig. 13. Course of friction coefficient depending on load of ceramics-12050 steel
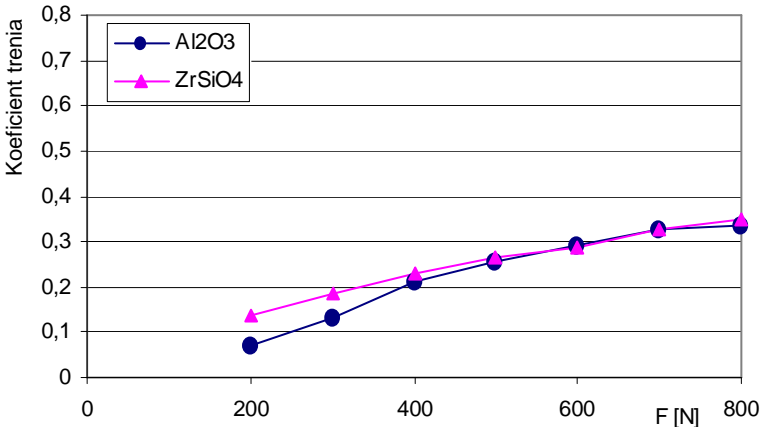
Fig. 14. Course of friction coefficient depending on load of ceramics-polyamide couple

CONCLUSIONS

1. Ceramic, sufficiently heated material produces relatively homogeneous coatings with few defects. Melted ceramic particles adapt well to the profile of the basic material or to that of the preceding layer. Discontinuities in the structure of the coatings may be divided into: voids, pores, cracks, small ball particles.

2. Among the investigated ceramic Al_2O_3 and $ZrSiO_4$ based coatings, in tribological couples with 19436 and 12050 materials, the Al_2O_3 coating showed the best properties under adhesive wear conditions; this material, mainly in combination with 19436 material, is suitable for friction nodes. The wear value is in accordance with the course of the friction coefficient of the investigated tribological couples.

3. The wear value is connected with the surface hardness of materials in the friction couple. In soft materials – 12050 steel – intensive wear of the ceramic coating surfaces takes place, which is connected with an increase of the friction coefficient and the subsequent taking-up of particles from the coating surface. These particles, with their grooving effect, change the adhesive wear process into a combined, adhesive-abrasive wear process.

4. The achieved results have shown that under the adhesive wear conditions the ceramics-polyamide couple appears to be high-prospective, since it shows a low friction coefficient and minimum wear and seizure tendency.

REFERENCES

1. Matejka D., Benko B.: *Plasma spraying of metal and ceramic powders*. Alfa, Bratislava 1988.
2. Chasuj A., Mogiraki O.: *Naplavka i napylenije*. Mašinostrojenije, Moskva 1985.
3. Suryanarayanan R.: *Plasma Spraying: Theory and Applications*. CNRS, London, 1993.
4. Chráska P., Dubský P., Kolman B., Ilavsky J., Forman J.: *Study of Phase Changes in Plasma Sprayed Deposits*. Journal of Thermal Spray Technology, vol. 1(4), 1992, pp. 301-306.
5. Krömmer W., Heinrich P.: *What is the meaning of technical gases under thermal spraying coatings*. In.: 16th workshop, Progressive technologies of surface treatments. ČVUT Praha, 2000, pp. 28-36.
6. Hrabovský M., Konrád M., Kopecký V., Sember V.: *Processes and properties of Electric Arc Stabilized by Water Vortex*. In.: Review of the literature related to water stabilized plasma and applications. IEEE TRANSACTIONS ON PLASMA SCIENCE, 25. No. 5, October 1977, pp. 833-839.
7. Chráska P., Hrabovský M.: *An Overview of Water Stabilized Plasma Guns and Their Applications*. In.: International Thermal Spray Conference & Exposition, Orlando, Florida, June 1992, pp. 81.
8. Matejka D., Pálka V., Benko B., Iinfner I., Koerten H.K.: *Applications of plasma spraying of metal and ceramic materials*. Welding, 44, No. 2, 1995, pp. 30.
9. Tech Plasty: *Polyamidy – vlastnosti materiálov*. Firemný katalóg, 2008.
10. Bačová V., Jankura D., Draganovská D.*: Influence of cyclic heat stress on the properties of plasma-sprayed ceramic coatings*. Metalurgija, 47, 2008, 2, pp. 125-128.
11. Kalendová A., Kalenda P., Čechalová V., Gojný J.: *The testing methods for coating*. Acta Mechanica Slovaca, 8, 2004, pp. 101-108.
12. Papcun P., Jankura D.: *Hodnotenie tribologických vlastností kompozitných povlakov na báze Al_2O_3*. Acta Mechanica Slovaca, 12, 4-B, 2008, pp. 215-220.

Ľuboš KAŠČÁK
Emil SPIŠÁK
Jacek MUCHA*

Technical University of Košice, Slovakia; *Rzeszow University of Technology, Poland

JOINING OF STEEL SHEETS FOR AUTOMOTIVE INDUSTRY USING PRESS JOINING METHOD

The paper deals with joining of steel sheets for automotive industry using press joining method. This method is a relatively new technique of car body sheets joining which is beginning to find its place in the automotive industry as an alternative to resistance spot welding, especially in joining materials of different qualities. Combination of two hot-dip galvanized steel sheets: microalloyed steel sheet H220PD of the thickness 0,8 mm and TRIP steel 40/70+Z100MBO of the thickness 0,77 mm were used for the experiments. The tensile test and metalographical analysis were used for evaluation of the press joints properties. The influence of the sheet's position in press joining of used materials on carrying capacity considering the active parts of the tool - punch and die was observed.

INTRODUCTION

The car body consists of combination of several materials. That is because of trends of material saving and energy saving that is applied in car body production. The car production with lower weight and consequently with lower fuel consumption is following ecological demands of emission reduction in the environment. There is a need to join various materials – various thickness, quality, surface treatment [1]. The application in car body production opens the new possibilities for the designers in optimal using of properties of various materials which can be combined to the one construction. For example the cheapest materials can be situated in the common parts of pressing in car body, quality sheets can be situated in the critical places of deformation and high-strength sheets can be used in the exposed places due to demands of construction – deformation zones [2].

These demands lead to research in the area of material joining with the accent mainly on carrying capacity of joints, quality of joints and corrosion resistance.

It is not always possible to achieve the required quality of joints in automotive industry when classical methods of joining like resistance spot welding and laser brazing are used. There is a need to research into the area of alternative methods of material joining. One of the alternative joining methods used in automotive industry is press joining [3]. This method should be used as an alternative to resistance spot welding, especially in joining of galvanized sheets. Another press joining method used in the automotive field is self-piercing riveting with the semi-tubular rivets [4].

The contribution deals with evaluation of joints made by press joining of material combination: microalloyed steel HSLA H220PD and TRIP 40/70+Z100MBO.

MATERIAL AND EXPERIMENT

For press joining methods, these steel sheets were used: microalloyed steel HSLA H220PD of thickness 0.8 mm and TRIP 40/70+Z100MBO of thickness 0.77mm. Their basic mechanical properties and chemical composition are shown in Table 1 and 2.

Table 1. Basic mechanical properties of used steels

Material	$R_{p0,2}$ [MPa]	Rm [MPa]	A_{80} [%]	n_{90}
H220PD	238	382	36	0.228
TRIP 40/70	450	766	26	0.278

Table 2. Chemical composition of used steel sheets

Material	Chemical composition in [%] wt.									
	C	Mn	Si	P	S	Al	Cu	Ni	Cr	Ti
H220PD	0.004	0.415	0.100	0.042	0.004	0.035	0.011	0.017	0.310	0.037
TRIP 40/70	0.204	1.683	0.198	0.018	0.003	1.731	0.028	0.018	0.055	0.009
	V	Nb	Mo	Zr						
H220PD	0.002	0.026	0.005	0.001						
TRIP 40/70	0.004	0.004	0.008	0.007						

According to orientation of punch and die to position of upper and lower joined material, following combinations of steel sheets for press joining were used:

H220PD ($a_0 = 0.80$ mm)   and   TRIP ($a_0 = 0.77$ mm)* - samples A
TRIP ($a_0 = 0.77$ mm)   and   H220PD ($a_0 = 0.80$ mm)*   - samples B
(*sheet on the die side of press joining tool)

The samples of 40 x 90 mm dimensions with the length of lapping 30 mm according to STN 05 1122 standard were used for the experiments. Six samples were prepared for every combination of sheets – sample A, B. The surfaces of samples were not cleaned before clinching.

Clinching was performed on the tension machine ZD 40 of Werkotoffruf-maschinen Leipzig Company with the loading range of 40 kN. The force needed for joining was 30 kN. The force for blankholder was 8 kN. Two types of samples were made by press joining: samples A with TRIP 40/70 steel on the side of die of press joining tool and samples B with microalloyed steel H220PD on the side of die of press joining tool.

The carrying capacities of joints made with press joining were evaluated according to standard STN 05 1122 – Tensile test of spot welded joints. This test was used for measuring the maximal carrying capacities Fmax of pressed joints. The test was carried out on the testing machine for determination of strength of metals TIRAtest 2300 made by VEB TIW Rauenstein with the loading speed of 8 mm/min.

The metallographical analysis was used for evaluation of quality of pressed joints.

ANALYSIS OF RESULTS

The measured values of carrying capacities of press joints after tensile test are shown in Table 3. The values of carrying capacities of resistance spot welds of the same material combination (H220PD of 0.8 mm thickness and TRIP 40/70 steel of 0.77 mm thickness) are shown in Table 3 for comparison of carrying capacities with press joints. The joint made with resistance spot welding achieved average carrying capacity of 7467 N and the joint of samples A made with press joining achieved average carrying capacity of 1007 N. The carrying capacity of the press joint of sample A is about 13 % in comparison with the resistance spot weld in researched material combination. The cracks in the lower part of TRIP steel on the die side were observed (Fig. 1 and Fig. 2c). Figure 2 shows example of failure in sample A.

Table 3. Measured values of carrying capacities of samples A, B and resistance spot welding

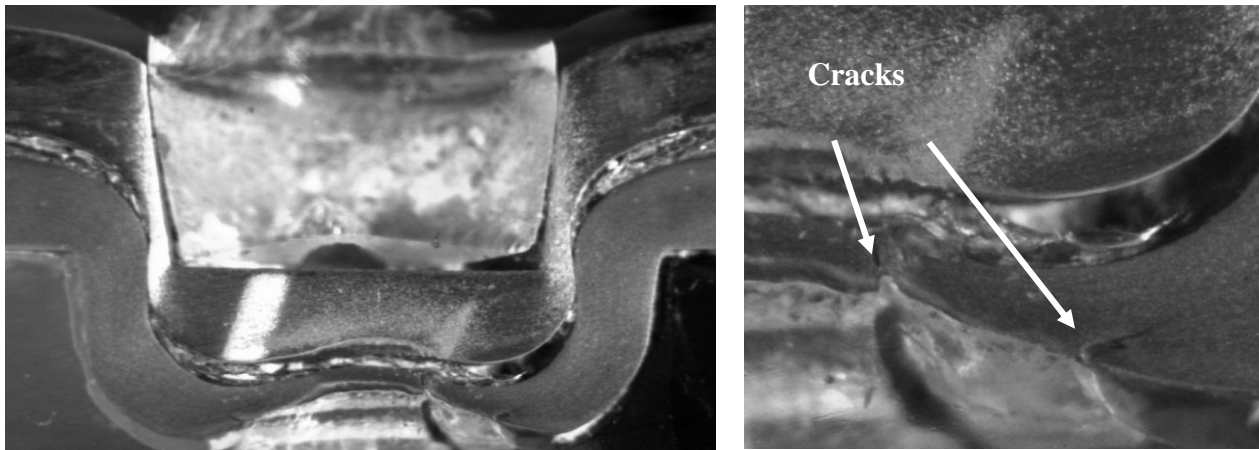| Number of sample	Carrying capacity Fmax [N]		
	Press joining – samples A	Press joining – samples B	Resistance spot welding
1	939	---	7310
2	985	---	7641
3	1016	---	7680
4	1080	---	7172
5	1083	---	7417
6	937	---	7581

Fig. 1. Macrostructure of sample A with cracks in lower TRIP sheet on the die side

The carrying capacities values of samples B are not mentioned in Table 3, because the press joints were not created. Only the part of upper TRIP steel sheet was cut off and pressed to the lower sheet (Fig. 3a). No cracks were observed on the lower part of sheet on the die side unlike the sample A (Fig. 3c).

Fig. 2. Sample A after tensile test: a) joint after failure, b) upper sheet of joint, c) lower sheet of joint -
on the die side
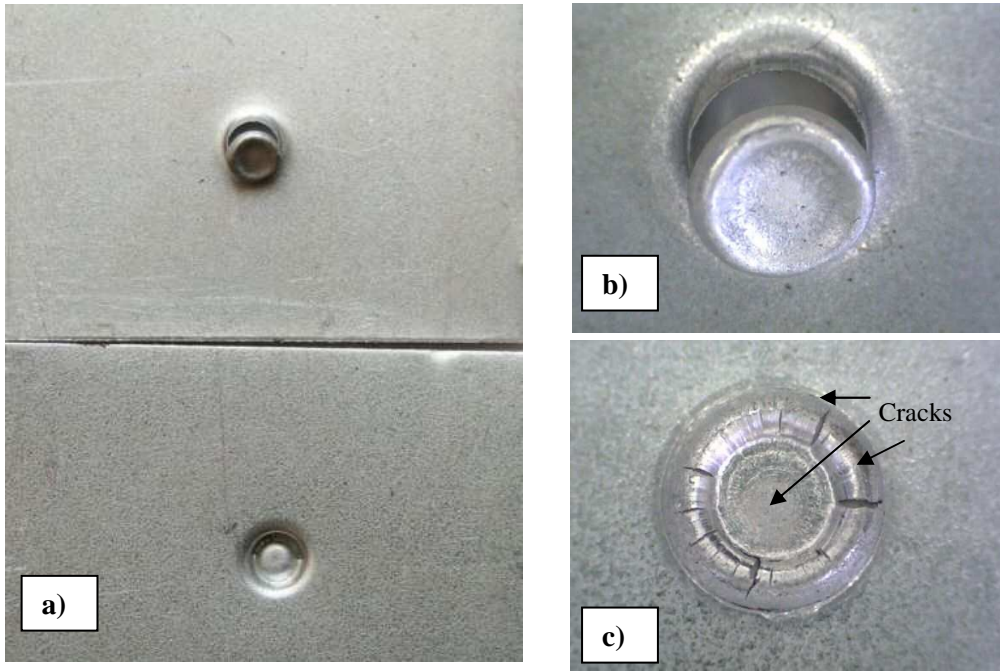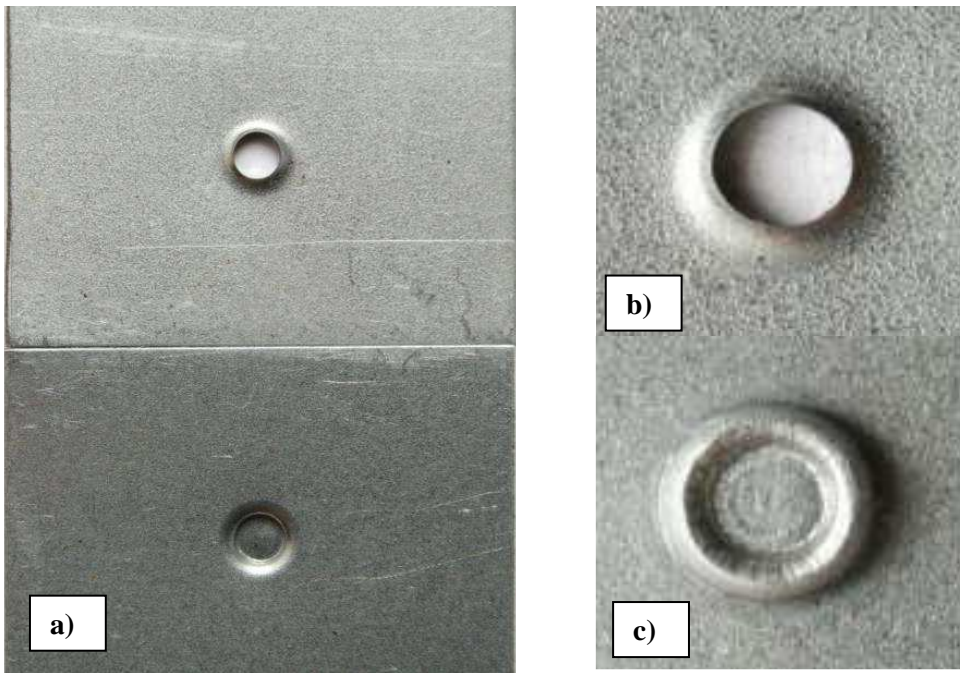

Fig. 3. Sample B after tensile test: a) joint after failure, b) upper sheet of joint, c) lower sheet of joint -
on the die side

Figure 4 shows characteristic grain deformation of the upper sheet in so called
critical area of the press joint. The failures during tensile test of samples A and failures
during the process of press joining of samples B were observed in the critical area.
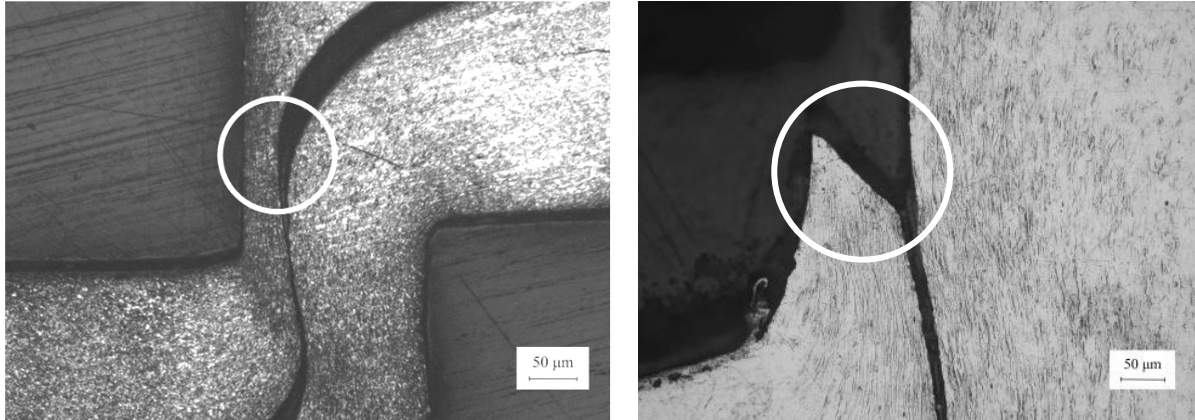
Fig. 4. The critical area in the press joint: a) H220PD steel on the upper side, b) TRIP 40/70 steel on the upper side

The details of the cracks in TRIP steel of the sample A are shown in Fig. 5.
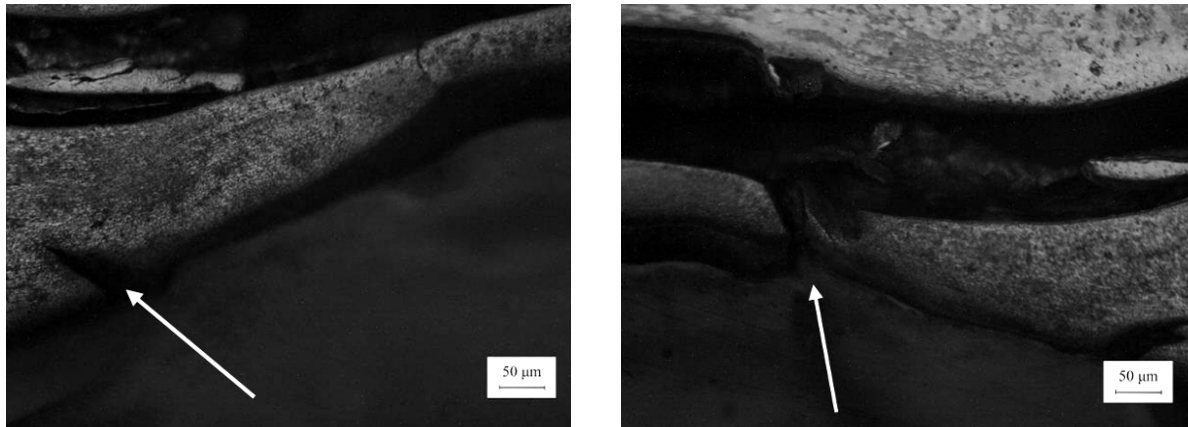
Fig. 5. Microstructure of sample A - details of cracks in TRIP steel

CONCLUSIONS

The contribution dealt with evaluation of press joints of material combination: microalloyed steel HSLA H220PD and TRIP 40/70+Z100MBO. The tensile test and metallographical analysis were used for evaluation of press joint properties. On the basis of the conducted experiment, the following conclusions can be formed:

- press joints of samples where TRIP steel was situated on the die side were created, their average carrying capacity was 1007 N, but cracks in TRIP steel were observed, which cannot be accepted as a quality joint,
- press joints of samples where H220PD steel was situated on the die side were not be created; only the part of upper TRIP steel sheet was cut off,
- metallographical analysis of the samples with TRIP steel on the die side confirmed appearance of cracks in the part of TRIP steel,
- metallographical analysis of both types of the samples confirmed failures in the press joints in the critical area – during tensile test in samples A and during the process of press joining in samples B.

On the base of results of quality evaluation of press joints it can be stated, that press joining method is not suitable method for joining of material combination of TRIP 40/70 steel and microalloyed HSLA steel H220PD.

REFERENCES

1. Kaščák, Ľ., Spišák E.: *Tlakové spájanie oceľových plechov pre automobilový priemysel*. PRO-TECH-MA 2005, Progressive Technologies and Materials, Rzeszów – Bezmiechowa 2005, s. 76 - 81.

2. Spišák E., Kaščák Ľ.: *Spájanie oceľových plechov v automobilovom priemysle*. In: MAT/TECH automobilového priemyslu 2005. s.97 – 102.

3. Kaščák Ľ.: *Nové metódy tlakového spájania materiálov*. Transfer inovácií, 8/2005, s. 99-100.

4. Mucha J.: *The influence of shape of tool die and blankholder on effect of deformation joint elements and rivetion load values*. In: Acta Mechanica Slovaca, 3-A/2008, s. 279-286.

5. Nong N., Keju O., Yu Z., Zhiyuan Q., Changcheng T. and Feipeng L.: *Research on press joining technology for automotive metallic sheets*. Journal of Materials Processing Technology, 137 (2003), p. 159-163.

Ľuboš KAŠČÁK
Ján VIŇÁŠ

Technical University of Košice, Slovak Republic

INFLUENCE OF WELDING PARAMETERS OF RESISTANCE SPOT WELDING ON THE QUALITY OF WELDED JOINTS

The paper deals with the influence of welding parameters of resistance spot welding on the quality of welded joints. Joints were made with combination of galvanized steel sheets DX51D + Z (EN 10142/2000) and TRIP 40/70+Z100MBO. It is an advanced material combination frequently used in designing car body parts. For evaluation of joints quality the shear tension test on spot joints according to DIN 50 124 standard was used. The basic mechanical properties of welded joints were evaluated. Some samples were prepared for metallographic analysis where the influence of the welding parameters on the structure of welded joint was observed. We also observed the influence of welding parameters on the dimensions of the weld nugget, as well as the occurrence of pores in the weld metal caused by evaporation of zinc from the coating. Hardness was evaluated on metallographic scratch patterns according to STN EN 1043-2 standard.

INTRODUCTION

Car producers make an effort to achieve the lowest possible fuel consumption, high active and passive safety of passengers while decreasing the amount of emission.

One of the possibilities of decreasing the car weight and consequently lowering the fuel consumption is using various combinations of materials, such as combination of conventional deep-drawn steel sheet and high-strength steel sheet. In the areas, where high passive safety is needed, high-strength steels such as TRIP and DP steels can be used. The usage of such steels can significantly reduce the car weight. Their strength properties allow reducing the thicknesses of particular segments of a car body.

The car body consists of several materials which need to be joined together to form one unit, usually by welding. Due to combining various types of materials having different mechanical properties and chemical composition, it is necessary to consider various methods of welding and joining. Specific demands on the weldability of particular types of materials must be taken into consideration to optimize welding parameters with the aim of eliminating defects in welded joints [1, 2].

Weldability issues of deep-drawn steels in car body production are generally well mastered. Weldability of TRIP steels is commonly classified as good. However, a combination of these types of materials in resistance spot welding requires thorough optimization of the welding parameters.

MATERIALS USED FOR EXPERIMENTS

Double-sided hot-dip galvanized steel sheets TRIP 40/70+Z100MBO of 0.77 mm thickness made by Voestalpine Austria, and DX51D + Z (EN 10142/2000) of 1 mm thickness made by U.S.Steel Košice, Ltd. were used for the experiments. Average thicknesses of zinc coatings measured by contact thickness gauge Quanix were as follows:

TRIP 40/70+Z100MBO - 18,2 μm

DX51D + Z (EN 10142/2000)- 16,8 μm.

The chemical composition of the observed materials and their basic mechanical properties declared by the producers are shown in Tables 1 to 4.

Table 1. Chemical composition of TRIP 40/70+Z100MBO

C	Mn	Si	P	S	Al	Cu	Ni
0.204	1.683	0.198	0.018	0.003	1.731	0.028	0.018
Cr	As	Ti	V	Nb	Mo	Zr	
0.055	0.008	0.009	0.004	0.004	0.008	0.007	

Table 2. Mechanical properties of TRIP 40/70+Z100MBO

$Rp_{0,2}$ [MPa]	Rm [MPa]	A_{80} [%]	n_{90}
450	766	26	0.278

Table 3. Chemical composition of DX51D + Z (EN 10142/2000)

C	P	S
max. 0.15	max. 0.040	max. 0.040

Table 4. Basic mechanical properties of DX51D + Z (EN 10142/2000)

Rm [MPa]	A_{min} [%], L_o = 80 mm]
max. 450	23

The formation of the weld nugget is indeed strongly dependent on the phenomena at the interfaces. The contact areas influence directly the macro-constriction of the welding current in the assembly: they vary throughout complex way, along the different phases of the process, are affected by the configuration of the assembly and by the profile of electrodes contact surface. The surface defects lead to micro-constriction effects taken into account by the electrical and the thermal contact resistances definition [3-5].

Resistance spot welding was carried out in laboratory conditions on a pneumatic spot welding-machine BPK 20 made by VTS ELEKTRO Bratislava. CuCr welding electrodes were used according to ON 42 3039.71 standard. The diameter of working area of the electrode was d = 5 mm. The welding parameters of resistance spot welding with marked tested samples are shown in Table 5. The welding parameters were determined according to the recommended welding parameters by IIW - International Institute of Welding, adapted to our welding machine and its possibilities.

Table 5. Parameters of resistance spot welding

Welding parameters	Samples			
	A	B	C	D
Fz – pressing force [kN]	6	6	6	6
T - welding time [per.]	12	12	12	12
I – welding current [kA]	6	6.6	7	5.4

Static tensile test

Tensile test according to DIN 50 124 standard was used for evaluation of carrying capacities of welded joints, with samples of dimensions as shown in Fig. 1. The samples were prepared by cutting against the direction of rolling. The length of lapping was 32 mm. The surfaces of the samples were degreased in concentrated CH_3COCH_3.

The tensile test was carried out on tensile machine TIRA test 2300 manufactured by VEB TIW Rauenstein with the load speed of 8 mm/min.
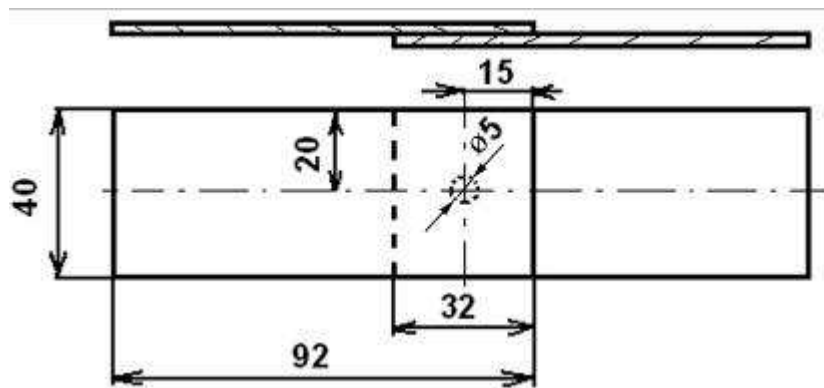
Fig. 1. Dimensions of samples for the tensile test

Metallographical analysis

The quality of welded joints was evaluated by light microscopy on metallographical scratch patterns prepared according to ISO 6507-1 and ISO 6507-2 standards on Olympus TH 4-200 microscope. The samples were etched in 3% solution of HNO_3.

ANALYSIS OF RESULTS

Analysis of the tensile test

Measured values of carrying capacities of joints on welding current are shown in Fig. 2. Only one type of the joint occurs in all chosen parameters of welding – fusion welded joint. The values of carrying capacity of welded joints were in the range from 6166 N to 7680 N.

Fig. 2. Dependency of carrying capacities of spot welds Fmax [N] on welding current I [kA]

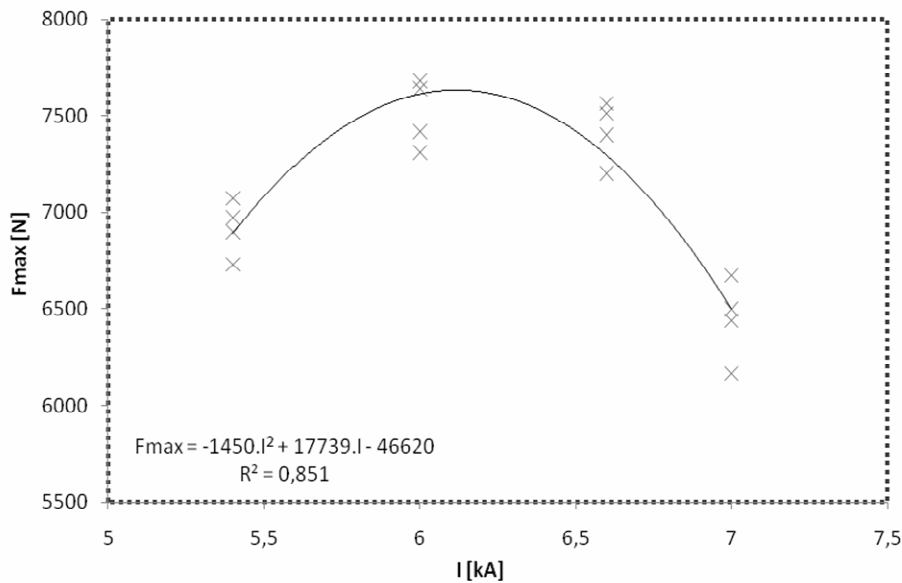Figure 3 and 4 show indentations formed by the welding electrodes. The most obvious indentations were on the surfaces of samples prepared with parameters B (I4 = 6.6 kA) and C (I4 = 7.0 kA). The least obvious indentations were on the surfaces of both welded steels prepared with welding parameters D (5.4 kA).

Fig. 3. Welding electrodes indentations on TRIP steels

Fig. 4. Welding electrodes indentations on DX51D + Z (EN 10142/2000) steels

As the measurement results show, the highest carrying capacity was measured on samples prepared with welding parameters A – with welding current 6 kA.

Metallographical analysis

The base material of DX51D + Z (EN 10142/2000) has a fine-grained ferrite-perlite structure. It is a fine-grained multi-phase structure with dominant ferrite component, bainite and retained austenite segregated on boundaries of ferrite grains.

The metallographical analysis confirmed formation of fusion welded joints with characteristic areas of weld metal, heat affected zone and base material. Figure 5 shows the macrostructure of a spot weld of the sample welded with parameters A.
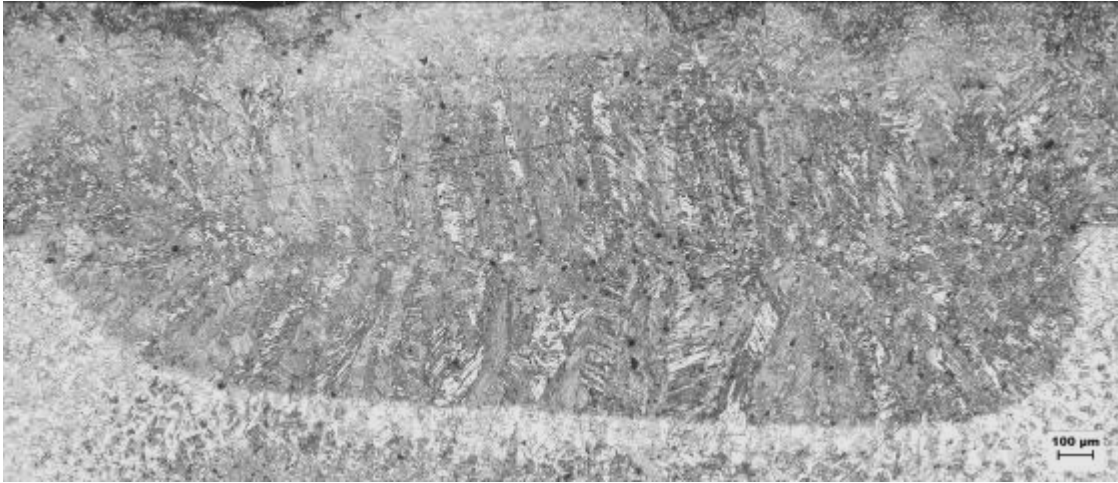
Fig. 5. Welded joint of an A sample

Figure 6 shows welded joint of a sample welded with parameters D with the lowest value of welding current – 5.4 kA. Therefore, the weld nugget is smaller in comparison with the weld nugget of sample in Fig. 5.

Fig. 6. Welded joint of a D sample

The macrostructures of a weld joint show the solidification process of weld metal with a characteristic dendrite structure typical for resistance spot welds.

The microscopic observation of macrostructures of the welds shows no pores and cavities occurring in the weld metal.

Figure 7 shows microstructure of weld metal of an A sample in the middle of weld nugget. The microstructure of weld metal consists of mostly fine-grained martensite arranged in typical lamellar formations. Such lamellar formations prevent the austenite from transformation; therefore the retained austenite occurs in the microstructure. Besides martensite, also ferrite and both forms of bainite occur in the microstructure of weld metal. Presence of formed carbide inclusions was also observed in the weld metal.
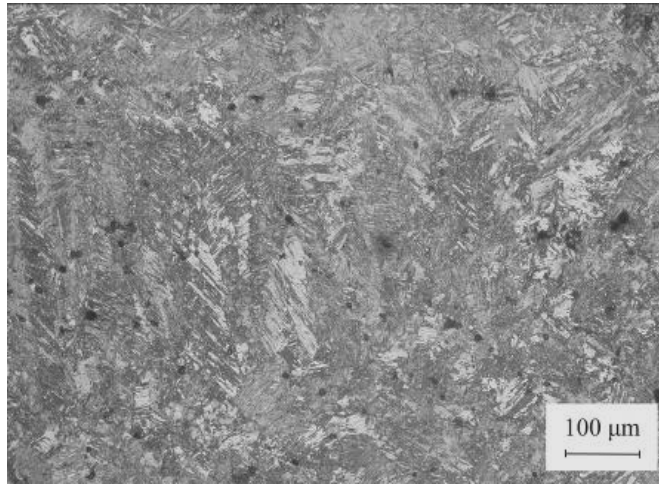
Fig. 7. Structure of weld metal in TRIP steel of an A sample

The microstructure of DX51D + Z can be characterized as a fine-grained ferrite-perlite structure. Because of heating in resistance spot welding, continual growth of grains towards the weld metal can be observed. A significant growth of perlite grains occurs in the heat affected zone. On the boundary of the heat affected zone and the weld metal, there is bainite transformation of perlite grains (Fig. 8).
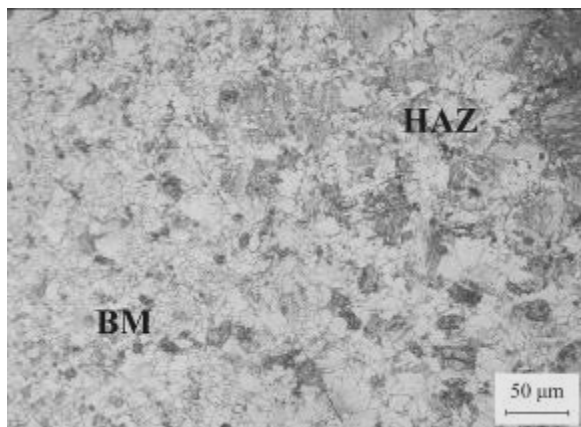
Fig. 8. Base material (BM) and heat affected zone (HAZ) of DX51D + Z steel
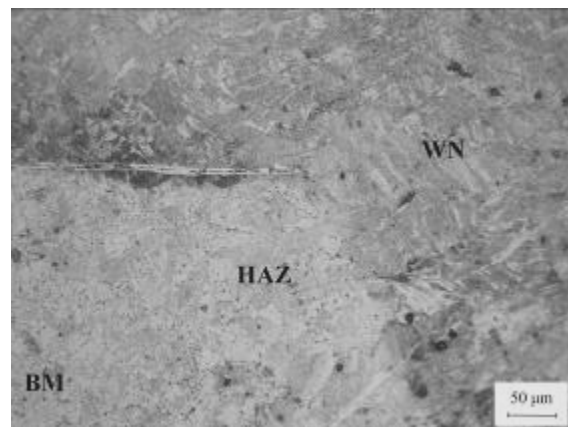
Fig. 9. Boundary of weld nugget (WN) and heat affected zone (HAZ) of DX51D + Z, sample A

In the part of the weld metal of DX51D + Z (Fig. 9), a bainite-ferrite microstructure can be observed. There are dispersed ferrite grains on the boundaries of bainite grains. In the part of the weld joint of DX51D + Z, the structure of well visible dendrites is the same as in the part of the weld nugget of TRIP steel, characteristic for solidification processes of the weld metal in resistance spot welding.

In the middle part of the weld metal, there is a narrow layer of weld metal mixing of both sheets, caused by the loading force of electrodes (Fig. 10). The core of the nugget (on the upper side of the figure) consists of martensite structure from the side of TRIP steel. Besides of martensite lamellas, ferrite grains and remains of retained austenite can be observed in the structure of TRIP steel.

132

On the side of deep-drawn steel, there are bainite grains with polyedric ferrite grains which were transformed into acicular ferrite.

Fig. 10. Area of weld metal of both types of steel

Fig. 11. Crack in the HAZ of TRIP steel above the weld nugget with parameters C

When using welding current 7 kA, there occurs cracking in heat affected zone of TRIP steel, as shown in Fig. 11.

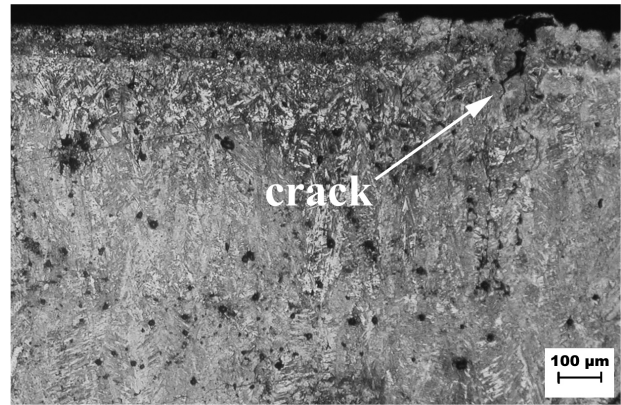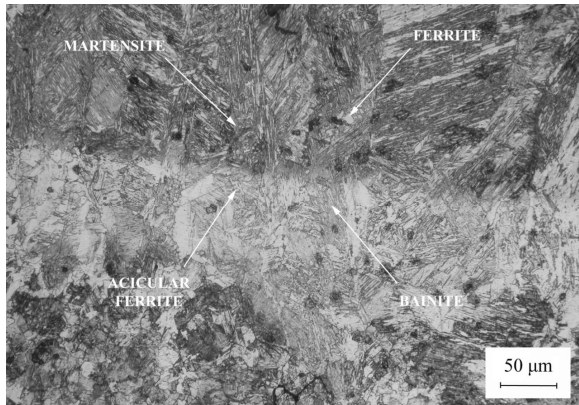Expressive indentations of electrode tips were observed on the sample surfaces made under welding parameters C. Current intensity had a significant influence on the height of the weld nugget. The character of cracks is intercrystalline. The amount of the heat and martensitic structure or transformation process of particular compounds of the structure during welding was the cause of their creation. However, a dynamic process of welding with a hard regime was used, cracks creations occur when using welding current over 6.6 kA.

Such cracks occur only in heat affected zone of TRIP steel. Evaporation of Zn coating from sheet surfaces in the area of welding tips contact was observed in all samples.

CONCLUSIONS

On the basis of the conducted experiment, the following conclusions can be formed:

- Fusion weld joints occur with all chosen parameters of resistance spot welding.
- The highest tensile strength was observed in samples made with welding parameters A (Table 6). The average carrying capacity of samples was 7520 N. The lowest values of carrying capacity were observed in samples made with welding parameters D, where the average value of carrying capacity decreased by 8.65 % in comparison to samples with parameters A.
- Increasing the parameters of the welding current above the value of 6.0 kA proved ineffective. The carrying capacities of samples made with parameters of B and C were not increased. In fact, the carrying capacities decreased, and we observed overheating of the weld metal and expansion of the heat affected zone, which proved to be a critical area in welding.
- The metallographical analysis confirms that the chosen combination of deep-drawn sheet and high-strength sheet is suitable for resistance spot welding. On the

basis of the results it can be stated, that welding current has a determining influence on the weld joint. When using the welding current of 5.4 kA, weld joint was of high quality, fusible and without defects, but the weld nugget had smaller dimensions in comparison with weld nuggets made under parameters of A and B. Weld joints of high quality were made with welding currents of 6.0 kA and 6.6 kA. Welding current of 7.0 kA is not suitable for the examined thickness and sheet combination, because cracking was observed in the heat affected zone of multi-phase material of TRIP.

- In the evaluated microstructures there was just a little amount of formed carbides in the weld metal (mainly in TRIP steel), which were initiated in isothermal stand in the bainitic zone. Fully killed steel by Al was determining and the content of Al in our case was 1.731%.

Both types of evaluated materials are suitable for welding of car body parts. The development of TRIP steels for automotive industry leads to development of bainite-ferritic structure with retained austenite.

REFERENCES

1. Zhang H., Senkara J.: *Resistance Welding: Fundamentals and Applications*. Taylor&Francis Group, New York 2006.
2. Kaščák Ľ., Spišák E.: *Resistance spot welding of three steel sheets for automotive industry*. In: PRO-TECH-MA '07: Progressive Technologies and Materials : International scientific conference, Rzeszów - Bezmiechowa, Poland, Rzeszów : Politechnika Rzeszowska, 2007. pp. 49-54.
3. Aslanlar S.*: The effect of nucleus size on mechanical properties in electrical resistance spot welding of sheets used in automotive industry*. Materials and Design 27, 2006, pp.125 - 131.
4. Rogeona P., Carrea P., Costaa J., Sibilia G., Saindrenanb G.: *Characterization of electrical contact conditions in spot welding assemblies*. Journal of Materials Processing Technology, 195, 2008, pp. 117–124.
5. Cretteur L., Koruk A. I., Tosal-Martinez L.*: Improvement of weldability of TRIP Steels by use of in-situ pre- and post- heat treatments*. Int. Conf. On TRIP, Ghent 2002, pp. 353-358.

Ľuboš KAŠČÁK
Ján VIŇÁŠ
Rudolf MIŠIČKO
Iveta TAKÁČOVÁ
Marek VOJTKO
Matej SCHMÖGNER
Milan MATTA*
Martin GATIAL*

Technical University of Košice, Slovak Republic; *U.S. Steel Košice Ltd., Slovak Republic

THE CAUSES OF FAILURES IN RESISTANCE SPOT WELDING OF CAR BODY SHEETS

The paper deals with analyzing of defects of resistance spot welds, which mostly occur in welding of materials used in car body production. The defects were evaluated with destructive and non-destructive tests. A non-destructive method was a visual control of weld surfaces of lapped joints. Metallographical analysis of weld joints on scratch patterns was used as a destructive method. The Influence of welding parameters on dimensions of weld nuggets was observed with light microscopy. The defects in weld and heat affected zone were documented too. The influence of surface treatment of car body sheets on occurring of defects was evaluated with chemical EDX analysis. EDX analysis was also used for evaluation of weld joints surfaces and for evaluation of influence of weld tips marks on surface quality.

INTRODUCTION

Resistance spot welding is one of the most used technologies of sheets joining in automotive industry. Welding, laser brazing, MIG welding and brazing, clinching, adhesive joining are the methods used in car body production. But the most used method of joining of black sheets, galvanized sheets and aluminium alloys is resistance spot welding. A middle class car contains from 2.500 to 5.000 spot welds. The quality of spot welds depends on optimization of welding parameters for the specific type of welding machine, used materials for welding. Surface treatment of joined materials has also significant influence on the quality of spot welds. Optimization of welding parameters is tested on the welded samples. The quality of welds is mainly evaluated with destructive tests: tensile test, cross-tension test, chisel test, pull test, fatigue test, dynamical impact test, evaluation of weld hardness, metallographical analysis. Non-destructive tests have only informative character and do not allow detecting for example cold joints, which are one of the most reason of spot welds failure [1, 2].

Incorrect choice of welding parameters in resistance spot welding cause following defects [1, 3]:
- cold joints,
- lower weld nuggets,

- higher weld nuggets,
- deep marks of electrodes,
- surface melting,
- asymmetric weld shape,
- insufficient weld diameter,
- cavities, pores,
- cracks.

USED MATERIALS

Influence of welding parameters on quality of welded joints was observed on materials, shown in Table 1.

Table 1. Chemical composition of evaluated materials declared by producer in % wt.

Sample	A	B	C	D		A	B	C	D
	DX52D + Z	H 420 LAD	TRIP *	DP 600 **		DX51D + Z	H 420 LAD	TRIP*	DP 600 **
Element	[%]	[%]	[%]	[%]	Element	[%]	[%]	[%]	[%]
C	0,15	0,10	0,204	0,072	Nb	-	0,09	0,004	0,002
Mn	-	1,50	1,683	1,807	Mo	-	-	0,008	0,203
Si	-	0,03	0,198	0,010	Zr	-	-	0,007	0,003
P	0,035	0,025	0,018	0,017	Cu	-	-	-	0,022
S	0,015	0,01	0,003	0,006	Ni	-	-	-	0,011
Al	0,04	0,015	1,731	0,056	Sn	-	-	-	0,002
Cr	-	-	0,055	0,220	Sb	-	-	-	0,002
As	-	-	0,008	0,002	SAL	-	-	-	0,056
Ti	-	0,15	0,009	0,001	TAL	-	-	-	0,057
V	-	0,2	0,004	0,003	N2	-	-	-	0,005

* TRIP 40/70+Z100MBO – full material specification

**DP 600 HCT 600X+Z – full material specification

Resistance spot welding was realized at the Laboratory of welding on pneumatic welding machine BPK 20 of VTS Elektro Bratislava producer with welding electrodes CuCr prepared according to STN EN 25 821 standard, with the diameter of working area ø5 mm.

Parameters of resistance spot welding are shown in Table 2 and process of welding parameters is shown in Fig. 1.

Table 2. Chosen welding parameters

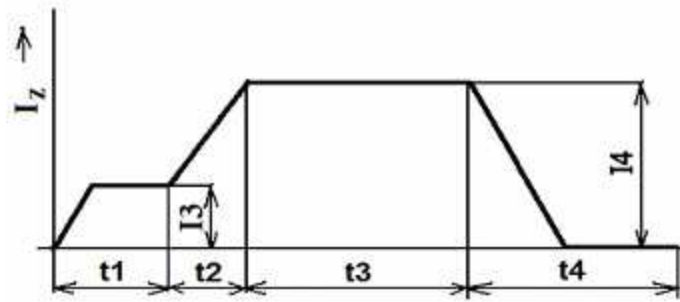| Welding parameters		Sample							
		A1	A2	B1	B2	C1	C2	D1	D2
Sheet thickness h	[mm]	1,5	1,5	1,5	1,5	0,8	0,8	1,5	1,5
Pressing force Fz	[kN]	4	4	2,6	2,6	4	4	2,6	2,6
Time of welding electrodes pressing t1	[per]	10	10	10	10	9	9	10	10
Time of application of required welding force t2	[per]	10	10	10	10	10	10	10	10
Welding time t3	[per]	12	12	14	14	12	12	14	14
Forging time t4	[per]	12	12	14	14	12	12	10	14
Build up current I3	[kA]	5,2	7,0	5,3	6,2	4	6,9	5,2	7,0
Welding current I4	[kA]	6,0	7,7	6,6	7,6	5	8	6,0	8,0

Fig. 1. Welding parameters process on welding machine BPK 20

ANALYSIS OF RECEIVED RESULTS

The quality of welded joints is analyzed primarily with non-destructive methods of testing and then with destructive methods. The basic method of non-destructive evaluation of all kind of welded joints is the visual control. In the case of negative result of the visual control, the weld is marked as inconvenient and the other control methods are not necessary. The dimensions of welded joint and influence of used pressing force on surfaces in the place of contact electrode – sheet are evaluated with this method. The mark depth of electrode tips in the area of joint is observed according to STN EN ISO 18595 standard, where maximum values of mark depth in the area of joint is 20 % of total thickness of joined materials.

Using high values of welding current or welding time in welding of galvanized sheets cause impurities on the joint – brass layer, which is created by Zn layer bonded from sheet surface of joined material to the electrode tip of Cu alloy. This layer negatively affects the transfer resistances between welding tip and welded material. The brass layer is released during welding and cause impurities on the joint as is shown in Fig. 3. The protective coatings on the steel sheets lead to the rapid decreasing of welding tips lifetime, which is notable problem in resistance spot welding, mainly in car body production in automotive industry.

Figure 2 and 3 show influence of used welding parameters on the weld surfaces of samples C1 and C2. Figure 4 shows the brass layer on the edge of weld joint.

Fig. 2. Weld surface on sample C1
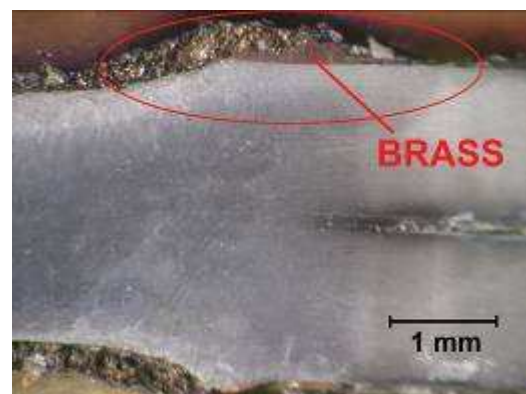

Fig. 3. Weld surface on sample C2

Fig. 4. Brass on joint surface on sample D2

The cold joints frequently occur in resistance spot welding of galvanized steel sheets, because of inconvenient welding parameters. The main influence on the cold

joint occurrence has low values of welding current, insufficient pressing force, short welding time and impurities on the surfaces of joined materials in the place of welding [3, 9].

The macrostructure of welded joint of DX52D+Z material is shown in Fig. 5. There is a typical cold joint without melting of joined material surfaces. Therefore the welding parameters used for sample A1 are insufficient for creation of qualitative fusion weld.

The macrostructure of sample A2 is shown in Fig. 6. The cavities in the middle of weld nugget occur after welding. The base material has ferritic-perlite structure. Bainitic structure, primary and acicular ferrite was observed in the weld metal.
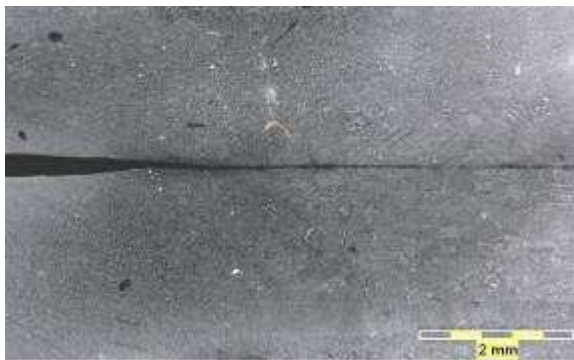
Fig. 5. Macrostructure of cold joint of A1 sample
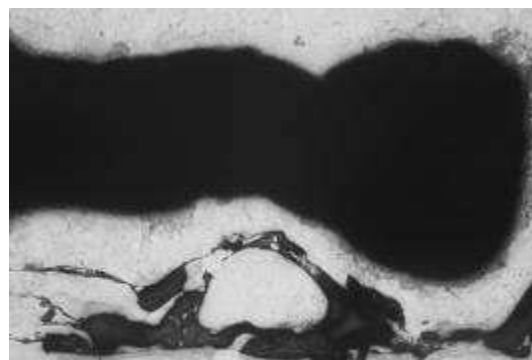
Fig. 6. Macrostructure of fusion joint
of sample A2

The detail of cavity in sample A2 is shown in Fig. 7. EDX analysis was realized in the cavity edge (Fig. 8) with the purpose to verify the influence of Zn on the cavity creation. Occurrence of Zn was not observed in the cavity, only occurrence of Al and Fe was documented. The same was observed in the middle of weld nugget. Used welding parameters caused the expulsion of Zn from the joint between joined materials during welding [4, 2].

Fig. 7. The cavity in the weld after expulsion
welding metal.

Fig. 8. Chemical composition in cavity of
from EDX analysis.

138

The influence of welding parameters on welding of micro-alloyed steels (HSLA) was observed too. The basic material of H 420 LAD consists of ferritic-perlite structure. Acicular ferrite structure in the weld metal was observed. Figure 9 shows the macrostructure of sample B1. The cavities in the weld metal are shown in Fig. 10. They were caused by low values of welding current and short welding time.
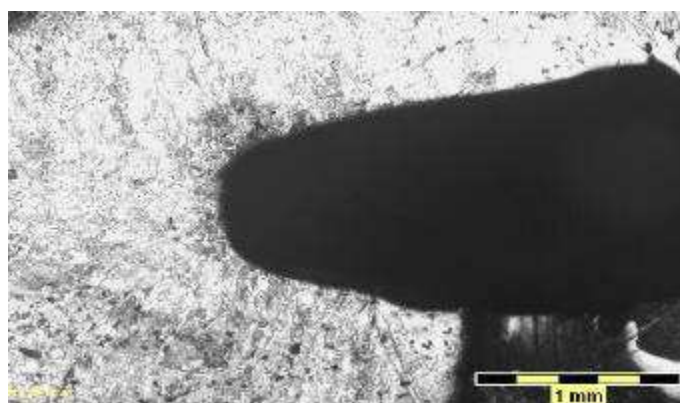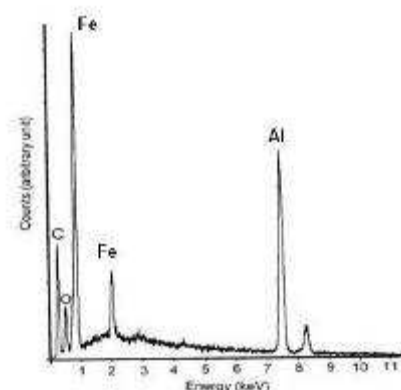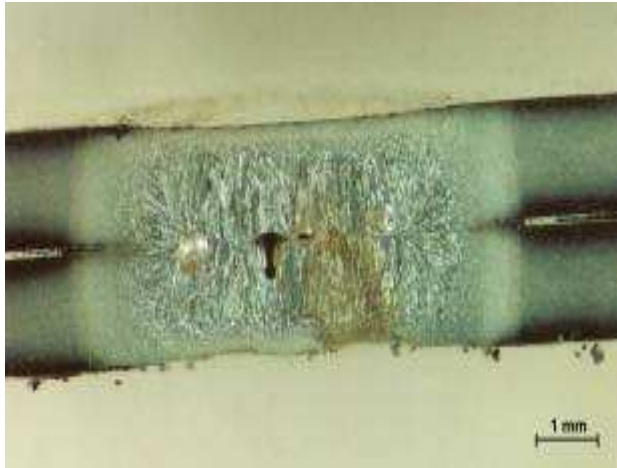

Fig. 9. Macrostructure of sample B1   Fig. 10. Detail of cavities in the middle of weld nugget of sample B1

Figure 11 shows characteristic dendritic microstructure of sample B2. Increasing values of welding current caused microcracks in the weld metal (Fig. 11 and 12). Initiation of microcracks starts from the middle of joint and their orientation is in direction of solidification of weld metal.

Fig. 11. Hot cracks in microstructure of sample B2   Fig. 12. Detail of cracks of sample B2

Resistance spot welding of high-strength multiphase steels is problematical. The optimization of welding parameters is very important and leads to use hard welding regime with short welding time. The macrostructure of sample C1 is shown in Fig. 13. The base material TRIP 40/70+Z100MBO has fine grain ferritic bainite structure and residual austenite is located on the boundary of ferrite grains [6].

Fig. 13. Macrostructure of sample C1

The microstructure of weld metal consists of soft grained martensite with characteristic needle shapes, residual austenite, both forms of bainite and ferrite.

The high–strength steels inclined to cracking during welding, which is shown in Fig. 14. The cracks occurred mainly in heat affected zone (HAZ) and weld metal, where obvious grain growth caused by heating was observed.
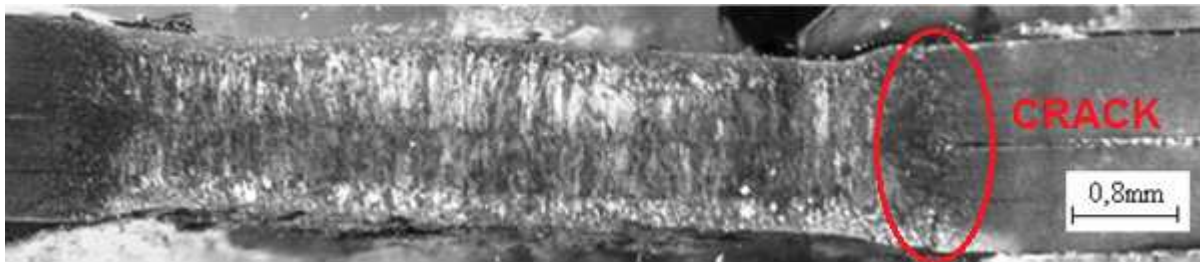
Fig. 14. Cracks in HAZ on sample C2

Figure 15 shows macrostructure of sample D1. The fusion welded joint was observed, but there were cavities in the middle of weld metal caused by insufficient pressing force of electrodes, short welding time with the combination of insufficient forging pressure. The dual phased structure with soft grained ferrite and martensite was observed in the base metal. The heating during welding causes obvious grain coarsening in the weld metal and transformation to the pure martensitic structure, which is shown in Fig. 16.
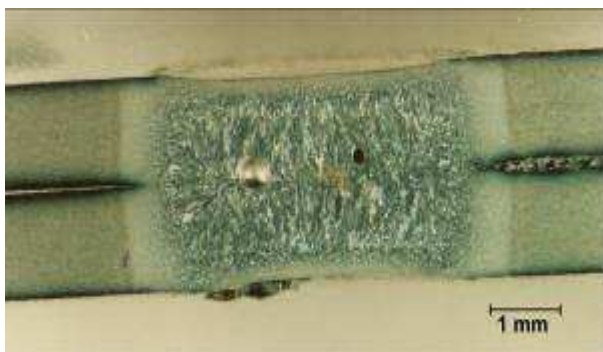
Fig. 15. Macrostructure of sample D1

Fig. 16. Details of cavities in the middle of weld nugget of sample D1

140

The strains with the combination of coarse-grained structure of martensite are the problems in welding of TRIP 40/70+Z100MBO steels and DP 600 HCT 600X+Z steels. The critical place for cracking of these materials is the boundary between heat affected zone and weld metal, as is shown in Fig. 14 and 16.

Microstructure of sample D2 is shown in Fig. 17. The fusion welded joint with the weld nugget of insufficient dimensions was observed. Obvious electrode marks on contact areas were observed on the macrostructure. The width of weld metal corresponds with diameter of used electrodes, but the height of weld nugget is almost through the whole cross-section of joined materials. Acceptable value of the weld nugget height is about 70 – 80 % of the thickness of joined materials [1].

The crack in the lower part of heat affected zone was observed and microstructure is shown in Fig. 18.
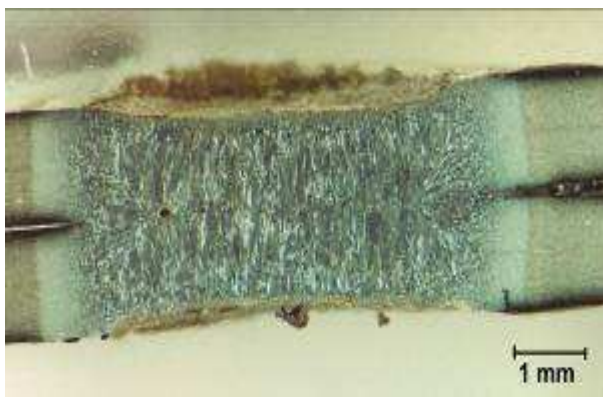
Fig. 17. Macrostructure of sample D2 Fig. 18. Intercrystalic crack in HAZ
                    on sample D2

CONCLUSIONS

Resistance spot welding is one of the most used methods of welding in car body production in automotive industry.

The paper describes the most occurring defects of resistance spot welds. Other occurring defects are asymmetric shapes of welded joints or weld nuggets caused by incorrect positioning or wearing of contact areas of welding tips. Asymmetric shapes of joints may be caused by relative position of the welded parts, which may led to the irregular heating in the weld and cause cracks initiation in the heated area, mainly in high-strength steels [5, 6, 7].

For welding the high-strength steels such as TRIP steels and DP steels is recommended to use hard welding regime with the aim to get minimum amount of heat required for welding nugget creation, but it is necessary to limit martensitic transformation and mainly grain growth. Therefore consistent optimization of welding process on the welding machine is important in welding this kind of steel. Narrow interval of welding parameters is suitable for welding. The application of high-strength materials is a perspective method of weight reduction of car bodies and reduction of fuelling. They are also used as the parts of passive safety of cars such as reinforcements, beams and others.

The effort to eliminate the particular types of defects in resistance spot welding is the aim of research and innovation in the car body production; for example the method

of resistance spot welding Delta Spot, which offers solving of problems with pollution of joint surface and the lifetime of welding tips in resistance spot welding of galvanized sheets.

REFERENCES

1. Lipa M.: *Odporové zváranie*. 1. vyd.. Bratislava: Weldtech, 1995. 265 s.

2. Zhang H., Senkara J.: *Resistance Welding: Fundamentals and Applications*. Taylor&Francis Group, New York 2006.

3. Maronek M., Kovačócy P., Púčik V.: *Technológia zvárania: Návody na cvičenia*. Bratislava : STU, 2006. 202 s. ISBN 80-227-2376-2

4. Viňáš J., Kaščák Ľ.: *Bodové odporové zváranie kombinácie vysokopevných a hlbokoťažných ocelí*. In. Transfer inovácii 11/2008,

5. Janota M.: *Procesy a riadenie odporového zvárania*. Bratislava: Výskumný ústav zváračský 1985.

6. Muranský O., Horňák P., Lukáš P., Zrník J., Šittner P.: *Investigation of retained austenite stability in Mn-Si TRIP steel in tensile deformation condition*. JAMME, Vol. 14, Issue 1-2, 2006, pp.26-30Bohler Thyssen Welding, UTP Schweiβmaterial FmbH, Bad Krozingen, 2004.

7. Kaščák Ľ., Spišák E.: *Resistance spot welding of three steel sheets for automotive industry*. In: PRO-TECH-MA '07: Progressive Technologies and Materials : International scientific conference, Rzeszów - Bezmiechowa, Poland, Rzeszów : Politechnika Rzeszowska, 2007. p. 49-54.

8. Viňáš J., Kaščák Ľ.: *Hodnotenie kvality zvarových spojov karosárskych plechov*. In Transfer inovácií 8/2005Košice: 2005,roč.2005,č.8,s.171.

9. Kaščák Ľ., Spišák E.: *Evaluations of properties of clinching and resistance spot welding*. In: Scientific Bulletins of Rzeszów University of Technology : Mechanics 73. no. 253 (2008), p. 161-166.

Michail KHEIFETZ
Sergey KOUKHTA

Polotsk State University, Belarus

SYSTEM ANALYSIS OF SURFACING AT INTENSIVE PROCESSING AND USING OF DETAILS

The research results of technological mediums with different physical-chemical properties are discussed. Combined processing methods, using different sources and uniting different operations and stages, are shown. Basic controlling statements of surfacing and using of details are defined.

At present level of development of science and technology, requirements on strength, hardness, viscosity, and wear resistance of surfaces are so high, that in some cases conventional surfacing methods fail to provide the necessary quality indexes of surface layers. So, in modern production, combined surfacing methods, applying plasma, electric arc, laser, electron beam, ion vacuum, and other power sources are used more and more often [3].

From the point of view of manufacturing and processing heredity, conventional surfacing methods can produce efficient design of modified layers. However, in case of successive or parallel formation of various surface layers, interconnection of the applied energy fluxes makes it necessary to examine the efficient design of modified layers.

1. SYSTEM ANALYSIS OF COMBINED PROCESSING METHODS

Initial and Boundary Conditions. If manufacturing processes are classified as the following: division of surfaced material into workpieces with volume V1 and manufacturing of workpieces with volume V2, coating (V2 > V1); heat processing (V2 ≈ V1); cutting (V2 < V1), and deformation (V2 ≈ V1), it is possible to formulate boundary conditions of an open manufacturing-processing system. Additional degrees of freedom of conventional boundaries, such as displacements and renewals, make it possible to control non-equilibrium state of the system. If tribological processes, involved in surfacing, are classified as the following: running-in with wear intensity U_0, developed friction and wear with intensity U1 (U1 < U0), and destruction with intensity U2 (U2 >> U1), it is possible to determine the initial conditions of changing of manufacturing system. Additional exposure to energy fluxes at the initial moment provides conditions, leading to stabilization of non-equilibrium manufacturing and operation processes [1].

The efficiency of combined surfacing and operation procedures, obtained by a combination of methods that change boundary conditions by introducing additional degrees of freedom, by displacement of a working body (a tool, production medium, allowance to be removed, the surface to be shaped), and methods that change initial conditions by using additional sources with different levels of energy concentration
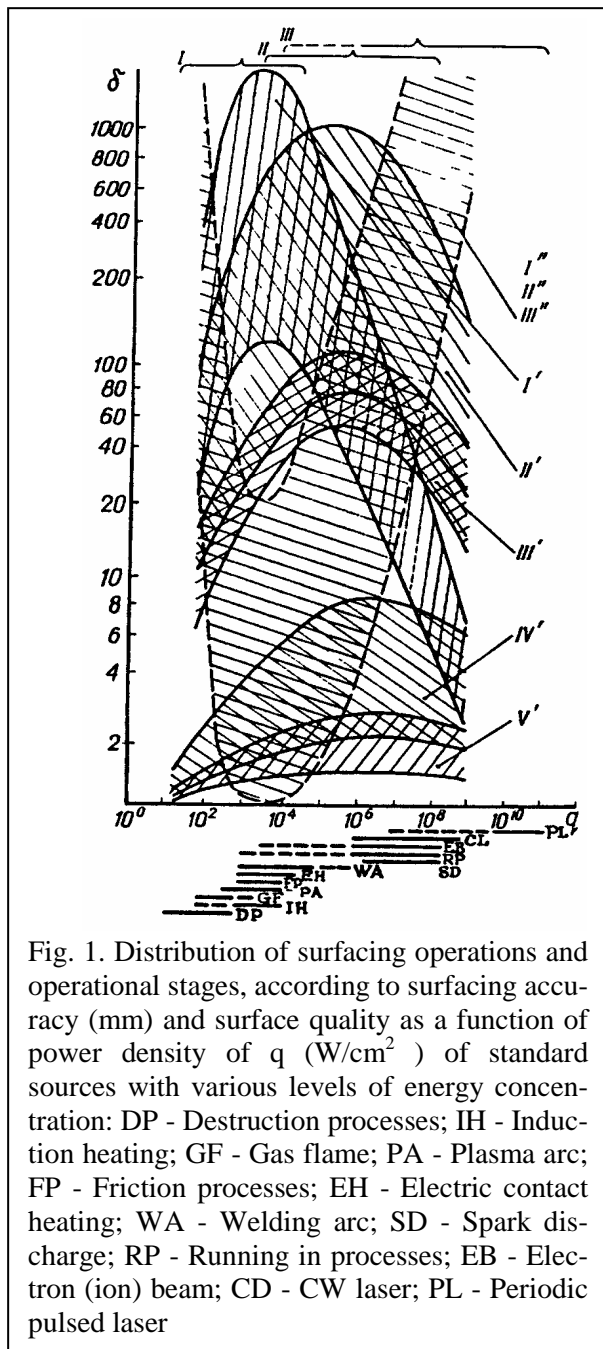
Fig. 1. Distribution of surfacing operations and operational stages, according to surfacing accuracy (mm) and surface quality as a function of power density of q (W/cm^2) of standard sources with various levels of energy concentration: DP - Destruction processes; IH - Induction heating; GF - Gas flame; PA - Plasma arc; FP - Friction processes; EH - Electric contact heating; WA - Welding arc; SD - Spark discharge; RP - Running in processes; EB - Electron (ion) beam; CD - CW laser; PL - Periodic pulsed laser

(with volume zone I, many local zones II, and single local III zone of heat generation) is analysed in Fig. 1.

As it is seen from the Fig. 1 nowadays most of the up-to-date methods can be implemented in industrial production and only few of them are not feasible, but these combinations of the joint actions are exhibited as side effects in shaping and operation of surfaces. Analysis has shown that the use of combined methods based on joint thermal and mechanical actions is efficient [2].

Distribution of combined surfacing and operation methods in the accuracy of surface shaping was studied on the basis of suggested table of classification according to the energy concentration level (I, II, III) for various standard sources (Fig. 1). For deformation and cutting surfacing accuracy was estimated from deviation of sizes and shapes and by waviness and roughness; for heat processing, it was estimated from heterogeneity of depth of thermal strengthening or softening and from the thickness of defective surface layer, and for coating and separation, all the indices enumerated were taken into consideration.

Analysis of surface shaping accuracy shows (Fig. 1) that power density increases from the first to the third energy concentration levels (I > II > III), which, in turn, leads to decrease in dimensions of heat generation zone. Decrease in dimensions of heat generation zones (from I$^{'}$ to V$^{'}$) and in number of operation stages (from III$^{''}$ to I$^{''}$) results in increase in concentration of stresses, whose field determines the surface to be shaped and its accuracy. It is evident that at level I accuracy does not increase as a result of an increase in size of heat generation zone rather than in energy concentration. At level II accuracy is minimal, because of forming the surface over stress concentrators scattered in a large volume and formed by many local heat generation zones. At level III accuracy does not decrease, but subsequently rises abruptly due to focusing of local heat generation zone, accompanied by enhanced growth of stress concentration.

From the conducted analysis it is possible to conclude that initial conditions can be provided efficiently by suitable selection of concentrated energy sources with preset boundary conditions for various surfacing operations and operational stages. Standard

sources of level I can be used in the most efficient way for shaping large volumes in case of deformation, substantial allowances in cutting and layers in application of coats, bulk heat processing, separation, and destruction of large-sized workpieces. Sources of level II decrease surfacing accuracy in the strongest way, so they can be used effectively in combination with cutting and deforming tools and also in coating and heat processing. Use of these sources does not damage surfaces greatly and has strong effect on surface friction. In all technological surfacing operations, sources of level III give the best results. In such operations these sources are most efficient in running-in processes. The data confirm this conclusion and studies of surfacing accuracy indicate that the classification of combined surfacing methods, suggested earlier, is effective [1].

Ways to Increase the Efficiency of Surfacing. The present survey is useful for outlining the ways to increase the efficiency of surfacing and operation of surfaces with preset accuracy and other quality indexes. The production and operation system of combined surfacing is open mainly for thermal and mechanical energy fluxes that determine changing of initial and boundary conditions for surfacing and operation of surfaces up to micrometer accuracy. An excess of the supplied energy above a certain limit, at which the system maintains dynamic equilibrium, should be able to be scattered and absorbed due to additional degrees of freedom of the system with the boundary, formed in this or in previous surfacing operation or stage of operation on a surface. In a thermo-mechanical system, additional degrees of freedom are expressed in terms of displacements, rotations, or other motions of a working body (tools, production and operation media and materials) as well as in presence of additional structures, phases, and in increase in number of surfaces that separate them, absorbing excess energy and simultaneously preserving surfacing or operation process in one or several certain states.

Consequently, efficiency of surfacing and operation of surface is increased by using additional energy fluxes and degrees of freedom of system components. As the energy concentration increases, as a result of evolution, a zone of interaction of energy flux with the surface is transformed from a volume-distributed system to many local systems, which are focused subsequently to a single spot. Because of additional degrees of freedom of system components, surfaces, phases, and structures can be renewed, thereby preserving processes of interaction between energy fluxes and the surface under certain conditions.

We will consider some methods, combining various surfacing operations and stages of operation of surfaces, in each of which one energy source from group I, II, and III is applied. A three-dimensional source, such as plasma arc, can be used for application of a coating of powder or wire and for preheating in the process of cutting and deformation by a freely rotating rotary tool. Many local sources are used for electromagnetic facing of powder, followed by plastic surface deformation and smoothing of the heated surface. A single focused surface is used for electron beam heating of surfaces with coatings, for modification of surfaces by ion implantation and ion sputtering and also allows surfacing operations to be combined with running-in in preceding a workpiece.

Since space and time scales of the considered processes involved in the use of combined methods differ substantially, different equipment and methods are used for

their examination. Now we will describe results of interaction of various matter and energy fluxes, involved in surfacing and surface operation by combined methods, successively extending and specifying recommendations for development of the next methods, considered. On the basis of the obtained results, general conclusions will be formulated for combined methods, irrespective of their specific features.

The present studies of dissipative structures and phases, developing in open manufacturing and operation systems with additional degrees of freedom, show the necessity to include the following into designing combined methods [2]:

1. In technological systems heredity is composed of matter and energy fluxes via formation of phases in a surface layer.

2. Structural stability of combined surfacing determines the phases of the layer formed and depends on the matter and energy sources used.

3. Due to additional degrees of freedom of a technological system, it is possible to control structural stability of phase formation in surface layer with the aid of matter and energy fluxes.

4. In operation stages the phases in the surface layer impose restrictions on degrees of freedom of the system and determine the order of actions in technological operations and opportunity to combine or separate them.

2. THERMODYNAMIC ANALYSIS OF TECHNOLOGICAL AND OPERATIONAL PROCESSES

From the point of view of production and operation heredity, conventional surfacing methods can produce efficient designs of modified layers. However, in the case of successive or parallel formation of various surface layers, interconnection of applied energy fluxes makes it necessary to examine the efficient design of modified layers.

System Analysis of Combined Surfacing Methods. In order to describe the development of surface layers, subjected to concentrated energy fluxes, it is necessary to study an open technological system with additional degrees of freedom D and to examine the formation of dissipative structures and phases that scatter excess energy. To produce of modified layers with certain structures and phases, it is necessary to examine relation of degrees of freedom of a system to forming phases, to determine the optimal number and structure of interconnections between degrees of freedom, and as a result, to locate particular phases in surface layers of a workpiece by optimising degrees of freedom.

The number of phases (structures) P, corresponding to the number of components C in structure, and the number of variables of imposed fields (energy fluxes) F is defined by Gibbs equation:

$$P = C + F - D.$$

The equation is obtained for a closed equilibrium system, proceeding from the fact that

$$F^* = U^* - T\varepsilon = const \text{ or } Z^* = H^* - T\varepsilon = const,$$

where F* – free energy of a system; U* – internal energy; T – absolute temperature; ε – entropy; Z* – thermodynamic potential; H* – enthalpy. Moreover, these conditions can be satisfied for an open system as well, when additional energy fluxes are scattered completely by dissipative structures. According to the second thermodynamic principle (ψ ≥ 0, σ ≥ 0), dissipation function and entropy production ψ = Tσ = Tdε/dτ increase with time τ in closed conditions, in the process of evolution with dε ≥ 0, a system tends to an equilibrium state, in which ε = max; in this case entropy production does not increase: dσ ≤ 0. In an open system evolution condition is preserved; dσ ≤ 0, and equilibrium condition assumes σ = min, dσ = 0 at the time derivative dσ/ dτ ≤ 0.

According to Prigogine − Glensdorff basic theorem, in the case of evolution to a stable state in τ, arbitrary systems with time-constant boundary conditions satisfy evolution condition (dσ ≤ 0), stable-state condition (dσ = 0), and stability condition (δσ ≥ 0).

Consequently, initial conditions are satisfied for both closed and open equilibrium systems, and for the latter − an additional constraint dσ/dτ ≤ 0 appears, and consequently, Gibbs equation allows examination of open systems.

In concrete operations of manufacturing process and in concrete stages of operation on a workpiece, with a constant number of components C of structure and supplied energy fluxes F, the degrees of freedom D of a system allow the developing phases P to be controlled in accordance with Gibbs equation.

Since a production-operation system is sensitive to initial conditions, it can be expressed rationally as a strange attractor, for which three degrees of freedom are sufficient to arise in a chaotic regime. Consequently, in order to avoid unpredictability of determinate matter and energy fluxes, for their dissipation a system should have no more than two degrees of freedom.

Projecting of Combined High-Performance Methods of Surfacing. According to energy concentration, that allows to describe interaction of energy fluxes with modified and operated surface, combined high-performance methods were studied, in each of which one type of source was used (Table 1).

Table 1. Number of Material Components C, Energy Fluxes F, Phases P, and Degrees of Freedom D in Different Stages of Technological Process and Operation of Workpiece

Stages	Energy interaction zones		
Technological process	I. Bulk	II. Multiply-localized	III. Single-focused
	C+F = P+D	C+F = P+D	C+P = P+D
a)	1+3 = 3+1	2+2 = 2+2	2+2 = 3+1
b)	1+3 = 4+0	2+2 = 4+0	2+2 = 4+0
c)	1+3 = 2+2	2+2 = 3+1	2+2 = 2+2
Operation	3+2 = 3+2	3+2 = 4+1	3+2 = 5+0
	C+P = F+D	C+P = F+D	C+P = F+D
	III′.Failure	II′.Friction	I′Running-in

I. A three-dimensional source was used for to apply coating and rotary cutting with plasma heating. Since homogeneous materials were used, the number of components is C = 1. Plasma preheating and normal and tangential loads, providing both translational and rotational deformation modes, determine the number of imposed fields F = 3.

Rotation of rotary tool over a wide range of velocities provides degree of freedom D = 1 to a technological system and forms phases P = 3: a coating of large thickness (3 - 4 mm) and zones of thermal effect and deformation hardening (Table 1, Ia).

In order to create an additional zone of thermodynamic hardening (P = 4), it is necessary to fix rotational velocity of the tool and deprive a technological system of degree of freedom D = 0 (Table 1, Ib). By virtue of self-organisation of thermal deformation processes in cutting and friction and by dissipation of excess energy, the system tends from this unstable state D = 0 to stable one D = 2, in which thermo-mechanical processes P = 2 occur over the entire depth (Table, Ic).

II. Multiple local sources were used for electromagnetic surfacing by superficial plastic deformation with the use of ferromagnetic powders, that were applied in a thin layer (up to 1 mm) to a steel substrate, so D = 2. Electromagnetic fields determine F = 2. Thermo-mechanical processes are provided by D = 2 degrees of freedom and form P = 2 phases, namely, a coating and a substrate (Table 1, IIa). An attempt to render the upper coating layer amorphous by intense heating failed, since the coating becomes (including partly) over its entire area of a small thickness under high-intensity heat removal to the substrate or it remains nonamorphous. At temperature gradients, necessary for rendering the surface amorphous, heat flux is directed to the substrate, which gives rise to a new zone of thermal effect, while the number of phases becomes P = 4, and the system loses degrees of freedom D = 0 (Table, IIb). The surface becomes amorphous only over the entire depth of the coating at P = 3, and the formed coating acquires a mechanical degree of freedom of motions D = 1 (Table 1, IIc).

III. A single focused high-energy source was used in electron beam heating of a coated surface and in combined ion modification of a surface. In these methods C = 2 components are used, namely, a substrate material and a material of an implanted or deposited coating (3-6 μm in thickness). The number of energy fluxes is F = 2, namely, a flux of deposited ions and an electron or ion beam. A wide range of intensity of electron or ion radiation provides a degree of freedom D = 1 to a system and forms P = 3 phases, namely, a coating, a substrate, and a zone of thermal effect or implantation (Table 1, IIIa). Layer-by-layer formation (as a result of thermo-capillary convection with beam-induced fusion of a surface) of hexagonal and cylindrical cells or formation of clusters of implanted ions gives rise to a new phase (P = 4) in a surface layer and deprives the system of degree of freedom (D = 0) (Table 1, IIIb). The system tends from this unstable state D = 0 to state with D = 2 degrees of freedom. In the process of structure forming, intense mixing of components takes place in liquid phase. At walls and in corners of the cells components, that reduce surface tension of the melt, are concentrated. In the case of intense formation of clusters, followed by deposition of a coating, phase interfaces are smeared. The described process results in formation of single phase of combined action, that, together with the substrate, forms P = 2 phases and provides D = 2 degrees of freedom to the system for the intensities of both coating deposition and beam surfacing (Table 1, IIIc).

I'. Two counterbodies and the medium (C = 3) participate in the operation of surfacing. The processes are thermo-mechanical (F = 2). During running-in, oxygen-doped amorphous-crystalline alloys are produced on the surfaces of the counterbodies, and the number of phases increases to P = 5, which deprives the system of degrees of freedom (D = 0) and makes the state unstable (Table 1, I').

II$^{'}$. At the stage of developed wear, an oxygen-doped alloy, common for counter-bodies, is produced in friction process, the number of phases decreases to P = 4 and a degree of freedom (D = 1) appears, that provides translational mutual displacements of coupled bodies (Table 1, II$^{'}$).

III$^{'}$. When a surface is damaged, one more degree of freedom D = 2 appears due to rotation of pricked-out particles, and the number of phases P = 3 becomes equal to that of the components (Table 1, III$^{'}$).

In technological systems heredity is composed of matter and energy fluxes via formation of phases in a surface layer. Structural stability of combined surface determines the phases of the formed layer and depends on the applied matter and energy sources. Due to additional degrees of freedom of a technological system, it is possible to control structural stability of phase formation of in a surface layer with the aid of matter and energy fluxes. In operation stages the phases in a surface layer impose restrictions on the degrees of freedom of a system and determine the order of actions in technological operations and the opportunity to combine or separate them.

Output, energy concentration, the number of additional degrees of freedom of sources, tools, technological medium and surfaced materials, and their interactions are increased by self-organisation, and this increase is evolutionary. Combined surfacing and processing of workpiece are determined by cooperative nonlinear phenomena and effects involved in the interaction of various matter and energy fluxes. Structures of the produced workpiece, such as phases, layers, and surfaces, are dissipative, self-organising and are inherited during formation and processing.

Location of the structures is described by boundary conditions and is determined by the position of technological and operational barriers, which can be defined as the second derivative of pulsed matter and energy transfer in time and space. The state of the structures is described by initial conditions and is determined by the magnitude of the barriers, and transition from one state to another should be accompanied by pulsed matter and energy transfer, that reorganises the barriers. In the process of formation and operation of a workpiece, an open production system can be controlled through interrelated boundary and initial conditions by changing position and magnitude of technological and operational barriers.

Dissipative self-organizing structures are inherited and reorganised during surfacing and processing of a workpiece. It is necessary that structures are to be inherited or reorganised into new state successively from operation to operation with minimum pulses of matter and energy transfer. It is reasonable that, while forming a workpiece surface, technological barriers and surfacing operations are to be arranged in the order, opposite to that of the technological barriers and actions in operation stages.

CONCLUSIONS

Nowadays improving quality of manufactured product, its safety and durability is a vital issue of the mechanical engineering. It is possible to find a solution to this problem through managing the technological processes taking place during the manufacturing of machine parts.

Performance of machine details is known to depend not only on the physical and chemical properties of the materials they are made of, but also, on the state of their

surface layers. It has been established that manufacturing of machine parts from one and the same material but using different techniques or modes of surface treatment results in dramatic changes in surface characteristics, the durability of such parts being radically different.

When applying the effects of energy or substance flows, it is necessary to thoroughly investigate the accuracy, physical and mechanical properties, taking into account the effect of maintenance heredity. It means that all the operations, their technological transitions and maintenance stages should not be studied separately, but as interrelated ones, since the characteristics of the treated surfaces are formed by the entire complex of technological effects and undergo changes in the course of machine parts maintenance.

In addition, it is necessary to consider synergetic effects created by the complex of technological effects whose total influence is greater than the sum of separate effects. Such an approach has become possible due to synergetics – the field of knowledge which deals with defining general laws in the processes of formation, stability and disintegration of ordered time and space structures in complicated non-equilibrium systems of diversified nature.

During the process of physico-chemical treatment the surface layer of the machine part absorbs a considerable amount of energy within a short period of time, which results in the formation of non-equilibrium structures accumulating excess energy. These non-equilibrium structures possessing great energy tend arbitrarily to a state with less free energy, which ensures the increase of strength, wear and other performance characteristics of the surface layer.

After a certain period of time the structures pass into a more stable state of a thermodynamic equilibrium when free energy of the surface layer is minimal. The amount of internal energy accumulated by the structures reduces, and the bound energy of the system described as a product of temperature multiplied by enthropy increases. As a result, part of absorbed energy of the ordered effect is transferred into the energy of the disordered process and, finally, into heat.

Thus, irreversible processes of heredity and self-organization take place in the surface layer, resulting in the formation of a complex of structures, since these processes are superimposed and act jointly subjected to flows of energy and matter introduced and transformed. Control over the energy and matter absorption processes with layer after layer being subjected to physico-chemical effects makes it possible to synthesize and create structures meeting the necessary maintenance demands and, also, "design" surface layers of a workpiece.

REFERENCES

1. Kheifetz M., Kozhouro L., Shipko A. & Senchilo I.: *Development of combined high-flux workpiece surfacing methds*. I. Analisis of thermomechanical surfacing, Journal of Engineering Physics and Thermophysics, Vol. 68, No. 6, pp. 748 – 757, ISSN 1062-0125, 1995.

2. Kheifetz M., Kozhuro L. & Mrochek J.: *Processes of self-organization as a result of surface layer*. IMMS NANB, ISBN 985-6477-09-3, Gomel, 1999.

3. Yashcheritsyn P. I., Kozhuro L. M., Kheifets M. L., & Chemisov B. P.: Dokl. Nats. Akad. Nauk Belarusi, 41, No. 3, 121-127, 1997.

Paweł KRZACZEK
Grzegorz DZIENISZEWSKI*

Uniwersytet Przyrodniczy w Lublinie, *Uniwersytet Rzeszowski

ANALYSIS OF ENERGETIC PARAMETERS OF JOHN DEERE 6620 AGRICULTURAL TRACTORS

Measurement of energetic parameters is one of the most important factors enabling efficient exploitation of agricultural tractors. Knowledge of these parameters is necessary for assessment of vehicle work economics but also enables determination of its present technical condition. Goal of this work was determination of energetic parameters of John Deere 6620 agricultural tractors. Courses of external characteristics of torque M_{oz}, power N_{ez}, hourly G_c and unitary fuel consumption g_{ez} were determined. Research concerned tractors equipped with straight 6 cylinder engine powered by dispenser supply system or by distributor injection pump with turbocharger and intercooler. Tractor engine energetic parameters obtained as a result of such investigations enable evaluation of energetic "saturation" of a tractor. Mainly its energy consumption and ability to work in changing work conditions including changes of load and rotation speed.

INTRODUCTION

Measurement of energetic parameters is one of the most important factors enabling efficient exploitation of agricultural tractors. Knowledge of these parameters is necessary for assessment of vehicle work economics but also enables determination of its present technical condition [1, 4, 8, 9].

There are approximately 12,2 million hectare of arable land, and level of mechanization of agriculture expressed in number of tractors per 100 ha of AL (arable land) increased from 7,4 in 1995 to 9,0 in 2005. At the same time number of exploited agricultural tractors showed growing tendency and in 2005 reached 1437 thousand units. Average nominal power of used tractors increased from 31,2 in 1995 to 39,5 kW in 2005 [2, 3, 7, 10].

The most commonly found in polish agriculture in 2005 were tractors with power ranging from 25-49 kW, which made up 32,3% of all tractors. At the same tame the least populated group were tractor of power above 100 kW, which made up 2,15% of all tractors. In years 1996-2005 number of tractors, in all ranges of power, increased. However, the greatest increase concerned vehicles which power ranged from 60 to100 kW (37,6%) and above 100kW (23,6%). The least increase was observed in case of tractors of power between 25 and 40 kW (1,3%). It should be noted that the most significant increase was observed for 60-100 kW tractors. According to various sources, such tractors will, in future, be a basis in many polish farms [5, 6, 11].

Above presented data reflects situation on Polish tractor market. Increase of number of 60-100 kW and above 100 kW tractors is observed as well as, expressed in percent, participation of these in the total number of all used tractors. Therefore, John

Deere 6620 agricultural tractors were chosen for this research as they represent power range form 60 to 100 kW. Goal of this paper was evaluation of energetic parameters such as torque, power, hourly and specific fuel consumption of John Deere 6620 tractors, and their comparison with other types of tractors used on Polish market.

METHODS

Research comprised John Deere 6620 tractors equipped with 6-cylinder, 6788 cm^3, in-line engine, marked 6068HL47 or 6068HL272. Engine nominal power $N_{Fnom} = 92$ kW at nominal rotational speed $n_{NOM} = 2300$ rpm, maximal power $N_{Fmax} = 97$kW at $n_N = 1900$ rpm, power on power take-off shaft $N_{Fwom} = 81$kW at nominal rotational speed WOM = 1000 rpm, maximal torque 508Nm at 1500 rpm, minimal specific fuel consumption $g_{Fmin} = 206$ g·kWh^{-1}, and transmission ratio between rotational speed of engine and power take-off shaft $i_{wom} = 2,208$. Engines were equipped with Denso dispenser supply system Common Rail HPCR or distributor injection pump DE10 with turbocharger and intercooler. They were cooled by means of coolant fluid with viscous fan and temperature adjustment. Construction of vehicle was based on a frame, enabling utilization of modular design concept, which facilitates configuration, use and servicing of a tractor.

Before conducting research, equipment and technical condition of investigated tractor had been checked by means of visual inspection and interview with tractor user.

Next action was readout information contained in on-board diagnostic system by liquid crystal display. After connection with on board diagnostic system was established, verification of previously gathered informations was conducted. During conducted research, in real time, following diagnostic parameters were monitored in on-board diagnostic system: air temperature T_{ot}, atmospheric pressure p_a, fuel temperature T_p, coolant temperature T_{ch} and temperature of hydraulic oil T_h.

In order to evaluate energetic parameters such as torque and power output of agricultural tractor, PT 301 MES device was used. It enabled measurements of these parameters on power take-off shaft (PTO). This device is a mobile dynamometric stand enabling measurements in vehicle workplace. The only limitation for its use is possibility of connecting it to a source of, depending on its load level, 400 or 240V current supply. Measuring range for maximal torque and maximal power, that can be absorbed by the brake, reaches 5800Nm and 340kW respectively, and depends on time of operation and conditions at the site.

In order to take measurements, the tractor was placed on even surface and in line with the brake axis and power take-off shaft of the tractor was connected with a terminal of the brake by properly chosen transmission shaft. Following task was determining rotation speed ratio of the engine and the dynamometric stand by establishing ratio of rotational speed between the tractor engine crankshaft and power take-off shaft $i_{wom} = 2,208$. Measurements of torque M_o and power N_e were carried out under full load and variable rotational speed. Relying on above mentioned data, reduced torque M_{ozr} and reduced power N_{ezr} were calculated. Obtained maximal values of measured parameters were compared with producer specifications. Measurements of energetic parameters: power and torque were carried out in conformity with DIN 70020 standard, while calculating them to reduced conditions according ISO 3046 standard.

Investigated vehicles were equipped with fully electronically controlled dispenser supply system Common Rail or distributor injection pump, hence, measurement of hourly fuel consumption G_l [l·h^{-1}] was carried out by means of FM3-100 measuring set. It required interference into fuel supply system by connecting to suction and return pipe (differential fuel flow measurement). In order to minimize influence of the device on functioning of fuel supply system, pipes of the set were installed on injection pump suction. The device is equipped with its own fuel container, filters, radiator, fuel heater, feed pump, control console and RS 232 interface connector. It must be noted that pressure, in the fuel supply system of the device, can be adjusted to requirements of investigated vehicle.

Measurements of hourly fuel consumption G_l were conducted simultaneously with measurement of torque M_o and power N_e. At the same time readings of air temperature T_{ot}, atmospheric pressure p_a were registered. Based on these measurements hourly fuel consumption G_c expressed in [kg · h^{-1}] was calculated according to formula:

$$G_c = G_l \cdot \rho_p \ [\text{kg} \cdot \text{h}^{-1}]; \tag{1}$$

Than specific fuel consumption was determined according to formula:

$$g_e = \frac{1000 \cdot G_c}{N_e} = \frac{1000 \cdot G_c}{M_o \cdot 2\pi \cdot n} \ [\text{g} \cdot \text{kWh}^{-1}]; \tag{2}$$

where: G_c – hourly fuel consumption [kg · h^{-1}], N_e – power output [kW], M_o – torque [Nm], n – engine rotational speed [rpm].

Moreover, flexibility coefficient e (3), enabling evaluation of suitability of vehicle for traction tasks, was determined. This coefficient is product of torque flexibility coefficient e_m (3) and rotational speed flexibility coefficient e_n (3).

$$e = e_m \cdot e_n = \frac{M_{max}}{M_N} \cdot \frac{n_N}{n_M} \ ; \tag{3}$$

where: M_{max} – maximal torque [Nm], M_N – torque at maximal power [Nm], n_N – maximal power rotational speed [obr · min^{-1}], n_M – maximal torque rotational speed [obr · min^{-1}].

METHODS OF INVESTIGATED ENERGETIC PARAMETERS EVALUATION

Relying on measured and calculated energetic parameters, for the investigated tractors, curves of external characteristics of reduced torque M_{oz}, reduced power N_{ez}, hourly G_c and specific fuel consumption g_{ez} were drawn. Than characteristic energetic parameters were determined:

- for engine nominal rotational speed: nominal power N_{nom}, torque for nominal power M_N, specific fuel consumption g_{ez};
- maximal power N_{max}, rotational speed for maximal power n_N, torque M_{Ne} and specific fuel consumption g_{ez};

- for power take-off shaft nominal rotational speed: power N_{wom}, torque M_{wom} and specific fuel consumption g_{ez};
- maximal: torque M_{max}, rotational speed n_{Mmax} and specific fuel consumption g_{ez};
- minimal specific fuel consumption g_{min} and rotational speed for this point.

RESULTS AND DISCUSSION

Obtained research results were presented in diagrams (Fig. 1-3), and comparison of, recorded during the course of research, characteristic diagnostic parameters and producer specifications were laid out in tables 1 and 2.

Investigated John Deere 6620 tractors yielded maximal power N_{max} ranging from 86,4 kW to 88,6 kW, what made up from 89,1 to 91,3% of value specified by a producer. Brake specific fuel consumption g_{Nmax} for maximal power was below mean for tractors used in Poland and ranged form 229,9 to 243,9 g·kWh^{-1}, while vehicles used in Poland stay within 225,0 to 273 g·kWh^{-1} range [5]. Obtained maximal torque M_{max} was from 452,3 to 473,3 Nm, that is 83,3 to 87,2% respectively of value specified by a producer. For investigated John Deere 6620 tractors nominal power N_{nom} ranging from 82,0 kW to 82,9 kW was recorded, what made up from 89,1 to 90,1% of value specified by a producer. Values of all presented parameters were lower than values specified by a producer. It can be noticed that 8,7% to 10,9% of energy is consumed during transmission of power to the power take-off shaft.

Other symptom of energy consumption is value of minimal specific fuel consumption g_{min}, which ranged form 229,8 to 238,8 g·kWh^{-1}, and was from 11,6% to 15,9% higher than specified by a producer. It must be noted that difference between data obtained and specifications results from necessity of powering subassemblies such as hydraulic system, electro-hydraulic gearbox control system and the like.

Fig. 1. Progress of changes in torque M_{oz}, power N_{ez}, hourly G_c and brake specific fuel consumption g_{ez} for John Deere 6620 tractor external speed characteristics on the basis of data from PT 301 MES and FM3-100 devices (measurement 3)
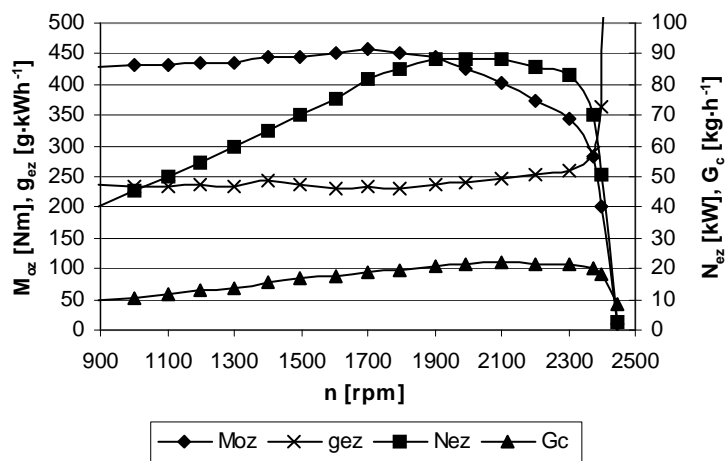
Power value at power take-off shaft N_{wom} was from 84,1 to 85,8 kW and was 3,8% to 5,9% higher than value specified by a producer, which proves that investigated vehicles were in a very good technical condition. It must be noted that, this is a parameter which describes condition of the vehicle best, and should be, for users, indicator to be taken into consideration when implements for a tractor are chosen.
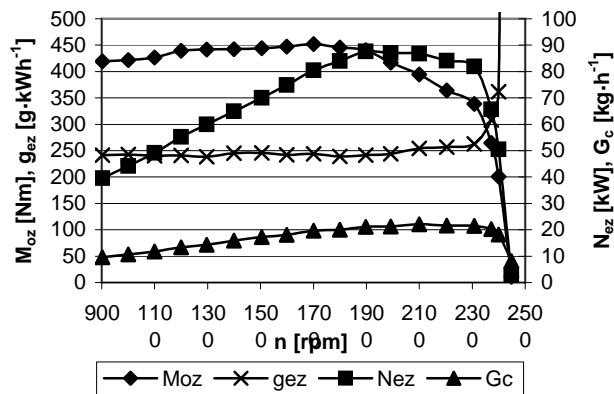
Fig. 2. Progress of changes in torque M_{oz}, power N_{ez}, hourly G_c and brake specific fuel consumption g_{ez} for John Deere 6620 tractor external speed characteristics on the basis of data from PT 301 MES and FM3-100 devices (measurement 4)
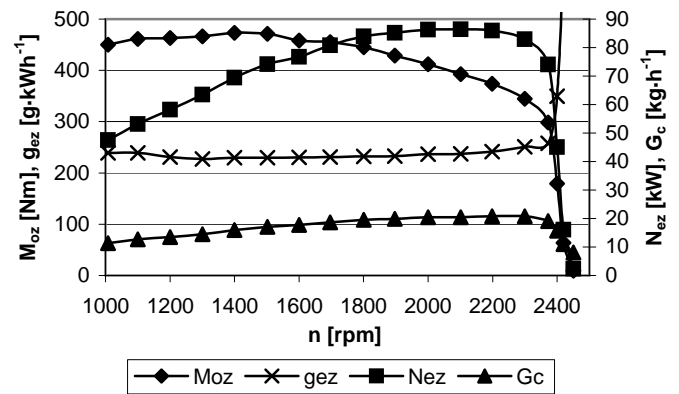
Fig. 3. Progress of changes in torque M_{oz}, power N_{ez}, hourly G_c and brake specific fuel consumption g_{ez} for John Deere 6620 tractor external speed characteristics on the basis of data from PT 301 MES and FM3-100 devices (measurement 8)

Table 1. Results of energetic parameters measurements of John Deere 6620 agricultural tractors

Model (meas. nr)	Maximum power				Maximum torque			Nominal power			
	N_{max} (kW)	n_{Nmax} (rpm)	g_{Nmax} (g·kWh⁻¹)	M_{Ne} (Nm)	M_{max} (Nm)	n_{Mmax} (obr·min⁻¹)	g_{ezm} (g·kWh⁻¹)	N_{nom} (kW)	n_{nom} (obr·min⁻¹)	M_N (Nm)	g_{ez} (g·kWh⁻¹)
6620 (4)	87,6	1898	241,3	440,6	452,3	1700	243,9	82,0	2300	338,7	262,5
6620 (3)	88,6	1992	239,1	424,8	458,1	1700	232,3	82,9	2300	344,3	260,2
6620 (8)	86,4	2101	237,2	392,7	473,3	1400	229,9	82,9	2300	344,4	250,9

Model (meas. nr)	PTO power				Specific consumption		Flexibility			Increse of torque - p [%]
	N_{wom} (kW)	n_{wom} (obr·min⁻¹)	M_{wom} (Nm)	g_{ez} (g·kWh⁻¹)	g_{min} (g·kWh⁻¹)	n_g (obr·min⁻¹)	e_m	e_n	e	
6620 (4)	84,1	2208	364,2	256,7	238,8	1800	1,03	1,12	1,15	34
6620 (3)	85,7	2208	371,8	252,9	231,9	1797	1,08	1,17	1,26	33
6620 (8)	85,8	2208	368,5	241,3	229,8	1502	1,21	1,50	1,81	37

Table 2. Comparison of research results and technical date for John Deere 6620 agricultural tractors

Model (meas. nr)	N_{max}/N_{Fmax} (%)	M_{max}/M_{Fmax} (%)	N_{nom}/N_{Fnom} (%)	N_{wom}/N_{Fwom} (%)	g_{min}/g_{Fmin} (%)
6620 (4)	90,3	83,3	89,1	103,8	115,9
6620 (3)	91,3	84,4	90,1	105,8	112,6
6620 (8)	89,1	87,2	90,1	105,9	111,6

Results of investigation of 6620 model show that torque flexibility e_m was from 1,03 to 1,21 and rotational speed flexibility e_n was from 1,12 to 1,50, while flexibility of the engine as a whole e ranged from 1,15 to 1,81. Obtained results are lower than values presented in literature concerning vehicles used in Poland [5].

During analysis of torque curve course, it was noted, except for measurement 8, that tractors had relatively flat course of torque curve. It results mainly from a method of controlling the vehicle engine work (fully electronic control). Based on course of torque and power curves, statement that, for the investigated vehicles, optimum engine rotational speed ranges form 1700 to 2300 rpm can be made. It is proven by course of

power curve, which value, within above presented rotational speed range, remained at similar level.

CONCLUSIONS

Measurements of energetic parameters: effective power N_e, torque M_o, hourly G_c and specific fuel consumption g_e, by means of utilization PT 301 MES dynamometric stand and FM3-100 measuring set, in range of nominal rotational speed of power take-off shaft, enable precise evaluation of technical condition of investigated tractors. For all investigated John Deere 6620 tractors value of obtained power N_{wom} exceeded values specified by a producer, which proves that the vehicles were in a very good technical condition.

Determining characteristics of torque, power and specific fuel consumption course, enabled determination of engine work optimum rotational speed range, which, in case of John Deere 6620, was from 1700 to 2300 rpm.

Measurement, carried out by means of mobile dynamometric stand utilization, enables evaluation of energetic parameters at site where vehicle is used. It eliminates necessity of transporting vehicles to special centres. However, the method of measuring fuel consumption requires interference in fuel supply system. Therefore, knowledge of technical documentation of this system is a must. Other solution could be utilization of on-board diagnostic system and implemented in it algorithms of fuel consumption measurement, what would eliminate need of disassembly of some of fuel supply system elements.

REFERENCES

1. Chłopek Z.: *Tendencje rozwojowe w napędach autobusów miejskich*. Eksploatacja i Nieza-wodność, 1/(29), 2006. s. 3-9.
2. GUS 2002: *Środki produkcji w rolnictwie w 2002 r.* Główny Urząd Statystyczny. Warszawa 2002.
3. GUS 2006: *Charakterystyka gospodarstw rolnych w 2005 r.* Główny Urząd Statystyczny. Warszawa 2006.
4. Havlíček M., Bauer F.: *Wpływ parametrów pracy agregatu do orki na ekonomiczność silnika ciągnikowego*. Inżynieria Rolnicza. Nr 3 (63), 2004. s. 197-200.
5. Kamiński J. R.: *Analiza parametrów energetycznych ciągnika URSUS 1134*. Inżynieria Rolnicza 3(91), 2007. s. 67-73.
6. Kruczkowski M.: *Ocena parku ciągnikowego krajowego rolnictwa – 2000*. Wieś Jutra. Wrzesień 9 (38), 2001.
7. Mróz M.: *Kierunki przemian w wyposażeniu rolnictwa w ciągniki różnych klas mocy*. Problemy Inżynierii Rolniczej Nr 3/2005. IBMER. Warszawa 2005.
8. Piekarski W.: *Analiza oddziaływania agregatów ciągnikowych na środowisko przyrodnicze*. Rozprawa habilitacyjna, Wyd. Akademia Rolnicza, Lublin, 1997, ISSN 0860-4355.
9. Rychlik A.: *Metody pomiaru zużycia paliwa pojazdów użytkowych*. Eksploatacja i Niezawodność, 4/(32), 2006. s. 37-41.
10. Skrobacki A.: *Motoryzacja polskiego rolnictwa na tle innych krajów Unii Europejskiej*. Wieś Jutra. Sierpień/wrzesień 8-9 (73-74) 2004.
11. Szeptycki A.: *Stan i kierunki rozwoju techniki oraz infrastruktury rolniczej w Polsce*. Praca zbio-rowa pod redakcją A. Szeptyckiego. IBMER Warszawa, 2005. s. 237.

Index of authors